UNIVERSITÀ DEGLI STUDI DI SALERNO

Dipartimento di Ingegneria Civile

Dottorato di Ricerca
in
Rischio e Sostenibilità
nei Sistemi dell'Ingegneria Civile, Edile ed Ambientale

XXXIV Ciclo (a.a. 2020-2021)

Multi-phase large deformation modelling of flow-like landslide interaction with protection structures

Angela Di Perna

Il Tutor
Prof. Sabatino Cuomo
Co-Tutors
Prof. Manuel Pastor
Dott. Ing. Mario Martinelli
Dott. Ing. Lorenzo Frigo

Il Coordinatore
Prof. Fernando Fraternali

Acknowledgments

The research was developed within the framework of Industrial PhD Course (POR Campania FSE 2014/2020) with the title “Sviluppo di sistemi ecocompatibili per la difesa del territorio e delle attività produttive”. The project involved the company Geosintex s.r.l (https://www.geosintex.com/) as industrial partnership and the department of “Matemática e Informática Aplicadas a la Ingenieria Civil” (Universidad Politécnica de Madrid) in the figure of Prof. Manuel Pastor. All the MPM simulations were performed using a version of Anura3D (www.anura3d.com) developed by Deltares, thanks to the collaboration with Dr. Mario Martinelli.

Abstract

The study on impact mechanisms of flow-like landslides against structures is still an open issue in the scientific literature. Many researchers have employed so far either experiments or numerical methods, but the evaluation of the impact forces on mitigation obstacles remains difficult especially if the solid-fluid interaction within the flow is considered. In addition, flow-like landslides are often characterized by large deformations, which depend on slope geometry, soil type and triggering mechanisms. Throughout the past decades many numerical methods aiming to simulate large deformations have been introduced, as for example Discrete Element Method (DEM), Smooth Particle Hydrodynamics (SPH), Updated Lagrangian Finite Element Method (UL-FEM) and Material Point Method (MPM). All of them are based on different theories, capabilities, and accuracy, but the complexity is their common feature. In fact, the response of landslide body under large deformations is still unclear, especially for Landslide-Structure-Interaction (*LSI*) problems, due to: i) the hydro-mechanical features of the impacting flow, ii) the geometry and stress-strain response of the structure, and iii) initial and boundary conditions for the specific *LSI* problem. Numerical methods greatly contribute to a safer and more cost-effective design of landslide mitigation works. However, most of these approaches are very recent, and still need comprehensive validation.

The advanced numerical technique of the Material Point Method (MPM) is used in this thesis to provide a novel contribution in investigating the dynamics and the impact mechanisms of flow-like landslides against protection structures, thanks to its capability of considering both the coupled hydro-mechanical behaviour of the propagating mass and large deformations of the approaching flow. The MPM numerical method is validated against observations coming from famous landslide benchmarks (like the Fei Tsui Road landslide or the Wenjia gully debris flow) or from well documented laboratory experiments investigating the impacts of granular

flows against rigid obstacles. Then, the model is used to explore the response of different flows impacting rigid barriers, focusing the attention on the potential efficiency of different types of barriers in intercepting the propagation of the flow under several impact conditions. The study principally highlighted that the soil-fluid interaction within the flow and the barrier geometry influence the type of impact mechanism, the kinematics of the flow, and the space-time trend of the impact forces against the structure.

The satisfactory validation of MPM also allows to derive simplified analytical and empirical models for estimating the temporal trend of the impact force on a rigid structure and the kinetic energy reduction of the flow during impact. However, the assumption of rigid body used for the design of these barriers must be analysed. For this reason, additional stress-strain analyses on two different mitigation options (such as Reinforced-Concrete walls and Deformable Geosynthetics-Reinforced Barriers) were conducted for examining the extent of internal deformations and the possible ultimate limit states of the structure under impact.

As a conclusion, the research shows how multi-phase, hydro-mechanical coupled and large deformations numerical methods are of primary importance for modelling flow-like landslides dynamics and for studying the interaction mechanisms between the landslide and the structure.

Contents

1. Introduction

1.1 Motivation

Rainfall-induced landslides of the flow type in granular soils are among the most complex natural hazards due to the variety of mechanisms which regulate the failure and propagation stages.

Different mitigation measures against such hazardous phenomena can be adopted, especially in areas with high loss potential or in restricted sites. Among these control works, artificial barriers can be used to reduce the runout and the dynamic impact forces of the flow-like landslides on the exposed structures and infrastructures.

Full understanding the interaction mechanisms between flow-like landslides and the impacted protection structures is still an open issue. In fact, while researchers have used several approaches, from experimental to numerical, it is true that the adequate assessment of the hydro-mechanical behaviour of the landslide body requires both a multiphase and large deformation approach.

The interaction of flow-like landslides with rigid walls, obstacles, protection structures and, more recently, single building or cluster of buildings have been investigated by a variety of numerical tools. The massive use of numerical methods is related to the inner complexity of Landslide-Structure-Interaction (*LSI*) mechanisms, which are related to: i) the hydro-mechanical features of the impacting flow, ii) the geometry of the structure, and iii) initial and boundary conditions for the specific *LSI* problem. Numerical methods greatly contribute to a safer and more cost-effective design of landslide mitigation works. However, most of these approaches are very recent, and still need comprehensive validation combined with more efforts

to reduce the computational cost, which is very high once realistic simulations are pursued.

The advanced numerical technique of the Material Point Method (MPM) is used in this thesis to provide a novel contribution in investigating the dynamics and the of impact mechanisms of flow-like landslides against protection structures, thanks to its capability of considering both the coupled hydro-mechanical behaviour of the propagating mass and large deformations of the approaching flow.

1.2 Objectives and methodology

The main objectives of the thesis are: i) understanding the landslide dynamics from triggering to final deposition and ii) investigating their interaction mechanisms against protection structures.

More specifically, the thesis wants to examine first the applicability of numerical modelling to simulate the mechanisms that influence the inception and propagation of both progressive and retrogressive flow-like landslides. In fact, without a comprehensive knowledge of these mechanisms, the *LSI* problems cannot be defined properly. Then, the thesis aims to test whether the advanced numerical modelling is feasible for analyzing all the key factors that role the impact mechanisms of flows against an obstacle, through the calibration and validation of laboratory experience. This can help to find novel simplified methods to easily obtain the main variables that govern the dynamics of the impact process and even to analyse the failure mechanisms that a protection structure can undergo under impact.

Thus, to achieve these goals in the best way a comprehensive hydro-mechanical-coupled and large-displacement-based approach would be desirable. To this aim, an innovative numerical technique known as the Material Point Method (MPM) is used. It can be considered as a modification of the well-known Finite Element Method (FEM), but particularly suited for large deformations. The continuum body is schematized by a set of Lagrangian points, called Material Points (MPs). Large

deformations are modelled by MPs moving through a background mesh, which also covers the domain where the material is expected to move. Such advanced approach allows combining a hydro-mechanical coupled approach, any of the well-known soil constitutive models proposed over the years in soil mechanics and a large-displacement formulation.

However, a conceptual model of *LSI* is needed to be employed in any model, be it numerical or analytical. This model must describe the *LSI* problem in a realistic but simplified way, focusing on the main features of both flow and protection structure.

1.3 Thesis layout

After this introduction, a general background about the flow-like landslides, the type of impact mechanisms and their modelling is proposed in Chapter 2.

In Chapter 3, the results of the advanced numerical modelling of some typical landslide dynamics cases are shown, focusing on the simulation of the inception of debris avalanches following the impact of an instable mass (Paragraph 3.1) and on the back-analysis of the pre-failure, failure and post-failure stages of the Fei Tsui Road landslide occurred in Honk Kong (Paragraph 3.2).

Chapter 4 is dedicated to testing the MPM numerical method in simulating the whole complex Landslide-Structure-Interaction (*LSI*) mechanisms. The laboratory experiments of reduced-scale tests with dry granular flows and some centrifuge tests of saturated mixtures impacting against rigid barriers are firstly simulated and analysed. Even the breakage of an Unreinforced Masonry (URM) wall is reproduced in 3D and 2D MPM models, in response to a known external pressure applied during the experimental test. After proving the capabilities of MPM in simulating the several *LSI* problems, its applicability to a real-scale landslide (the Wenjia gully debris flow case from China) is tested, even considering some rigid barriers along

the flow path, and finally to investigate different impact scenarios between flows and fixed/unfixed rigid barriers.

In Chapter 5, more simplified models (such as analytical and empirical models) are proposed to estimate the impact force and the kinetic energy temporal distributions. The calibration and validation of the analytical and empirical models are pursued, respectively, based on the MPM numerical results of the model, and referring to a large dataset of field evidence for peak impact pressure. Finally, the performance of the newly proposed methods is compared to those of the methods available in the literature.

Chapter 6 introduces and discusses the applicability of Reinforced-Concrete (RC) walls and Mechanically Stabilized Earth (MSE) walls as protection structures against flow-like landslides. Trough MPM numerical modelling, the Ultimate Limit States (ULS) of several structure geometries are investigated, considering two flows with different initial kinetic energy. Finally, the two proposed typologies of barriers are compared, and their advantages and drawbacks are pointed out.

Chapter 7 comprises a summary of the conclusions, even highlighting the future developments of the research.

2. Background

2.1 Features of flow-like landslides

Flow-like landslides are dangerous for people and structures around the world (Pastor et al. 2009), due to the long travel distances up to tens of kilometres and the high velocities even in the order of metres per second. According to the updated Varnes'classification (Hungr et al. 2014), such landslides show a complex behaviour with a continuum passage from sliding to flowing. This category includes dry granular flows and saturated flows with excess pore-water pressure such as flowslides or debris flows.

This type of landslides is often characterized by large deformations, which depend on slope geometry, soil type and triggering mechanisms (Cascini et al., 2010). Soil deformations may concentrate along relatively thin shear bands or occur within the whole landslide body. In the former case, a "localized" type of failure is observed, and it is challenging to reproduce the exact location of the shear bands with high soil shear strains inside, while most of the landslide body is almost undeformed. In the second case, again, a challenging task arises because the failure is "diffuse" inside the whole slope, generally with very large soil deformations. In both cases, there is the need to: *i*) smoothly reproduce the transition from "small" to "large" soil deformation when, and where, volumetric and shear strains develop, *ii*) accurately simulate soil large deformation during landslide propagation, and *iii*) capture the return from large to small deformation rates during deposition.

The solid-like behaviour (for small deformations) and the fluid-like behaviour (for large deformations) of the involved soils are very different, and such a contrast is exacerbated in the so-called flow-like landslides, which predominantly affect poorly consolidated granular soils, weathered materials, and loess all over the world (Prodan et al., 2017; Cuomo, 2020).

Unsaturated soil condition is often a key factor in the pre-failure, failure and post-failure stages of rainfall-induced flow-like landslides. Before failure, the additional strength related to matric suction is fundamental for the equilibrium of granular soil slopes steeper than the effective friction angle. During the landslide pre-failure stage, soil suction gradually reduces because of rain infiltration. At failure or in the immediate post-failure stage, peculiar soil mechanical responses may even occur such as capillary collapse, i.e., a strong reduction of soil volume related to wetting (Yuan et al. 2019) or static liquefaction (Cascini et al. 2013b). But also, during landslide propagation, pore-water pressures (positive or negative) undergo a spatial-temporal evolution depending on the accumulated deformation within the landslide body.

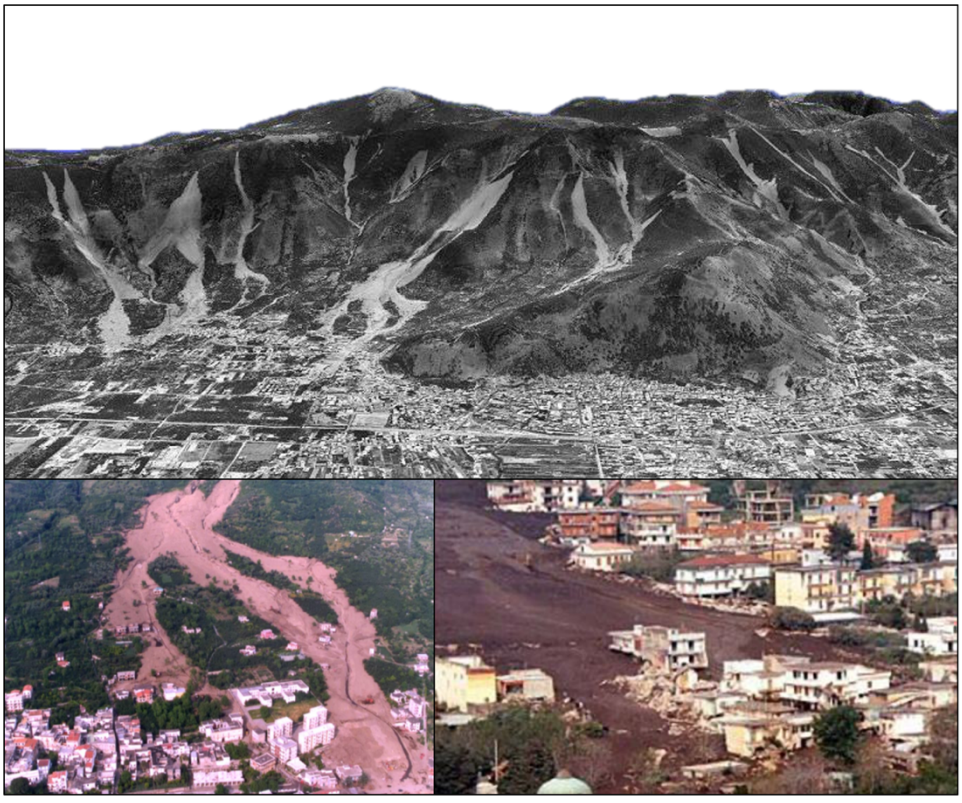

Figure 2-1. Damage caused by flow-like landslides in the Sarno area, Campania, Southern Italy, 1998 (from Cascini et al., 2011).

Flow-like landslides has been attracting the attention of scholars for (i) the threat to populations and structures and (ii) the scientific challenges related to their understanding and modelling.

The need to tackle the fundamental and sometimes urgent issue to protect populations has favoured several theories and approaches to be proposed, tested, and applied. Landslide risk zoning demonstrated to be a formidable tool to deal with technical, economic, and social aspects within a single unitary framework, applicable from site-specific cases to regional scale. Related to landslide risk zoning, either land use planning, restrictions, or regulations for the areas at risk, warning systems and communication strategies have been used to manage the threat of potential catastrophic landslides impacting urban areas.

In each of the previous tools, the topics of landslide propagation and impact process on structures must be necessarily addressed and a model (simplified or sophisticated) for landslide impact is always adopted.

For the sake of the simplicity, one may consider that any structure impacted by a flow-like landslide will be destroyed. In other term, the vulnerability of the impacted structure is assumed equal to one (i.e., total loss of the exposed element). This safe approach is widely used for risk analysis over large areas.

However, it is frequently observed that the impacted structures suffer different types of damage: (i) complete collapse, (ii) partial destruction, (iii) only damage to non-structural elements. The occurrence of any of these three cases depends at least on the urban area (dense or sparse), construction features (type, materials, age, etc.), exposure (direct or limited) and impact (frontal or lateral), and other site- or case-specific features. Thus, the analysis (and zoning) of such issues must be addressed at detailed scale. Examples are reported in Figures 2-2 and 2-3, with the different type of construction and the diverse amount of damage easily recognizable. In all the cases of those figures, flow-like landslides were induced by rainfall according to different triggering mechanisms (Cascini et al., 2008). Then, the unstable masses propagated downslope as debris flows, debris avalanches or combined phenomena (Cuomo et al., 2017a). Independent on the type, all the flows recorded in 1998, 1999,

and 2005 (and as already occurred in the previous centuries) arrived at high velocity and impacted the inhabited areas causing destruction or damage to structures.

Figure 2-2. Example of damage caused by the impact of flow-like landslides in the Sarno area, Campania, southern Italy, 1998 (from Mavrouli et al., 2014)

Figure 2-3. Example of a building destroyed by a debris avalanche occurred in the Nocera Inferiore area, Campania, southern Italy, 2005 (from Cascini et al., 2011).

2.2 Impact mechanisms of flow-like landslides against structures

The impact of flow-like landslides causes the partial or complete destruction of the hit structures (Mizuyama 1979; Hungr et al. 1984; Armanini 1997; Zhang 1993; Hu et al. 2011; Shieh et al. 2008; Hübl et al. 2009; Moriguchi et al. 2009).

Many studies focus on real-scale observations through the measurement of the impact forces of real debris flows (Zhang 1993, Wendeler et al. 2007, Hong et al. 2015) or in large-scale experiments using special equipment (Bugnion et al. 2012; Sovilla et al. 2016; Hu et al 2011; among others). The main problem however is the high cost of the installation and the maintenance of these instrumentations, given the large landslide volumes. In addition, some quantities, such as velocity, depth and other flow parameters are often difficult to know. Therefore, a second group of studies concern reduced-scale laboratory experiments (Moriguchi et al. 2009; Cui et al. 2015; Choi et al. 2016; Zhou et al. 2018, Yifru et al. 2018). Among these, centrifuge tests allow studying the soil behavior under the same stress levels of the in-situ problems, and their applicability to flow analysis has been widely confirmed (Schofield 1980, Bowman et al. 2010, Ng et al. 2017; Song et al. 2017, 2018).

In the relatively simple case of a flow impacting a vertical barrier, the dynamic mechanisms of flow-structure interaction can be grouped in two categories: complete reflection and vertical bulge (Armanini 1993, 1997, 2011; Canelli et al. 2012; Choi et al. 2015; Ng et al. 2017; Zhou et al. 2018). In the first case, a reflected wave forms and propagates away from the wall in a straight direction and with a constant wave speed. Conversely, the vertical bulge occurs when the flow propagates along the vertical wall and then falls creating a hydraulic jump.

Experimental evidence showed that for Froude number lower than unity the mechanism of reflected wave predominates, otherwise the vertical bulge takes place, and these mechanisms are observed both in homogeneous fluids and two-phase flows (Armanini et al. 2011, Song et al. 2017).

When the flow is composed by solid grains and interstitial liquid, the reflection

mechanism can be associated to the deposition of granular material just behind the structure in the so-called “dead zone”. Such deposition of debris can develop in turn according two scenarios: pile-up and run-up, as reported in the schematic of Figure 2-4 (Law 2008; Sun and Law 2011; Choi et al. 2015; Ashwood and Hungr 2016; among others).

In the former scenario (pile-up), the material behind the barrier is compressed by the approaching material, which transforms into a thin jet rising up the face of the barrier, but without overflowing. This is typical case for dry granular flows and the slope of the final debris deposit is comparable to the internal friction angle of sands (Ashwood and Hungr 2016; Ng et al. 2017; Song et al. 2017).

The run-up scenario instead is characterized by the formation of a triangular-shaped deposit behind the wall, which is overridden by the approaching flow. The latter in part goes beyond the barrier developing a vertical jet and in part settles due to the friction with the dead zone forming a new and larger material wedge. This is the typical case of partially or fully saturated granular flows which also generally have an almost-flat debris deposit (Ng et al. 2017; Song et al. 2017, 2018; Zhou et al. 2018). The time for debris filling is higher (hence the impact force is lower) for dry granular flows than two-phase flows, as observed in flume tests (Law 2008; Zhou et al. 2018). In fact, the impact depth of a dry granular flow is always less than barrier height (for moderate inclines obviously), because the flow energy decreases for the contact shearing between grains (Choi et al. 2015; Ng et al. 2017; Wendeler 2016; Song et al. 2017, 2018).

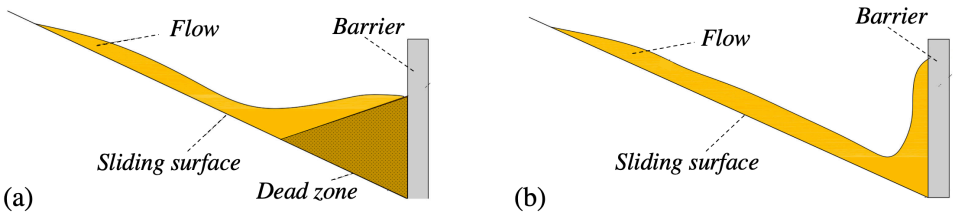

Figure 2-4. Schematic for pile-up (a) and run-up (b) impact mechanisms

The impact mechanism can be even a combination of the previous scenarios (Law 2008, Ashwood and Hungr 2016). The transition from run-up to pile-up depends on the amount of solid grains in the flow, since high solid fraction produces a well evident dead zone (Takahashi 2014; Song et al. 2017), or likewise from the water content of the flow, as a progressive accumulation of granular material behind the barrier is related to low water content (0-10%) while discrete flow surges occur for high water content (20-30%) during the impact (Zhou et al. 2018).

The availability of measurements obtained from the direct observation of impact of flow-like masses against monitored structures has been fundamental for the development of predicting impact models. On such a topic, the literature provides a few of full-scale flume experiments (De Natale et al., 1999; Bugnion et al., 2012) and a large variety of reduced-scale laboratory tests (Hübl et al., 2009; Armanini et al., 2011; Canelli et al., 2012; Ashwood and Hungr, 2016; Vagnon and Segalini, 2016). Those reduced-scale laboratory tests have been used to derive and validate the most common empirical formulations used to assess the peak impact pressure in the design of protection measures against landslide (Schield et al., 2013; Scotton and Deganutti, 1997; Arattano and Franzi 2003; Hübl et al., 2009; Proske et al., 2011; Bugnion et al. 2012; Canelli et al. 2012; He et al. 2016; Song et al., 2021). It is true that laboratory tests are affected by scale effects that cannot be properly monitored (Iverson 1997; Hübl et al. 2009), but this limitation is usually overcome by appropriate scale analysis.

The existing empirical methods can be classified into three groups: (i) hydro-static methods, which require only flow density and thickness for evaluating the maximum impact pressure; (ii) hydro-dynamic methods, based on flow density and the square velocity of the flow; (iii) mixed methods, that accounts for both the static and the dynamic components of the flow. The weak point is that the empirical formulations greatly depend on empirical coefficients which are difficult to estimate for practical applications due to their wide range of variation. Common to those approaches are the following assumptions: (i) the impact load is assumed to be totally transferred to the structure without any dissipation during the impact, and (ii) the

size, stiffness and inertial resistance of the artificial barrier are not considered (Vagnon and Segalini, 2016). These assumptions generally lead to safe assessment of the peak impact force but with large overestimation of the barrier design. Hence, enhancements will be proposed in this thesis on both these topics.

It is also remarkable that a wide set of reduced-scale laboratory experiments on dry granular flows allowed Faug (2015) to propose a so-called phase-diagram (Figure 2-5) based on: (i) Froude number (*Fr*) and (ii) obstacle height relative to the flow depth (*H*/*h*). The diagram comprises four zones: a) Dead zone (i.e. gradual accumulation of material behind the obstacle): this is the case of relatively slow flows the case of relatively slow flows (*Fr*≈*1*) impacting relatively small obstacles (*H*/*h*≈*1*); b) Airborne jet (forming downstream of the obstacle): this stands for rapid flow (*Fr*>>*1*) and obstacle height low (*H*/*h*<<*1*); c) Standing jumps (propagating downstream of the obstacle with steady-state conditions): for rapid flow (*Fr*>>*1*); d) Bores (a granular jump hits the obstacle and propagates upstream of it): in the case of a rapid flow hitting a wall spanning the entire height of the flow (*H*/*h*>>*1*) with unsteady conditions. While all these results are extremely useful and will be referred later on, a comprehensive knowledge it is still missing about the quantities from which these complex impact mechanisms of depend on, and even more important would be to assess the role of interstitial fluid on the intensity and the time-dependency of the impact actions.

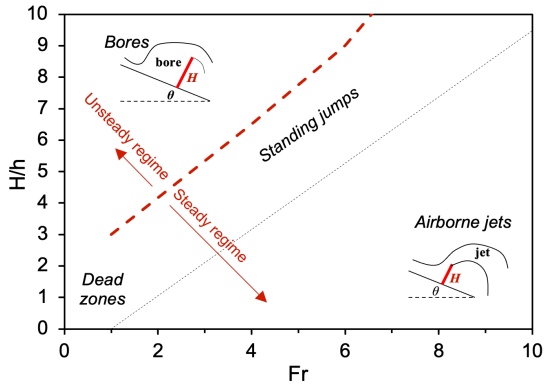

Figure 2-5. Interaction diagram for a flow impacting an obstacle (adapted from Faug, 2015)

2.3 Modelling of flow-like landslides

2.3.1 General remarks

Numerical modelling, particularly coupled hydro-mechanical large-deformation models, greatly helps in properly simulating the complex failure and post-failure mechanisms of flow-like landslides. The affected soils, in fact, evolve from none or small deformation rates to large deformation rates during the initiation stage and vice-versa during deposition, with relevant interactions between the solid skeleton and interstitial water.

Despite their potential especially for the back-analysis of case histories, the so-called empirical methods (Corominas, 1996; Cascini et al., 2011a), which relate field observations of landslide volume, morphology, etc. to the landslide run-out distance, they may quantify landslide mobility but cannot provide enough accurate information about landslide dynamic features, such as propagation height, velocity and pressure inside the moving mass. The knowledge of those features is fundamental to assess the impact forces on structures.

Therefore, analytical methods are required as they can simulate landslide propagation using physical-based equations coming from fluid dynamics, soil mechanics or mixture theories (Pastor et al., 2009; Hungr and McDougall, 2009). Among them, the Eulerian and Lagrangian approaches use a different strategy to represent the movement of a highly deformable and mobile body such as a landslide.

The Eulerian approach is common if not standard in fluid mechanics applications. The computational nodes are fixed, organized into a computational mesh, regular or not, and from there the phenomenon is described by means of the governing equations. In a sense, this is the most intuitive way of describing the motion of fluids, flows or similar phenomena such a fluid-like material while it exhibits very large displacements. There are examples of models using Finite Difference Method (FDM) to compute height and velocity of different types of flows in 2D or 3D conditions (O'Brien, 1993; Cascini et al., 2011b; Arbanas et al., 2014).

But there are also Finite Element Method (FEM) models with an Eulerian formulation (Pastor et al., 2002). However, the material properties are advected across the fixed computational grid. Such a procedure causes a spurious (numerical) diffusion of history variables (e.g., plastic strains) and interfaces of heterogeneous material setting are smoothed in space through time. In addition, different than fluids, a flow-like landslide has a non-negligible amount of solid, about 50% or more as so specific requirements are needed in those models. For instance, rheological formulations including any feature of the solid particle, or definition of pore water pressure inside the moving mixture must be included.

In a Lagrangian framework, while the material is deforming, there are the computation points which are linked to it. This class of method includes the Finite Element Method (FEM), the Discrete Element Method (DEM) and Smoothed Particles Hydrodynamics (SPH).

FEM has been extensively used in Lagrangian formulation for applications in solid- and soil-mechanics, especially to simulate small strains accumulated prior of failure (pre-failure stage) and eventually also during the failure stage. The strength of such models is that accurate assessment can be done by using complex constitutive laws capable to take into account the stress path of the soil (Zienkiewicz et al., 1999; Pastor et al., 2004) and strain history including accumulation of irreversible strains. However, there is the tendency of the computational mesh to be distorted until inaccuracy and numerical instability may prevent FEM to proceed further. With such premises the description of a soil flowing at high velocity becomes demanding.

On the other hand, DEM has been conceived for modelling the motion of granular materials. Many applications are reported in the literature about modelling of granular flows compare to experimental evidence (Favier et al., 2009, Faug et al., 2011; Li et al., 2019). However, large domains and long-time series are difficult to manage due to the high number of unknowns and large time for computing the particle connectivity. However, landslides can be schematized in most of the cases and continuous media and so the discontinuous description used by DEM can be inconvenient.

SPH, although originally proposed for describing clusters of individual points/bodies, has been later used for geophysical and continuum-mechanics applications. Since many years applications to landslide propagation problems have been proposed including a number of special features such as pore water pressure (Pastor et al., 2009), bed entrainment (Cuomo et al., 2014), special boundary conditions (Lin et al., 2019).

As common feature, in the Lagrangian FEM, SPH and DEM, the computational points coincide with material points (Figure 2-5). However, this correspondence could be also avoided as proposed in some alternative methods. Among these, the Finite Element Method with Lagrangian Integration Point (FEMLIP) (Moresi et al., 2002), which has been derived from the Particle-In-Cell method (Sulsky et al., 1994), and the Material Point Method (MPM), which has been applied also to a number of different slope stability and landslide cases (Wang et al., 2016; Ghasemi et al., 2019; Cuomo et al., 2019a). Both methods, among others similar, are based on material points dissociated from the computational nodes of the Eulerian finite element mesh. The material points are used as integration points at a given material configuration. The resolution of the equilibrium equation at the mesh nodes gives a velocity field. At the end of each step, the velocity is interpolated from the nodes to the material points which are moved accordingly throughout the fixed mesh up to a new configuration. Internal variables and all material properties are stored at the material points, so that they are accurately tracked during the advection process. Thanks to the distinction between mesh nodes and material points, such approach benefits both from the ability of the Eulerian FEM (the mesh is kept fixed) to support large transformations, and from the possibility of the Lagrangian FEM to track internal variables during the material movement.

Hence, MPM is one of the most suitable method to deal with: i) static equilibrium of elasto-plastic materials in the pre-failure stage, ii) large deformations upon failure, iii) large displacements during the propagation stage while still tracking the history of material properties. A more exhaustive literature review on these topics is

provided by Cuomo (2020) and other similar contributions, while more specific details on MPM can be in Al-Kafaji (2013), Fern et al. (2019), among others.

About Landslide-Structure-Interaction (*LSI*) modelling, what is really challenging is to find a mathematical framework to properly describe the so different materials and behaviour of both the flow-like landslide and the impacted structure.

A flow-like landslide, for its inner nature, consists of a multi-phase material travelling long runout distances at high velocity, with a total volume depending on source area, hillslope features, entrainment, etc.; in addition, soils are non-linear materials with irreversible deformations depending on specific stress path. Thus, staying within reasonable computational time usually requires depth-averaged approaches or meshless numerical techniques with some mandatory assumptions about water pressure, effective stress distribution or rheological behaviour.

The impacted structure is usually a building, made of bricks or concrete elements eventually reinforced with steel bars, or eventually a passive protection structures (reinforced concrete walls, check dams, geosynthetics-reinforced barriers, etc.). It means that linear and planar structural elements are connected in complex 3D configurations. Furthermore, even if the behaviour of each single material can be nicely reproduced in continuous mechanics framework, the combined materials (e.g. bricks and mortar, or concrete and steel, soils and reinforcement) requires a structural scheme to be defined.

The interaction of flow-like landslides with rigid walls, obstacles, protection structures and, more recently, single building or cluster of buildings have been investigated by a variety of numerical tools. The massive use of numerical methods is related to the inner complexity of *LSI* mechanisms, which are related to: i) the hydro-mechanical features of the impacting flow, ii) the geometry of the structure, and iii) initial and boundary conditions for the specific LSI problem.

Recent simulations of flows interacting with rigid barriers have been afforded through Discrete Element Method (DEM) as reported by Leonardi et al. (2014), Calvetti et al. (2017) and Shen et al. (2018) or continuum mechanics models based on Eulerian methods (Moriguchi et al. 2009), Lagrangian particle-based methods

such as Smoothed-Particle Hydrodynamics (SPH), Particle Finite Element Method (PFEM), Finite Element Method with Lagrangian integration points (FEMLIP), Material Point Method (MPM), (Idelsohn et al. 2006; Bui and Fukagawa 2013; Cuomo et al. 2013, 2019b; Llano-Serna et al., 2016; Dai et al., 2017; Ceccato et al., 2018a) or coupled Eulerian-Lagrangian methods (Qiu et al. 2011; Jeong and Lee 2019).

However, none of those contributions address both the solid-fluid hydro-mechanical coupling inside the flow and the role of fluid in the soil-structure interaction.

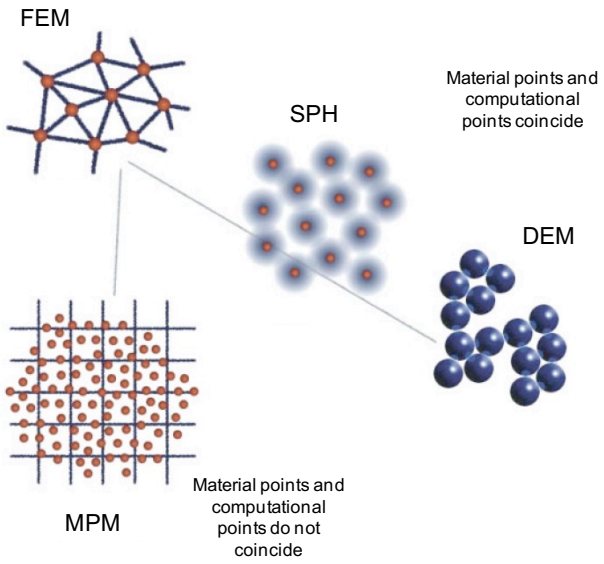

Figure 2-6. Different methods for modelling soil deformation and landslides (modified from Cuomo, 2020).

2.3.2 Examples of depth-integrated SPH modelling

Among all the methods listed above, SPH and MPM are the most promising tools for analysing flow-like landslides, therefore some examples from the literature review about the SPH method are provided in the following.

The examples chosen range over increasingly complex of mathematical formulations, going from the simple assumption of one-phase material under undrained behaviour to a two-phase material modelling with a proper propagation-consolidation formulation that considers the soil permeability and volume stiffness.

Example n° 1

Pastor et al. (2007) applied a depth-integrated SPH with coupled pore pressure to a series of flow-like landslides occurred in Hong Kong. Among these cases, the Fei Tsui Road landslide was analysed. This landslide (described in detail in Sect. 3) involved 14.000 m^3 of material, due to a combination of a weaker material together with an increase in groundwater pressure following a prolonged heavy rainfall.

The authors modelled the landslide assuming the propagating mass as a monophase frictional fluid, with an apparent friction angle (equal to 26°) smaller than the effective friction angle in order to include the existence of induced pore pressures in a simplified way. They also assumed that the time of propagation is much smaller than that of pore pressure dissipation, thus the flow was supposed to have an undrained behaviour during propagation.

The results show a good agreement about the planar extent of the landslide and about the depth of the debris deposit (Figure 2-7).

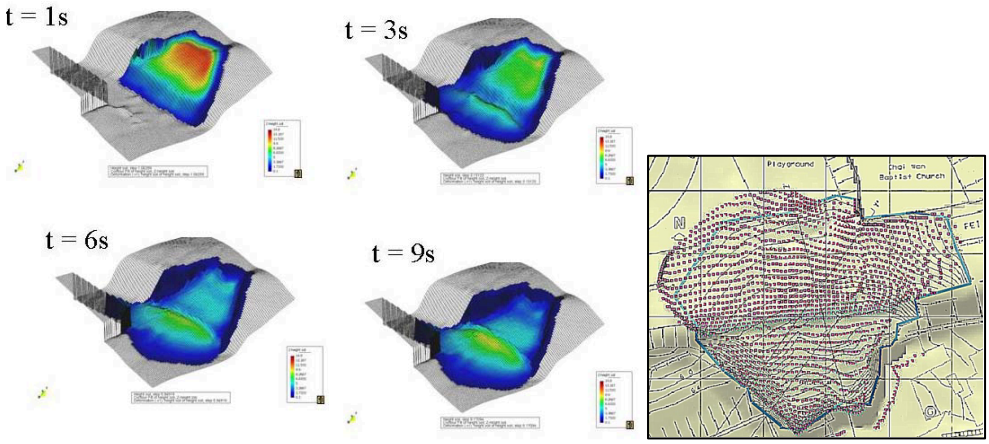

Figure 2-7. Depth-integrated SPH modelling of the Fei Tsui Road Landslide (Pastor et al., 2007).

Example n° 2

The contribution of Cascini et al. (2016) considers a more advanced SPH modelling than Pastor et al. (2007), introducing the role of the pore-water pressures during the propagation stage of flow-like landslides. In particular, the authors used the numerical model proposed by Pastor et al. (2015), which combines a 3D depth-integrated hydro-mechanical coupled SPH model for the propagation analysis and a 1D vertical FDM (Finite Difference Method) model for the evaluation of the pore-water pressures along the height of the flowing mass.

Since many flow-like landslides have small average depths in comparison with their length or width, the governing equations can be integrated along the vertical axis and the resulting 2D depth-integrated model offers an excellent combination of accuracy and simplicity. Thus, the model is 2D as it concerns its mathematical formulation, while it is 3D in its general output, which include the spatial location (X_1, X_2 in Figure 2-8a) of the deformable propagating mass and the propagation height (X_3, in Figure 2-8b) at each point of the mass. The reliability of the combined SPH-FDM model was tested for the well documented experimental laboratory tests of Iverson et al. (2010), performed in a 90 m long, 31° steep flume.

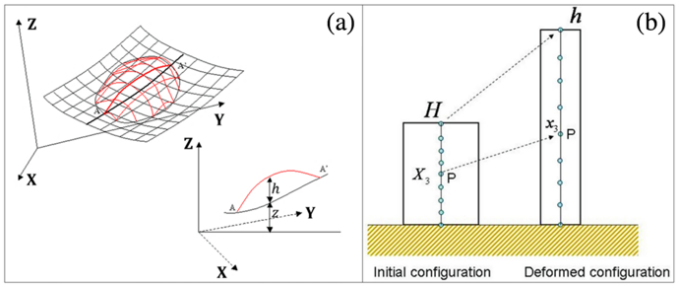

Figure 2-8. Reference system (a) and initial and deformed configuration of a column of the landslide mass (b) from Pastor et al. (2015).

Example n° 3

Tayyebi et al. (2021) tested the capability of the SPH two-phase model to reproduce the complex behaviour of natural debris avalanches where pore-water pressure

evolution plays a key role. The model is applied to reproduce the complex dynamic behaviour observed in Johnsons Landing debris avalanche. The work also evaluates the potentialities of the SPH model to simulate the bottom drainage screens like structural countermeasure for reducing the impact of debris flows (Mizuyama, 2008).

Conversely to Cascini et al. (2016), here the adopted SPH model includes the two-phase fluid-solid description of the flowing mass, considering the pore-pressure evolution taking into account the soil permeability (Pastor et al., 2021). The generalized two-phase mathematical model involves the balance equations of mass and linear momentum, completed by a suitable consolidation equation and the Voellmy rheological equation.

The numerical results show the high capability of the developed two-phase SPH model and illustrate the significant importance of the pore pressure evolution to properly reproduce the dynamics behaviour of debris flows, including the simulation of the observed bifurcation caused by the flowing out of part of the moving mass from the mid-channel (Figure 2-9a). The results also demonstrated the possibility to evaluate how the installation of the bottom drainage screens can dissipate a significant amount of energy and reduce the debris avalanche's run-out distance (Figure 2-9b).

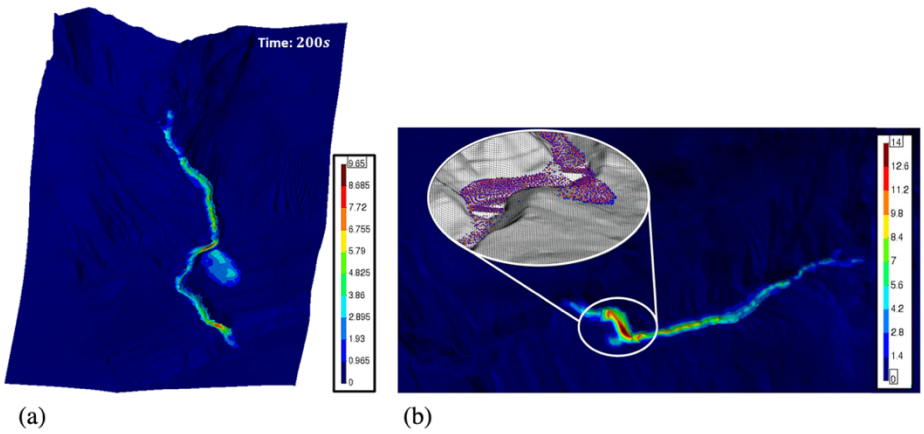

Figure 2-9. Thickness of the final deposit for SPH simulation of the Johnsons Landing debris avalanche: (a) without screens and (b) with screens (Tayyebi et al., 2021)

Advantages and limitations

Depth-integrated SPH models provide a good combination of simplification and accuracy, therefore are very useful for scientists and engineers. As all the numerical methods, the SPH method has undergone a great improvement over the years, as demonstrated by the three chosen examples.

Many advantages can be outlined from this literature review, as for examples (i) the possibility of considering the real 3D topography and thus allowing a better understanding of the spatial distribution of the final landslide debris; (ii) very contained computational time, since the SPH model allows to separate the computational mesh consisting of moving nodes or particles from the topographical mesh which can have a structured nature; (iii) excellent combination of accuracy and simplicity, providing important information of flow-like landslides, such as velocity of propagation, depth of the flow, pore-water pressure temporal distribution at specific locations; (iv) the possibility of introducing some debris flows countermeasures (such as drainage screens) in the computations.

However, some limitations are inherent in depth-integrated methods, such as the impossibility to obtain the stress distribution and accurate flow depth in the proximity of an obstacle (that could be a protection barrier). This is a crucial aspect for analysing *LSI* problems.

The MPM model avoids these drawbacks since the stress-strain variables are carried by the moving material points, allowing the spatial and temporal tracking of the history of the material motion. For all the reasons, the MPM will be employed in all analyses in the following.

3. Landslide Dynamics (LD) modelling

3.1 Progressive landslides

3.1.1 Introduction

Among flow-like landslides, debris avalanches are characterised by distinct mechanisms which control the lateral spreading and the increase in soil volume involved during the propagation. Two different stages can be individuated for debris avalanches, i.e., the failure stage and the avalanche formation stage: the former includes all the triggering mechanisms which cause the soil to fail; the latter is associated to the increase of the unstable volume. Regarding these issues, in the literature, either field evidence or qualitative interpretations can be found while few experimental laboratory tests and rare examples of geomechanical modelling are available for technical and/or scientific purposes.

Generally, for analysing the triggering of a landslide, classical approaches like Limit Equilibrium Methods (LEMs) are often employed, which completely neglect the soil deformations and rely only on equilibrium equations under simplified hypotheses. Alternatively, or in conjunction to that, stress-strain analyses through Finite Element Methods (FEMs) have been also performed, considering the soil deformations generally "small". This simplification may be a reasonable hypothesis when the pre-failure and the failure are the only issues of the analysis. In addition, the hydro-mechanical coupling between the solid skeleton and the pore water pressure can be rigorously considered.

On the other hand, the propagation stage of such kind of landslides has been mostly analysed in terms of soil displacements, but not so much in terms of hydromechanical coupling during soil evolution. The simulation of the propagation stage during slope instability was managed through several approaches, such as

discrete element method (Zhao et al., 2020) or Lagrangian particle-based methods such as SPH, PFEM, FEMLIP, MPM (Cuomo et al. 2013, 2017a; Ceccato et al. 2018b; Cuomo, 2020; Yuan et al. 2020).

In the next paragraph a contribution is provided about the advanced numerical modelling of the inception of such hazardous debris avalanches. Particularly, the case of the impact of a failed soil mass on stable deposits is considered. This means that a small translational slide occurs; the failed mass causes the soil liquefaction of further material by impact loading; the landslide volume increases inside triangular-shaped areas during the so-called "avalanche formation", and soil erosion along the landslide propagation path also plays an important role.

To this aim, MPM proves to be a powerful numerical method, able in simulating the complex mechanics of landslide motion during the failure, propagation, and deposition stages.

3.1.2 Inception of debris avalanches

According to the most recent landslide classification (Hungr et al. 2014), the term "debris avalanche" states for "very rapid to extremely rapid shallow flow of partially or fully saturated debris on a steep slope, without confinement in an established channel". They typically occur in open slopes, i.e., shallow soil deposits with almost constant depths and slope angles generally between 30° and 45°. Debris avalanches start with small volumes involved (failure stage) and then turn into larger landslides because of the increasing in mobilized volume through further failures or eventual soil entrainment and resulting as a triangular-shaped area (post-failure stage).

Additional to that, soil unsaturated condition may be a key factor, in the failure and post-failure stages. Before failure, the additional strength related to matric suction is fundamental for the equilibrium of granular soil slopes steeper that the effective friction angle. During the failure stage of rainfall-induced landslides, the

soil suction gradually reduces due to rain infiltration and peculiar mechanical responses can even occur such as the capillary collapse (strong reduction of soil volume related to wetting). But also, during the propagation stage soil suction may evolve towards higher or smaller values depending on the amount of deformation in the landslide body. Thus, it would be desirable to have a comprehensive hydro-mechanical-coupled and large-displacement-based approach to include and accurately analyse all these issues.

Referring to failure and post-failure stages, four different zones can be distinguished (Figure 3-1). Zone 1 corresponds to small failures that occur at natural or anthropogenic discontinuities of soil deposits (respectively, bedrock outcrops and cut slopes). Zone 2 is the impact zone of the previously mentioned failed masses that usually corresponds to water supplies from bedrock (either karst spring or water runoff at bedrock outcrops); if zone 1 is absent, zone 2 is the source area of small landslides triggered by water supplies from bedrock. Zone 3 corresponds to distinct mechanisms: thrust of the failed mass upon the downslope stable material and/or soil entrainment due to the propagating mass. Zone 4 exclusively corresponds to soil entrainment. It is worth noting that while zones 1 and 2 are few tens of metres large, the width of zones 3 and 4 is not known a priori and its forecasting is a challenging task.

Considering the relevance of the topic, essentially related to the destructiveness of these phenomena, an advanced modelling of debris avalanches could provide a valuable tool to improve (i) the understanding of the inception (i.e. triggering mechanism and avalanche formation) of debris avalanches, (ii) the capability to forecast these landslides and (iii) the evaluation of the mobilised volume inside the avalanche source area, which is a crucial point for hazard and risk assessment and zoning.

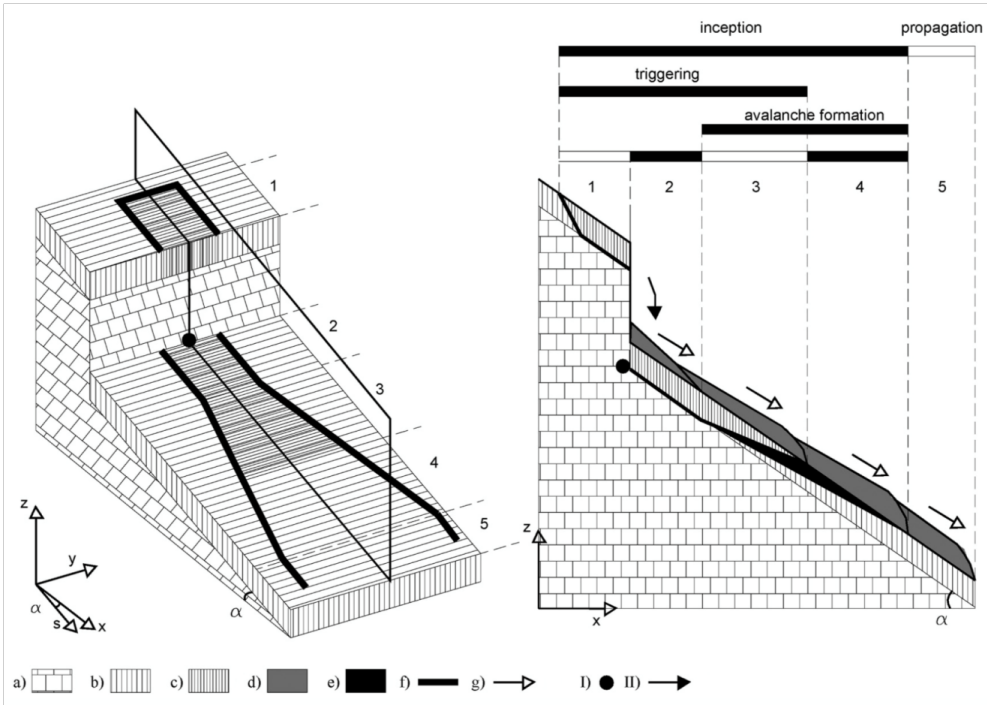

Figure 3-1. A reference scheme for the inception and propagation of a debris avalanche. General features: a) bedrock, b) stable soil deposit, c) failed soil, d) propagating failed mass, e) entrained material, f) boundary of debris avalanche and g) propagation pattern. Triggering factors: I) spring from bedrock, II) impact loading. Zone 1–2 triggering; zone 3 thrust of failed material and/or soil entrainment; zone 4 soil entrainment, zone 5 propagation (Cascini et al. 2013a).

Some simplified calculation schemes were considered to analyse the different mechanisms leading to the inception of a debris avalanche from the impact of a mobilized mass of a slope above. The general reference scheme is represented in Figure 3-2, in which the unstable mass (Material 1) is in a fully saturated condition while the soil on the slope downstream (Material 2) is stable in unsaturated condition due to the presence of soil suction (s_0). The unstable mass with uniform depth $H_{slope,1}$, length $B_{slope,1}$ and slope i_1 falls from a height H and crashes on the stable slope with depth $H_{slope,2}$, length $B_{slope,2}$ and overall inclination i_2.

Some relevant cases were considered to understand the influence of different geometries and boundary conditions on the triggering and propagation stages, as

reported in Table 3-1. In particular, the role of suction and the length extension of the Material 2 have been investigated in this study.

Suction value and soil properties, such as shear strength, stiffness, saturated permeability, and unit weight (Table 3-2), are those typical of the coarser superficial ashy soils (silty sands), having been widely investigated by Bilotta et al. (2005). On the other hand, the saturated hydraulic conductivity and water bulk modulus are typical of fine sands.

About the material constitutive models, both Materials 1 and 2 were modelled using a linear elastic-perfectly plastic behaviour. Furthermore, the water retention characteristic curve for the unsaturated material was set as linear function ($1 - a_v s_0$) for simplicity with parameters $a_v=0.01$, whereas relative permeability curve is neglected, and so hydraulic conductivity was kept constant.

The boundary condition $u=0$ is set along the ground level, leading to a decrease in suction over long time due to consolidation. In any case, the analyses last a very short period (some tens of seconds), so the consolidation phase has no influence.

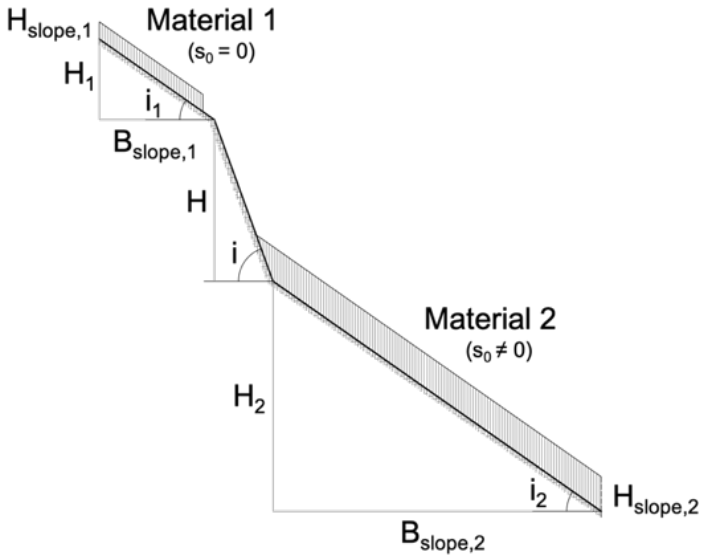

Figure 3-2. Reference scheme for numerical analyses.

Table 3-1. Simulation cases and related geometric/boundary features.

	H_1 (m)	$H_{1,slope}$ (m)	$B_{1,slope}$ (m)	i_1 (°)	H (m)	i (°)	H_2 (m)	$H_{2,slope}$ (m)	$B_{2,slope}$ (m)	i_2 (°)	s_0 (kPa)
Case 1	10	1.50	14	35	40	70	73	3	105	35	5
Case 2	10	1.50	14	35	40	70	34.5	3	45	35	5
Case 3	10	1.50	14	35	40	70	73	3	105	35	0

Table 3-2. Material properties used in the numerical analyses.

	ϱ_m (kg/m^3)	n (-)	K_0 (-)	E (MPa)	ν (-)	c' (kPa)	ϕ' (°)	ϕ'_b (°)	ψ' (°)	k_{sat} (m/s)	K_L (MPa)	μ_L (Pas)	a_v (-)
Mat 1	1315	0.58	0.38	5	0.29	0.1	38	38	0	10^{-3}	50	10^{-3}	-
Mat. 2	1315	0.58	0.38	5	0.29	5.0	38	38	0	10^{-3}	50	10^{-3}	0.01

3.1.3 Modelling the impact-induced debris avalanche

The innovative MPM numerical technique is used to combine a hydro-mechanical coupled approach, any of the well-known soil constitutive models proposed over the years in soil mechanics and a large-displacement formulation.
The numerical analyses were performed adopting a 2D geometrical configuration taken from field evidence and previous research (Cascini et al. 2013a, Cuomo et al. 2013). Triangular 3-noded elements computational meshes are used, characterized by elements with average size of 1 m (Figure 3-3). The contact between soils and base material is managed through a frictional contact algorithm (Al-Kafaji, 2013). The boundary conditions are set for both liquid and solid phase. The velocities are fully fixed in both directions along all the boundaries of the domain, whereas the right edge of the Material 2 is fixed only in the X direction.

The initial stress state of the soils was initialized assuming a geostatic condition, with a k_0 coefficient set to 0.38. The water table was set at the bottom for the partially saturated material with a constant suction profile at the beginning of the simulation.

The numerical results aimed to assess the time-space evolution of some quantities, such as stress, strain, pore pressure and velocities, for all the above-mentioned cases.

Firstly, the spatial distribution for some relevant time lapses was considered.

The results show that the impact of the mass in the Case 1 (Figure 3-4) apparently has no effect in the first moments (up to about 50 s), as well shown by the velocity distribution in the material downstream, which remains in stable condition. However, the degree of saturation is increasing during this period and a perched water table is forming in the lower part of the slope. After that, the material becomes unstable due to the increasing in pore-water pressure and reaches high velocities (over 6 m/s).

Similar results were achieved for the Case 2 (Figure 3-5), even if the reduced length of the stable material causes a delayed failure compared to Case 1. In fact, soil begins to move at about 85 s against the 60 s of the previous case. Furthermore, the velocity reached by the moving mass does not exceed 4 m/s.

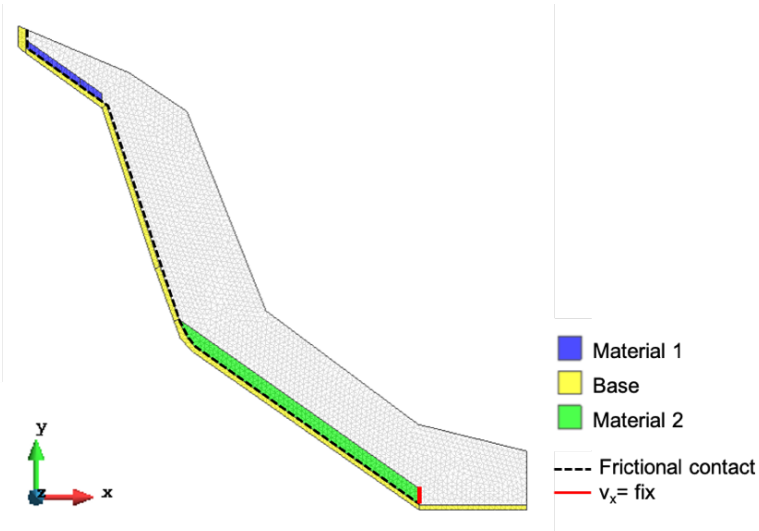

Figure 3-3. Computational domain and materials.

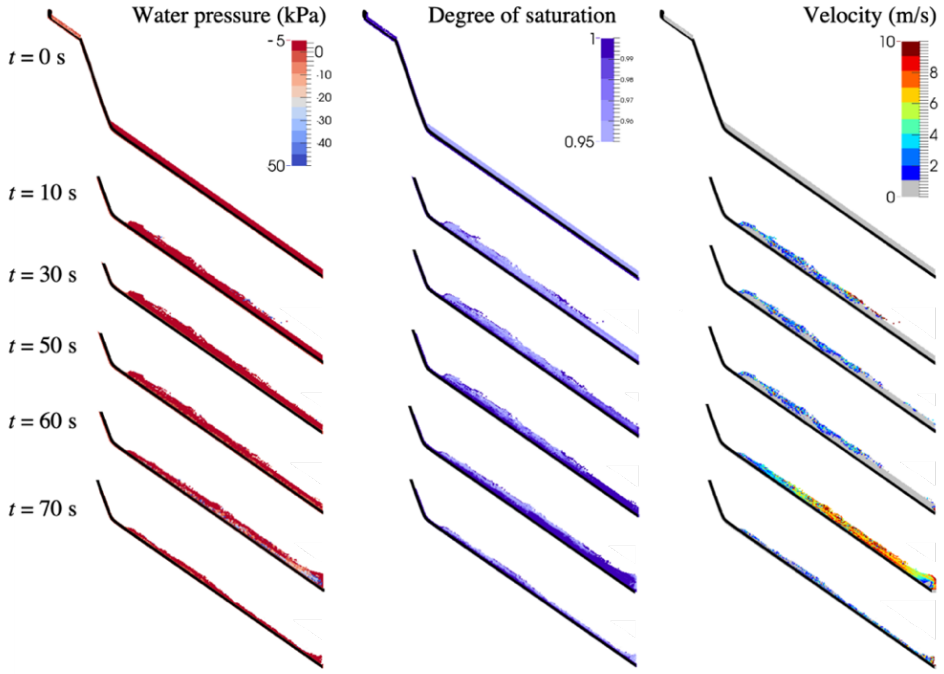

Figure 3-4. Spatial distribution of water pressure, degree of saturation and velocity (Case 1).

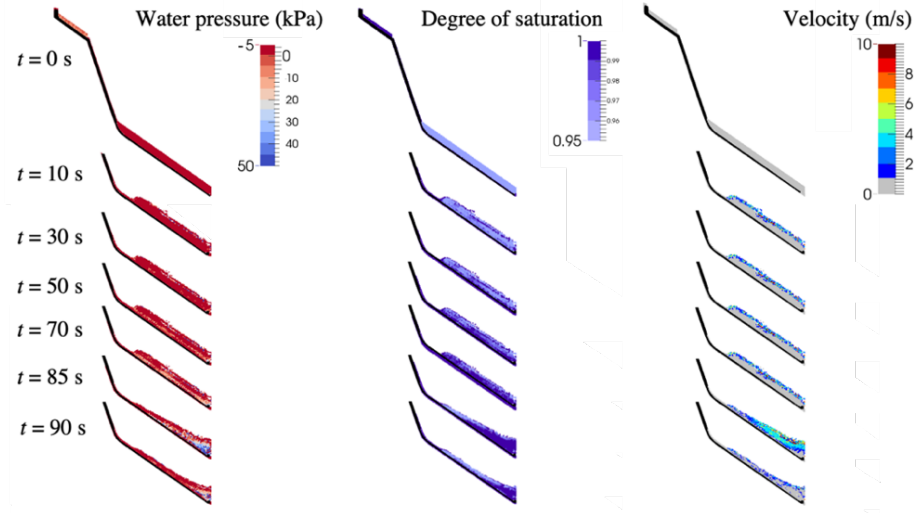

Figure 3-5. Spatial distribution of water pressure, degree of saturation and velocity (Case 2).

Completely different is the case in which suction is not taken into account (Figure 3-6). The impacting mass suddenly leads the below material to instability, due to the increase of pore-water pressure at impact. The material behaves like a flow which quickly propagates downstream, reaching very high velocity (over 10 m/s) during the simulation. It is worth noting that in this case there is no delay for the formation of the avalanche, which develops in few seconds.

Additional to the analysis of the spatial distribution of some relevant quantities, it may be useful to investigate their trend over time in specific zones of the impacted mass. The elements of the mesh taken as reference fixed zones are 5, equally spaced and at half depth. The numerical results are displayed only if at least one material point is present in the element. If the element becomes empty (e.g. the material points leave the element after failure) no temporal trend is shown in the plots.

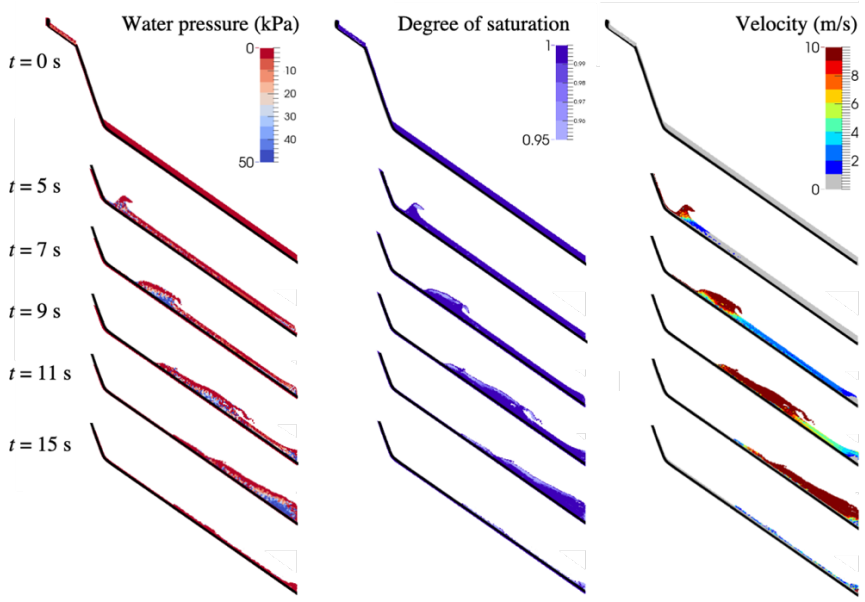

Figure 3-6. Spatial distribution of water pressure, degree of saturation and velocity (Case 3).

To analyse the stress state condition, the mean effective stress (p'), the total mean stress (p), deviatoric stress (q) and water pressure (u) were considered, as

defined in Equations 3-1, 3-2 and 3-3. In particular, the ratio q/p' was compared to the critical state (Equation 3-4).

Both q/p' and u/p were considered over time since they are dimensionless quantities and so more easily comparable for the three reference cases. In conjunction, the velocity pattern and the deviatoric strain ε_q (Equation 3-5) were also considered to add more information about the inception and propagation mechanisms.

$$p' = \frac{\sigma'_{xx}+\sigma'_{yy}+\sigma'_{zz}}{3} \tag{3-1}$$

$$p = p' + u \tag{3-2}$$

$$q = \frac{1}{\sqrt{2}}\sqrt{(\sigma'_{xx} - \sigma'_{yy})^2 + (\sigma'_{yy} - \sigma'_{zz})^2+(\sigma'_{xx} - \sigma'_{zz})^2 + 6\sigma'^{2}_{xy} + 6\sigma'^{2}_{yz} + 6\sigma'^{2}_{zx}} \tag{3-3}$$

$$M = \frac{6sin\varphi'}{3-sin\varphi'} \tag{3-4}$$

$$\varepsilon_q = \frac{\sqrt{2}}{3}\sqrt{(\varepsilon_{xx} - \varepsilon_{yy})^2 + (\varepsilon_{yy} - \varepsilon_{zz})^2+(\varepsilon_{xx} - \varepsilon_{zz})^2 + 6\varepsilon_{xy}^2 + 6\varepsilon_{yz}^2 + 6\varepsilon_{zx}^2} \tag{3-5}$$

Comparing these above-mentioned ratios for Case 1 (Figure 3-7), it emerges that following the impact of the unstable mass, the stable material reaches the critical line for an instant (excluded point E, which doesn't seem to notice the impact) then the slope quickly finds a new equilibrium configuration. In the meantime, pore-water pressure is increasing, starting from the lower zone (point E). Suddenly, the q/p' ratio reaches the critical value M in all points and so the slope begins to move, as also shown by the trend of velocity and deviatoric strain (Figure 3-8), which increases from below upward.

Even for Case 2 (Figure 3-7), the stable material reaches the critical state for a while but in this case also in point E, due to the reduced length of the slope. The only

exception is point B which remains in yielding condition, but without affecting the equilibrium of the whole mass. After reaching the new equilibrium configuration in the other zones, also here pore-water pressure increases, but this time more markedly from the above (point B). After few tens of seconds, the q/p' ratio goes beyond the critical line M in the central zone (points B, C and D), where the highest velocity and deviatoric strain are reached (Figure 3-8). Completely different is the Case 3 (Figure 3-7), in which q/p' is very close to M just from the beginning, due to the absence of suction. Then, following the impact, the mass begins quickly to move from the above (point B) and propagates downward very fast, as shown by the velocity trend (Figure 3-8). While the mass is propagating, the points that are farther away from the triggering become more stable due to the compression wave, until their q/p' ratio crosses the critical value. Differently from the other cases, in Case 3 the shear strain evolves over time with the propagation of the unstable mass, as well shown in Figure 3-8.

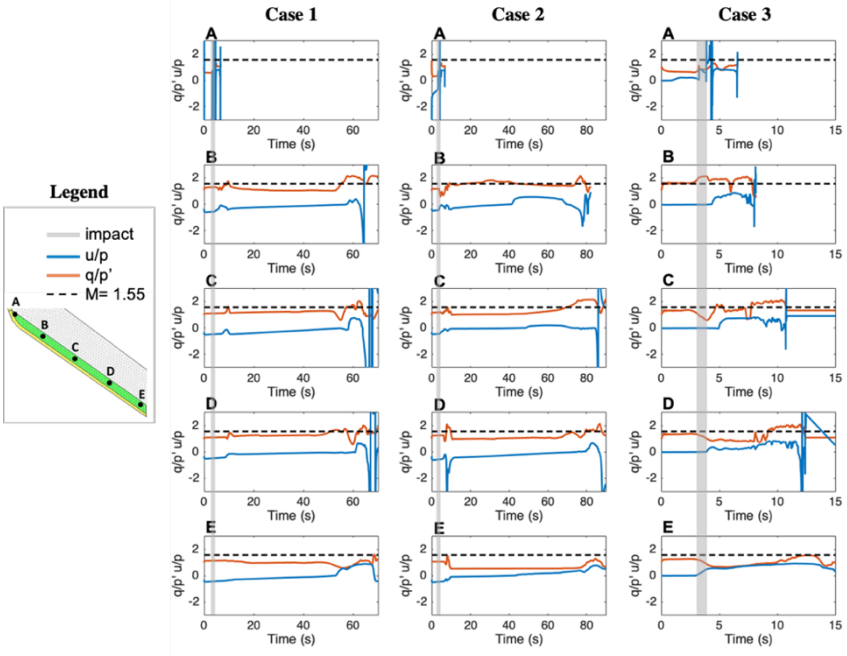

Figure 3-7. Stress distribution over time for the reference cases.

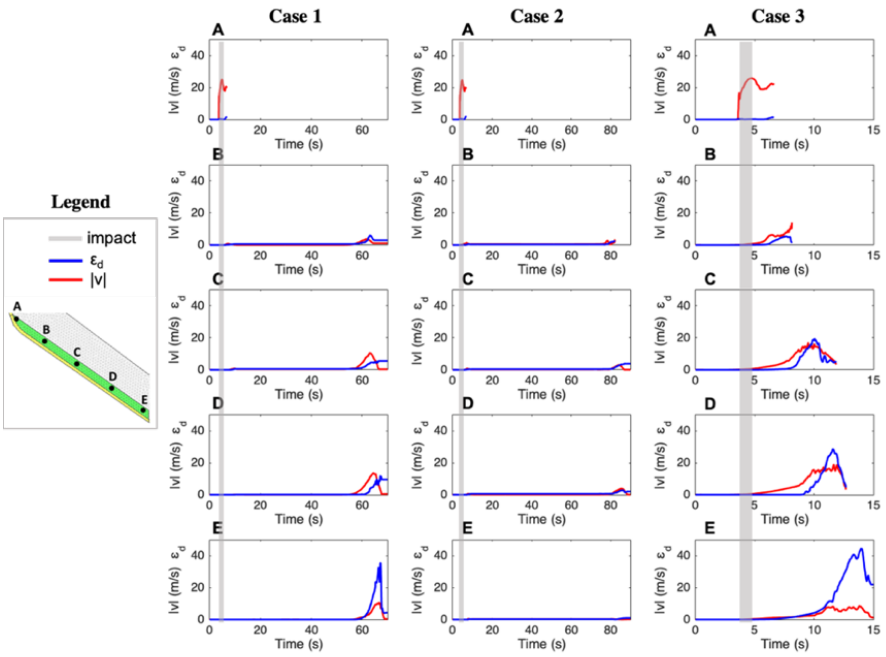

Figure 3-8. Velocity and strain distribution over time for the reference cases.

3.1.4 Remarks on the inception mechanisms

The MPM numerical modelling of the simplified schemes above analysed allows improving the understanding of the inception of a debris avalanche.

Among the new insights obtained from MPM modelling, the limits of the different zones indicated in the reference scheme of the inception stage (Figure 3-1) have been investigated. Except for the Zone 1 which depends on the size of the fallen mass, the individuation of Zones 2, 3 and 4 for the three considered cases is reported in Figure 3-9 for different cases. The area of the slope triggered by the impact of the failed mass (i.e., Zone 2) is quite easily identifiable through MPM simulations and doesn't change during the formation of the avalanche. Conversely, the other zones change over time and so it may be reasonable to understand how their modification occurs, regarding the different boundary conditions taken into account. In fact, while Zones 1 and 2 are few tens of metres large, the size of Zones 3 and 4 is not known a priori and its assessment and/or forecasting are challenging tasks.

Knowing that Zone 3 corresponds to the area in which the thrust of the failed mass and/or soil entrainment occur, and Zone 4 is exclusively related to soil entrainment, their individuation in some crucial instants can be made. In fact, what emerges from Figure 3-9 is that for all the cases the length of Zone 3 ranges from few meters (when the most part of the downslope material is stable) to many tens in the final configuration. The increase of the initial failed volumes can be associated with further failures occurring inside this zone. The transition from initial slide to a real debris avalanche is also related to soil entrainment along the path of the failed mass (Zone 4). In particular, the comparison between the reference cases in Figure 3-9 shows that this zone is very elongated if suction is present, while it is shorter but involves more failed volumes in the Case 3, where suction is not considered. Relevant remarks can also be made by comparing Cases 1 and 2 in terms of time. For instance, at the same instant of 70 s, the deposited material along the slope in Case 1 is representative of Zone 3 only, while Case 2 is characterized by both Zones 3 and 4, highlighting a sort of delay in the formation of these zones.

Another interesting observation can be outlined, since the evolution over time of Zones 3 and 4 allows to understand that during the formation of the debris avalanche Zone 4 in a certain instant becomes Zone 3 in the immediately following instant, and so this leads to the continuous enlargement of Zone 3. At final configuration, most part of the slope is represented by Zone 3, as result of the soil entrainment, while most failed volumes included in Zone 4 during propagation have turned into a stationary deposit beyond the edge of the slope.

In conclusion, the entrainment of further material makes the propagation patterns complex, so the use of an advanced numerical technique like MPM is useful to provide new insights in the understanding of the debris avalanches inception mechanisms.

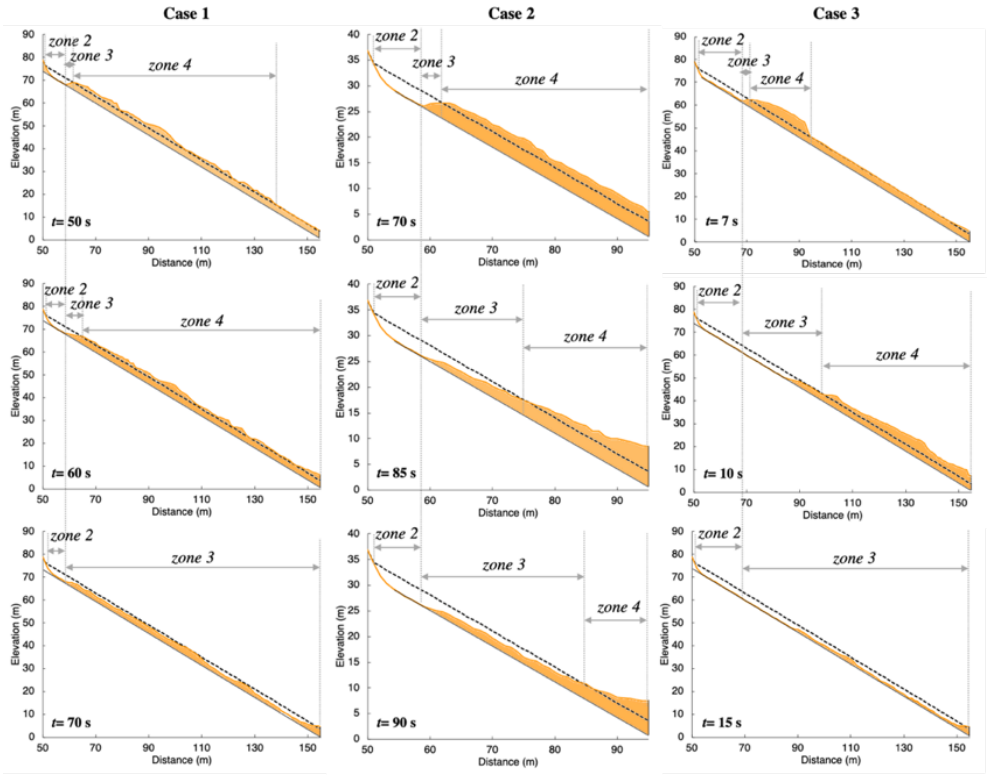

Figure 3-9. Comparison among soil depths for some relevant timesteps.

3.1.5 Concluding remarks

Debris avalanches are complex natural hazard for which several field evidence or qualitative analyses are provided in the current literature, even if few examples of laboratory tests and/or geomechanical modelling are available for this kind of phenomena.

The study proposed herein aimed to provide a general overview of the current potentialities for the geomechanical modelling of such dangerous phenomena. In particular, the inception of a debris avalanches due the impact of a failed soil mass on a stable deposit was analysed through an advanced numerical modelling, such as MPM, able to consider the hydro-mechanical coupling between solid skeleton and pore-water of a flowlike landslide from triggering to final deposition.

The numerical results provided new insights in understanding the complex impact mechanism through the computation and time-space tracking of some quantities, such as stress, strain, pore-water pressure, soil velocities, which cannot be easily monitored and obtained from laboratory experiments. In particular, the achieved results outline that failure induced by impact loading can cause further failures in downslope stable deposits. Due to the impact of an unstable mass, greater volumes can be mobilized due to the increase in pore-water pressures, as well simulated through 2D hydro-mechanical coupled analyses.

Furthermore, the influence of initial suction and length of the downslope deposit was highlighted, demonstrating that their effects play a crucial role in the formation of a debris avalanche. In fact, the presence of both suction and shorter slope length delays the occurrence of failure and also leads to different inception mechanisms, as well shown by the temporal distribution of stresses and inception zones.

The method also allowed confirming that the entrainment of further material along the landslide path plays an important role, as previous studies already had noticed. Particularly, the entrainment causes the downward spreading of the unstable mass, and it also modifies the kinematic features, i.e. velocity and propagation patterns, of the debris avalanche.

In conclusion, the achieved results open new frontiers to the study of the mechanisms governing the inception and formation of debris avalanches, thus encouraging the application of the proposed framework to further real cases to enhance the current capability to forecast the occurrence of these hazardous phenomena.

3.2 Retrogressive landslides

3.2.1 Introduction

Most of the geotechnical analyses allow the separate modelling of the failure

(Merodo et al. 2004) and propagation stage of rainfall-induced landslides (Pastor et al. 2009). Regarding that, Cascini et al. (2010) highlight that the drained failure of shallow covers, caused by rainfall infiltration, can be adequately simulated through Limit Equilibrium Methods (*LEMs*) (Janbu 1955; Morgenstern and Price 1965). However, the most catastrophic landslides often involve complex interaction between the solid skeleton and the interstitial pore water. Hence, seepage analysis and stress-strain analyses should be jointly solved, and soil deformation properly taken into account. Several models based on the Finite Element Method (*FEM*) have been proposed for this aim. Hydro-mechanical coupled formulations have significantly developed over the years, based on the fundamental contribution of consolidation theory (Biot, 1941), and later generalizations (Pastor et al. 2004). However, soil deformations have been generally considered "small", that is reasonable when only pre-failure and failure are investigated. Globally, an enormous variety of applications of *LEM* and *FEM* approaches has been proposed for the last 30-40 years.

The Material Point Method (*MPM*) has the potential to reproduce entirely those complex processes. However, a comparison with standard tools (e.g. *FEM*: Finite Element Method, *LEM*: Limit Equilibrium Method) may guide in the optimal choice (or in the combined use) of the various modelling approaches. A framework is here proposed based on a multi-tool approach consisting in the combination of: a) *no-deformation LEM*, b) *small-deformation FEM*, c) *large-deformation MPM*. The *LEM* slope stability analyses are performed for a realistic assessment of the major slip surface(s) and to back-analyse uncertain slope parameters. The *FEM* stress-strain analyses assess the progressive failure, the onset of initial velocity and the later acceleration of the landslide body, until large deformations occur in the slope and numerical convergence of *FEM* is lost. The MPM analyses are used to reproduce the whole landslide process, from the initiation to propagation and final deposition. Such an integrated framework is tested for an international landslide benchmark (the 1995 *Fei Tsui Road* landslide in Hong Kong). The results achieved through the different approaches are discussed in relation to the wide scientific literature available for the

general topics and the specific case study. The analyses in this paragraph highlights that the fully-coupled hydro-mechanical large-deformation model properly reproduces the complex failure and post-failure mechanisms of rainfall-induced landslides. However, *no-deformation LEM* analyses and *small-deformation FEM* analyses allow a reasonable understanding of both the pre-failure stage and the failure mechanism. These more traditional tools are confirmed as indispensable tools in the engineering practice and research.

MPM can model the coupled hydro-mechanical behaviour of a landslide process, and significant achievements are very recent. Some *MPM*-based studies investigate the failure of an unsaturated slope disregarding the infiltration process and imposing the critical phreatic surface (i.e. at slope failure) as initial condition for numerical modelling (Soga et al. 2016; Nguyen et al. 2021). Alternatively, short heavy rainfall is schematized as an assigned linear time decrease of suction along the ground surface (Yerro, 2015, Yerro et al., 2016). In other studies (Wang et al. 2018; Lee et al. 2019; Lei et al. 2020) a zero pore-water pressure along the ground surface is assumed. In both the last two cases, a pore-water pressure condition is imposed (e.g., ponding) at the ground surface boundary, and not a seepage inflow (e.g., rainfall intensity) as easily doable in more traditional approaches.

The introduction of a flux boundary condition in the *MPM* context for rainfall infiltration modelling was firstly done by Bandara et al. (2016), using a coupled hydro-mechanical formulation for saturated and unsaturated soils. This formulation is for instance employed by Liu et al. (2020) considering a constant water inflow (equal to the soil saturated hydraulic conductivity) applied to the ground surface for 1 hour. Some other *MPM*-based studies focused on landslide propagation (Li et al. 2016; Conte et al. 2019; Yerro et al. 2019).

The proposed study provides a framework useful to perform different types of analyses, where: (i) different assumptions on soil deformations are done; (ii) quantitative realistic solutions are achieved at each modelling level. The proposed framework is applied to an international landslide benchmark (the 1995 *Fei Tsui Road* landslide in Hong Kong), and the achieved results are discussed in relation to

the wide literature available for the specific case study.

3.2.2 The framework proposed

The basic idea of this work is to propose and test a framework for landslide modelling in unsaturated slopes, from initiation to final deposition.

The framework is based on a multi-tool approach, which aims to emphasize the combined use of standard and advanced computation models. *FEM* is one fundamental tool for simulating the pore water pressure regime in saturated and unsaturated conditions. Then, the slope evolution analysis can be pursued at three levels, under different hypotheses depending on the goals: a) no-deformation *LEM*, b) small-deformation *FEM*, c) large-deformation *MPM*. From a) to c) the modelling capability increases as well as the importance to well manage such advanced tools.

The novelty of such a framework relies on the capability of *MPM* to simulate from small- to large-deformation rates and vice-versa, as occurring during the landslide process, through a single mathematical approach.

A fundamental characteristic of the proposed framework is that the very different stress- and strain-rates during the initiation and propagation stages are tackled unitarily through *MPM*, provided that a proper soil mechanical model is adopted. The current discrepancy among the large varieties of small-strain soil constitutive models available and the more limited rheological models for propagation modelling also testifies the value of bridging such a gap.

The multi-scale timing is another feature of the proposed approach. There is, in fact, also a significant contrast in the times scales of the phenomena, which is afforded in this framework. For instance, the landslide propagation and deposition may last a few tens of seconds, or a few minutes at most (10^2 s). Whilst, a landslide triggering mechanism typically develops during rainfall and can last from few to tens of hours (10^5 s). The initial slope condition, for instance the initial water table height and the suction profile above the water table both depend on the many weeks or months before (10^7 s). In the proposed framework, the attention is posed on the

combination of long- and short-term analyses (time scale from 10^5 to 1 s and less). For instance, one will be simulating the antecedent rainfall over 1-2 days (for instance, through *LEM* and *FEM*), and then looking for landslide transformation into a flow, propagation, and deposition, all lasting some tens of seconds in total (through *MPM*). It is interesting noting that most of the current approaches alternatively allow the modelling of the long-term slope behaviour until a failure (time scale of 10^5 to 10^7 s) or solely focus on the propagation stage (10^2 s). Aimed to keep affordable the computational cost of an *MPM* modelling of the whole landslide process, a multi-resolution time schematization is adopted. A time step of 1 hour and permeability expressed in m/h is used for hour-long simulation, when the slope is mostly undeformed, and the acceleration of the solid skeleton are negligible. Then, a unit time of 1 second is used for the simulation of the landslide dynamics. For each of these two successive analyses the time step is automatically reduced if needed to ensure numerical stability.

The integrated use of three above-mentioned tools (*LEM*, *FEM*, *MPM*) is encouraged. Once their similarities and connections are outlined, then their results can be consistently compared. It will be shown, for instance, that the simpler *LEM* and *FEM* are sufficient to fully describe the landslide triggering, while *MPM* is necessary to cope with retrogressive failure. The three tools are hereafter presented from the most comprehensive formulation (*MPM*) to the most simplified one (*LEM*), presenting the various simplifications made.

3.2.3 Case study: The Fei Tsui Road landslide (Hong Kong)

The Fei Tsui Road landslide (Figure 3-10) occurred in the Chai Wan District of Hong Kong, after the heavy rain of 12th and 13th August 1995 (Figure 3-11). A cumulative rainfall of 374 mm was recorded in the last 12 hours before failure (maximum intensity of 60 mm/h), combined to the highest rainfall amount recorded on the site for a storm longer than a week (943 mm in 15 days before failure). The landslide took place in two stages: the first failure occurred at about 00:55 on 13th August 1995

in the superficial part of the slope, involving some tens of cubic meters; about 20 minutes later, a large failure moved down about 14,000 m^3 of weathered volcanic rock. The debris travelled 70 m, invaded the Fei Tsui Road, which is beneath the cut-slope, entered a playground and accumulated for about 6 meters at a corner of a Church (Figure 3-10).

Landslide propagation also included moderate lateral spreading, so that it will be interesting to study the slope evolution in the main cross-section (in plane strain condition Figure 3-12a) and also to analyse the landslide following the radial pattern of the unstable material (in axisymmetric condition, Figure 3-12b). The maximum width and the average depth of the debris deposit were 90 m and 15 m, respectively (Figure 3-13).

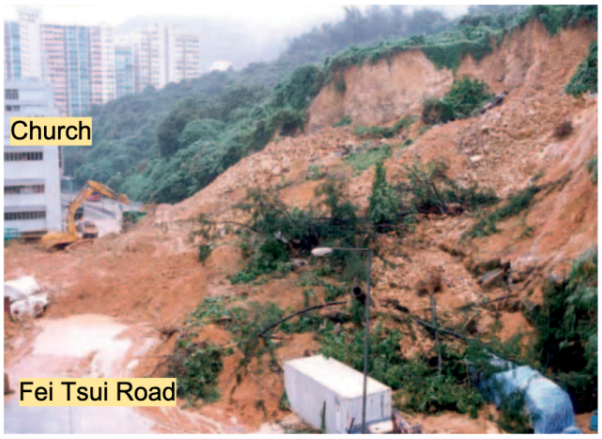

Figure 3-10. Landslide overview (modified from Ho and Lau, 2010)

The first technical investigation was carried out by the Geotechnical Engineering Office (GEO) of Hong Kong, and described in the report No. 188 (Knill, 1996). It was ascertained that before the landslide, there was a densely vegetated cut-slope with a maximum height of 27 m and an overall inclination of 60° towards the North. The lower part of the slope (up to 8 m high from the ground) was constituted by exposed rock, grading from fresh to slightly decomposed volcanic rock. Above this

material, kaolinite-rich layer (0.6 m in thickness) and moderately to completely decomposed tuff were arranged as shown in Figure 3-13 (modified from Knill, 1996 and Kirk, 1997), in which the materials are also associated with their degrees of weathering (GCO, 1988a).

The sliding surface of the landslide followed the kaolinitic layer only in the lower part, whereas such a layer is beneath the slip surface in the upper part of the slope (Figure 3-13). From the field evidence, the lowest part of the cut-slope (composed by moderately to slightly decomposed tuff) did not form part of the landslide. The geotechnical properties of the landslide materials were available from the above-mentioned GEO report n°188 (Knill, 1996), which outlines the results of several laboratory tests including particle size distribution, Atterberg limits, oedometer, triaxial compression and direct shear tests.

A wide literature is available for this specific case study. The first slope stability analysis was performed through *LEM* by Knill (1996) for the diagnosis of the landslide mechanism. At that time, the unsaturated soil features were not considered, although important insights were obtained: (*i*) a shear strength (φ') at failure of the altered tuff layer likely in the range of 26.5°–31.5°, (*ii*) a perched water table at failure from 1 m up to 4 m above such layer.

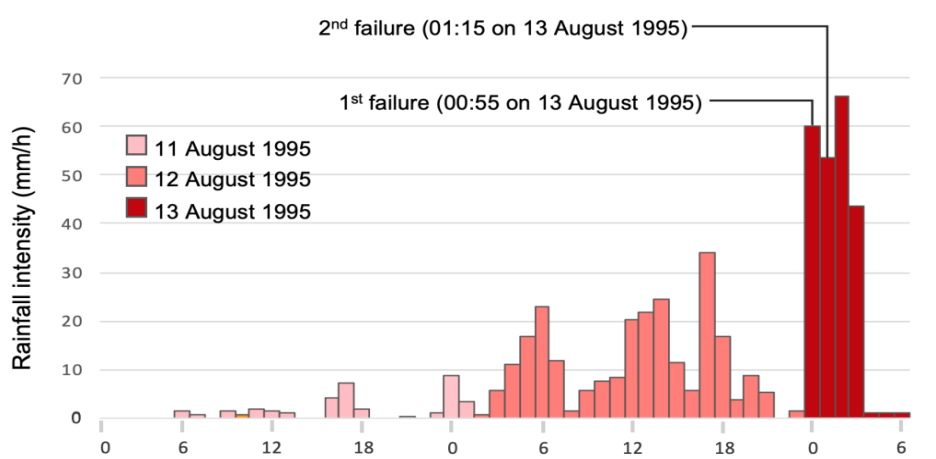

Figure 3-11. Hourly rainfall intensity in the 2 days before failure (modified from Knill, 1996)

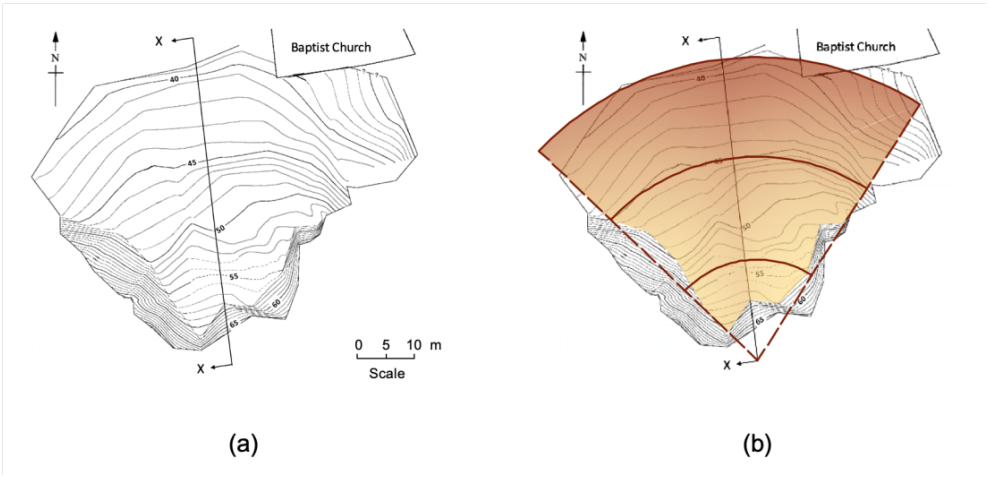

Figure 3-12. Plan view of final landslide deposition: (a) contour lines and (b) radial pattern of the debris

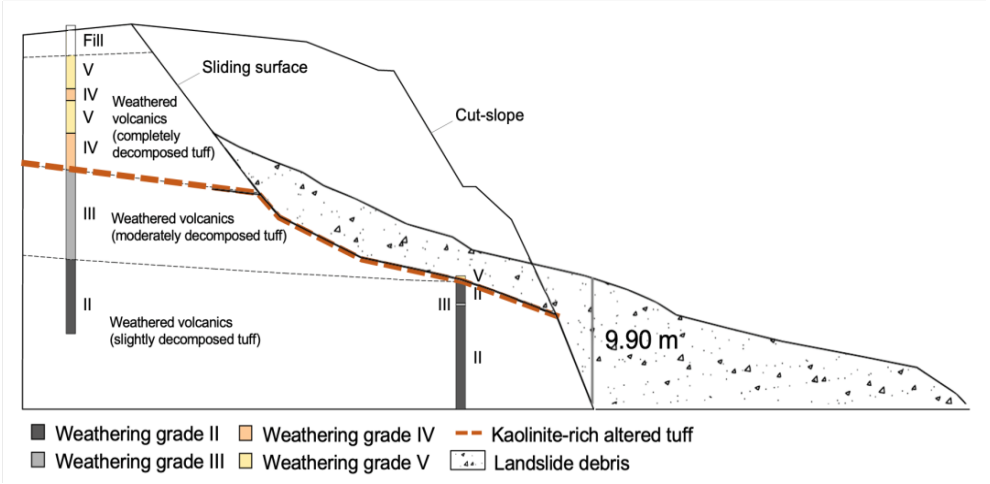

Figure 3-13. Stratigraphic profile of the cut-slope (section X-X of Figure 3-12)

The only *FEM*-based modelling of landslide triggering stage is that proposed by Cuomo et al. (2020a), which highlights a potential progressive failure occurred into the slope. Indeed, the rest of the literature focuses on landslide propagation, through *SPH* modelling (Chen and Lee 2000; Wang and Sassa 2010; Sanchez et al. 2013; Pastor et al. 2014; Calvello et al. 2017; Cuomo et al. 2017b; Koo et al. 2017) or

MPM modelling (Ghasemi 2019; Lee et al. 2019). The best estimates are achieved with the assumption of two basal friction angles, precisely 22°–26° along the kaolinitic layer and 30°–35° on the urbanized area. A recent *MPM*-based contribution (Liu et al., 2020) considers the unsaturated soil condition, and simulates the landslide triggering and propagation. However, some major simplifications are still included: (*i*) behind the scarp of landslide, a cohesion of some hundreds of kPa is assumed, i.e. practically undeformable, so that the computed soil deformations are constrained along a given soil contact layer, (*ii*) a water inflow equal to soil saturated permeability (k_{sat}) is assigned to the ground surface. However, in unsaturated slopes, soil suction creates the chance for infiltration rates higher than k_{sat} at the beginning of rainfall, and then equal or lower than k_{sat} as the time goes ahead, (Cuomo and Della Sala, 2013; among others). This simplification also prevents the estimate of the initial soil suction in the slope. Consequently, a quick landslide motion (about 160 seconds) is reproduced and either the long-term infiltration process or the real spatio-temporal evolution of the landslide is not captured.

In the present study, the measured 26 hourly rainfall intensity values are used as input of the three types of approaches mentioned before, among which the *large-deformation MPM* modelling. The achievement of a "perfect" back-analysis is far from the goal of this study, which instead discusses different approaches for a well-documented case study, whose input data have been worldwide available and used for testing alternative methods.

3.2.4 No-deformation LEM analyses

This section aims to assess the initial soil suction (i.e. before critical rainfall), which surely played a role in slope instability and landslide evolution. Firstly, pore-water pressures are modelled to compute the changes induced by the heavy rainfall (24 hours long) that preceded the landslide event. The groundwater modelling is performed through the commercial FEM code Seep/W (GeoStudio, 2012), with a mesh of 2,240 triangular elements, 1 m sized on average (Figure 5). The saturated

hydraulic conductivity value is equal to $5 \cdot 10^{-5}$ m/s, and the soil water retention curve and conductivity function are taken from Cuomo et al. 2019a. The geotechnical parameters of the completely decomposed tuff (CDT) are taken from Ng et al. (2011). A flux boundary condition equal to the hourly rainfall intensities (Figure 3-11) is assumed at the ground surface. As initial condition, the unknown suction distribution is assumed homogeneous all over the slope section and varied among different scenarios (from 40 to 60 kPa, with a 5 kPa interval).

Independent on the initial suction assumed, the seepage analysis clearly outlines that: (*i*) a perched water table arises above the kaolin-rich layer, (*ii*) above the water table, soil suction is progressively lowered over the time, (*iii*) in agreement with the literature (Knill, 1996), the water table depth is in the range 1.5–4.5 m above the kaolinitic layer, at the time of the deepest slope failure (i.e. t=25 h).

Those pore water pressures are used as input data for the slope stability analyses to assess the spatio-temporal evolution (during rainfall infiltration) of the Factor of Safety (*FS*) along superficial or deep slip surfaces.

The Morgenstern-Price (1965) method, and the commercial code Slope/W (GeoStudio, 2012) are used. A rigid perfectly plastic constitutive model is adopted, considering the extended Mohr-Coulomb failure criterion proposed by Fredlund et al. (1978) for the unsaturated soils. More than 2,000 pseudo-circular slip surfaces are specified through a grid of centres and a range of radius (Figure 3-14). Estimates of the internal friction angle of the kaolinitic layer (22–29°) and the effective cohesion of the completely decomposed tuff (0–10 kPa) are taken from the literature. All the used soil parameters are listed in Table 3-3.

The spatial distribution of the *FS* computed for some reference time lapses is reported in Figure 3-15. It is noted that the LEM analyses well reproduce the observed slope instability only assuming an initial suction of 50 kPa. In this case, the slope is simulated as initially stable (Figure 3-15a). It remains stable ($FS>1$) during the first 12 hours of rain (Figure 3-15b), with $FS>1.1$.at any potential slip surface, while the perched water table is rising.

After about 24 hours, *FS* drops below unity along a shallow slip surface (Figure 3-15c). After 1 hour more, a deeper slip surface reaches a similar unstable condition (Figure 3-15d). For several slip surfaces, *FS* progressively reduces over the time, for the shallow surfaces first and then for the deep ones. This slope evolution resembles the retrogressive failure mechanism reported by the eyewitnesses.

It is also noted that the time-trend of *FS* is quite different for the shallow (Figure 3-16a) and deep slip surfaces (Figure 3-16b). For the shallow slip surfaces, *FS* rapidly decreases during rainfall infiltration, *FS* drops when the perched water table has formed at the base of the slope. The deep slip surfaces encounter a slower reduction of the factor of safety over the time.

A satisfactory agreement with field evidence is globally achieved. (*i*) For both the shallow and deep slip surfaces, *FS* diminishes below unity approximately at the time observed in the field for the two failures. (*ii*) The depth of the critical water table falls in the range reported in the literature. However, more sophisticated analyses are conducted to better understand the slope evolution from the occurrence of the shallow landslide until the deep failure.

Table 3-3. Material properties used as input for the LEM analysis

Materials	ρ_m *(kg/m³)*	k_{sat} *(m/s)*	*E (MPa)*	*ν (-)*	*c' (kPa)*	*φ' (°)*	*ψ (°)*	*α (kPa)*	*β (-)*	S_{res} *(-)*
CDT	1937	$5\ 10^{-5}$	10	0.3	5	35	0	64	0.47	0.275
Kaolinitic layer	1937	10^{-7}	10	0.3	0	29	0	-	-	-

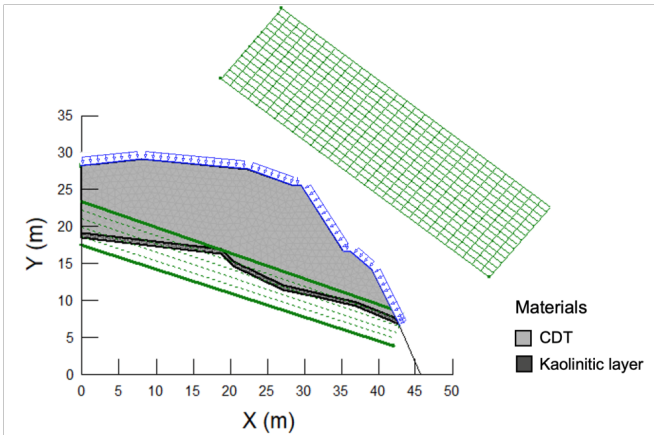

Figure 3-14. Computational FEM mesh used for the seepage analysis with the indication of the soils, the rainfall boundary condition, as well as the grid of points and the radius lines used to define more than 2000 slip surfaces.

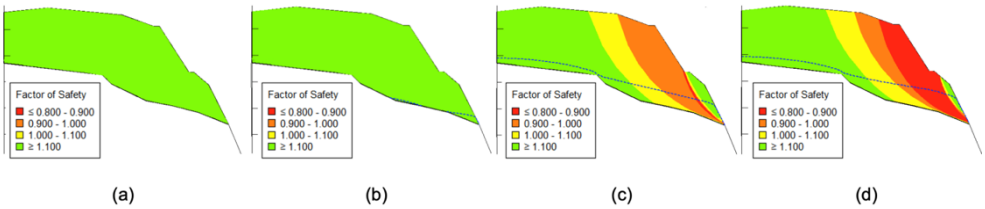

Figure 3-15. Factor of safety spatial distribution for s_0=50 kPa: (a) t=0; (b) t=12 h; (c) t=24 h and (d) t=25 h

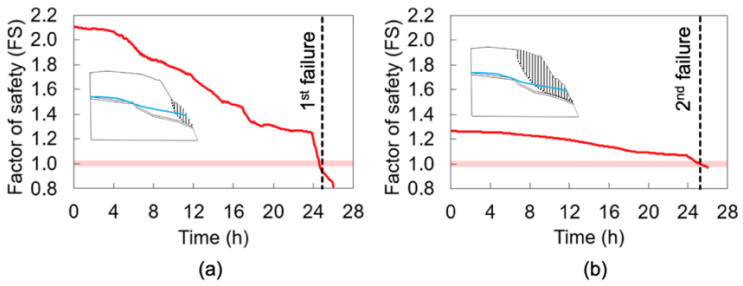

Figure 3-16. Factor of safety changing in time for s0=50 kPa: along (a) shallow and (b) deep slip surface

3.2.5 Small-deformation FEM analyses

Hydro-mechanical coupled stress-strain FEM analyses are carried out using the commercial code Plaxis 2D (Plaxis 2D, 2018). The computational mesh is made of 6-noded triangular elements 1 meter large, similar to the uncoupled seepage analysis. The updated mesh Lagrangian formulation of McMeeking & Rice (1974) is used. The materials included in the analysis are the completely decomposed tuff and the kaolinitic layer (schematized as a contact layer). The input parameters are the same as Table 3-4. The bottom of the computational domain is assumed as fully fixed (in both X- and Y-directions) (Figure 3-17).

After computing the initial equilibrium geostatic stresses, a fully-coupled flow-deformation analysis is performed to simulate rainfall infiltration, with the consequent decrease in soil suction and rise of the perched water table. A fully implicit integration scheme is used, which allows large time steps and fast computation (Haxaire et al. 2011; Plaxis 2D, 2018). The analyses are carried out both in plane-strain and axisymmetric conditions (Figure 3-18).

The time-trend of displacement is computed in 5 control points located at the toe of the slope (Figure 3-17) to compare the numerical results with the observed occurrence time. The failure time is deducted from any asymptotic-like time-trend of the computed displacements.

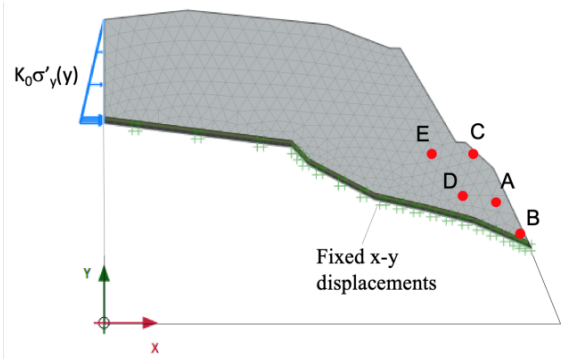

Figure 3-17. FEM computational domain, with the element mesh, boundary constraints and monitored points.

In all the cases, a slope failure is simulated at the lowest part of the slope (point B). Far from here, the displacements are smaller or negligible (points D and E). This is consistent with the field evidence of a retrogressive landslide. The initial suction leads to slightly different failure scenarios. For a lower initial suction (e.g. 50 kPa) the displacements are more differentiated inside the slope and the displacement rates are lower (Figure 3-18) compared to a higher initial suction (e.g. 60 kPa).

The simulated failure time is shorter for an initial suction of 50 kPa than for 60 kPa, especially in plane-strain condition. This confirms that the initial suction in the slope must be carefully considered in the slope stability analysis. In the axisymmetric simulations, the failure is reached later, obtaining a good correspondence with the observations for both an initial suction 50 and 60 kPa (Figure 3-18). The shape of the shallow slip surface is given by the spatial distribution of the simulated plastic strains: (*i*) the results are similar in plane-strain (Figure 3-19a) and axisymmetric (Figure 3-19b) conditions, (*ii*) however, in the first case the slope failure is reached for an higher water table. As a main limitation, the second and deeper failure is not simulated because the analysis stops (lack of numerical convergence) once the first small failure occurs. A large-deformation analysis (e.g. *MPM*-based) may overcome such limitations.

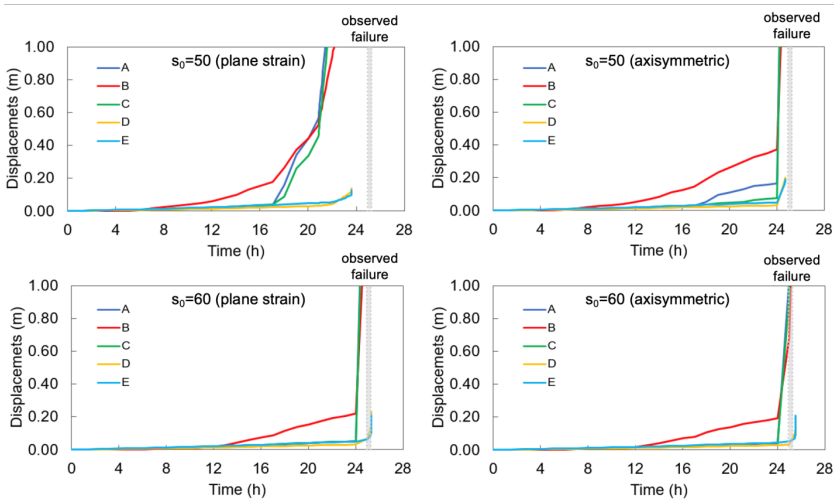

Figure 3-18. Trend of displacements over time for two different initial suction values considering plane strain or axisymmetric schematization.

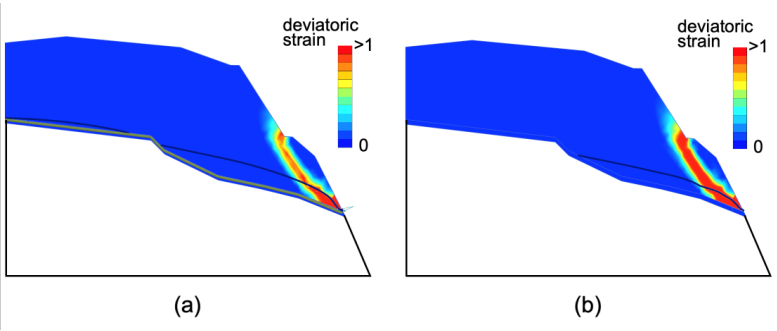

Figure 3-19. Plastic deviatoric strain distribution at failure for s_0=50 kPa: (a) plane strain; (b) axisymmetric.

3.2.6 Large-deformation MPM modelling

In this study, the formulation summarized in Martinelli et al. (2020) is used. The main simplifications are: (*i*) the governing equations for the gas phase are neglected, (*ii*) the mass exchange of air and water between the liquid and gas phases are also neglected, (*iii*) air pressure is set to zero. Compared to more general three phases formulations (solid, water, air), for instance proposed by Yerro et al. (2016), Ceccato et al. (2019) outline that in many real cases of geohazards the differences between three phases and two phases formulations are negligible, and that the simplified formulation reduces significantly the computational cost.

The concept of Bishop (1954) effective stress is used to include the effect of partial saturation soil condition (Equation 3-6), where $s = -p_L$ is the matric suction, and $\boldsymbol{I}$ is the identity matrix.

$$\boldsymbol{\sigma'} = \boldsymbol{\sigma} - S_r s \boldsymbol{I} \tag{3-6}$$

The relationship between soil degree of saturation (S_r), from unity to the residual degree of saturation (S_{res}), and soil matric suction is modelled through the van Genuchten (1980) equation as reported below, being α and β the function shape factors:

$$S_r(p_L) = S_{res} + (1 - S_{res}) \left[1 + \left(\frac{p_L}{\alpha} \right)^{\frac{1}{1-\beta}} \right]^{-\beta} \quad (3\text{-}7)$$

Given the saturated permeability (k_{sat}), the current permeability in a partially saturated state is equal to the product of k_{sat} multiplied by the relative permeability (k_{rel}). The latter is expressed as a function of the degree of saturation, as proposed by Mualem (1976), equal to 1 for a saturated soil down to lower values as the saturation degree diminishes (Equation 3-8).

$$k_{rel}(S_r) = \left(\frac{S_r - S_{res}}{1 - S_{res}} \right)^{0.5} \left[1 - \left(1 - \left(\frac{S_r - S_{res}}{1 - S_{res}} \right)^{\frac{1}{\beta}} \right) \right]^2 \quad (3\text{-}8)$$

The dynamic behaviour of a partially saturated soil (Martinelli et al. 2020) is described under the following general assumptions: (*i*) incompressible solid grains, isothermal condition, and no mass exchange between solid and liquid, as not relevant for most of the landslides, (*ii*) smooth spatial distribution of porosity and degree of saturation in the soil, as a reasonable assumption in most of the engineering applications (Mieremet et al. 2016; Ceccato et al. 2019).

Two different boundary conditions can be specified at ground level: (a) "ponding", i.e. pore-water pressure is set equal to zero, or (b) "infiltration", with a user-specified inward seepage flow, with the pore water pressures computed at the boundary. True velocity fields for both liquid and solid are used in this numerical algorithm (Martinelli et al., 2020), instead of Darcy's seepage velocity, used in other implementations (Bandara et al., 2016).

The maximum liquid pressure ($p_{L,max}$) is initially assumed equal to water cavitation pressure (100 kPa), which is reasonable for coarse-grained soils. Then, additional to the equation to proposed by Lee et al. (2019), the maximum liquid pressure is reduced as the cumulative deviatoric strains increase ($F_{red} \cdot p_{L,max}$). The reduction factor F_{red} that multiplies the maximum suction ($p_{L,max}$) is reported in Equation 3-9, where ε_d is the cumulative deviatoric strain, $\varepsilon_{d,thres}$ is the deviatoric

strain where the suction vanishes and a is a parameter controlling the trend of suction reduction. The rationale of such a hypothesis relies on theoretical explanations and experimental evidence demonstrating the reduction of bonding capillary forces with the increasing distances of soil grains (Scholtès et al. 2009; Gras et al. 2013; Zhao et al. 2019). For instance, during the slope instability evolution, the shearing among the soil grains may lead to the breakage of water menisci. For this reason, soil suction here is decreased with increasing deviatoric strains and vanishes of soil large deformations.

$$F_{red} = 1 - \left(\frac{\varepsilon_d}{\varepsilon_{d,thres}}\right)^a \tag{3-9}$$

Parametric analysis

A large-deformation MPM analysis is conducted to simulate the pre-failure, failure and post-failure landslide stages through a unified mechanical model. One issue for the combined simulation of rainfall infiltration and slope failure mechanisms is related to the different time scales during the landslide process (Figure 3-20a): a) the pre-failure stage (about 24 hours), for which rainfall infiltration is the main issue to be tackled, the slope is stable and soil deformations are very small (from t_0 and t_{24}), *b*) the instability evolution, which includes the two failures (delayed of about 20 minutes) and *c*) the propagation and final deposition of the debris during few tens of seconds (from t_{24} to t_f).

In the first stage (*a*) the time interval is assumed equal to 1 hour, while the slope instability stage (*b-c*) is discretized in seconds. The computational *MPM* scheme is given in Figure 3-20b. The upper Completely Decomposed Tuff (*CDT*) is included in the numerical analyses, and the lower kaolinite-rich layer is schematized as a contact surface, where a frictional contact algorithm is implemented. Another contact surface is considered between the urbanized zone and the landslide moving mass.

The stress-strain response of the completely decomposed tuff is modelled as an elasto-plastic material with Mohr-Coulomb failure criterion. The soil unsaturated material is tackled through the two-phase single-point formulation, while the one-phase single-point formulation is applied for the contact surfaces. The background calculation mesh is composed of 6,753 triangular 3-noded elements, with an overall size of about 1 meter assigned to the whole domain, and local refinements of the mesh. The rainfall input is the hyetograph of Figure 1 and the initial suction value at the beginning of the rain is set as constant along the depth as done in the previous *FEM* analyses.

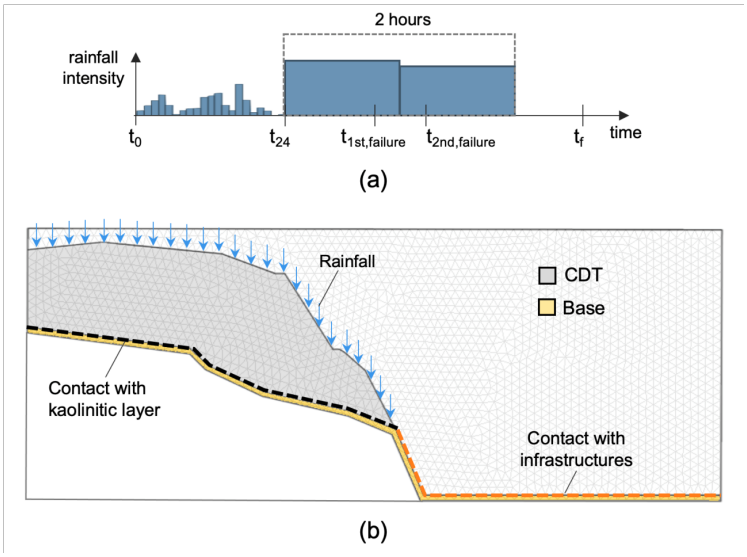

Figure 3-20. (a) Simulations stages: infiltration (t_0-t_{24}) and propagation (t_{24}-t_f); (b) domain schematization including soil materials and contact surfaces

A parametric analysis is conducted by changing the input parameters which may affect more the landslide mechanisms: (*i*) the initial soil suction (s_0), (*ii*) the basal friction contacts along the kaolinitic layer (φ'_b) and (*iii*) the exponent *a of* eq. 10, which controls the trend of suction reduction, (*iv*) the contact friction along the Fei Tsui Road to well reproduce the debris deposit. Both plane-strain and axisymmetric conditions are considered to point out the effects of lateral deformations. A recent

version of the Anura3D code, developed by Deltares (Martinelli et al. 2020), is used to perform the *MPM* simulations. The goal is to achieve the closest correspondence with the field evidence in terms of occurrence time of the two failures, shape of the sliding surface and final configuration of the debris deposition.

Some selected results are reported in Tables 3-4 and 3-5 for the plane-strain and the axisymmetric simulations, respectively, and two Kiviat diagrams are also used (Figure 3-21).

The difference between the plane strain and the axisymmetric conditions is highlighted by the simulations named PS4 (plane strain) and A4 (axisym.), with the same input parameters. The PS4 simulation indicates a slope failure at 17 hours, the A4 simulation at about 24 hours, with the slope failing in the field at about 25 hours. If the initial suction is increased by 2.5 kPa, the PS5 (plane strain) also captures the failure time. This small difference between plane strain and axisymmetric formulations is because in the axisymmetric simulation the rainfall infiltration is supposed to be radial, thus the water seepage inside the slope is slightly less than in plane strain condition.

It is found that an increased initial suction in the slope delays the whole progressive failure and reduces the landslide runout. As expected, an increasing friction angle of the kaolinitic layer (*PS1* vs *PS3*) also delays the slope failure, which occurs progressively instead of being abrupt, and also the final landslide runout is reduced. Instead, the larger is the suction reduction parameter (*a*), the greater is the amount of soil displaced during the landslide process, the shorter are the simulated failure times (e.g. *A4* vs *A1*), and smaller is the runout distance. Finally, the feature of the road influences exclusively the time of second failure and moderately the landslide runout. The field observations are well captured for: $s_0 = 50 - 52.5\ kPa$, $\frac{tan(\varphi_{kaolin})}{(\varphi'_b)} = 0.75 - 1.00$ and $\varphi'_{kaolin} = 29°$. These back-analysed values are consistent with both: (*i*) the *LEM* and *FEM* shown in the previous section, and (*ii*) field observation (Figure 3-21).

Table 3-4. input and output of plane strain simulations

	INPUT				OUTPUT		
ID	s_0 *(kPa)*	$tan(\varphi_{kaolin})$	$tan(\varphi_{kaolin})/tan(\varphi'_b)$	*a*	*1st failure (h)*	*2nd failure (h)*	*run-out (m)*
PS1	50	0.55	1.00	-∞	24.97	25.42	55
PS2	55	0.55	0.75	5	25.25	25.92	72
PS3	50	0.4	1.00	-∞	20.00	20.00	63
PS4	50	0.55	0.75	5	17.50	18.25	80
PS5	52.5	0.55	1.00	1	24.44	24.89	83

Table 3-5. input and output of axisymmetric simulations

	INPUT				OUTPUT		
ID	s_0 *(kPa)*	$tan(\varphi_{kaolin})$	$tan(\varphi_{kaolin})/tan(\varphi'_b)$	*a*	*1st failure (h)*	*2nd failure (h)*	*run-out (m)*
A1	50	0.55	0.75	1	24.63	25.17	78
A2	50	0.55	0.50	5	24.56	24.75	83
A3	52.5	0.55	0.75	5	24.75	25.03	71
A4	50	0.55	0.75	5	24.56	24.92	74
A5	55	0.55	0.75	5	25.42	25.72	77

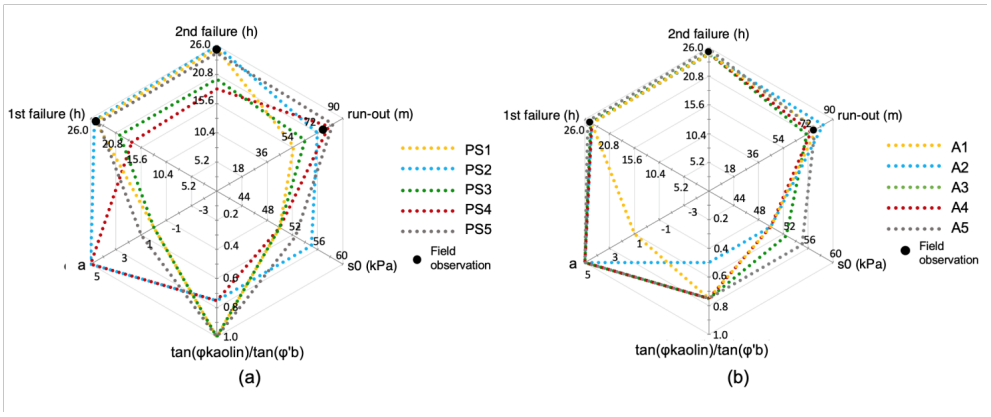

Figure 3-21. Comparison of the numerical results with the field evidence as function of the input data: (a) plane strain (PS1-PS5) and (b) axisymmetric simulations (A1-A5)

Numerical results versus field evidence

The best-fit simulations (plane strain and axisymmetric) are discussed here. The landslide evolution in the case of PS5 plane-strain simulation is commented on starting from 24 hours, until when the slope is stable (Figure 3-22a). The soil slides along a newly formed shear band as time goes ahead, and a shallow failure is simulated in good agreement (slightly before) with what reported by Knill (1996), see Figure 3-22b. This happens because the heavy rainfall makes the wetting front move downward and forms a perched water table of about 2 m above the kaolinitic layer contact. A deeper failure is highlighted by a new shear band and a retrogressive failure mechanism occurs approximately when the second failure was observed (Figure 3-22c).

In axisymmetric conditions (case A1, Figure 3-23) the evolution of the cumulative plastic strain, displacements and liquid pressure are similar, and the failure mechanism practically the same as those reported before. The simulated failure time is slightly delayed and the material deposited (Figure 3-23c) is smaller than before, but still consistent with the failure times observed in the field.

Table 3-6. CDT properties used as input for the MPM analysis

ρ_S (kg/m^3)	n (-)	k_{sat} (m/s)	E (MPa)	ν (-)	c' (kPa)	φ' (°)	ψ (°)
2650	0.4	5×10-5	10	0.3	5	35	0
ρ_L (kg/m^3)	K_L (MPa)	μ_L (Pas)	α (kPa)	β (-)	S_{res}	$\varepsilon_{d,thres}$	a
1000	100	10-3	64	0.47	0.275	1	1

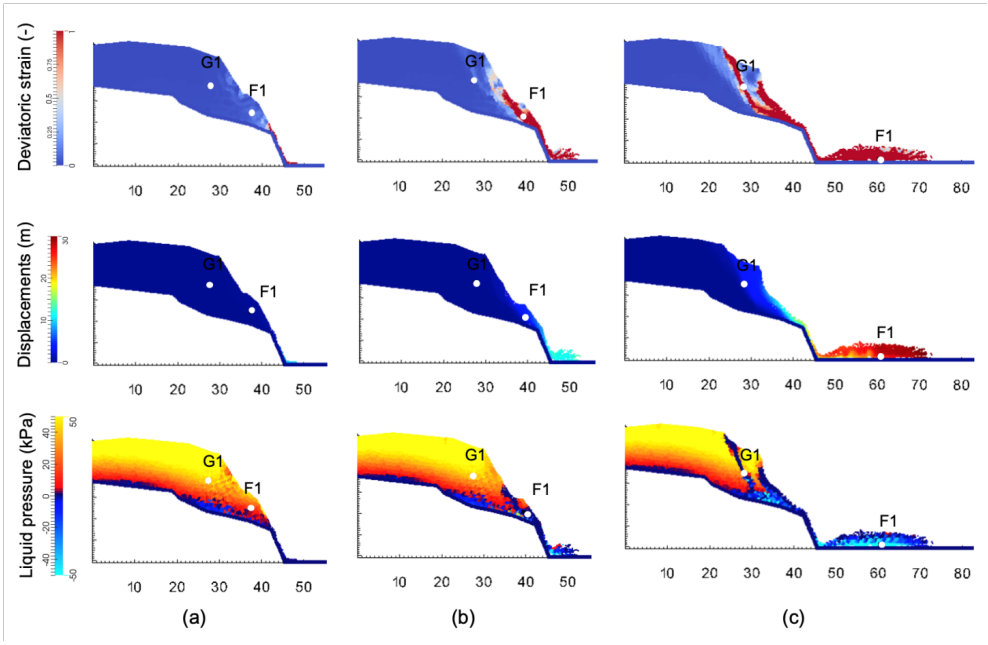

Figure 3-22. Trend of deviatoric strain, velocity and displacements computed in plane strain condition and for an initial suction of 50 kPa: (a) t= 24 h; (b) t= 24.44 h (first failure) and (c) t=24.89 h (second failure)

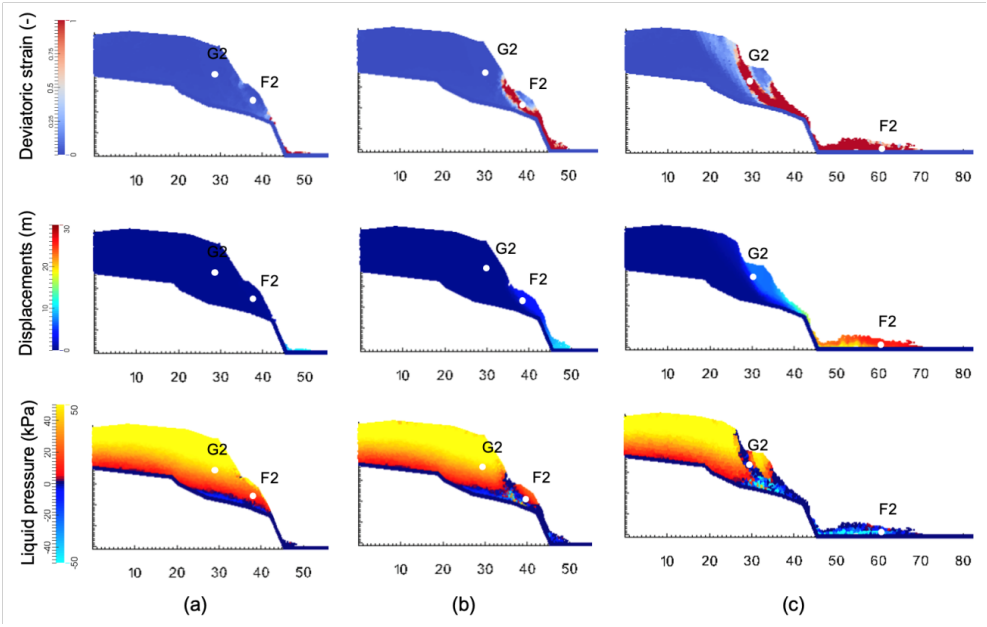

Figure 3-23. Trend of deviatoric strain, velocity and displacements computed in axisymmetric condition and for an initial suction of 50 kPa: (a) t= 24 h; (b) t= 24.63 h (first failure) and (c) t=25.17 h (second failure)

The displacement time-trend (Figure 3-24a) of two points located along the shallow (points *F1* and *F2*) and deep (points *G1* and *G2*) slip surfaces (Figures 3-22 and 3-23) provide more insights. At *F1-F2*, the computed displacements suddenly increase, indicating the occurrence of the first small failure, about at the time reported by eyewitnesses. At *G1-G2*, the displacements grow suddenly after about 20 minutes (as observed in the field), indicating that the second major failure occurs. In the plane-strain simulations, the two failures are simulated slightly before than in the axisymmetric ones. The computed mean effective stresses decrease much when either the first (F1-F2 points) or the second failure (G1-G2 points) occurs. After failure, the mean effective stress slightly increases due to soil consolidation. This plot also helps better understand the progressive failure mechanism of the landslide. In fact, while the F1-F2 points located in the shallow slip surface are characterized by a sudden stress decrease due to the first slope failure, the stress values in the G1-G2 points are still high and drop to zero during the second failure.

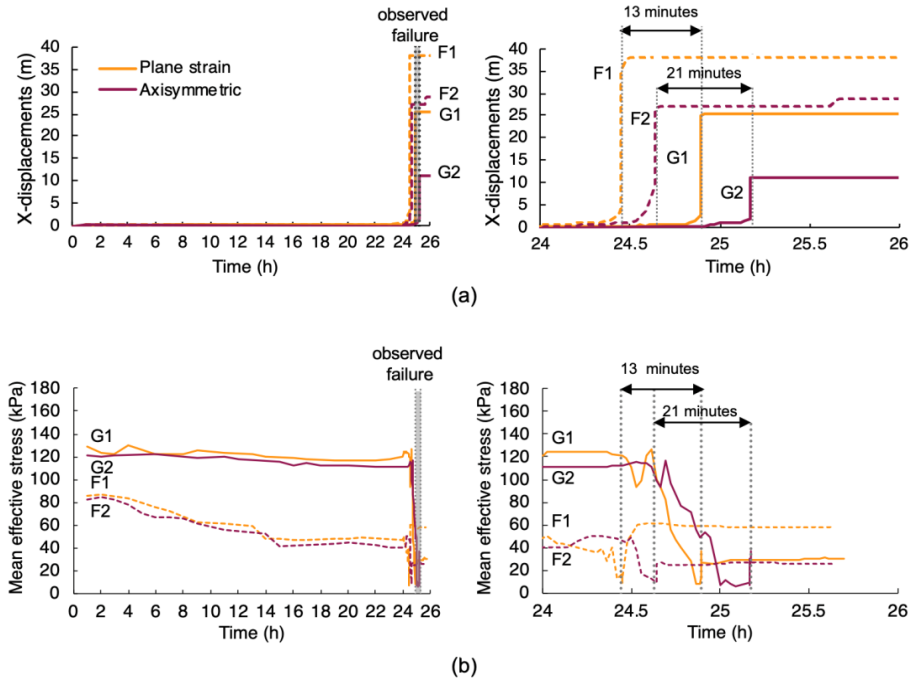

Figure 3-24. Temporal trend of the horizontal displacements (a) and mean effective stress (b)inside two reference points in both plane strain and axisymmetric assumptions

Plotting the computed stress paths at these control points (Figure 3-25) is also of interest. The most relevant insights are that: (*i*) failure is always reached at low stress state, i.e. in the lower left corner of the graph; (*ii*) when the F-points (shallow slip surface) reach the Critical State Line (*CSL*), the G-points (deep slip surface) are still at high stress levels; (*iii*) the stress paths calculated in plane strain and axisymmetric conditions are similar.

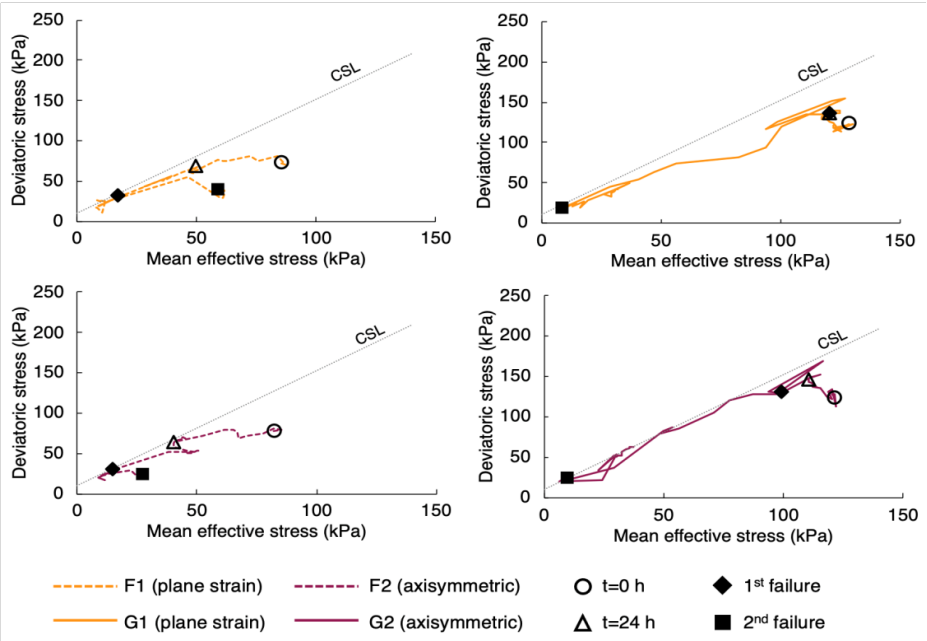

Figure 3-25. Stress paths inside the two reference points in both plane strain and axisymmetric assumptions

The back-analysed values of the initial suction and the basal friction angle at contact surfaces also allow a good simulation of the observed debris deposition (Figure 3-26), highlighting the potential of MPM analysis to reproduce the whole landslide process.

The difference between the plane-strain and axisymmetric assumptions can be better understood looking at the debris deposition. In plane-strain condition (Figure 3-26a), the calculated final deposition volume per unit width is about 140% of that measured in the field; in the axisymmetric simulation it is equal to 90% (Figure 3-

26b). Anyway, the deformations, displacements and liquid pressure are very similar for both simulations. In fact, the deviatoric strain distribution is everywhere much greater than 1, indicating that the landslide body undergoes large deformations and is completely remoulded. The spatial distribution of the displacements also indicates displacements of the failed mass greater than 30 m from its original position.

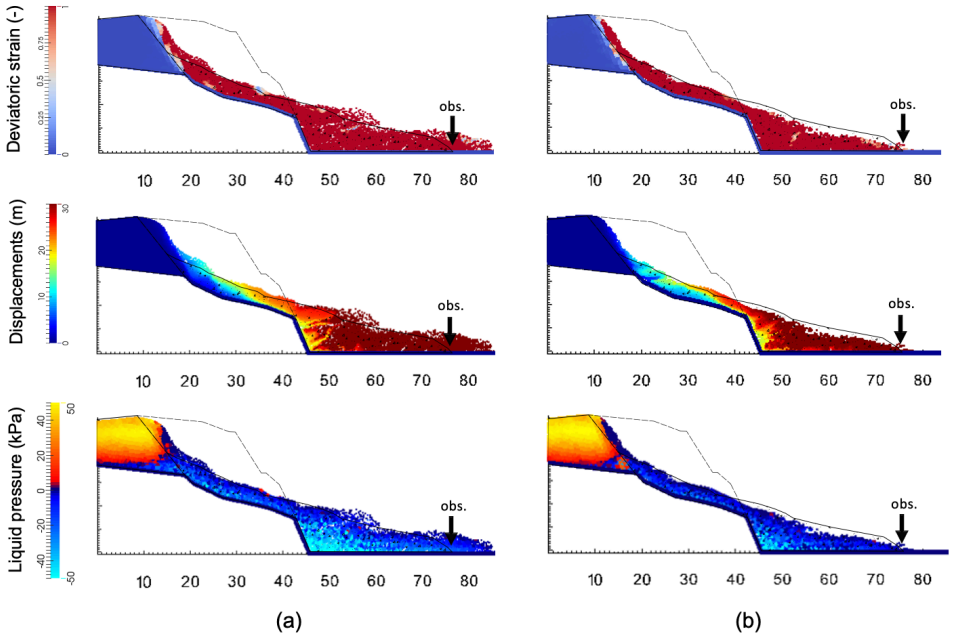

Figure 3-26. Observed and simulated debris deposition: (a) plane strain; (b) axisymmetric.

Finally, the liquid pressure distribution is also an interesting result to comment more. Inside the landslide body, the liquid pressure: (*i*) increases during the pre-failure rainfall infiltration, (*ii*) is increased more during landslide triggering and propagation, and (*iii*) finally is lowered during deposition. The scar of the landslide remains stable due to the presence of suction. Here, the computed suction is almost unchanged during the whole landslide process, which well explains the field evidence. In previous literature contributions, this portion of the slope has been simply schematized as firm rock (Lee et al., 2019) or practically undeformable soil, i.e. with a cohesion of hundreds of kPa (Liu et al., 2020).

3.2.7 Discussion

The results achieved highlight the similarities and differences among the models based on: 1) *no-deformation FEM* (also named *uncoupled seepage FEM* in the literature), 2) *small-deformation FEM* (i.e. hydro-mechanical coupled stress-strain FEM), and 3) *large-deformation MPM* (i.e. hydro-mechanical coupled stress-strain *MPM*) in analysing the instability evolution of the slope.

A general agreement among the three computed spatio-temporal distributions of the pore water pressure is observed. This overall agreement validates the independent hypotheses made in each method, and also using independent codes, namely: Seep/W for no-deformation FEM, Plaxis 2D for small-deformation FEM, and Anura 3D for large-deformation *MPM*. For instance, the spatial distributions of pore-water pressure computed at a specific time lapse (t=18 h), for an initial soil suction uniform along the vertical and equal to 50 kPa, are compared in Figure 3-27. Either the unsaturated zone or the water table is very similar in the three models. This is because slope failure is not reached yet and soil deformations are still moderate. However, at specific points, some local differences can be noted in the temporal trend of pore-water pressure computed through the three methods (Figure 3-28). The 24-hours time trends of the two hydro-mechanical coupled stress-strain models (*small-deformation FEM* and *large-deformation MPM*) are very similar, whereas the *no-deformation FEM* model provides some difference. This is because the model disregards the effect of soil deformations on soil stress and pore-water pressures. Thus, the coupled analysis provides a faster drop of suction compared to the uncoupled model, as expected. In addition, the very fast drop in suction at the rear part of the slope at about 25 hours is only captured by the *large-deformation MPM* model.

A good agreement between the *small-deformation FEM* model and the *large-deformation MPM* model is also achieved for the time trends of displacements, computed both in plane strain (Figure 3-29a) or axisymmetric (Figure 3-29b) conditions until 22-24 hours. As the slope failure starts, some differences arise, with

the large-deformation *MPM* model being the only one capable of reproducing some sudden accelerations. At a certain stage of the landslide process, the *small-deformation FEM* analysis does not converge while the *large-deformation MPM* model reproduces the whole soil deformation process also including propagation and deposition.

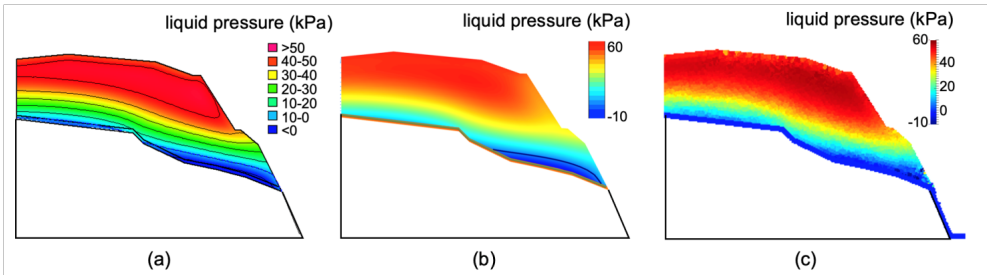

Fig. 3-27 Pore-water pressure distribution for s_0=50 kPa at t=18 h: (a) no-deformation FEM (b) small-deformation FEM and (c) large-deformation MPM analysis

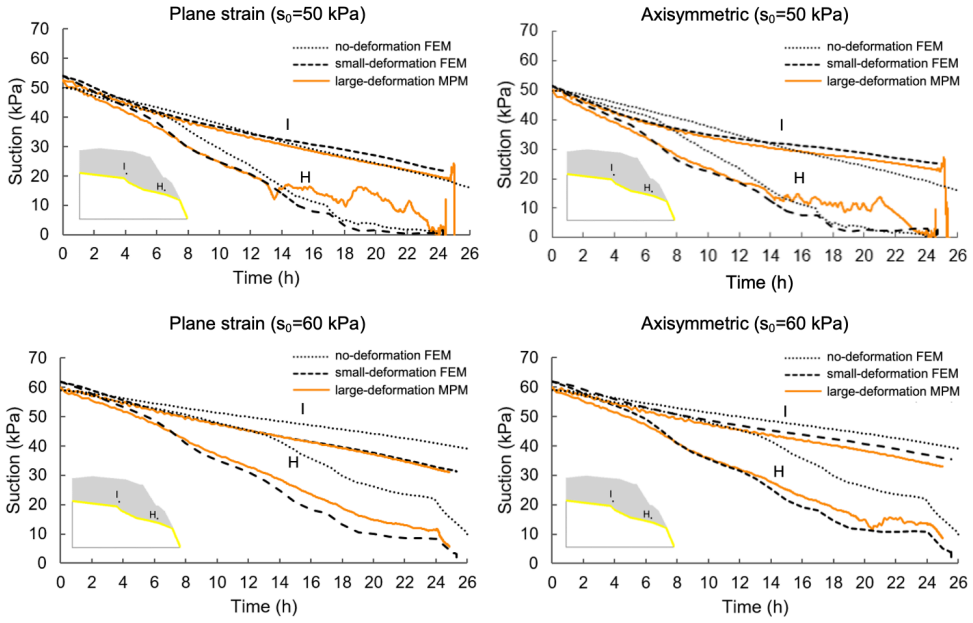

Figure 3-28. Comparison among no-deformation FEM analysis, small-deformation FEM analysis and large-deformation MPM analysis in terms of pore-water pressures over time, in axisymmetric and plane strain conditions, for different initial suction.

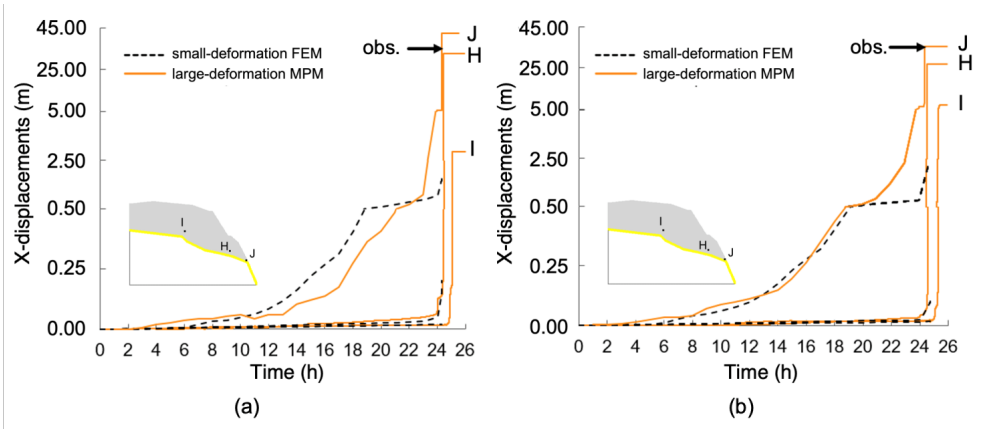

Figure 3-29. Comparison among small-deformation FEM and large-deformation MPM results in terms of horizontal displacements for s_0=50 kPa: (a) plane strain; (b) axisymmetric.

3.2.8 Concluding remarks

The presented study deals with the simulation of rainfall-induced landslides in an unsaturated slope, by proposing a framework based on a multi-tool approach for modelling. The framework is based on three levels, *no-deformation LEM*, *small-deformation FEM*, *large-deformation MPM*, and it is applied to an international benchmark landslide case (the 1995 Fei Tsui Road landslide in Hong Kong), for its complexity and also for the wide site-specific scientific literature.

A comprehensive series of *LEM*, *FEM* and *MPM* analyses is performed to get insights on various landslide characteristics. The *no-deformation LEM* analysis are used to back-analyse some important unknowns (e.g., initial suction distribution) or uncertain quantities (e.g. critical water table depth) by comparing the observed failures with the safety factor computed at some selected slip surfaces. More comprehensive stress-strain *small-deformation FEM* analyses outline the influence of the initial suction on type and time of slope failure. The more general *large-deformation MPM* (two-phase single-point) modelling simulates the landslide dynamics from failure onset up to soil deposition. The effect and evolution of soil suction in relation to soil shear strain during the whole landslide process is taken into

account. In addition, the *MPM* analyses in axisymmetric conditions assess the effects of lateral spreading during the propagation stage.

Based on the achieved results, fully coupled hydro-mechanical large-deformation models are needed to properly reproduce the complex failure and post-failure mechanisms of rainfall-induced landslides. However, no-deformation *LEM* analyses and small-deformation stress-strain *FEM* analyses provide useful quantitative indications towards the understanding of the failure mechanisms. Moreover, some important quantities that play an important role in the pre-failure and failure stages are properly investigated.

A key issue is the fine-tuning of landslide diagnosis. LEM and FEM analyses are the standard tools for pre-failure and failure stages. However, the modelling of progressive failure, retrogressive landslides, and other cascading effects requires more advanced tools. It is true that enhanced FEM formulations combined with sophisticated soil constitutive equations have much contributed in recent times to the simulation of complex slope instabilities. However, MPM and other large-deformation modeling tools will play a significant role in the future developments about landslide modeling. Thus, while promoting the new emerging numerical tools (among which *MPM* deserves attention), it is still important stressing the value and the indispensable role of more traditional tools in the current engineering practice and research.

4. Landslide-Structure-Interaction (LSI) modelling

4.1 Reduced-scale experiments on impact behaviour of dry granular flows

4.1.1 Experimental tests of Moriguchi et al. (2009)

Small-scale experiments were conducted by Moriguchi et al. (2009) to evaluate the impact force of a dry granular flow on a rigid wall after propagating at different slope angles (θ). The Toyoura sand (Tab. 4-1) was used, with 50 kg put into a 50x30x30 cm box situated at the top of a plastic transparent flume. The sand was released by the outer opening door of the box, and after sliding 1.80 m, impacted against a wall 0.3 m high. The configuration of the slope model is shown in Figure 4-1. The upper side of the flume box is not closed hence the sand can overcome the barrier. Some sand was glued on the base of flume to create friction with the mass flowing down, whereas the impact surface of the wall can be considered as smooth.

The inclination of the flume was varied from 45 to 65° at intervals of 5°. The impact force on the wall was recorded using a load cell placed inside the wall itself and for each inclination five trials of experiment were conducted. Among various results, the peak impact force increases rapidly with higher inclinations, except for 45°and 50° where the peak cannot be uniquely identified (Figure 4-1).

Table 4-1. Characteristic of the Toyoura sand adopted in the experiment

ρ (kg/m^3)	e_{min}	e_{max}	D_{min} (mm)	D_{max} (mm)	C_U
1379	0.61	0.97	0.102	0.425	1.37

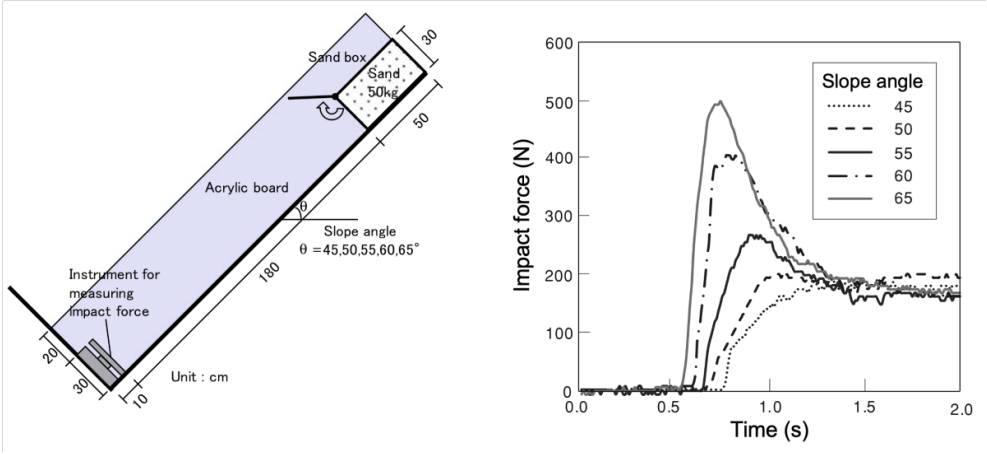

Figure 4-1. Flume configuration and impact forces recorded in the experiments of Moriguchi et al. (2009)

4.1.2 MPM one-phase modelling

The numerical model schematizes the cross-section of the flume in plane strain conditions. The 2D mesh consists in 23,511 triangular elements with an average size of 0.02 m. The simulations consider: the granular material with elasto-plastic failure behavior, the sliding plane with a contact friction coefficient and the barrier with a rigid behavior (Figure 4-1). The *one-phase single-point formulation* is adopted to schematize all the materials and the mixed-integration is used to calculate the internal forces of the system (see Al-Kafaji, 2013; Fern et al., 2019; among others).

The first stage of the analysis aimed to determine the most likely value of a chosen set of parameters including internal friction angle (φ'), Young modulus of soil (E) and contact friction angle (φ'_b). For the calibration of these parameters, the flume inclination of 45° was considered. The other slope angles (50°, 55°, 60° and 65°) were then used for model validation.

The parameters obtained from calibration are shown in Table 4-2, with also some other values used later in a sensitivity analysis. The friction coefficient at contact with the sliding surface $tan(\varphi'_b)$ was assumed as equal to $\tan(\varphi')$, since the flume was coated with sand, whereas the wall was considered smooth and thus the friction

coefficient is set to zero. The calibration of model parameters was pursued by comparing the flow configurations at four time lapses (0.4, 0.8, 1.2 and 1.6 seconds), for which the snapshots of the experiments and the numerical results were both available (Figure 4-3).

Table 4-2. Input used for the calibration and validation of the MPM model

Material	Constitutive model	ρ_s (kg/m^3)	n (-)	E (MPa)	ν (-)	c' (kPa)	φ' (°)	φ'_b (°)	ψ (°)
Dry sand	MC	2650	0.48	10 20 30	0.2	0	30 35 40	0 20 40	0
Plane	LE	7850	0	infinity	0.3	-	-	-	-
Rigid wall	LE	7850	0	infinity	0.3	-	-	-	-

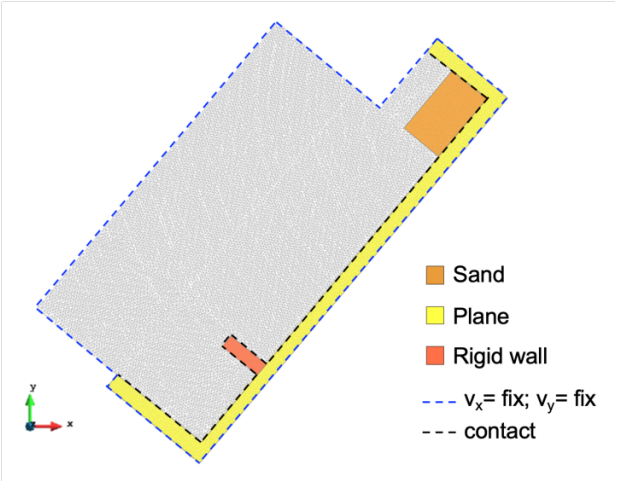

Figure 4-2. Computational mesh and materials

The trend of the impact force F over time was also used as observation for the model calibration. The contact formulation was used to ensure that no interpenetration occurs, and the tangential forces are compatible with the shear strength along the contact. The reaction force at node i was calculated as follows:

$$\boldsymbol{F}_{contact,i} = \boldsymbol{m}_{i,\mathrm{S}}\boldsymbol{\Delta a}_{S,contact} + \boldsymbol{m}_{i,\mathrm{L}}\boldsymbol{\Delta a}_{L,contact} \quad (4\text{-}1)$$

where $\Delta a_{S,contact}$ and $\Delta a_{L,contact}$ are the change in acceleration induced by the contact formulation, for both solid and liquid phase, and $m_{i,S}$ and $m_{i,L}$ are the corresponding nodal masses. The total reaction force is the integral of the nodal reaction forces along the barrier.

The calibrated parameters allow a good agreement between simulated and experimental results also in terms of impact force (Figure 4-4).

The model was then validated with the tests with inclinations of 50°, 55°, 60° and 65° as shown in Figure 4-5, where it is clear a good match between simulation and experiment for each inclination of the flume. Such correspondence is even emphasized in Figure 4-6, which shows that both the simulated peak force and time to peak deviate from the experiments by a maximum of 15%. All the output from simulations were post-processed in order to eliminate the outliers and to obtain a mean trend of the impact force curves. In this case, the Gaussian function available in Matlab's "curve fitting" tool was employed.

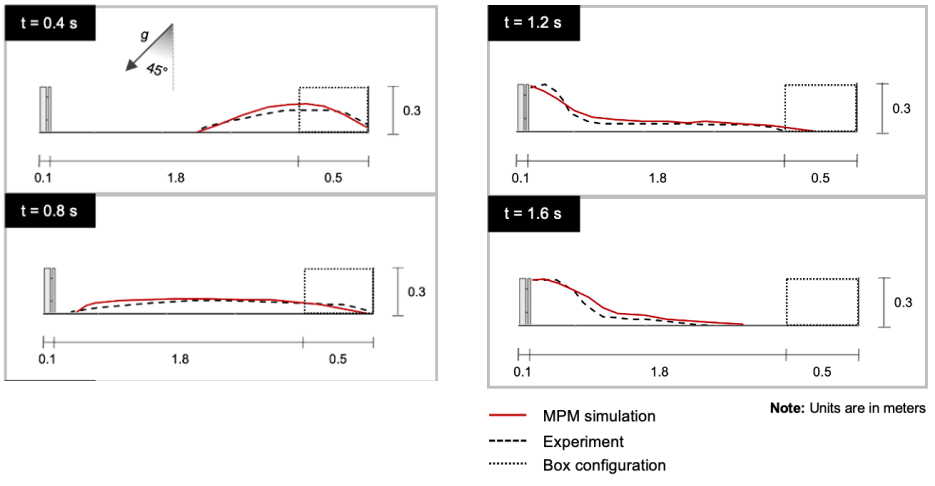

Figure 4-3. Comparison between experimental and simulated flow configurations

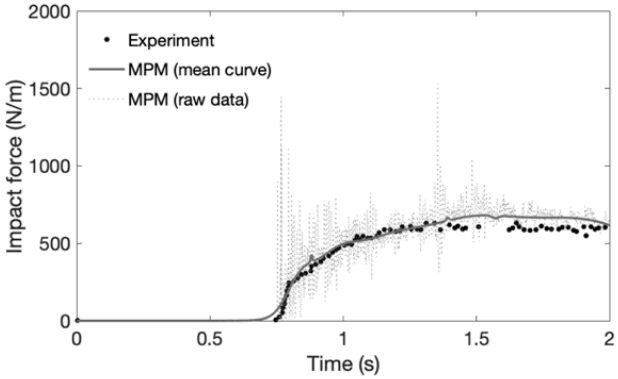

Figure 4-4. MPM model calibration for slope inclination θ= 45°

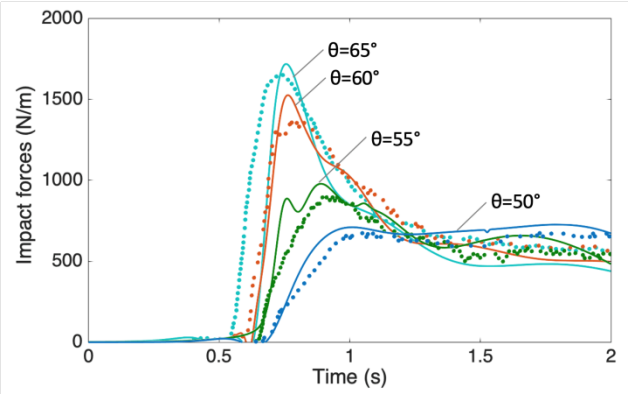

Figure 4-5. Validation of MPM model for different inclinations: experimental results in dotted lines and simulation results in continuous lines

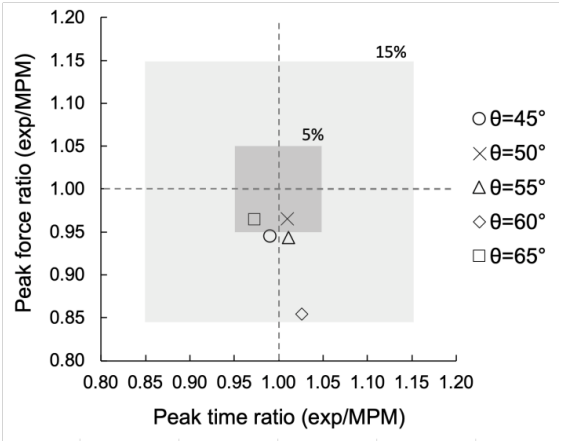

Figure 4-6. Observations versus simulation results

4.1.3 Discussion of the results

The trend in space and time of many physical variables (e.g. stress, strain, velocity, pore pressure and other state parameters) was also investigated. For example, the distribution of deviatoric strain during impact allowed understanding that in the case of dry granular flows if the contact shear stress is high (as for inclination of 45° in Figure 4-7a) the impact mechanism results in a pile-up without evident peak load, as also highlighted by Choi et al. (2015). If the inclination angle is high (like 65° in Figure 4-7b) the impact mechanism of the dry flow resembles the run-up mechanism, which is typical of partially or fully saturated flow (Ng et al. 2017; Song et al. 2017, 2018; Zhou et al. 2018). Also in this case, the impact force trend is consistent with the vertical jet mechanism, previously outlined in the literature, with such behaviour mainly linked to the lower shear stress and easily identifiable from the computed deviatoric strain distribution.

The tempo-spatial distribution of both velocity and depth of the approaching flow is another useful result achieved through the MPM simulations. These quantities are correlated to the Froude number through the well-known equation:

$$Fr(x,y,t) = \frac{v(x,y,t)}{\sqrt{gh(x,y,t)}} \tag{4-2}$$

It is possible to identify the impact mechanism patterns by comparing the spatial distribution of the Froude number at the impact and the obstacle height relative to the flow depth (H/h). The obvious benefit compared to laboratory experiments or depth-integrated models here is that the flow velocity and depth are not averaged. Let's define h the flow depth at the upstream section of the granular jump (namely bore), $L_{(+)}$ and $L_{(-)}$ the length of the zones of influence upstream and downstream of the wall, respectively (Faug, 2015).

If the flume is inclined of 45°, a thick granular layer moves upstream of the wall (subcritical flow) and intercepts the grains from the incoming rapid flow (supercritical flow). This is immediately visible from the spatial distribution of Fr

(Figure 4-8). The impact mechanism resembles the bores regime in the phase diagram proposed by Faug (2015), since a granular bore is formed at the transition between the subcritical and the supercritical flow. As H/h decreases, a stationary granular jump is formed leading to a steady value of $L_{(+)}$, while a part of the incoming supercritical flow runs over the wall, forming a jet with very low energy ($L_{(-)}$ much smaller than $L_{(+)}$).

In the case of 65° inclined slope, a granular airborne jet is observed downstream of the wall. As highlighted in Figure 4-8, the incoming flow is characterized by low H/h and high Fr. In this situation, the flow can easily move over the wall forming a large granular airborne jet. When steady state is reached, the downstream length $L_{(-)}$ is much larger than $L_{(+)}$, which is close to the barrier height.

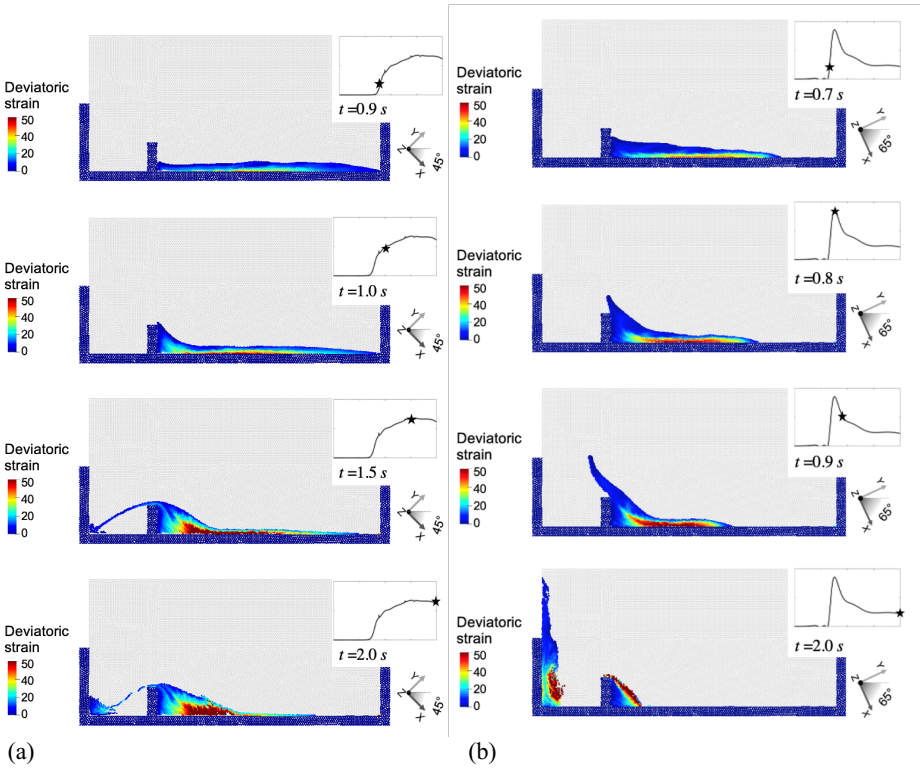

Figure 4-7. Tempo-spatial distribution of soil deviatoric strain for the inclination of 45° (a) and 65° (b)

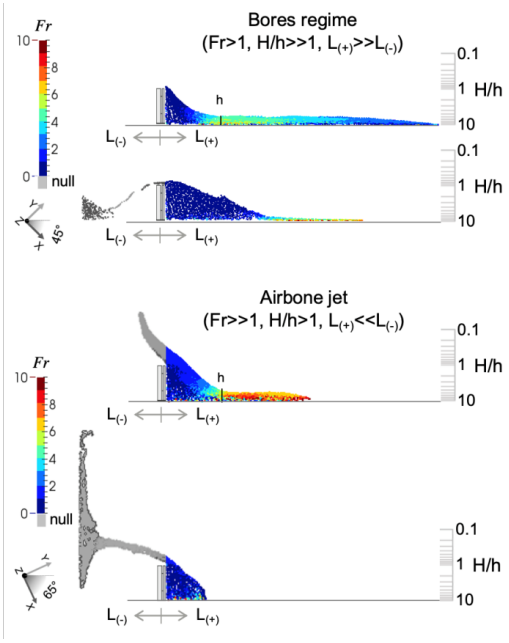

Figure 4-8. Impact mechanism regimes for slope inclinations of 45° and 65°

Based on the satisfactory calibration and validation of the proposed MPM model, it is now possible investigating the role played by some parameters on the flow impact behaviour. It has been seen that a variation of the soil Young modulus E is not significant in terms of flow propagation and it neither influences the impact force trend (Figure 4-9a), contrarily to soil effective friction angle (φ') and base contact friction (φ'_b) that create substantial differences. Decreasing φ', the granular flow propagates faster (Figure 4-9b), the dynamic force increases, while the static component of the force is not much influenced. Other considerations are made with the base contact friction (φ'_b) changed (Figure 4-9c): i) if φ'_b is reduced to $\varphi'/2$, the impact mechanism changes from pile-up to run-up and the related impact force now reaches an evident peak, ii) if φ'_b is put equal to zero (i.e. completely smooth slope), the peak force increses much.

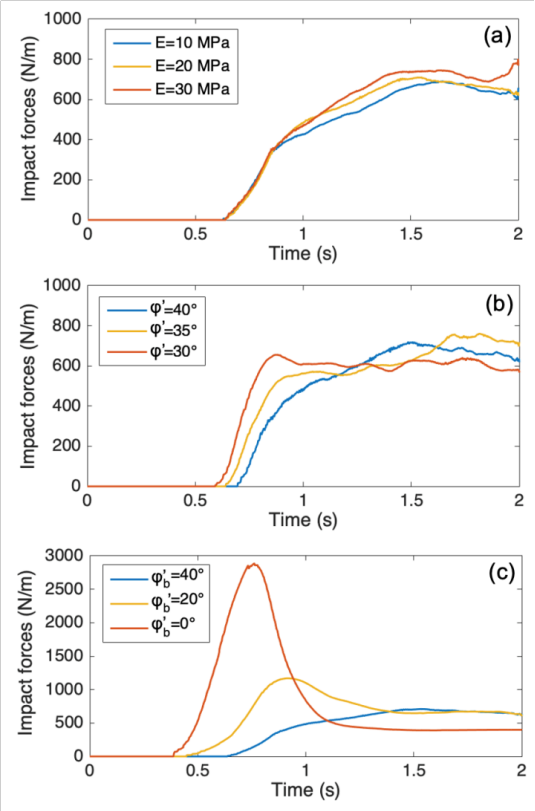

Figure 4-9. Impact force over time: comparison between experimental and MPM results for different (a) E, (b) φ' and (c) φ'b

4.2 Centrifuge tests of flows impacting rigid barriers

4.2.1 Experimental evidence of Song et al. (2017)

The material was put in a container of 0.03 m^3 (model scale) to reproduce a prototype flow-like landslide with a volume of about 170 m^3 and dropped from a height of 500 mm onto the slope by opening a bottom door of 200 mm (Figure 4-10). A steel barrier, equivalent to a reinforced concrete wall (0.9 m thick and 4.5 m high) was used. A centrifuge scale factor (N) of 22.4 g is here referred to convert the model quantities to the prototype scale, being the value of the gravity acceleration at

the mid-height of the barrier during the centrifuge tests. In particular, forces and the times in the prototype scale are amplified of N^2 and N times, respectively, while the conversion factors for other quantities are reported by Song et al. (2017). The authors examined the flow impact behaviour by varying the solid fraction among the values of 0.0 (fluid case), 0.2, 0.4, 0.5 and 0.58. The Leighton Buzzard (LB) fraction C sand was adopted, characterized by grains of 0.6 mm diameter and a specific gravity of 2.679. The viscous liquid adopted is a solution of water and carboxy methyl cellulose (CMC), with the same density of water and viscosity equal to 0.022 Pa·s in the model scale. The properties of the materials used in the tests are summarized in Table 4-3. During the tests, 15 sets of semiconductor strain gauges, 5 dynamic load cells fixed inside the barrier and a high-speed camera able to measure the velocity of the flow through PIV (Particle Image Velocimetry) analysis were used.

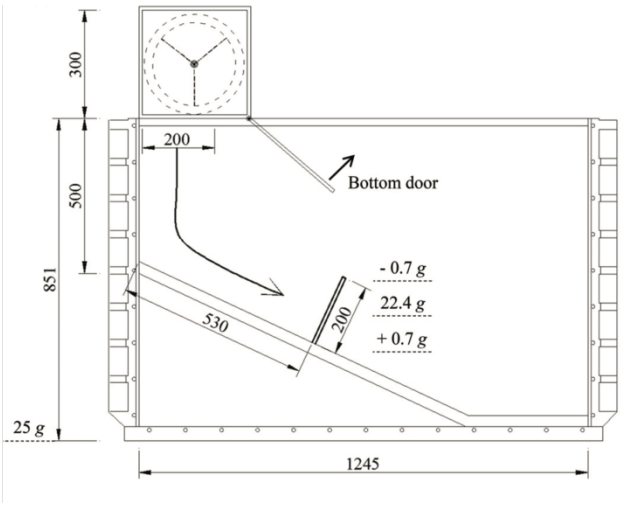

Figure 4-10. Centrifuge apparatus used in the experiment (Song et al., 2017)

Table 4-3. Properties of the materials used in the tests, whose ID are reported in brackets

Material	ρ_S (kg/m^3)	μ_L (Pas)	n (-)	φ' (°)
Viscous fluid	1000 (L)	0.022	-	-
LB sand (fraction C)	1825 (SL50) 1660 (SL40)	-	0.5 0.4	31

4.2.2 MPM two-phase modelling

The centrifuge device is numerically schematized by a 3-node triangular unstructured mesh with an average element size of 0.015 m. In order to avoid unrealistic movements of the flow at impact against the barrier, an additional contact node is considered in the top left corner of the barrier allowing the presence of two normals on each adjacent side (Figure 4-11). The dimensions in the numerical model are the same of the experiment and a gravity multiplier of 22.4 is considered.

It is worth noting that during the tests the flow undergoes a radial increment of N, principally affecting the dropping of the mixture from the box. For instance, the sample is initially triggered at about *17.8 g*-level. However, the numerical model cannot consider a linear change of g with the distance from the centre of the centrifuge. To overcome such difficulty, a size re-adjustment of the sizes of the numerical model is performed along the vertical direction, considering that in the centrifuge test the *g*-level differs from 17.8 (at the storage container) to 22.4 (at middle height of the barrier). First, a uniform 100 mm discretization is done and then each discretized length Δy_i is multiplied by the local N_i in order to obtain the local prototype dimensions, which are finally rescaled to the model size through the N factor of 22.4. In this way, the new dimensions of the box are equal to 238 mm (i.e. 300 mm x 17.8 g / 22.4 g) and the distance between the bottom of the storage container and the top of the slope is 454 mm (i.e. $\sum_i \Delta y_i \, N_i/22.4$). Without this specific procedure, the numerical model would correspond to a prototype debris flow volume of 340 m^3, twice than in the experiments.

The MPM model is calibrated for the mixture with 50% solid fraction (SL50 test), that is representative of real flow-like landslides. The model is then validated in the case of 40% solid fraction (SL40 test) whose impact force diagram is reported in Song et al. (2018). The *two-phase one-point* formulation is used to model the mixture with a fully hydro-mechanical coupled behaviour, while the flume and the rigid barrier are modelled with the *one-phase one-point* formulation.

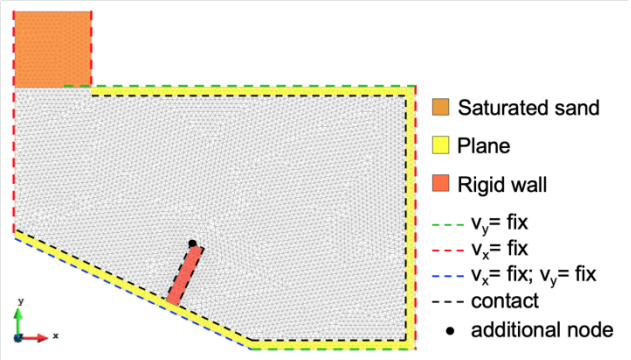

Figure 4-11 Computational mesh and materials

The *two-phase one-point* formulation is generally adopted in problems with small gradients of porosity, and laminar and stationary flow in slow velocity regime because the contribution of the spatial variations of liquid mass is neglected and Darcy's law is used to model solid-liquid interaction forces. To investigate the non-linear contribution of the seepage velocity on the solid-liquid interaction forces, which could be relevant in high porosity mixtures where seepage velocity is high, the drag force vector is calculated according to Equation 4-3 (Martinelli and Rohe, 2015). The coefficient F_E in Equation 4-3 is computed through Equation 4-4, where A and B are two constants which can be set respectively to 150 and 1.75, according to Ergun (1952).

$$\mathbf{f}_d = n\left[\frac{\mu_L}{k} + n\rho_L \frac{F_E}{\sqrt{k}}|\mathbf{v}_L - \mathbf{v}_S|\right](\mathbf{v}_L - \mathbf{v}_S) \tag{4-3}$$

$$F_E = \frac{B}{\sqrt{A}\, n^{3/2}} \tag{4-4}$$

The interactions between the flow and the flume or the barrier are handled through the same frictional contact algorithm used before. An elasto-plastic behavior is assumed for the sand at failure, while the barrier and the slope are assumed as linear elastic materials. The pore-fluid bulk modulus is set to a low value in order to decrease the computational cost, but still large enough to have negligible influence on the results. The intrinsic permeability of the sand mixture can be estimated by the

empirical relationship proposed by Iverson and George (2014), which links the porosity *n* to a reference permeability k_0 (Equation 4-5).

$$k(n) = k_0 e^{(n-0.4)/0.04} \tag{4-5}$$

The calibration of the permeability value of the soil in the container $k(n_0)$, Young modulus E and friction angle φ' is done by comparing the simulation results to the impact forces measured over time during the test SL50. The initial values adopted for the calibration are $k = 10^{-9}\ m^2$, $E = 10^3\ kPa$, and $\varphi' = 31°$ (equal to the critical friction angle of the sand). These values are then adjusted for a best-fitting of the results in these ranges: $k = 10^{-13} \div 10^{-8}\ m^2$ (Iverson and George, 2014); $E = 10^2 \div 10^4\ kPa$ (Iverson, 1997); $\varphi' = 25 \div 45°$ (Iverson, 1997).

Five zones corresponding to the five load cells used in the experiment are considered to calculate the impact pressure at different barrier heights. Each pressure is then multiplied by the influence zone (in the prototype scale) of the corresponding load cell and then integrated over the height of the barrier to obtain the overall impact force. The initial interaction times between the flow and the barrier are reset to 1.0 s (0.045 s in model scale) as made by Song et al. (2017).

From model calibration a good match is achieved between the experimental evidence (Figure 4-12) and the simulation outcomes either in terms of flow motion, where both flow configuration and velocity are well captured (Figure 4-13), and even in terms of impact pressures in almost all the reference points. The impact pressure results have been post-processed using the robust lowess smooth function available in Matlab with a span equal to the 3% of the data.

The impact forces are calculated by modelling the soil-water interaction forces both through the linear Darcy's law and through the non-linear velocity contribution (Equation 4-3). It was interesting to discover that in this case study, the two formulations give negligible differences in the results, even if the non-linear velocity term leads to a slightly better fit of the results (Figure 4-14).

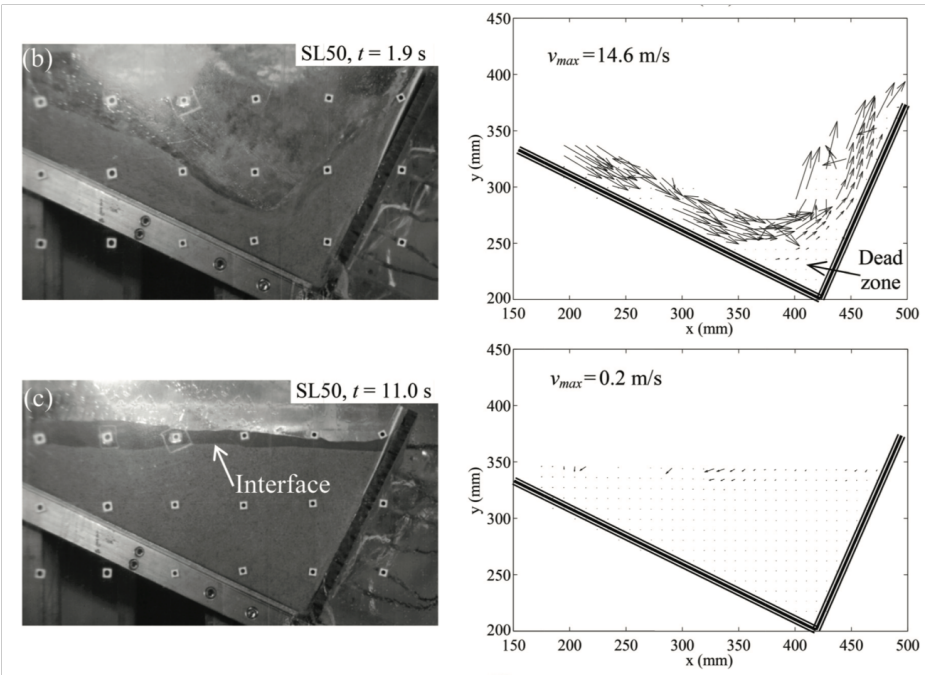

Figure 4-12. Experimental observations with PIV analysis on the rigth

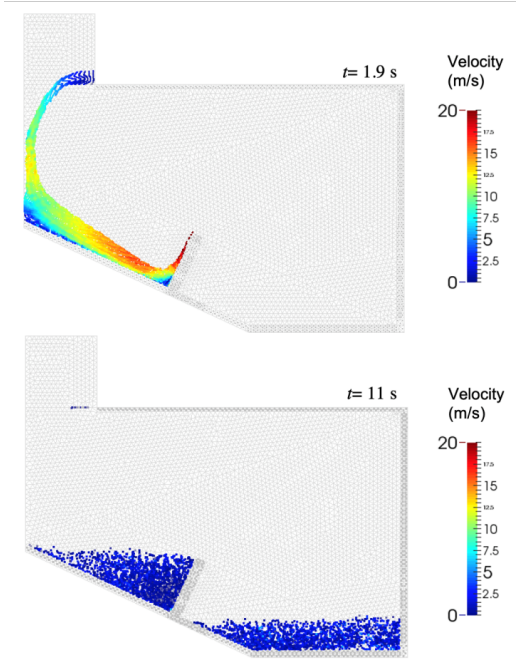

Figure 4-13. MPM simulation snapshots showing the velocity distribution for SL50 test (calibration)

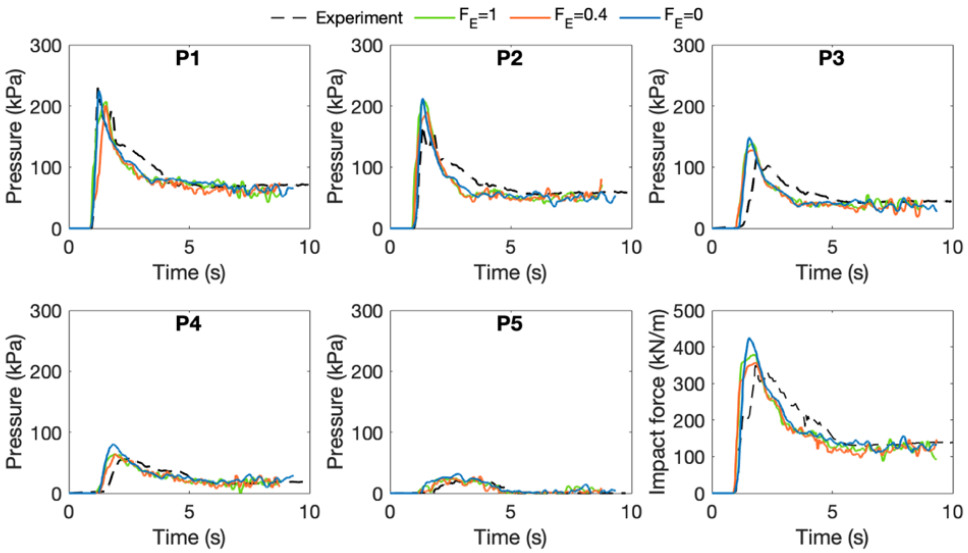

Figure 4-14. Experimental and simulated values of impact force over time for test SL50 (calibration)

According to the two-phase single-point formulation, the liquid mass can vary depending on porosity changes. Anyway, this limitation seems to have an irrelevant role in the computation of the impact forces, since porosity change is very large only after the impact against the barrier, not before it. In fact, the values of the porosity in the part of the soil located upstream of the barrier vary between 0.455 and 0.512. Such values of the porosity variation do not produce a relevant increase in terms of mass mixture, with a consequently negligible effect in terms of impact forces. If the non-linear velocity contribution is included, the porosity distribution is more uniform, varying between 0.472 and 0.510 since the soil globally becomes less permeable during the flow. However, for the soil parameters chosen in this study, its contribution in terms of reaction forces against the barrier is negligible. It can be concluded that, although this formulation should be still improved, it seems sufficiently accurate for the case study described in this study.

The calibrated parameters are reported in Table 4-4, and they allow quite good results also for the model validation on the SL40 test (Figure 4-15). However, some

discrepancies between the pressure distribution measured for the SL40 test and the numerical results are also noted. This is probably because flows with low solid fraction are dominated by viscous stresses (Song et al. 2017). Consequently, if viscous stresses are not taken into account higher mobility is developed during the impact mechanism. On the contrary, in the case of larger solid fraction, many studies have demonstrated that viscous shearing is less effective in energy dissipation compared to grain shear stresses (Iverson and George 2014; Choi et al. 2015; Ng et al. 2017; Song et al. 2017). In addition to this, viscosity inside debris flow is not easily measurable. For this reason, the mathematical formulation used in this study voluntarily neglected the viscous stresses inside the flow.

Table 4-4. Materials properties employed in the MPM simulations

Material	*Constitutive model*	ρ_m *(kg/m³)*	n_0 *(-)*	E *(MPa)*	ν *(-)*	c' *(kPa)*	φ' *(°)*	φ'_b *(°)*	ψ *(°)*
Saturated sand	MC	1825* 1660**	0.5* 0.6**	1.5	0.2	0	31	31	0
	k(n_0) *(m^2)*	*k_0* *(m^2)*	*K_L* *(MPa)*	*μ_L* *(Pas)*					
	1.2×10^{-8}	9×10^{-10} * 9×10^{-11}**	50	0.022					
Material	*Constitutive model*	ρ_m *(kg/m³)*	n_0 *(-)*	E *(MPa)*	ν *(-)*				
Plane	LE	7850	0	infinity	0.3				
Rigid wall	LE	7850	0	infinity	0.3				

*SL50 test; ** SL40 test

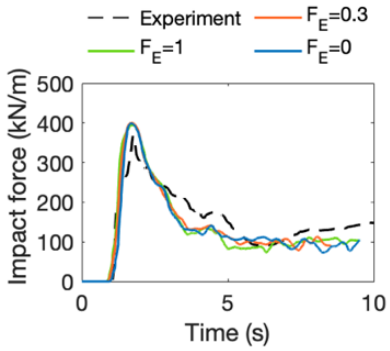

Figure 4-15. Experimental and simulated values of impact force over time for test SL40 (validation)

Globally, the impact mechanisms of the two tests can be well analysed referring to the simulation snapshots of Figure 4-16, which show the spatial distribution of the Froude number at impact. As observed in the laboratory, the two debris flows are both characterized by a run-up mechanism with the formation of a dead zone behind the barrier. The latter one acts as a springboard along which the remaining flow accelerates, and finally creates a vertical jet. The extent of the dead zone strongly depends on the percent of solid fraction in the flow, since it is larger when the solid fraction increases (Bagnold 1954; Takahashi 2014; Song 2017). The impact mechanisms described through the MPM analysis agree with those observed in the laboratory by Song et al. (2017). Even the Froude number at impact is very close to the one calculated in the experiment: in fact, from laboratory observations Fr is equal to 3.6 and 5 for the SL50 and SL40 tests, respectively. Even for this case study, the role of some quantities on the impact behaviour is pointed out. Different permeability of the sand has significant effects on porosity distribution within the flow during the impact stage (Figure 4-17). For an initial porosity n_0 of 0.5 (SL50 test) and the highest permeability, the dead zone behind the barrier is characterized by a lower porosity (Figure 4-17a). If permeability is lower than the previous case, then the porosity of the material behind the barrier gradually increases, as shown in Figure 4-17b and Figure 4-17c. This is related to the hydro-mechanical coupling, which makes that a change in soil permeability affects the liquid pressure inside the flow, which in turn modifies the stress and strain depending on material constitutive response. As further issue, the volumetric strains change the porosity distribution inside the flow. The higher the volumetric strain, the higher the porosity inside the flow, as observable for the airborne jet where very high porosity are simulated. For low permeability value, the porosity in the dead zone results higher than the initial value. Since permeability is low, pore-fluid cannot easily escape from the soil at impact moment, so the soil tends to dissipate the excess pore-pressure by increasing porosity. In contrast, for the case with high permeability, the porosity diminishes in the dead zone probably because the flow moves more slowly than the previous case and so the material within the dead zone undergoes a sort of consolidation.

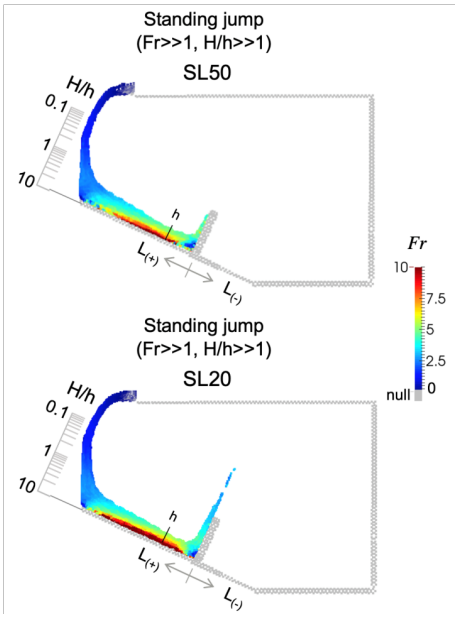

Figure 4-16. Spatial distribution of Froude number during impact (t=1.9 s)

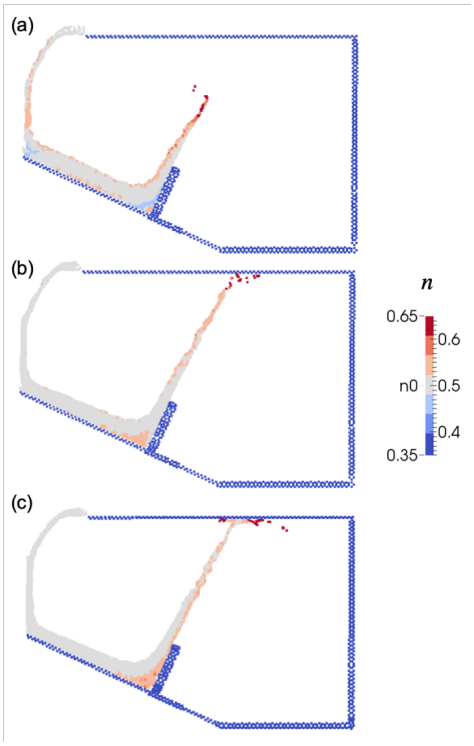

Figure 4-17. Influence of intrinsic permeability on porosity change: (a) $k_0 = 10^{-10}\ m^2$; (b) $k_0 = 10^{-11}\ m^2$; (c) $k_0 = 10^{-12}\ m^2$

4.2.3 Discussion of numerical results

The MPM numerical simulations provide new insights in understanding the impact mechanisms of both dry and saturated granular flows, related to the many physical properties (e.g., stress, strain, liquid and solid velocity, pore pressure and other state parameters) that can be accurately computed either in space and time.

The phase diagram proposed by Faug (2015) for granular flow-structure interaction is here used to comment more on some of the numerical results. For the sake of brevity, the combination of H/h and Fr are limited to the most relevant cases of this study, i.e., the dry flow simulated along the 45° to 65° inclined slope and the saturated flow observed in the SL50 and SL40 tests (Figure 4-18). For the dry granular flows, the impact mechanism changes in relation to slope inclination. The impact mechanism resembles the bore regime (slope angle equal to 45°), then becomes a standing jump (50° and 55° inclinations) and finally reaches the airborne jet regime (60° and 65° slopes). This is principally governed by Fr number, since for higher inclinations the flow velocity increases while the flow depth h remains almost the same. Different is the case of the saturated granular flows, since both the considered cases (SL50 and SL40 tests) can be assimilated to a standing jump regime. The solid-fluid interaction is however highlighted in the phase diagram. Higher solid fractions lead to a decrease in Fr number, confirming the effectiveness of solid fraction in energy dissipation and reduction of debris mobility pointed out by Song et al. (2017).

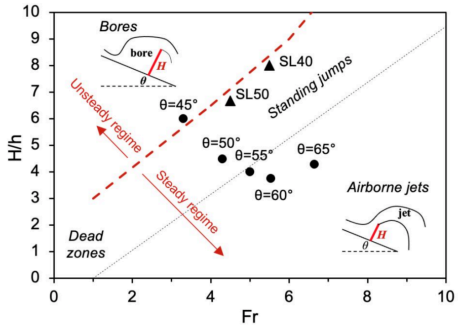

Figure 4-18. Comparison of the MPM results within the phase diagram proposed by Faug (2015).

4.2.4 Concluding remarks

The presented study showed the potential of an advanced numerical method such Material Point Method (MPM) in simulating the impact mechanisms of dry or saturated granular flows against rigid walls, providing novel insights additional to those from laboratory experiments.

The laboratory flume tests reported by Moriguchi et al. (2009) and Song et al. (2017) were simulated in a MPM context. In both the sets of simulations, the calibration and validation of the numerical model led to a satisfactory correspondence among the experimental and the numerical results in terms of flow kinematics and impact force trend over time. It was possible investigating the influence of some material properties (such as solid Young modulus, internal friction angle, friction at contact surfaces, permeability, Froude number) on the impact behaviour of the flow.

The numerical results provided new insights in understanding the complex impact mechanisms through the computation and time-space tracking of some quantities, such as stress, strain, pore pressure, solid and liquid velocities, which cannot be easily monitored/obtained from laboratory experiments. Specifically, it is observed that the presence of liquid phase inside the granular flow can lead to different impact regimes in respect to the dry flows, highlighting the importance of considering the solid-fluid interaction in the analyses. The accurate knowledge of the impact mechanism of the flows is crucial for the design of protection structures against avalanches. For example, the accurate estimate of the length of an airborne jet must prevent that the retaining structure is overtopped by a jet, thus being ineffective. Differently from the many empirical equations available in the literature and currently used for the design of these structures, advanced numerical methods like MPM allow to consider all such important aspects of the granular flows. Further research could focus on the verification of the equations proposed in the literature to evaluate the impact forces against obstacles, even considering the presence of viscous stresses inside saturated granular flows, in order to understand the conditions

in which these stresses could change the hydro-mechanical behaviour of the flow. It is also worth stressing that the proposed study is focused on the modelling of flows with a significant volumetric content of solids, this means that the statements could be extended for instance to real debris flows, but hardly to the case of hyperconcentrated flows.

Successful simulation of centrifuge tests is an important achievement. In fact, from centrifuge tests come the most accurate measurable (and repeatable) evidence of such processes at a prototype scale not so far from reality. Further research could try to simulate real-scale case histories, aware that the data from the field are generally few and sometimes uncertain.

4.3 Full-scale tests on breakage of masonry walls

4.3.1 Introduction

This paragraph discusses the topic of fast-moving flow-like landslides against structures such as masonry walls and buildings. Once a physically-based modelling of landslide has been completed, one should address the effects and damage of buildings in consequence of the impact of such fast-moving mass.

A set of numerical simulations is developed through the Material Point Method (MPM) to investigate the failure mechanism of Unreinforced Masonry (URM) walls, since field evidence have often shown that the collapse of infill panels can occur independently from the failure of the bearing frame, implicating a risk for the people inside.

Some experimental results available in the literature for masonry walls made of clay bricks and mortar joints are simulated in 2D and 3D conditions appropriately reproducing the overall stiffness, resistance and displacement of the wall in out-of-plane loading, until plastic hinges are formed, and complete collapse occurs. In these cases, a known external pressure is applied to the wall. The potential of a unitary approach for simulating the fast propagation of a saturated soil and the stress-strain response of a structural element is discussed.

4.3.2 Collapse mechanisms of infill panels in RC buildings

Based on the observations of damage on Reinforced-Concrete (RC) buildings with URM walls caused by the impact of flow-like landslides, some collapse mechanisms have been pointed out for both structural and non-structural elements. With reference to such collapse mechanisms, the ultimate bearing capacity of both the overall building and its constituent members could be computed (Faella and Nigro, 2003). Particularly, the load bearing capacity of a RC frame cannot be affected by the destruction of the external URM walls, as building collapse occurs only in the case

of impact-induced formation of plastic hinges in the pillars of the ground floor. Anyway, the collapse of non-structural elements represents a serious danger to the safety of people in their own home.

The failure mechanisms of masonry infill can be divided into two groups: (i) In-Plane failure (IP, Figure 4-19a) due to the interaction with the frame structural members (Parisi & Sabella, 2016), and (ii) Out-Of-Plane failure (OOP, Figure 4-19b) under a pressure perpendicular to the wall face (Trapani et al., 2018).

The frame-wall interactions have been largely investigated under IP and OOP seismic loads, through the adoption of theoretical (e.g., equivalent diagonal struts method as in Di Trapani et al., 2018), numerical models (Pantò et al., 2017; Abdulla et al., 2017), or also through experimental tests (Griffith & Vaculik, 2007; Ricci et al., 2018; Valera-Rivera et al., 2011; Graziotti et al., 2019).

In general, the proper modelling of the OOP response of an URM wall would require considering the effect of the IP loading resistance to accurately assess the performance of a three-dimensional structure. Anyway, in the case of buildings impacted by flow-like landslides, one could assume that the OOP response is more relevant than the IP behaviour.

Under OOP loads an infill wall can exhibit a significant resistance thanks to the formation of an arching mechanism. The latter is generated by (i) two-way bending mechanism if the panels are well confined in both directions by the surrounding RC structure (Figure 4-20b), or by (ii) one-way bending if the opposite edges are supported (Figure 4-20a).

The occurrence of a two-way rather than a one-way mechanism strongly depends on support conditions (Figure 4-20), as highlighted by numerous studies (Varela-Rivera et al., 2011; Vaculik & Griffith, 2017; Tomassetti et al., 2018; Graziotti et al., 2019). The wall with top and bottom or the two lateral sides supported is characterized by one-way spanning and uniaxial bending (vertical for horizontal span and vice versa), as shown in Figure 4-20a. In this situation, the cracking has the same direction of the supported edges.

Two-way spanning walls supported on at least two adjacent edges (Figure 4-20b) have more complex behaviour, (Derakhshan et al. 2018), since they are subjected to biaxial bending, in both the horizontal and vertical directions. In this case, the wall cracking becomes a combination of vertical, horizontal and diagonal crack lines. In turn, the internal moments along the different types of crack lines can consist of a combination of flexure and torsion (Graziotti et al., 2019).

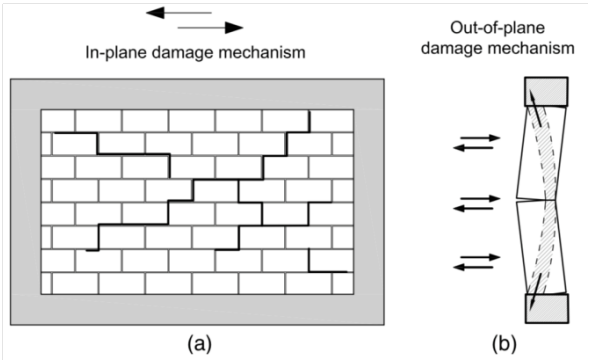

Figure 4-19. Damage mechanisms of URM infill walls:
(a) In-Plane (IP), and (b) Out-Of-Plane (OOP), from Di Trapani et al. (2018).

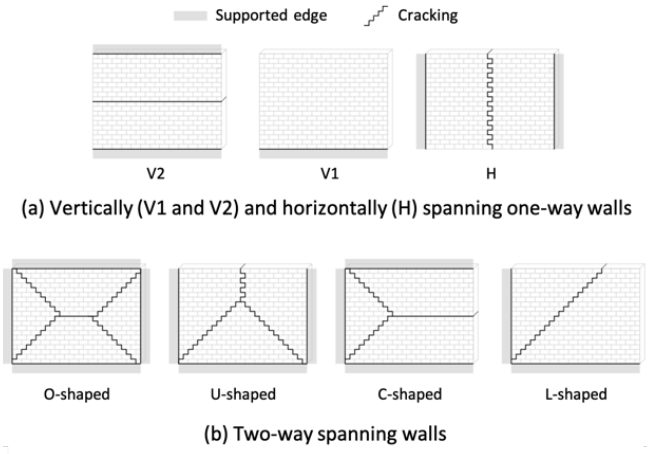

Figure 4-20. Crack patterns for different kinds of wall supports (from Vaculik, 2012).

The ultimate horizontal pressure bearable from a URM wall in OOP conditions can be determined through the load-displacement curve (Figure 4-21).

An uncracked URM wall subjected to an OOP pressure shows first a linear-elastic behaviour until its flexural tensile strength is achieved and consequently initial cracks start forms. As the deformations increase, cracking also spread along the mortar-joints of the panel, leading to a reduction of the wall stiffness.

Many experimental tests carried out on URM walls under seismic loads have demonstrated that the ultimate strength is generally reached with displacements approximately in the range 20–40 mm, since the cracks are such to lead to a collapse mechanism (red line in Figure 4-21). Both strength and stiffness continue to decrease with the increasing of deformations until the wall becomes fully cracked (rocking mechanism). However, the wall is characterized by a residual load capacity due to gravity effects. The ultimate displacement capacity is reached with the balance between resisting and destabilizing moments, and it occurs when the wall reaches a deformation approximately equal to its thickness (Vaculik, 2012). Beyond this point, the wall is unstable.

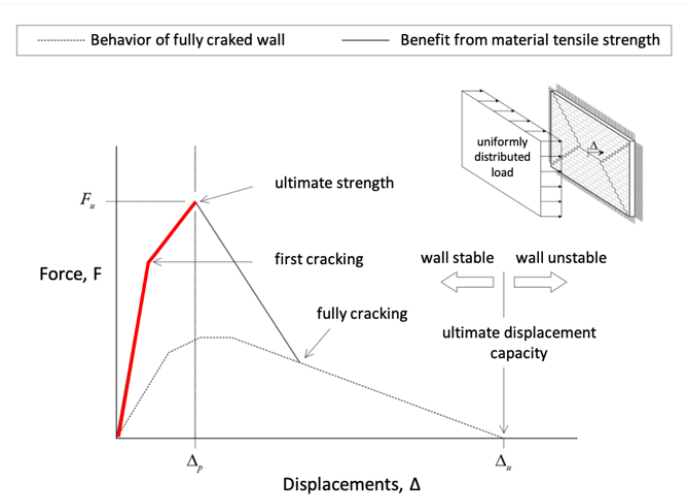

Figure 4-21. Load-displacement curve for an URM wall subjected to OOP bending (Vaculik, 2012).

Focusing now the attention on the attainment of the ultimate strength and considering a vertical cross-section of the wall 1 m wide, the collapse mechanism is part of the one-way typology. Even the force-displacement curve strongly depends on the type of restraints at the top and bottom extremities (Figure 4-22), which can be fixed-fixed or pinned-pinned.

In the fixed-fixed case, the first cracking arises at the top of the wall (point A) since the axial load due to the wall weight is lower around that point. When the external load increases, the second plastic hinge occurs at the bottom (point B) and finally at the mid-height of the wall (point C), generating a collapse mechanism.

In the pinned-pinned case, failure occurs quickly at the formation of just one plastic hinge located at the wall mid-height (point D).

Looking at the force-displacement curve, it emerges that the ultimate load capacity of the URM wall is higher in the case of fixed-fixed supports than the pinned-pinned case and is reached with three different levels of stiffness (Tomassetti et al., 2018).

In order to simulate such complex mechanisms, large displacements of the wall material must be accurately simulated, and accurate landslide propagation modelling must be also possible in the same mathematical approach.

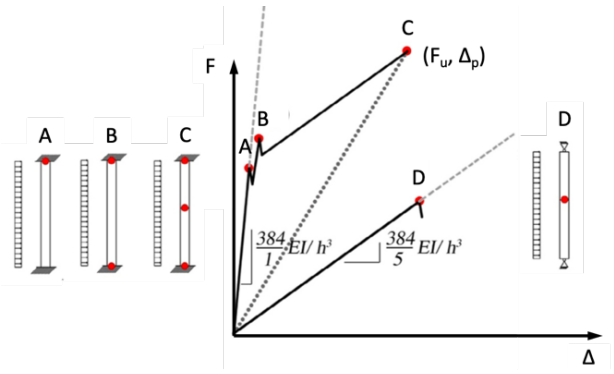

Figure 4-22. Load-displacement curve for different support conditions (Tomassetti et al., 2018).

4.3.3 Modelling URM wall breakage

Input and methods

Aimed to test the potential of MPM in properly simulating the response of a URM wall, some literature experiments are here considered. Particularly, the URM walls used in the experimental tests of Vaculik (2012) were considered in the numerical simulations.

The walls were made of two components: standard Australian clay bricks with nominal dimensions 230 mm × 110 mm × 76 mm, perforated with two rows of five holes and mortar joints with standard thickness of 10 mm using a composition of 1:2:9 (portland cement, lime and sand). The dimensions of the wall are h=2494 mm and B=4080 mm, with the lateral boundary confined in embedded return wall, each 480 mm long (Figure 4-23). The mechanical properties of these materials and other similar are shown in Table 4-5, reporting Young modulus (E), Poisson's ratio (v), cohesion (c'), friction angle (φ') and tensile strength (σ_t).

The MPM computational domain has been set both in 3D and 2D for different purposes. The 3D scheme is used to properly reproduce the mechanical response of the wall including under out-of-plane two-way bending and traction at the central part of the wall, as well as propagation of extension mode and cracking inside the wall plane. In such model all the boundary conditions can be considered, either as the fixities or as mortar joints.

Masonry elements subjected to out-of-plane loading resist the load by flexural action. The load capacity of unreinforced masonry wall panels depends upon the dimensions and support conditions, the level of compressive stress in the wall and the tensile strength of the masonry. As main advantage, such model could reproduce generalized deformation mechanisms and limit states including complex patterns of deformation, failure and post-failure of the wall. It is worth reminding that MPs have no restriction to move within the computational domain. This feature of MPM is very well suited when the impact of a flow-like landslide is considered as external action against the wall, as very large displacements are expected.

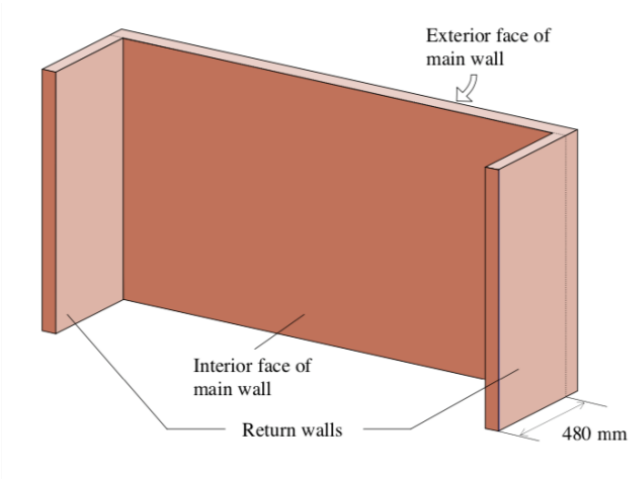

Figure 4-23. Schematic of the wall used in the experiments of Vaculik (2012).

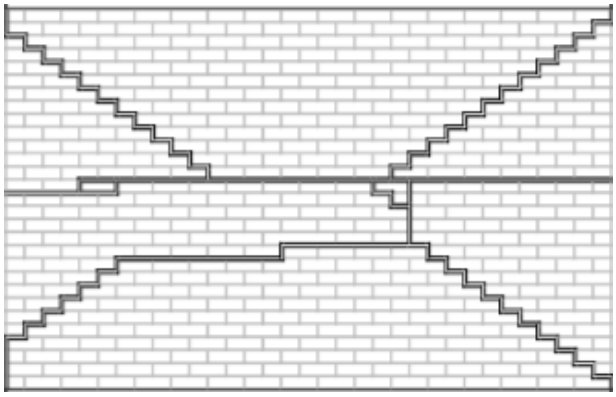

Figure 4-24. Schematic of the interior face of the wall as cracked during the experiments of Vaculik (2012).

Table 4-5. Some material properties from literature

Material	$^{(*)}E$ *(MPa)*	$^{(*)}\nu$ *(-)*	c' *(kPa)*	φ' *(°)*	σ_t *(kPa)*
Brick	52700	0.2	1500 (**)	15 (**)	686 §
Mortar bed joints	442	0.2	180 (***) 81 ÷ 206 §	30 (*) ÷32 (***)	110÷140§§ 170÷500§§§

(*) Vaculik, 2012; (**) Hulse & Ambrose, 1982; (***) Graziotti et al., 2018; § Magenes et al., 1992; §§Varela-Rivera et al., 2012; §§§Wei & Stewart, 2010

On the other hand, the 2D model is here conceived as a simplified scheme to be validated for later extensive application to design-oriented analyses. The minimum requirement for such 2D model is to properly reproduce the out-of-plane bending, formation of plastic hinges at the top and bottom of the wall, simulation of tension cracking in the wall associated to the accurate evaluation of the load-displacement curve.

In both the 3D and 2D model, the URM wall is schematized as an equivalent uniform continuous frictional-cohesive material, with the mechanical parameters (Tab. 4-6) selected as follows. The density (ρ=1936 kg/m^3) and the Poisson ratio (ν=0.2) are those measured for the wall by Vaculik (2012). The Young's modulus (E) is taken from the experimental evidence for the wall (E=2240 kPa) reported by Vaculik (2012), as for combo p1-p3 of Table 4-6 or assumed as equal to that of the mortar (E=442 kPa), in combo p4. The cohesion of the wall material (c'=180 kPa) is that reported by Graziotti et al. (2018) in combo p4 or is varied between 100 kPa and 130 kPa to get numerical results similar to the experimental ones for combos p1-p3. The internal friction angle (φ') is set equal to the average value reported by Vaculik (2012) and Graziotti (2018) for the mortar bed-joints. The K_0 value is determined as 1-senφ' using the friction angle of the brick since it is plausible that the horizontal and vertical stress distribution is similar to that of a brick column. The tensile strength (σ_t) of the wall is simply obtained as the ratio between cohesion (c') and friction angle ($tan\varphi'$), assuming that the friction angle is the same both in compression and extension. From there, 6 combos of material properties were individuated (Table 4-6).

Table 4-6. Sets of masonry properties used for modelling

	$^{(*)}\rho$ (kg/m^3)	$^{(*)}\nu$ (-)	$^{(*)}E$ (MPa)	c' (kPa)	φ' (°)	K_0 (-)	σ_t (kPa)
p1	1936	0.2	2240	100	31	0.74	166
p2	1936	0.2	2240	130	31	0.74	216
p3	1936	0.2	2240	115	31	0.74	191
p4	1936	0.2	442	180	31	0.74	300
p5	1936	0.2	442	115	31	0.74	191
p6	1936	0.2	442	80	31	0.74	133

(*) Vaculik, 2012

Inspection of full 3D wall response

In this case, the domain is 1.00 m × 4.08 m × 3.00 m and inside there is a fixed Eulerian 3D mesh made of 116325 4-noded tetrahedral elements with average size of about 0.1 m inside and outside the wall (Figure 4-25).

Some of the results achieved are reported in Figure 4-26, with reference to the deviatoric strain defined as $\varepsilon_d = \frac{2}{3}\sqrt{(\varepsilon_x - \varepsilon_y)^2 + (\varepsilon_y - \varepsilon_z)^2 + (\varepsilon_z - \varepsilon_x)^2}$, for combo *p6* of material properties allowing the best-fitting of the experimental evidence. Before focusing on such satisfactory comparison, which is not the most important outcome, it is worth evidencing what are the physical processes correctly reproduced or not.

Masonry elements subjected to out-of-plane loading resist the load by flexural action. The load capacity of unreinforced masonry wall panels depends upon the dimensions and support conditions, the level of compressive stress in the wall and the tensile strength of the masonry. Particularly, the crack patterns depend on the different kinds of wall supports (Figure 4-20) and the load-displacement curve also depends on the different support conditions (Figure 4-22). In this specific case, being fixed all the boundaries (Figure 4-25) yielding occurs as follows: (i) first at the top of the wall, (ii) then at the bottom of the wall, (iii) at the side boundaries of the wall. From now on, yielding zones enlarged along the boundaries where they appeared but (iv) a plastic hinge forms at the mid-height of the wall, and (v) yielding also appears along inclined directions as expected for a two-way spanning wall and as observed by Vaculik (2012) in the experiments.

The formation of the first two plastic hinges at the vertical extremities of the wall gives starting to the collapse mechanism by reducing the overall stiffness of the panel (Figure 4-26). Later, for similar increments of the external pressure, the deviatoric strains and the horizontal displacements increase more and more.

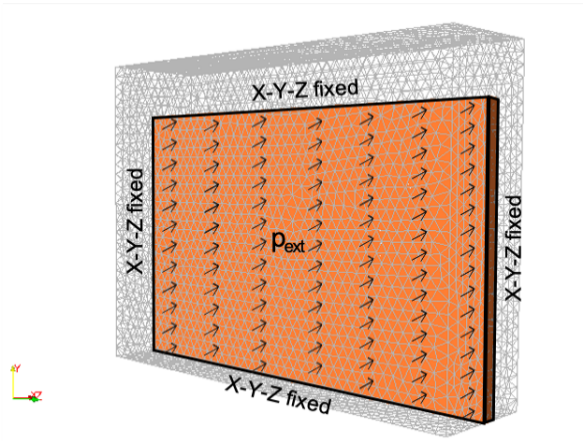

Figure 4-25. Computational 3D domain used to simulate the experiments of Vaculik (2012).

Also, the out-of-plane displacements are correctly simulated (Figure 4-27). Interestingly, the activation of the first plastic hinges and the corresponding reduction in wall stiffness (for F_u=30.5 kN) does not correspond to the collapse, because most of the stress redistribution and strains occur inside the plane. Later on, the out-of-plane deformations and displacements start, and collapse become unavoidable. Quantitative comparison of the horizontal displacements computed along different vertical sections versus the measurements is provided in Fig. 16, where it is shown that the 3D deformation mode is well captured by the model. Indeed, during the experiment (dashed line in Figure 4-28), once the maximum horizontal displacement reached about 15 mm, then the external load was decreased so that the maximum displacement was about 30 mm with a final recovery of about 15 mm.

In Figure 4-28 we can also assess how the stress-independent aliquot of the wall strength (cohesion) is capable to influence: (i) the stiffness of the wall, not at the origin of the plot but after that some deformation has already occurred, i.e., when yielding starts, and (ii) the ultimate load that the wall can sustain, as expected. While passing from combo p4 to p5 and p6, the decrement of cohesion is almost linear the response in the F-Δ plot is non-linear both for reduction in the ultimate load and decrease in the wall stiffness.

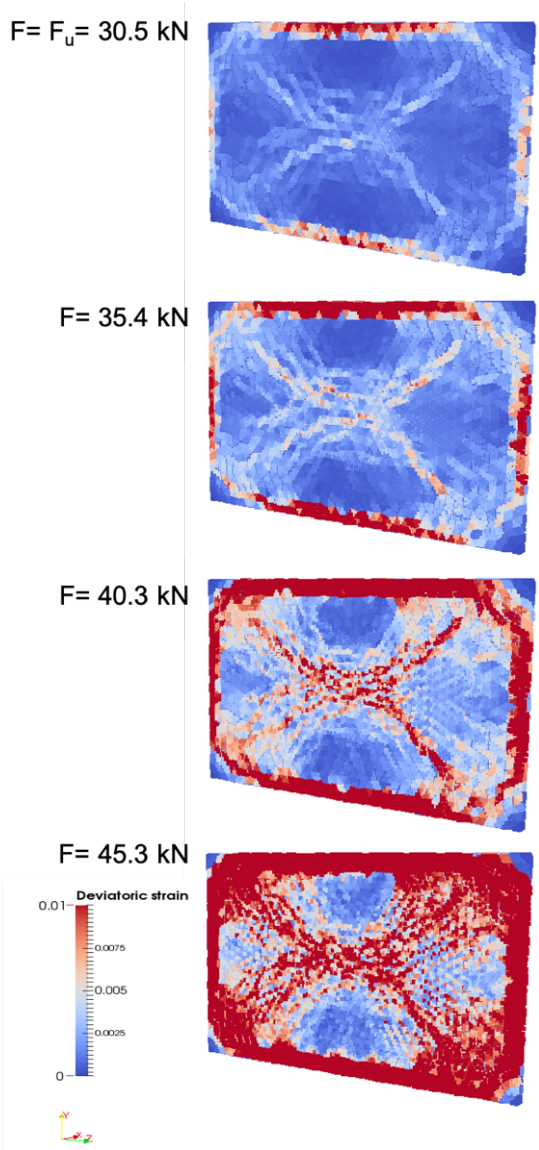

Figure 4-26. Deviatoric strain computed in the 3D domain for different external force and combo p6 of materials.

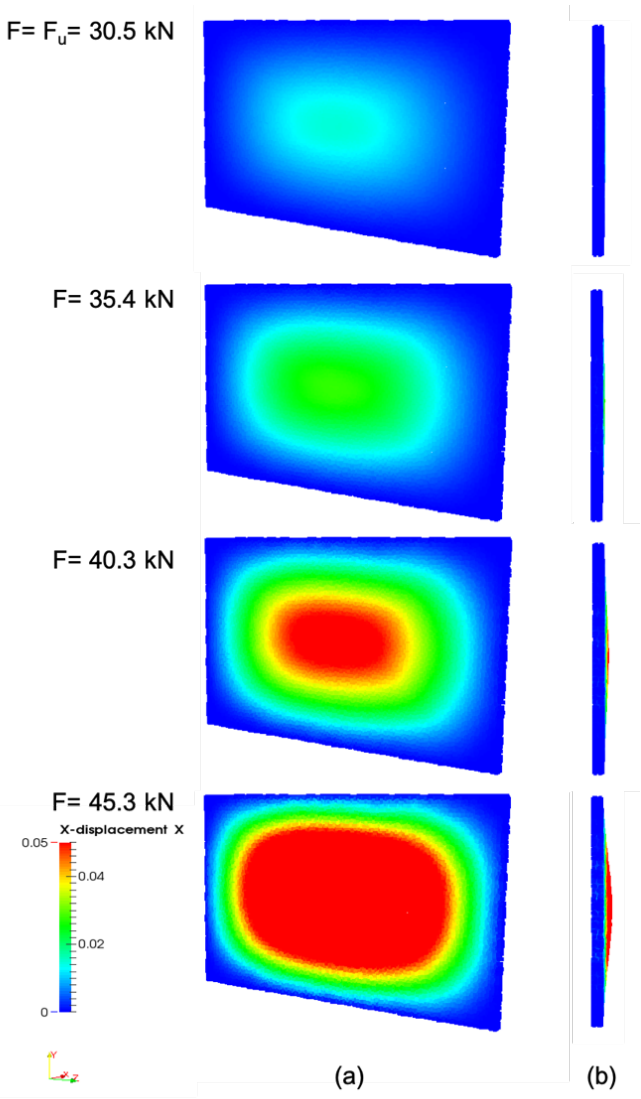

Figure 4-27. Computed horizontal displacements in the 3D domain at different values of the external force for combo p6 of materials.

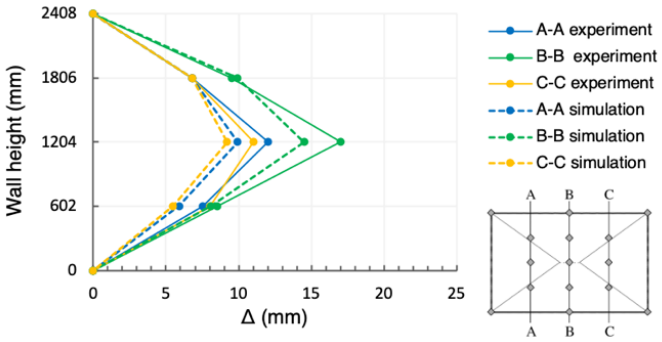

Figure 4-28. Displacements computed via 3D modelling for the combo p6 of material properties of Tab. 2 compared to those measured at the ultimate strength of the wall (F_u=30.5 kN) by Vaculik (2012).

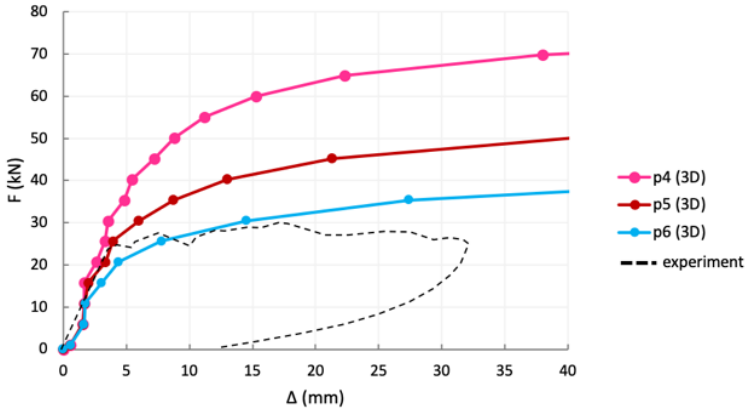

Figure 4-29. Load-displacement curves computed via 3D modelling for different combos of material properties of Tab. 2 compared to those measured by Vaculik (2012).

Modelling in a simplified 2D scheme

While the 3D model has the evident advantage to carefully reproduce the deformation mechanisms, there is still an issue of long computational time especially when large structures are considered. And, on the other hand, in many applications and research investigations cross-section will be always a valuable schematization of the reality. Thus, it makes sense to try interpreting the same experiments seen before by means of a 2D model, whose parameters and performances must be evaluated again.

In the 2D case, the domain is 3.50 m × 3.00 m large, and made of 2605 3-noded triangles, 0.08 m sized inside (consistent with the 3D mesh size) and around the wall while 0.50 m sized more far (Figure 4-30). The wall is considered fixed at top and bottom sides. Also in this case, a number of simulations were performed arriving to assess the combo p3 of Table 4-6 as the best-fitting set of parameters for simulating the experiments of Vaculik (2012).

Interestingly, when the external load reach about F=30.5 kN, two hinges are simulated, then for F=34.5 kN the yielding at mid-height of the wall, and finally the progression of yielding at the central zone of wall for F=40.3 kN (Figure 4-31). Such results are consistent with 3D model, and it entails that also a 2D simplified model scheme could be used in real applications.

A quantitative comparison of the computed horizontal displacement versus the experimental values is provided in Figure 4-32, clearly identifying the combo p3 of materials as the best-fitting the experimental evidence. Other numerical results in terms of *F*-Δ curve are reported in Figure 4-33, where the higher cohesion and related traction resistance (from p1 to p3 and then p2) result in higher strength and higher stiffness after the first cracking point.

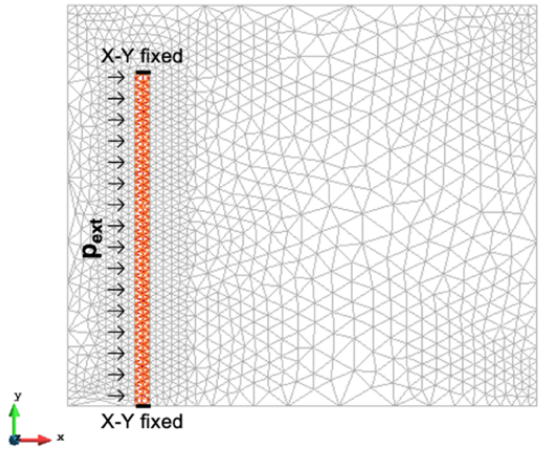

Figure 4-30. Computational 2D domain
(barycentral vertical cross-section of the 3D domain).

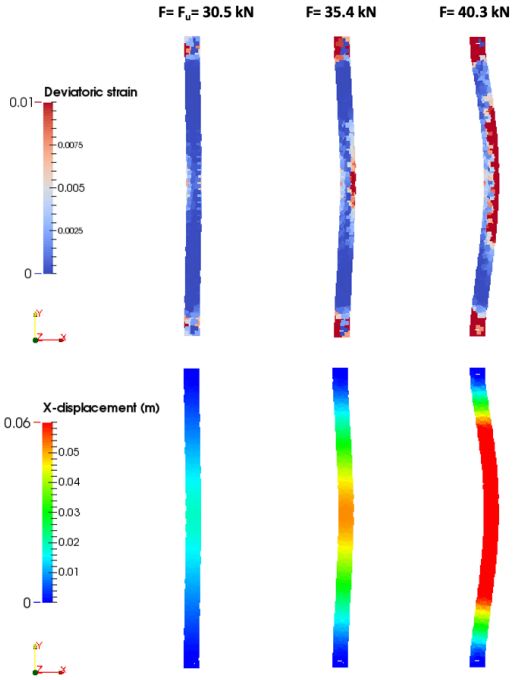

Figure 4-31. Deformed configuration and deviatoric strains simulated at different times for combo p3 of Table 4-6.

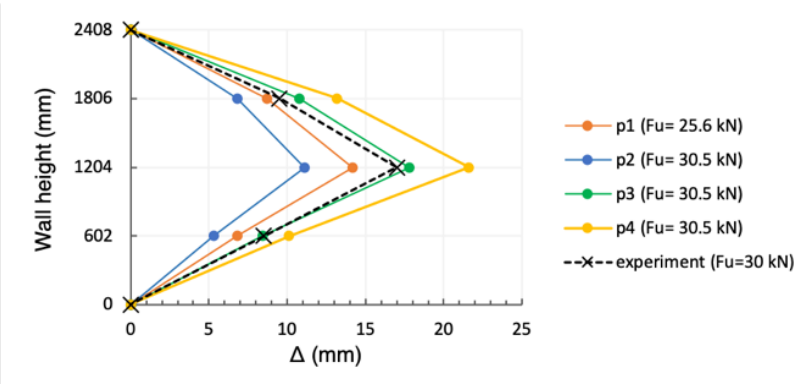

Figure 4-32. Horizontal displacements versus measurement.

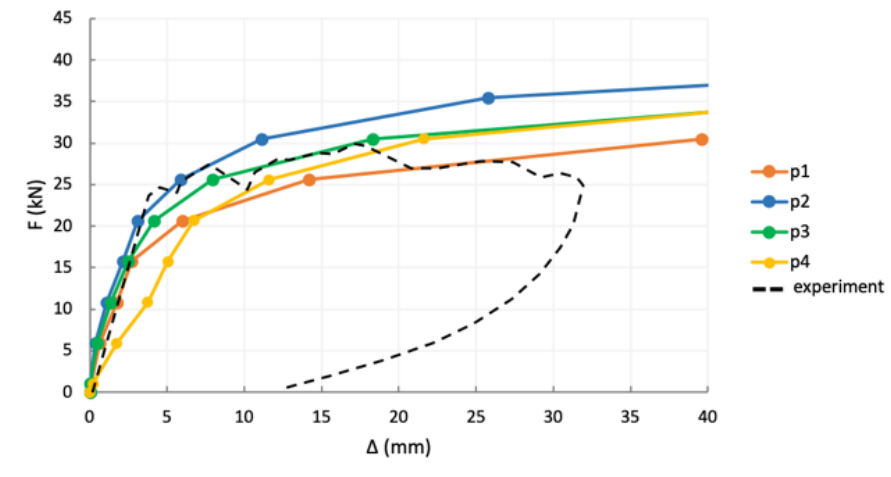

Figure 4-33. Load-displacement curves simulated for the wall via 2D modelling versus the measurements of Vaculik (2012).

4.3.4 Concluding remarks

This paragraph investigated how Material Point Method (MPM) modelling could be used to simulate the dynamic impact of fast-moving flow-like landslides against structures such as single masonry wall or groups of non-structural walls in a reinforced concrete building.

The potentiality of MPM was tested in simulating literature experimental results available for masonry walls, made of clay bricks and mortar joints, under a known uniform external pressure. The simulations in 2D and 3D conditions appropriately reproduced the overall stiffness, resistance and displacement of the wall in out-of-plane condition, until the formation of plastic hinges and complete collapse.

The presented study even furnished the tools for analysing and modelling the complex interaction between a flow-like landslide and a building in a context of large deformations for both saturated flow and infill frame panels. The potential of using a unitary approach for simulating the landslide propagation of a saturated soil and the stress-strain response of a structural element could be an interest topic for future research development.

4.4 Applicability of MPM to real landslide cases

4.4.1 Introduction

After proving the reliability of MPM in simulating some experimental evidence, the numerical method is then used to provide a contribution in investigating the impact mechanisms of a large flow-like landslide against rigid barriers, considering the coupled hydro-mechanical behaviour of the propagating mass and large deformations of the approaching flow.

A case study from China is selected, the Wenjia gully landslide, which occurred on 13 August 2010 when a heavy rainfall led to the movement of almost 30 million of cubic meters of debris. While the landslide kinetic energy can be reduced by fixed protective structures installed inside the torrent, in the specific case study some existing check dams were destroyed by the debris flow. Thus, the landslide-structure interaction is worth of investigation.

In this study, the innovative technique Material Point Method (MPM) is used. The numerical analyses are performed adopting the geometric model of a literature study, which reported the 2D cross-section of the slope, the amount of mobilized debris in the source area, together with the features of three check dams. The interaction between the propagating flow and the barriers is examined, providing fundamental information on the loading actions, which are needed for the design of the control works. The results are encouraging and show that MPM can properly simulate the propagation stage of the landslide and even the complex landslide-structure-interaction mechanisms during the impact against the protective structures.

4.4.2 The Wenjia Gully debris flow case study

The Wenjia Gully has become one of the most studied geohazard sites in China after the 2008 Wenchuan earthquake, since a huge amount of debris deposits was transformed into source material for a giant rainfall-induced landslide. The gully is

located on the left bank of the Mianyuan River, Qingping area near Mianzu County, Sichuan.

Before the earthquake, the depth of the gully was 30-50 m with a length of 3 km and an average slope steepness of 45°. The earthquake caused a deep co-seismic landslide in the gully that initiated with a total volume of 27.5×10^6 m^3, of which the 70% filled the Hanjia Platform (Zone of Accumulation I), while the rest stopped in the 1,300 m Platform (Zone of Accumulation II) as shown in Figure 4-34a. A cross section and the geological profile are reported in Figure 4-34b. The estimated volume of the loose deposits in the latter zone was 30×10^6 m^3. The landslide transformed into a rock avalanche and entrained a large amount of shallow sand-gravel materials during its movement (Xu et al., 2012).

Following the heavy rainfall on 13 August 2010, a catastrophic debris flow occurred mobilizing a total volume of about 3×10^6 m^3, flowing into the Mianyuan River and reaching 1,500 m from downstream. The deposit fan immediately blocked the river, causing many victims, burying houses and destroying most of the downstream check dams along the channel (Xu et al., 2012). The triggering cumulative rainfall was 55 mm over 11 hours (Xu et al., 2012). The material deposited on the Hanjia Platform was not eroded by the flow, hence the finer material deposited in the lower part of the Wenjia catchment (near the 1,300 m Platform) can be considered as the main source for the debris flows.

The debris material was composed of limestone rock fragments, clay and silty clay with an average total unit weight of 21 kN/m^3 and an average effective friction angle of 27.5°, according to consolidated undrained tests (Huang et al., 2019; Yu et al., 2014). For more details regarding the main features of debris flows occurred after the Wenchuan earthquake, the readers can refer to the exhaustive reviews published by Xu et al. (2012), Huang et al. (2019) and Tang et al. (2012).

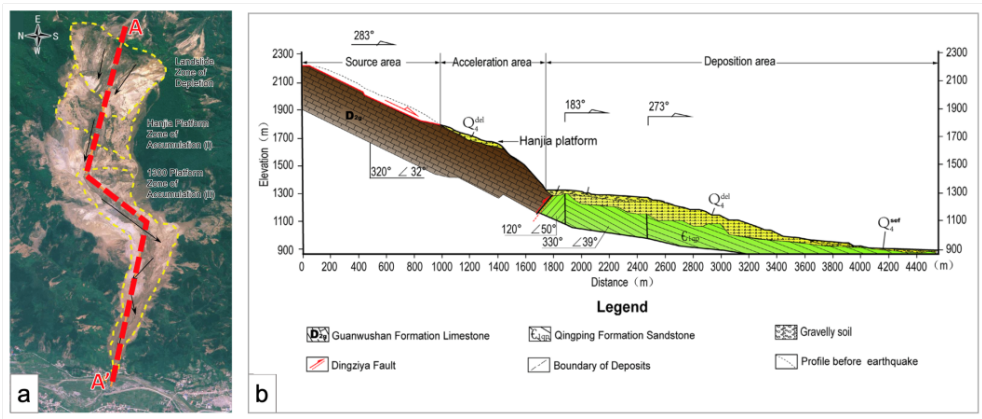

Figure 4-34. The landslide debris after the 2008 Wenchuan Earthquake: a) accumulation areas of debris in the gully (Liu et al, 2017); b) geological profile of cross section A-A' (Deng et al., 2017)

Scheme and input data

The numerical analyses were performed adopting the geometric model of Dai et al. (2017), that is the 2D cross-section of the debris stopped in the 1,300 m Platform together with three check dams located at about 300 m downstream from the toe of the landslide body. Each barrier has a height of 10 m and a width of 6 m and the distance between them is about 200 m.

The triangular 3-noded computational mesh is characterized by elements of 8 m nearby the landslide body, while in the proximity of the barriers this size gradually reduces to 1.5 m. The computational mesh and the material point distribution (12 per element) is shown in Figure 4-35. Both liquid and solid phase velocities are fully fixed in x-y directions along the boundaries of the computational domain. Two reference points (named A and B) were taken into account for monitoring the characteristics of the flow during the propagation and the interaction with the barriers.

The work focuses on the post-failure behaviour of the debris flow, disregarding the modelling of the triggering stage. The initial stress state of the debris amount is initialized through a K_0-procedure, being the slope unstable. The water table was set at the ground level, as resulted from limit equilibrium stability analysis performed

with an internal friction angle equal to 27.5° (the procedure can be found in Cuomo et al., 2019a).

The debris flow material is modelled as a continuous two-phase body, with an elasto-plastic constitutive model, while the check dams are simulated as rigid materials with an elastic behaviour. The parameters of both materials are reported in Table 4-7.

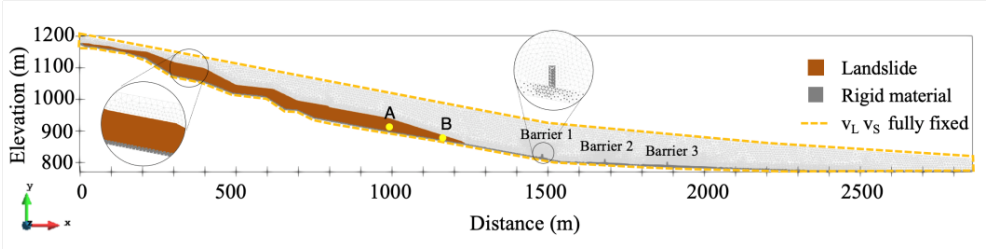

Figure 4-35. Computational domain and input materials.

Table 4-7. Material parameters used in the numerical analyses

Soils	ρ_m *(kN/m³)*	*n (-)*	K_0 *(-)*	*E (MPa)*	ν *(-)*		
Debris	21	0.3 0.4 0.5	0.5	2.5 5 10	0.2		
	c' *(kPa)*	φ' *(°)*	φ'_b *(°)*	ψ *(°)*	*k* *(m²)*	K_L *(MPa)*	μ_L *(Pas)*
	0	27.5	14 18 27.5	0	10^{-10}	100	10^{-3}
	ρ_m *(kN/m³)*	*n (-)*	K_0 *(-)*	*E (MPa)*	ν *(-)*		
Rigid	25	0	0.5	∞	0.2		

4.4.3 Numerical results

A sensitivity analysis was conducted to point out the influence of some material properties (such as porosity, soil stiffness and basal friction) on the kinematics and propagation of the landslide.

The propagation of the landslide can be shown for different time lapses, reporting the spatial distribution of some quantities, such as cumulative deviatoric strain,

velocity and pore-water pressure of the moving mass. For example, by examining the cumulative deviatoric strain (Figure 4-36), it can be seen that firstly the upper part of the landslide is failed, since an evident slip surface is formed (t= 5 s). Then, while the flow is moving (t > 5 s), the deviatoric strain distribution is everywhere greater than 2, indicating that the soil mass has undergone large deformations and therefore it is completely remoulded.

The spatial distribution of pore-water pressure is also an interesting result (Figure 4-37). Starting from a hydrostatic distribution, excess pore pressure arises either when the soil is moving (t= 5−20 s) and either when the flow impacts against the barriers, as well-shown in the zoom box at t= 40 s. However, the excess pore pressure is reduced when the flow is passing from the first to the last barrier. When the mass reaches a steady configuration, the water pressure returns to the hydrostatic values (t= 75 s).

Finally, the spatial distribution of flow velocity is shown in Figure 4-38. As mentioned before, the upper part of the debris deposit is the first zone to start moving (t= 5 s), then pushing the zone downstream and propagating with very high velocity (> 35 m/s) at t= 40 s. Focusing on the flow-barrier interaction, the velocity of the flow is effectively dampened by the presence of the three barriers, since it passes from 35 m/s (barrier 1) to 25 m/s (barrier 2) and 10 m/s (barrier 3). At t= 75 s, the entire flowing mass is stopped.

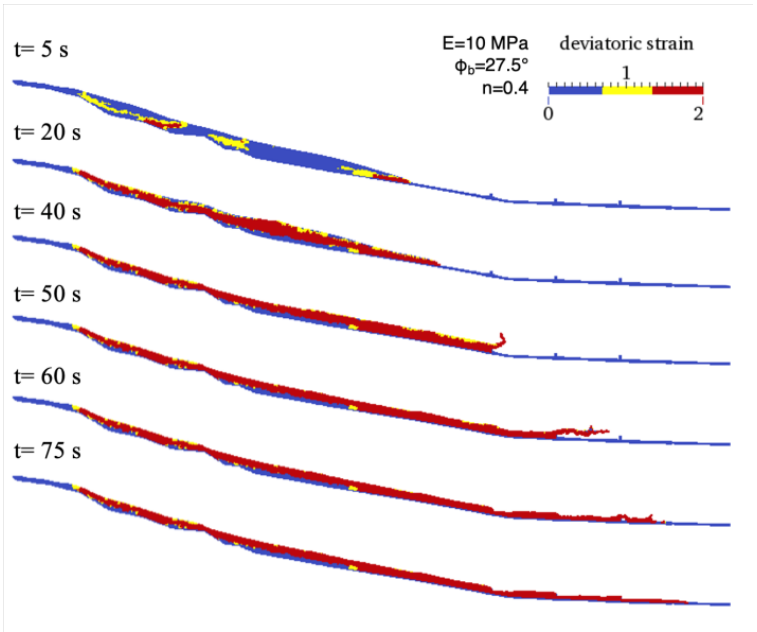

Figure 4-36. Spatial distribution of cumulative deviatoric strain in some time lapses.

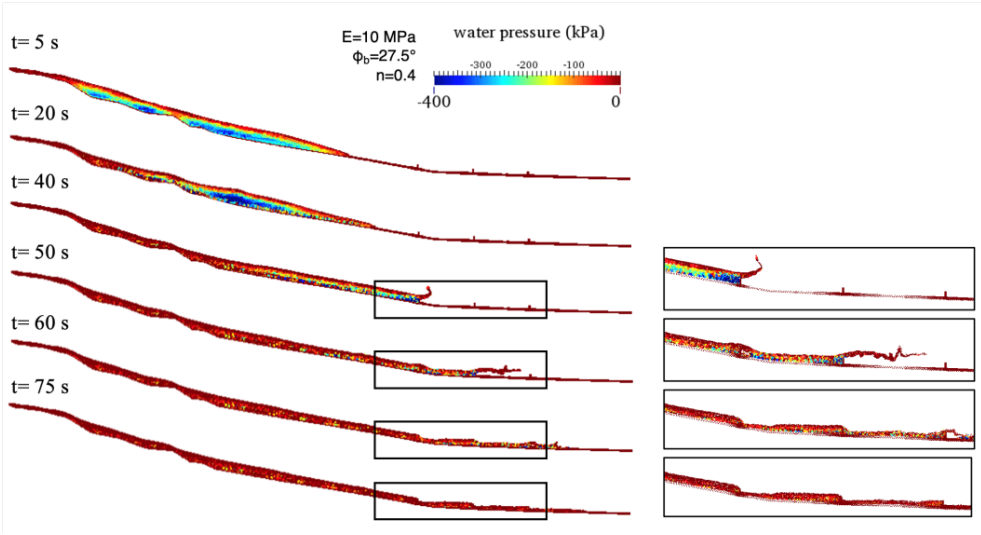

Figure 4-37. Spatial distribution of water pressure in some reference time lapses.

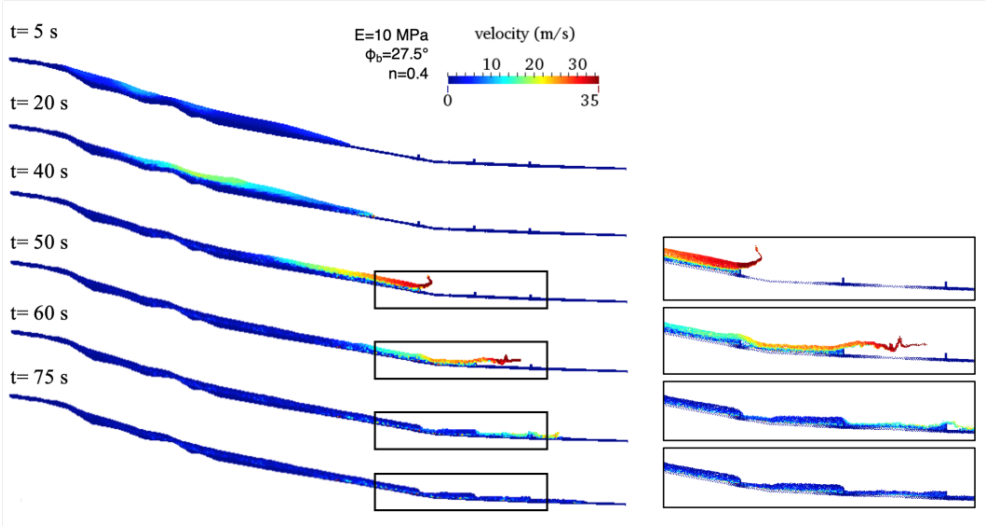

Figure 4-38. Spatial distribution of flow velocity in some time lapses.

Among several results, the changes in kinetic energy, the displacements trend and impact pressure of the flow on the barriers were considered.

The kinetic energy distribution over time (Figure 4-39) is characterized by a peak when the flow reaches the first barrier. Afterwards, the landslide-structure interaction reduces the energy of the flow. This peak value is higher as the porosity of the flow increases (Figure 4-39a) and as the soil stiffness decreases (Figure 4-39b), while it remains almost constant as the friction at contact varies (Figure 4-39c). The displacements trend over time of two points (A and B) of Figure 4-35 is instead shown in Figure 4-40. As the soil porosity increases, generally the horizontal displacements are higher (Figure 4-40a) due to the decrease in the weight of the flow. Such behaviour is typical of flowslides with high pore-water pressures (Cuomo, 2020). Also in this case study, the amount of water in the landslide body affects the flow as it can be discussed referring to soil porosity. The higher the porosity (hence the more water inside), and the lighter is the landslide material. Therefore, the initial potential energy of the landslide is less, but also the effective stresses and the resisting stresses are smaller. Therefore, the landslide travels faster and reaches an

earlier and higher peak of kinetic energy (Figure 4-39 a). Such different behaviour also reflects on the interaction mechanisms.

The changing in soil stiffness has also some effects (Figure 4-40 b), since the displacements are larger with low values of the soil stiffness. Less significant is the change in friction at the base, since the displacements are quite the same (Figure 4-40 c).

Figure 4-41 shows the impact pressure evolutions on the three check dams for a reference simulation. The flow approaches the first barrier at a time of 33 s, reaching the maximum impact pressure of 1,587 kPa at about 38 s and then decreases gradually before reaching the steady value of 380 kPa. The second barrier begins to be impacted by the debris flow at about 42 s with a maximum value of the impact pressure equal to 1,300 kPa, which is much smaller than the first dam. Finally, the impact force evolution on the last barrier is characterized by a peak value of 1,240 kPa at about 49 s, but then suddenly drops to the static value. The obtained values are in the range of those presented by Dai et al. (2017).

Comparing the three curves, the maximum impact pressure of the first barrier is much larger than the others two, since the kinetic energy of the flow is decreasing after the first impact (as also showed by the blue curve in Figure 4-39b). The final steady values of the three dams are quite similar, even if the last barrier has a slightly smaller value due to the less material behind it.

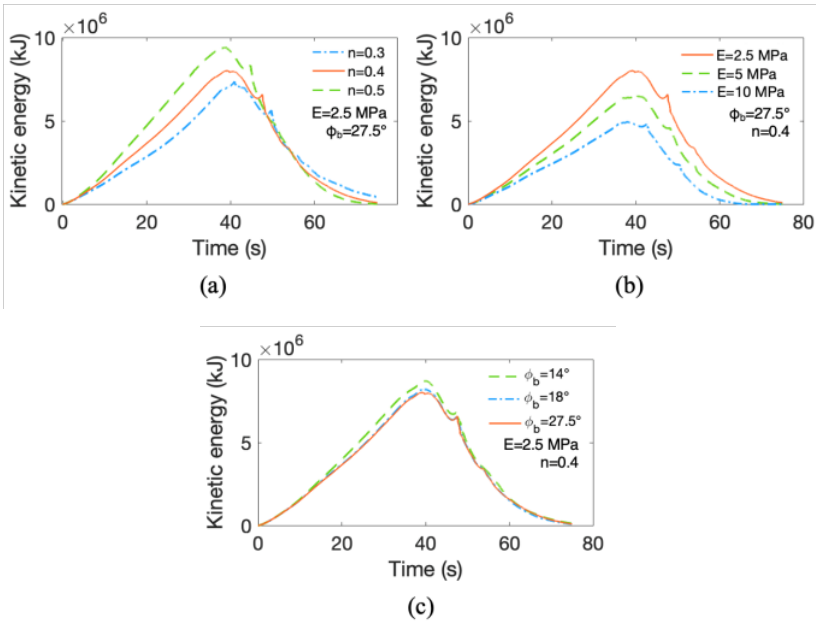

Figure 4-39. Effects of changing porosity (a), soil stiffness (b) and frictional contact (c) on kinetic energy distribution.

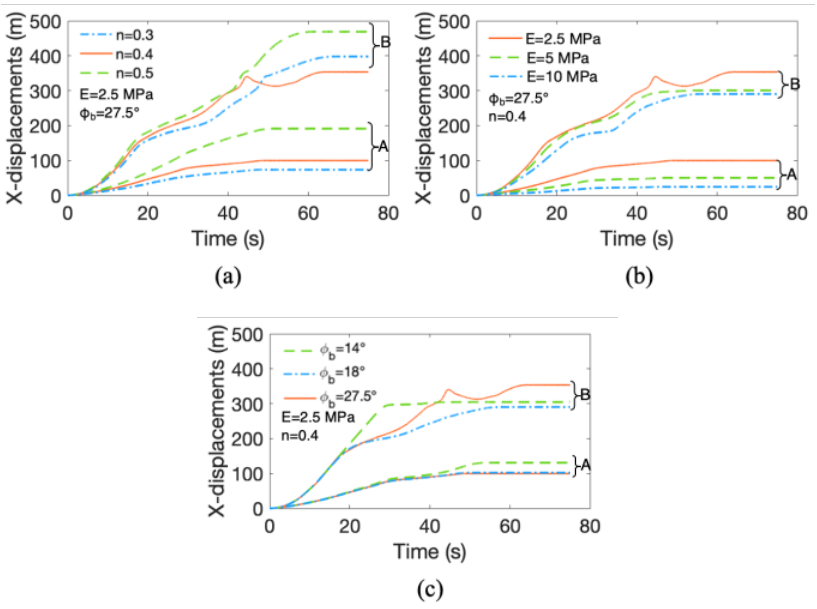

Figure 4-40. Effects of changing porosity (a), soil stiffness (b) and frictional contact (c) on horizontal displacements.

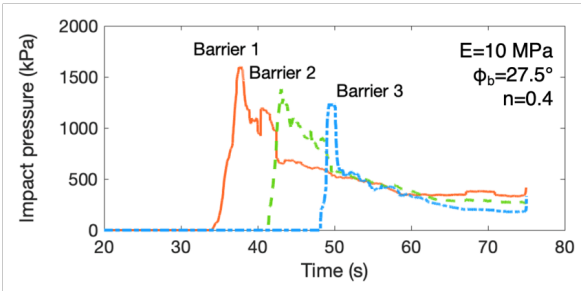

Figure 4-41. Example of impact pressure distribution over time along the barriers.

4.4.4 Concluding remarks

The paragraph shows the potential of an advanced numerical method such as the Material Point Method (MPM) in simulating the impact mechanisms of a large landslide against rigid walls.

The Wenjia Gully debris flow was simulated in a MPM context. The flow kinematics and impact force trend over time were studied by conducting a sensitivity analysis on some material properties (such as soil porosity, stiffness and basal friction).

The numerical results provided new insights in understanding the complex impact mechanisms through the computation and time-space tracking of some quantities, such as stress, strain, pore pressure, velocities and displacements, which cannot be easily monitored/obtained in the field.

Another contribution of this work refers to the possibility of simulating the complex hydro-mechanical behaviour of the propagating mass, thus permitting a better understanding of the impact mechanisms of saturated flows against rigid barriers. It was shown that the presence of water inside the debris flow must be considered in the numerical formulations, especially when simulating both landslide propagation and interaction with structures. In fact, excess pore-water pressure occurs favouring the mobilization of the landslide material and the overtopping of the barriers.

4.5 Impact scenarios for artificial barriers

4.5.1 A conceptual model for Landslide-Structure-Interaction (LSI)

The proposed conceptual model assumes a flow-like landslide mass that impacts against a protection barrier, unfixed to the base ground, and free to slide over it (Figure 4-42), as proposed by Cuomo et al. (2019c). The landslide body has the following features: unitary width, length L_1, depth h, density of the mixture ρ_m, initial uniform velocity $v_{1,0}$, pore-water pressure p_L and friction angle along the base ground equal to $\tan \varphi_b$. The geometric characteristics of the barrier are the greater base B, smaller base b, height H, inclination of the impacted side β.

The *LSI* problem is described through the following timelines: initial configuration (t_0), landslide propagation ($t_0 < t < t_{imp}$), impact of the landslide front (t_{imp}), time of the peak impact force (T_1), start of the inertial stage (T_2), end of *LSI* (t_f).

Before the landslide reaches the barrier ($t_0 < t < t_{imp}$), i.e., during the propagation stage, the *LSI* problem is governed by the basal frictional force F_1 (Equation 4-6), which acts along the bottom of the flow (L_1) and controls the reduction in flow velocity, resulting in a decrease of the impact forces.

Once the flow starts to interact with the barrier ($t_{imp} < t < T_2$), additional stresses (mostly orthogonal to the impacted surface, hence horizontal in many applications) are produced at the impacted side of the barrier. Many studies (e.g., Cui et al., 2015; Song et al. 2017) demonstrated that the total impact force-time history can be simplified as a triangular force impulse, usually with a rise time (T_1) much shorter than the decay time ($T_2 - T_1$).

According to the Newton's Third law of motion, the mutual impact forces (F_2) between the landslide and the barrier are equal and opposite. Such mutual stress makes: (i) the flow to decelerate and (ii) the barrier to slip along the base and to deform itself. The evaluation of the impact forces applied on the inclined side of the

barrier (L_2) is fundamental to design the structural characteristics of the barrier (Equation 4-7).

It is also worth noting that the flow may overtop the barrier during the impact, generating an additional force F_3 on the structure (Equation 4-8), mainly dependent on the flow-barrier frictional contact ($\tan\delta$).

After the impulsive stage of the *LSI* ($T_2 < t < t_f$), then problem is mostly governed by the inertial resistance force F_4 (Equation 4-9), which depends on the amount of friction mobilized along the base (b) of the barrier ($\tan\delta_b$). The final displacement Δx of the barrier depends on both the amount of energy transferred to the barrier and that dissipated by friction.

If the barrier must be fixed to the base, the stability of the barrier can be determined through the evaluation of the constraint reactions by solving the equilibrium of forces F_1, F_2 and F_3 and their moments. In this way, it is possible to assess the ultimate strength to which the foundation systems must be designed, or to understand what resistance must be mobilized at the base so that the barrier does not move. The latter option can be put into practice by placing a layer of soil material suitable to give an assigned frictional resistance to the base of the barrier.

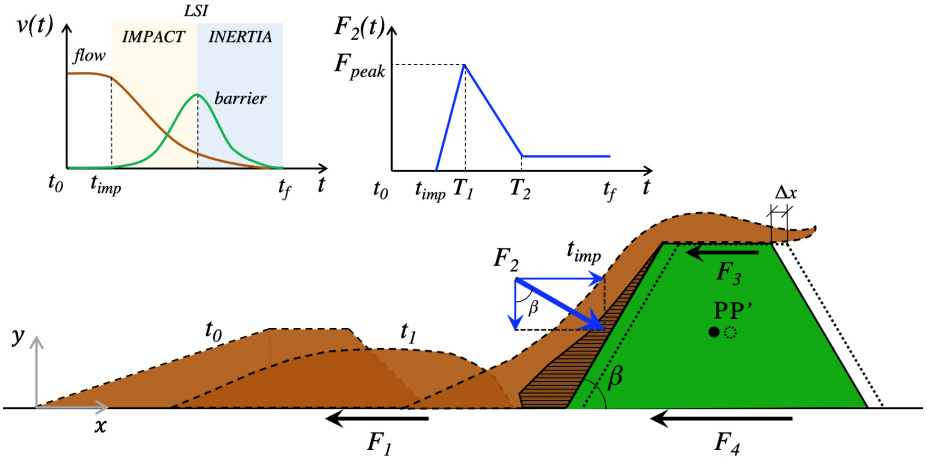

Figure 4-42. Conceptual scheme for Landslide-Structure-Interaction (LSI)

$$F_1(t) = \int_0^{L_1(t)} (\rho_m - \rho_L) g h(x,t) \tan\varphi_b \, dx \quad (4\text{-}6)$$

$$F_2(t) = \int_0^{L_2} (\rho_m - \rho_L) a(t) h(x,t) dx + \int_0^{L_2} p_L(x,t) dx \quad (4\text{-}7)$$

$$F_3(t) = \int_0^{b} (\rho_m - \rho_L) g h(x,t) \tan\delta \, dx \quad (4\text{-}8)$$

$$F_4(t) = \frac{1}{2}\rho_b g H(b+B) \tan\delta_b + \int_0^{L_2} (\rho_m - \rho_L) a(t) h(x,t) cos\beta \tan\delta_b \, dx + \int_0^{b} (\rho_m - \rho_L) g h(x,t) \tan\delta_b \, dx \quad (4\text{-}9)$$

4.5.2 Numerical modelling

Scheme and input data

To schematize the problem in a realistic way, multiple materials are considered such as: the flow-like landslide, the protection barrier, and the base soil. The latter is necessary to ensure the frictional contact at the base of the moving barrier (Figure 4-43). In such an approach the build-up of excess pore pressure in the flow material during the impact is considered as well as the hydromechanical coupled behaviour and the yield criterion of the flow material.

It is quite difficult to propose a standard landslide configuration as initial condition since it must represent the shape of the flow in a certain moment of its propagation stage. As known, this configuration strongly depends on the flow-path topography and on the geomorphological conditions that can vary from site to site. However, many studies have demonstrated that the front is often higher than the rear portion due to friction with the ground topography (Iverson, 1997; Thouret et al., 2020). For this reason, the chosen initial configuration of the landslide is characterized by a 45°-inclined front and a tail of length equal to three times the flow height. To consider different flow volumes, an i number of squares have been placed between the head and tail portions. Given this shape, the landslide has the same volume of an equivalent rectangular with the same height h and a length $L_m = (2+i) \cdot h$, and unitary width.

For the barrier it is assumed: non-porous material, frictional contact all around and rigid behaviour. If the barrier is unfixed, the frictional resistance along the base is set equal to the 80% of the strength properties of the base material (Cuomo et al., 2019c). In particular, the contact algorithm in combination with the moving mesh algorithm is used to model the frictional contact between the barrier and the above soil and also between the barrier and the flow. The moving mesh zone is attached to the barrier and moves with the same displacement. The elements of this zone keep the same shape throughout the computation. This numerical technique has the advantage to reduce numerical instabilities related to the crossing of material points into the neighbouring elements. All additional information about the moving mesh algorithm can be found in Al-Kafaji (2013), Fern et al. (2019), Martinelli and Galavi (2021), among others. The flow and barrier are modelled through the single-point MPM formulation, respectively with 2-phase and 1-phase, that are both described in the Al-Kafaji (2013), Fern et al. (2019), among others.

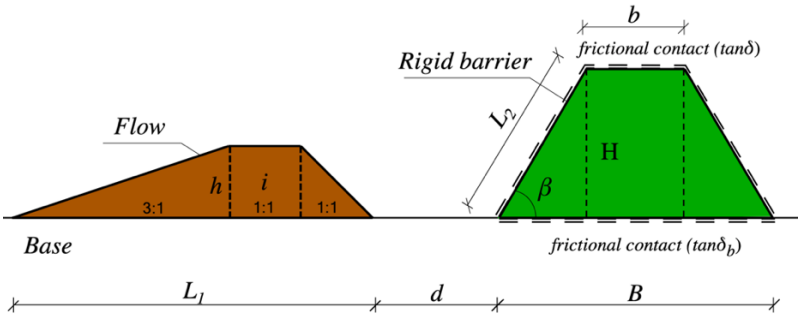

Figure 4-43. Geometric schematization for the LSI numerical simulations with rigid barrier

The geometric features of both the landslide and the barrier are summarized in Table 4-8, also considering different impact scenarios. Although simplified, the landslide scheme resembles its main characteristics such as velocity, impact height, non-zero interstitial pressures, with the geometric details shown in Table 4-8.

The numerical MPM analyses evidently allow the simultaneous simulation of flow propagation and flow-structure interaction. The flow is a saturated mixture with linear distribution of initial pore-water pressure, and non-associative (zero dilatancy)

elasto-plastic Drucker-Prager behaviour. The mechanical properties of the saturated flow mass and the friction angle at the contact with the barrier are reported in Table 4-9. The computational unstructured mesh is made of 20,515 triangular 3-noded elements with dimensions ranging from 0.20 to 1.00 m (Figure 4-44). The landslide is assumed as approaching the barrier with a fixed geometric configuration and constant velocity, until *LSI* starts. The phase diagram proposed by Faug (2015) for granular flow-structure interaction is here used here to predict the type of impact mechanism expected for each scenario (Table 4-10). The Froude number is here calculated as $v_{1,0} sen\beta / \sqrt{gh}$, considering the inclination β of the impacted side of the barrier. For practical applications, this could be useful to preliminary assess the potential efficiency of the barrier in intercepting the propagation of the flow under different impact conditions.

Table 4-8. Geometric features for different scenarios

ID	L_1 (m)	L_m (m)	i $(-)$	h (m)	V_1 (m^3/m)	$v_{0,1}$ (m/s)	$E_{k1,0}$ (kJ)	β (°)	d (m)	L_2 (m)	B (m)	b (m)	H (m)
1	21.00	15.00	3	3.00	45.00	10	4050	60	3.00	6.95	11.00	4.00	6.00
2	15.00	9.00	1	3.00	27.00	10	2430	60	3.00	6.95	11.00	4.00	6.00
3	27.00	21.00	5	3.00	63.00	10	5670	60	3.00	6.95	11.00	4.00	6.00
4	21.00	15.00	3	3.00	45.00	10	4050	80	3.00	6.08	8.50	6.50	6.00
5	21.00	15.00	3	3.00	45.00	10	4050	72	3.00	7.87	8.38	3.63	7.50
6	21.00	15.00	3	3.00	45.00	20	16200	60	3.00	6.95	11.00	4.00	6.00
7	47.00	45.00	43	1.00	45.00	10	4050	60	3.00	6.95	11.00	4.00	6.00

Table 4-9. Mechanical properties

Flow-like landslide									
ρ_m (kg/m^3)	n $(-)$	K_0 $(-)$	φ' (°)	c' (kPa)	E' (MPa)	ν $(-)$	k_{sat} (m/s)	μ_L (Pas)	K_L (MPa)
1800	0.5	0.66	20	0	2	0.25	10^{-4}	10^{-3}	30

Barrier		
ρ (kg/m^3)	$\tan(\delta)$ $(-)$	$\tan(\delta_b)$ $(-)$
2000	0.29	0.29

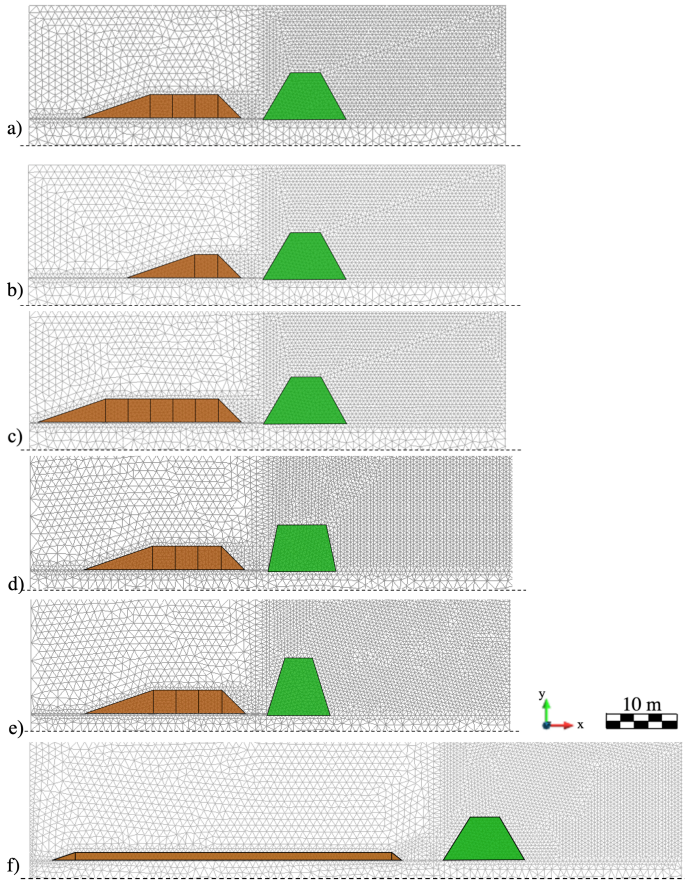

Figure 4-44. Computational mesh for different scenarios of Table 4-8: a) cases 1 and 7; b) case 2; c) case 3; d) case 4; e) case 5; f) case 6

Table 4-10. Expected impact mechanism

ID	Fr $(-)$	H/h $(-)$	Impact mechanism*
1	1.596	2.00	Standing jump
2	1.596	2.00	Standing jump
3	1.596	2.00	Standing jump
4	1.815	2.00	Standing jump
5	1.753	2.50	Standing jump
6	3.193	2.00	Airborne jets
7	2.765	6.00	Bores

*from the application of the diagram proposed by Faug (2015)

Numerical results

The influence of different types of impact mechanisms (by varying the ratio H/h and the Froude number Fr), the amount of flowing mass (by setting different landslide lengths), the slope β of the impacted side of the barrier and the basal constraint for the barrier (fixed/unfixed) have been investigated. Selected results are shown as for instance the spatial distribution of pore-water pressure at different time lapses of the propagation stage (Figures from 4-45 to 4-50) for the several schemes of Table 4-8. From an overall comparison, it emerges that the initial liquid pressure ($< 30\ kPa$) changes during the impact, with the maximum value in the first instants of the impact process (t=1 s) and later diminishing down to nil in some cases. However, the maximum value of pore water pressure ($p_{L,max}$) reaches different values depending on the type of flow and the type of barrier.

For the cases of Figure 4-45, it is noted that as the landslide volume increases, larger zones with very high interstitial pressure (p_L> 50 kPa) emerge. This favours the so-called "run-up" mechanism, which consists in the formation of a jet with high speed that overruns the barrier. This is the typical case of partially or completely saturated granular flows (Song et al. 2017). Looking at the flow in the final configuration (t=6 s), it is noted that the material that goes beyond the barrier is larger passing from L_1 = 15 m (Figure 4-45a) to L_1 = 27 m (Figure 4-45c).

Comparing fixed (Figure 4-45) and unfixed barrier typologies (Figure 4-46), no significant differences emerge about the liquid pressure distribution and the impact mechanism of the landslide. In fact, in both cases an elongated flow jet is formed, confirming the standing jump mechanism predicted trough the phase-diagram of Faug (2015). However, if the barrier is free to move, the maximum pore-water pressure values at impact are slightly lower and also the amount of material that is retained by the barrier ($V_{f,LH}$) is larger than in the cases of fixed barrier. This is more evident for larger landslide volumes (Figures 4-46b and 4-46c), since the displacement of the barrier is noticeable and therefore the energy of the flow is transferred to the barrier and dissipated by its movement.

The results also show that the inclination β and the barrier height H give interesting results. In fact, for a fixed barrier the value of $p_{L,max}$ turns out to be around 150 kPa regardless the shape of the barrier, as shown from the comparison between Figures 4-45b, 4-47a, 4-47b. However, a more inclined impacted side and a higher barrier are further efficient in terms of volume retained by the barrier. This efficiency increases if the barrier is unfixed (Figure 4-48), since pore-water pressure diminishes from 151 kPa (Figure 4-47a) to 146 kPa (Figure 4-48a) for β=80° and from 147 kPa to 123 kPa for H=7.5 m.

Different flows are also considered to investigate other impact mechanisms (Figures 4-49 and 4-50). A higher flow velocity (Figures 4-49a and 4-50a) than in case 1 produces an increase of $p_{L,max}$ of 42% from 152 kPa (Figure 4-45b) to 260 kPa (Figure 4-49a) in the case of fixed barriers. It is worth noting that the rate of increase is halved for unfixed barrier, as pore-water pressure increases from 135 kPa (Figure 4-46b) to 172 kPa (Figure 4-50a). Also in this case, the moving barrier inhibits the building-up of water pressures inside the landslide, thus reducing the overtopping of the barrier. The expected impact mechanism is an airborne jet (Table 4-10) and it is confirmed very well from the numerical simulation. A very prolonged jet with high energy is formed after impact thus the amount of material that is retained by the barrier is quite smaller than the standing jump cases. Completely different is the case of a shallow flow (Figures 4-49b and 4-50b), where the flow hits the obstacle and propagates upstream of it in unsteady conditions (bores regime). The flow has a very low kinetic energy and so the potential prevails, not allowing the flow to overtop the barrier and preventing the movement of the barrier.

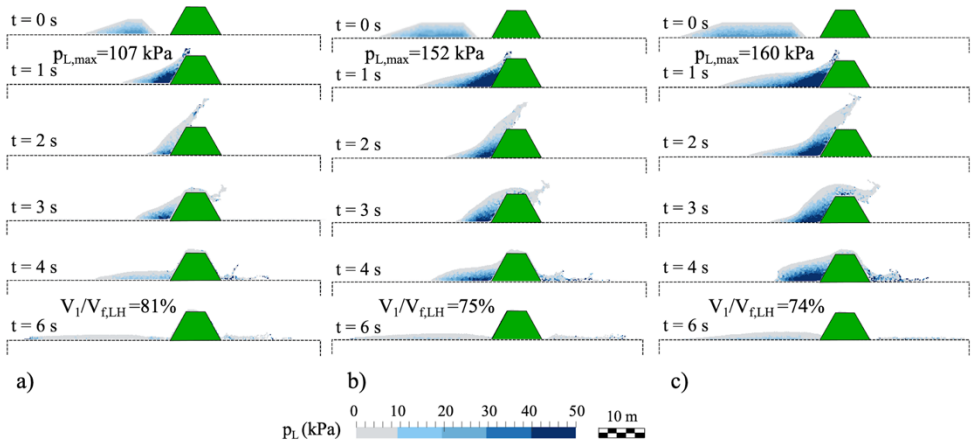

Figure 4-45. Influence of different flow lengths on pore-water pressure distribution for fixed barriers:
a) L_l=15 m (case 2); b) L_l=21 m (case 1); c) L_l=27 m (case 3)

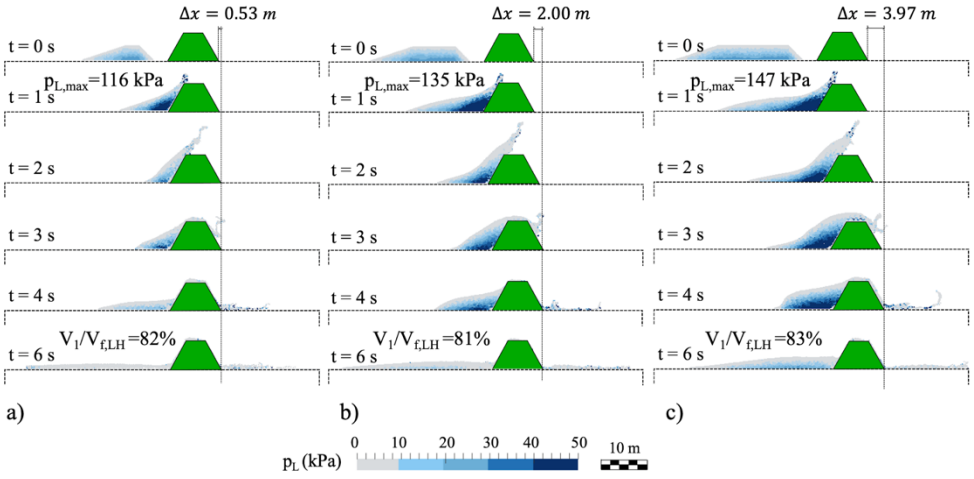

Figure 4-46. Influence of flow length on pore-water pressure distribution for unfixed barriers:
a) L_l=15 m (case 2); b) L_l=21 m (case 1); c) L_l=27 m (case 3)

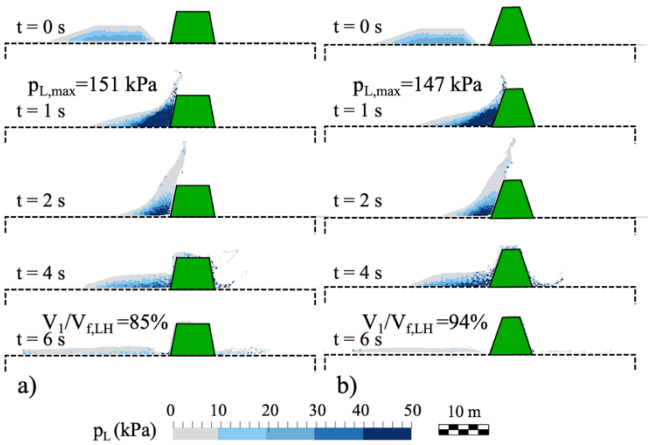

Figure 4-47. Influence of impacted side inclination and height of the barrier on pore-water pressure distribution for fixed barriers:
a) β=80°; H=6 m (case 4); b) β=72°; H=7.5 m (case 5)

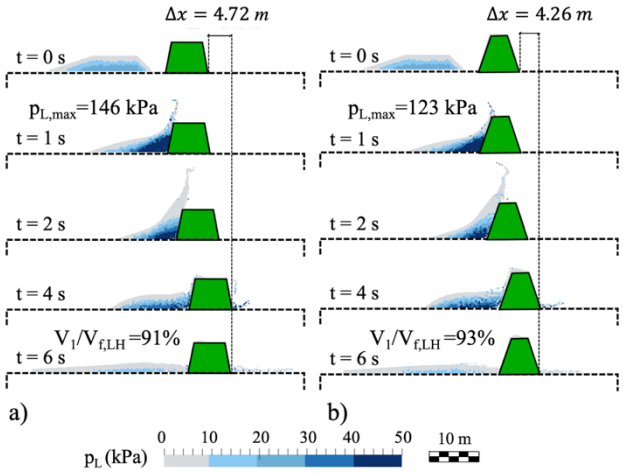

Figure 4-48. Influence of impacted side inclination and height of the barrier on pore-water pressure distribution for unfixed barriers:
a) β=80°; H=6 m (case 4); b) β=72°; H=7.5 m (case 5)

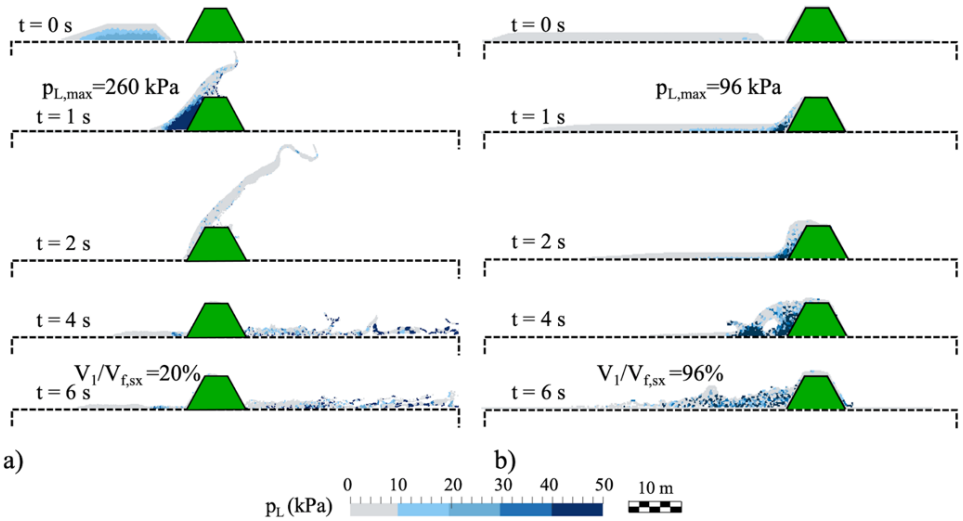

Figure 4-49. Influence of flow velocity and flow depth on pore-water pressure distribution for fixed barriers:
a) $v_{1,0}$=20 m/s; h=3 m (case 6); b) $v_{1,0}$=10 m/s; h=1 m (case 7)

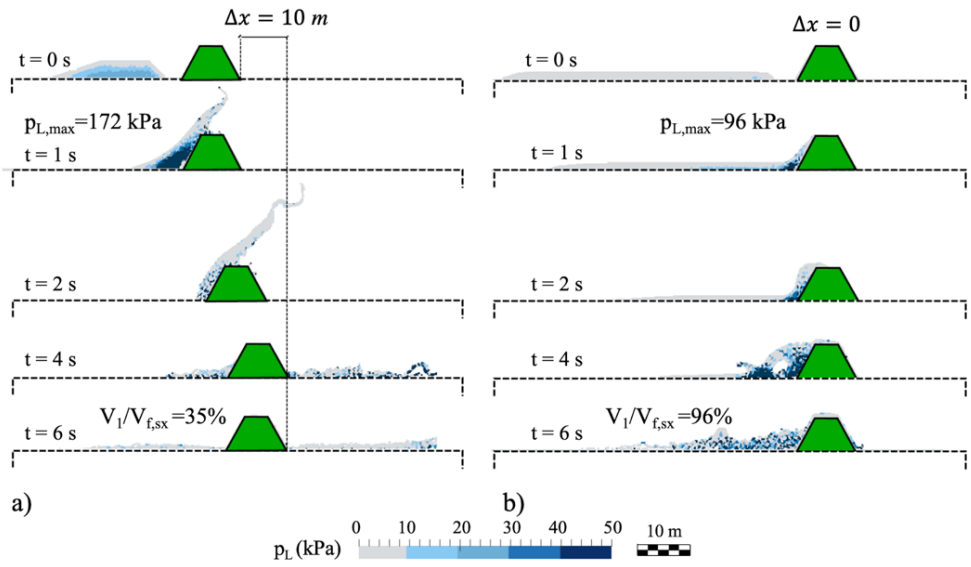

Figure 4-50. Influence of flow velocity and flow depth on pore-water pressure distribution for unfixed barriers:
a) $v_{1,0}$=20 m/s; h=3 m (case 6); b) $v_{1,0}$=10 m/s; h=1 m (case 7)

The MPM numerical simulations allow investigating the landslide-structure interaction from both a dynamic and kinematic point of view. Figure 4-51 shows an overall comparison between all considered cases in terms of impact forces (F_2, F_3 and F_4, introduced in Figure 4-42) and in terms of kinetic energy trend for both flow and barrier. For the sake of simplicity, the flow basal frictional force F_1 is assumed as nil in all the cases through a smooth contact not to influence the flow height and velocity at impact.

In general, the peak of the horizontal impact force $F_{2,x}$ is quite similar for all the standing jump cases, while its trend is distinctly different for the other types of impact mechanism. The different between fixed (Figure 4-51a) and unfixed (Figure 4-51b) barriers is more evident in the cases where the displacement of the barrier is larger. In contrast, the vertical component $F_{2,y}$ has a different trend for each impact scenario, as will be discussed specifically below.

Focusing on the temporal trend of $F_{L,2}$ (Figure 4-52), that is the impact forces generated within the liquid phase, it emerges that the horizontal component $F_{L,2,x}$ reaches values that are halved with respect to the total force $F_{2,x}$, but the vertical component $F_{L,2,y}$ and $F_{2,y}$ remains almost similar. However, main feature that can be appreciated from the graphs in Figure 4-52 is that for unfixed barriers the impact forces exerted by the liquid phase are always lower than the case of fixed barriers.

The temporal variation of the forces F_3 and F_4 is also obtained. The frictional force above the barrier F_3 is due to the overtopping of the barrier by the flow and so it is dependent on the amount of flow that goes beyond the barrier. This force can also have sign changes when the flow, instead of going beyond the barrier, falls within the volume retained by the barrier. However, compared to the frictional force at the base of the barrier F_4 can be neglected due to the low values achieved.

The frictional force F_4 reaches the maximum value in correspondence of the maximum shear resistance that can be mobilized at the interface between the barrier and the above soil. This shear strength is assumed equal to the 80% of the strength properties of the base material (Cuomo et al., 2019c), to which a friction angle of

20° and nil cohesion have been set. When the resultant of all the forces acting on the barrier exceeds this resistance, the barrier can move along the base until these actions decrease. This is the reason why the barrier remains immobile in case 7, where is well evident from the F_4 temporal trend that the maximum shear strength at the base cannot be reached at any time.

The kinetic energy of the incoming flow (in solid lines) has a quite similar trend for most of the impact scenarios. In order to make a more comprehensive comparison, the curves are divided by the initial kinetic energy of the flow ($E_{k1,0}$), whose values are reported in Table 4-8. All the curves (apart from case 7). show a sudden reduction up to $t \cong 2\ s$, that is the moment from which the formed jet takes the downward direction. This means that energy is transforming from kinetic to potential. Furthermore, the decay of flow kinetic energy is faster for greater inclinations β and for smaller landslide volumes, for both fixed and unfixed barriers.

From $t > 2\ s$ all the trends are very different, since it represents the kinetic energy of the overcoming jet (especially for cases 1-2-3-6) combined with the energy of the reflecting flow (especially for case 4 and 5). Completely different is the trend of case 7, that is characterized by a slower and constant reduction because the impact mechanism does not provide for the formation of any jet.

The main differences between fixed and unfixed barriers in term of kinetic energy are: i) the fixed barriers allow a more consistent reduction of flow kinetic energy than unfixed barriers until $t \cong 2\ s$; ii) from $t > 2\ s$ the energy of the flow is higher than the cases of unfixed barriers, where part of the kinetic energy of the jet/reflecting flow is transformed into the kinetic energy of the barrier (in dashed lines), and therefore more flow kinetic energy is transformed into work produced by the movement of the barrier.

Going into details for the temporal of horizontal and vertical components, Figures 4-53, 4-54 and 4-55 shows the influence of the landslide length, the inclination of the impacted barrier side and the type of impact mechanism, respectively.

Figure 4-53 shows a comparison between the total impact forces for fixed and unfixed barriers, also taking into account different landslide lengths. The force distributions between fixed and unfixed barriers are very similar for a 15 m landslide. This is because the maximum displacement of the moving barrier is few cm, and so does not affect the dynamics of the impact. On the other hand, for larger landslide volumes, where the movements of the barrier exceed the 2 m, there is a decrease in the peak value of about 100 kN/m. On the other hand, the main influence of the landslide volume resides in the integral of the force over time (i.e. the impulse), which is greater for larger landslide lengths, thus even the impact period lasts longer.

As shown in Figure 4-54, the inclination β has a significant influence on the peak of both horizontal and vertical impact force. The peak value of $F_{2,x}$ is bigger for higher inclinations, while the vertical component $F_{2,y}$ reaches lower values for greater inclinations β. This happens because the vertical component of the impact force is strictly linked to the weight of the flow that propagates beyond the barrier. For this reason, the vertical impact force plays an important role in the prediction of the barrier maximum displacement, which increases when the vertical force approaches to zero. Also here, the difference in the peak value of $F_{2,x}$ between fixed and unfixed barriers is highlighted, obtaining a decrease of about 100 kN/m for the unfixed barrier cases.

Concluding, Figure 4-45 shows the influence of flow velocity and flow depth on the impact force trend. In fact, in the case of an airborne jet (case 6) the peak force is more evident than the other cases, while in the case of a bores regime (case 7) it is quite difficult to individuate a unique peak at the impact moment. The latter impact force trend is typical for impact mechanisms which are not characterized by the formation of a jet. Moreover, going from bores to airborne jet regimes the influence of the barrier basal constraint becomes more evident.

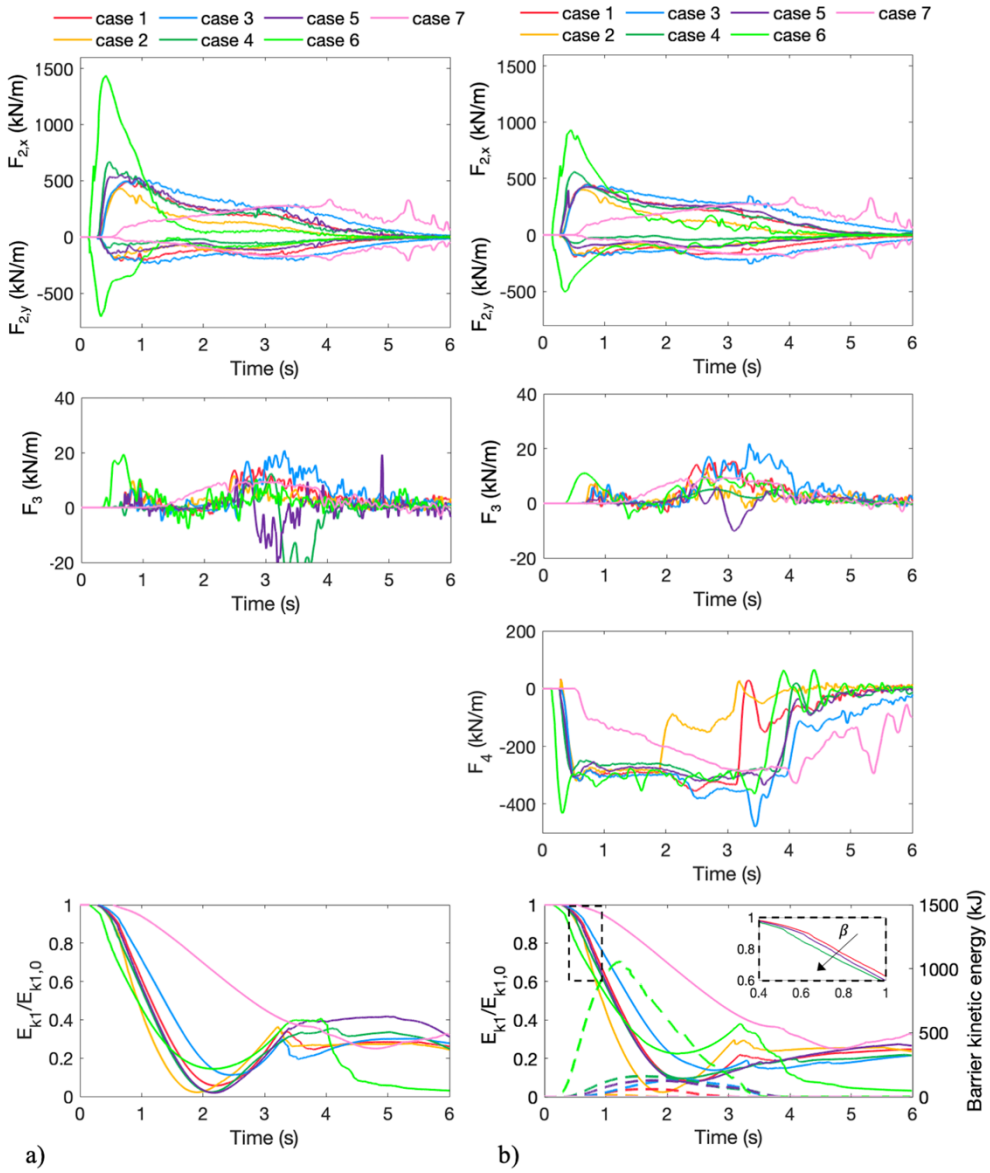

Figure 4-51. Impact forces and kinetic energy of the flow different scenarios (solid lines) and barrier kinetic energy (dashed lines): a) fixed barrier; b) unfixed barrier

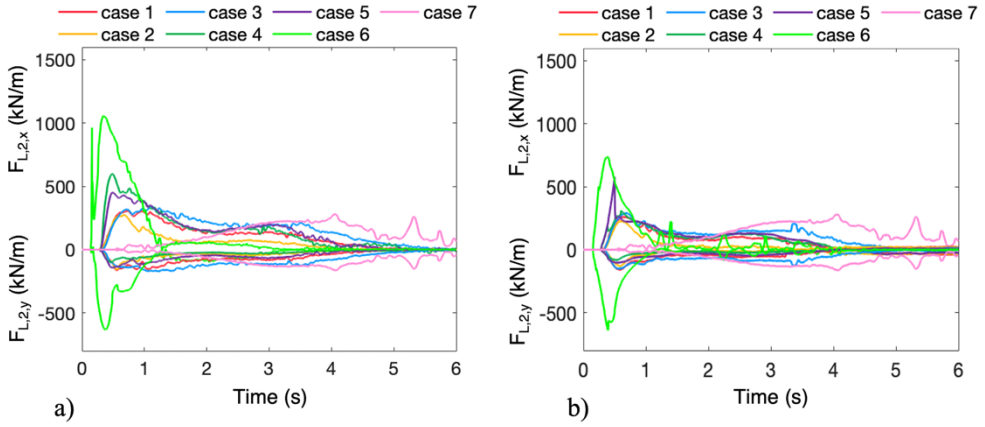

Figure 4-52. Impact forces of liquid phase for all the considered scenarios: a) fixed barrier; b) unfixed barrier

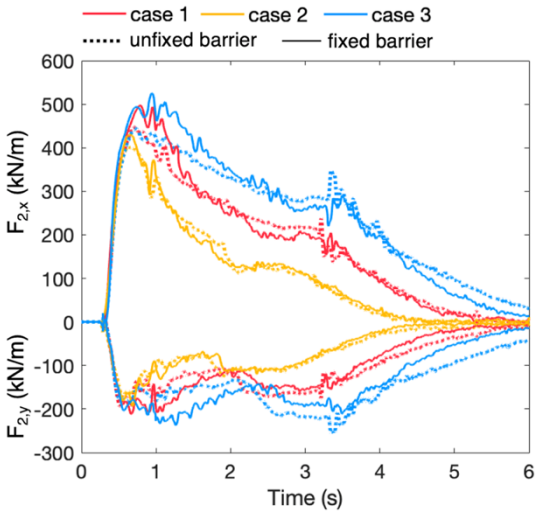

Figure 4-53. Influence of flow length on impact forces distribution for fixed and unfixed barriers

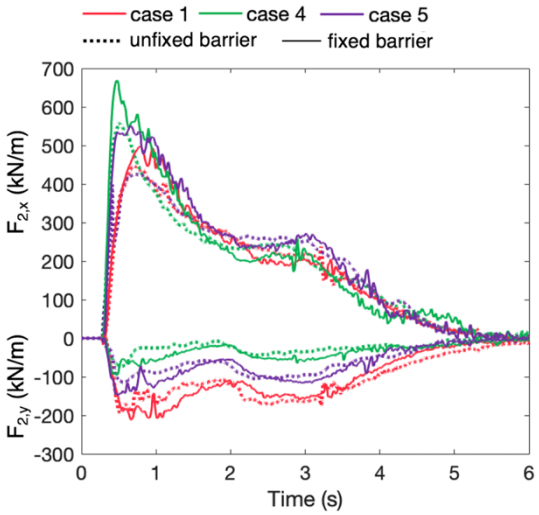

Figure 4-54. Influence of impacted side inclination and height of the barrier on impact forces distribution for fixed and unfixed barriers

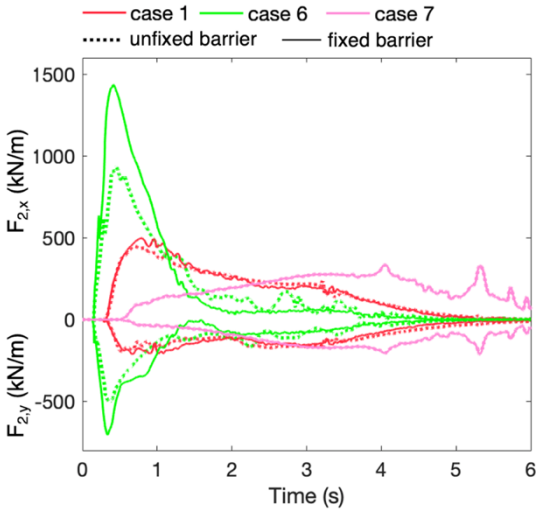

Figure 4-55. Influence of flow velocity and flow depth on impact forces distribution for fixed and unfixed barriers

4.5.3 Conclusions

The study concerned the modelling of the flow-structure interaction in a context of large deformations for both the saturated flow and the barrier. The attention was focused on the potential efficiency of different types of barriers in intercepting the propagation of the flow under several impact conditions.

As novel contribution to the existing literature, the study also provides a new alternative for the calculation of the impact pressure, that is typically evaluated using conservative empirical formulations. Through MPM modelling it was possible to accurately derive the spatial and temporal distribution of the stresses generated from the impact on the structure, also separating the contribution of the impact force referred to the liquid phase. It has been shown that the increase in interstitial water pressure can favour the overtopping of the barrier. This issue should be taken into consideration for a correct design of the mitigation structure.

Many works in the literature have evaluated the impact forces assuming the that the energy of the flow is dissipated exclusively within the landslide mass. On the contrary, the proposed study took into consideration other ways for dissipating the flow energy, considering the movement of the barrier.

The numerical results show that a fixed barrier to the base undergoes greater impact forces than an unfixed barrier, since the reaction to the impact of the flow is transferred to the constraints at the base. For this reason, the case of an unconstrained barrier was investigated also considering the role of different landslide volumes. The installation of unfixed barriers also inhibits the overtopping mechanism of the barrier by the flow as the movement of the barrier reduces the increase of liquid pressure within the landslide.

Based on these preliminary results, it appears that unfixed barriers may be a reasonable solution to stop the propagation of flow-type landslides. However, further studies are needed to investigate the feasibility of these structures and their practical implications in the framework of the landslide risk mitigation and management

5. Two novel simplified methods for LSI analysis

5.1 A new analytical method

5.1.1 Formulation

An analytical model is set up where the landslide body and the barrier are considered as two colliding bodies (Figure 5-1a). The approaching flow is schematized as a rectangular volume V_1, with mass m_1, length $L_{1,0}$, depth h, unitary width, density ρ_m, and initial velocity $v_{1,0}$. The barrier is rigid, with its own mass m_2 and it is free to slide along the base. The frictional contact at the base is equal to $\tan(\delta_b)$, which is set as the 80% of the strength properties of the subsoil base material (Cuomo et al., 2019c).

The case of a fixed barrier is also possibly considered, setting the mass of the barrier to a very high value compared to that of the flow (i.e., $m_2/m_1 \to \infty$).

The interaction between the landslide and the barrier (*impact* stage) is schematized by an inelastic collision (Figure 5-1b), therefore after the impact the two bodies reach the same velocity v_{CM}, applied in the centre of mass (*CM*) of the system. The impact force F is a spatio-temporal function since the approaching volume of the landslide increases with time until T_1 and then diminishes due to the dissipation of flow energy. The quantity s_1 represents the change in flow geometry after the impact and it is computed as positive in the direction opposite to the flow movement. The maximum value $s_{1,max}$ is reached when the impact force is equal to the peak value. This means that only a part of the total volume of the landslide contributes to the interaction with the obstacle. Once the interacting volume (hs_1) has contributed to increase the impact force, it may overtop the barrier creating a vertical jet or may be completely reflected. If a vertical jet is formed, supposing that

all the interacting volume has overtopped the barrier for the sake of safety, the amount of flow mass that can be found beyond the barrier will be at most equal to the $\rho hs_{1,max}$. After reaching the maximum impact pressure, the flow mass decelerates and the interacting volume decreases in time until nil, i.e., $s_1 = 0$ at $t = T_2$. During the interaction, the barrier can slide along its base of a quantity equal to Δx.

At the end of the *impact* stage, the motion of the system is governed by the inertial forces and the length s_1 is assumed to be zero (Figure 5-1c). Due to friction, both the colliding bodies decelerate so that their velocity ($v_{INERTIA}$) decreases over time. The final configuration (Figure 5-1d) is reached when the two bodies are completely stopped and have travelled for a total distance of Δx_f.

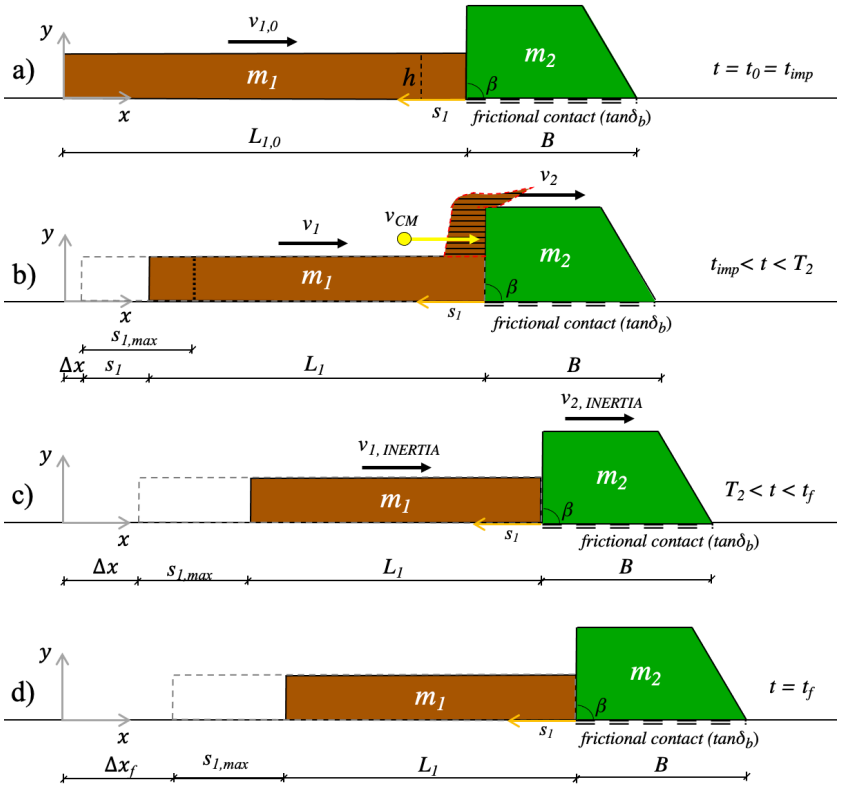

Figure 5-1. Conceptual scheme in the analytical model: (a) at the early stage of impact, (b) during the impact, (c) during the inertial phase, d) at final condition

Impact governing equations ($t_{imp} < t < T_2$)

According to the Newton's Third law of motion, the mutual impact forces of body 1 (i.e., the landslide) and body 2 (i.e., the barrier) are equal and opposite. In the following, the quantities referring to body 1 will be taken into consideration.

The reaction force between two colliding bodies can be written as in Equation 5-1, where s is time-dependent and represents the longitudinal interacting length of the considered body.

$$F(s) = m_1 \frac{dv_1}{ds_1} \cdot \frac{ds_1}{dt} \tag{5-1}$$

The velocity variation can be supposed to be linear along x and can be computed through Equation 5-2, which consists in the ratio between the velocity variation during the impact period (t_{imp}, T_2) and the maximum interacting length of body 1.

$$\frac{dv_1}{ds_1} = \frac{v_{1,0} - v_{CM}}{s_{1,max}} \tag{5-2}$$

For inelastic collision, the final velocity v_{CM} of the two bodies is the same and can be obtained from the conservation of linear momentum of the system if there is no friction between the sliding bodies and the surface (Equation 5-3). If $m_2 \to \infty$, the final velocity of the body 1 goes to zero. This is a valuable assumption for the case of a fixed barrier.

$$v_{CM} = \frac{m_1 v_{1,0} + m_2 v_{2,0}}{m_1 + m_2} \tag{5-3}$$

During the collision between the two bodies, the kinetic energy of the system is not conserved and the total variation of kinetic energy of the system can be obtained from Equation 5-4.

$$\Delta E_k = \frac{1}{2}\left(m_1 {v_{1,0}}^2 + m_2 {v_{2,0}}^2\right) - \frac{1}{2}(m_1 + m_2){v_{CM}}^2 \quad (5\text{-}4)$$

Using Equation. 5-2 and 5-3, Equation 5-1 can be written as in Equation 5-5.

$$F(s) = \left(\frac{m_1 m_2}{m_1 + m_2}\right) \cdot \left(\frac{v_{1,0} - v_{2,0}}{s_{1,max}}\right) \cdot \frac{ds_1}{dt} = K_1 \cdot \frac{ds_1}{dt} \quad (5\text{-}5)$$

It is worth noting that the quantity $K_1 = \left(\frac{m_1 m_2}{m_1 + m_2}\right) \cdot \left(\frac{v_{1,0} - v_{2,0}}{s_{1,max}}\right)$ is a characteristic of body 1. Let introduce a new variable q_1 such that multiplied by the maximum interaction length of the body 1 ($s_{1,max}$) gives the work done by the impact force (Equation 5-6).

The function $F(s)$ is not known a priori since $\frac{ds_1}{dt}$ is unknown. For this reason, the trend of F along s is assumed to be less than linear (Eq. 5-7), because this assumption considers the fact once the interaction has started, the additional volumes interacting with the barrier generate smaller and smaller increases in impact pressure with time. From Equations 5-4 and 5-6, the variation of $\frac{ds_1}{dt}$ (Eq. 5-8) and the relationship between s_1 and t (Equation 5-9) can be determined. The impact force trend $F(t)$ in Equation 5-10 can be obtained from Eq. 5-7 by placing the formulation of $s_1(t)$ reported in Equation 5-9.

The unknown quantities q_1 and T_2 can be obtained by solving the system in Equation 5-11, which reports the understandable conditions: (i) the integral of s_1 over the impact time is equal to the maximum interacting length ($s_{1,max}$) and (ii) the work done by the impact force is equal to the dissipated kinetic energy by the system (ΔE_k in Equation 5-4). The formulations of T_2 and q_1 obtained by solving the system in Equation 5-11 are reported in Equations 5-12 and 5-13, respectively.

$$q_1 s_{1,max} = \int_0^{s_{1,max}} F(s) ds_1 \quad (5\text{-}6)$$

$$F(s) = q_1 \sqrt{s_1} \quad (5\text{-}7)$$

$$\frac{ds_1}{dt} = \frac{1}{2}\left(\frac{q_1}{K_1}\right)^2 t \tag{5-8}$$

$$s_1(t) = \frac{1}{4}\left(\frac{q_1}{K_1}\right)^2 t^2 \tag{5-9}$$

$$F(t) = \frac{1}{2}\frac{{q_1}^2}{K_1} t \tag{5-10}$$

$$\begin{cases} \int_0^{T_2} \frac{ds_1}{dt} dt = s_{1,max} \\ \int_0^{s_{1,max}} F(s) ds_1 = \Delta E_k \end{cases} \tag{5-11}$$

$$T_2 = \frac{8}{3}\frac{s_{1,max}}{(v_{1,0} - v_{2,0})} \tag{5-12}$$

$$q_1 = \frac{3}{4}\frac{K_1(v_{1,0} - v_{2,0})}{\sqrt{s_{1,max}}} \tag{5-13}$$

Once known the quantities involved in the evaluation of the impact force over time and along s, the trend of the acceleration (Equation 5-14) can be obtained from Equations 5-1 and 5-8. The velocity of body 1 is simply the integral of acceleration over time (Equation 5-15) and so the trend of kinetic energy over time can be computed (Equation 5-16).

$$a_1(t) = \frac{q_1^2}{2K_1 m_1} t \tag{5-14}$$

$$v_1(t) = v_{1,0} - \frac{q_1^2}{4K_1 m_1} t^2 \tag{5-15}$$

$$E_{k,1}(t) = \frac{1}{2} m_1 v_1^2(t) \tag{5-16}$$

The same equations can be obtained for the body 2, considering the quantities related to the barrier. However, the frictional contact along the base of barrier causes its deceleration and therefore must be considered in Equation 5-14. The deceleration is equal to ratio between the frictional contact force and the mass of the barrier (Equation 5-17) and remains constant during the interaction with the flow.

The formulation derived for the acceleration, velocity and kinetic energy of the barrier are reported in Equations 5-18, 5-19 and 5-20, respectively. The barrier displacement Δx (Figure 5-1) can be obtained by integrating the velocity trend over time (Equation 5-21).

$$\left|a_{fr}\right| = \frac{F_{fr}}{m_2} = \frac{m_2 g \tan(\delta_b)}{m_2} = g \tan(\delta_b) \tag{5-17}$$

$$a_2(t) = \frac{q_2^2}{2K_2 m_2} t - g \tan(\delta_b) \tag{5-18}$$

$$v_2(t) = v_{2,0} - g \tan(\delta_b)\, t + \frac{q_2^2}{4K_2 m_2} t^2 \tag{5-19}$$

$$E_{k,2}(t) = \frac{1}{2} m_2 v_2^2(t) \tag{5-20}$$

$$\Delta x(t) = v_{2,0} - \frac{g}{2} \tan(\delta_b)\, t^2 + \frac{q_2^2}{12K_2 m_2} t^3 \tag{5-21}$$

The presented formulations consider that the impact force trend over time is a linear function that reaches the peak value at $t = T_2$. However, many studies (e.g., Song et al. 2017) have demonstrated that the total impact force-time history can be simplified as a triangular force impulse, usually with a rise time (T_1) much shorter than the decay time ($T_2 - T_1$). To consider this more realistic trend, the above-mentioned formulations can be rewritten, introducing the dimensionless ratio in Equation 5-22 in such a way that the different triangular trends ($t_{imp} - F_{peak} - T_2$) all have the same area (i.e., the impulse of the impact force does not change with τ).

To this aim, the general formulation $f(t)$ is converted into a new one $f(t')$ through a change of variables from t to t', as reported in Equation 5-23.

$$\tau = \frac{T_1}{T_2} \tag{5-22}$$

$$\begin{cases} f(t') = f\left(\frac{t}{\tau}\right) & 0 < t' < T_1 \\ f(t') = f\left(\frac{T_2 - t}{1-\tau}\right) & T_1 < t' < T_2 \end{cases} \tag{5-23}$$

Inertia governing equations ($T_2 < t < t_f$)

After impact, the interaction between the two bodies can be neglected since the motion is mostly governed by the friction at the base. In this stage, the change in velocity over time (Equation 5-24) can be calculated referring to the uniformly decelerated motion equations, with the constant acceleration reported in Equation 5-17. Since the barrier is assumed to slide over the distance Δx, the amount of energy that has been transferred to the barrier $E_{k,2}(T_2)$ is equal to the amount of energy dissipated by friction ($W_{fr} = F_{fr}\Delta x$).

The final displacement Δx_f of the barrier (Figure 5-1d) is simply the sum of Equation 5-21 with $t = T_2$ and Equation 5-25, as reported in Equation 5-26.

$$v_{INERTIA}(t) = v_{CM} - |a_{fr}|\Delta t = v_{CM} - g\tan(\delta_b)\,(t - T_2) \tag{5-24}$$

$$\Delta x = \frac{{v_{CM}}^2}{2\,g\tan(\delta_b)} \tag{5-25}$$

$$\Delta x_f = \frac{{v_{CM}}^2}{2\,g\tan(\delta_b)} + v_{2,0}T_2 - \frac{g}{2}\tan(\delta_b)\,{T_2}^2 + \frac{q_2^2}{12K_2m_2}{T_2}^3 \tag{5-26}$$

The quantities q_1 (Equation 5-13) and T_2 (Equation 5-12) are the model primary unknows. Once known both T_2 and T_1, that can be achieved by fixing the ratio $\tau = T_1/T_2$ (for example from experimental evidence), the description of the impact dynamics is complete. The model parameters that must be appropriately individuated are $s_{1,max}$ and τ.

Once known both T_2, the value of T_1 can be achieved from T_2 by fixing the ratio $\tau = T_1/T_2$ (for example from experimental evidence), the description of the impact dynamics is complete. The model parameters that must be appropriately individuated are $s_{1,max}$ and τ.

Parametric analysis

In this analytical model two quantities $s_{1,max}$ and τ must be evaluated, and it is useful to understand the meaning of these variables in the assessment of both impact force and kinetic energy variation in time (Figure 5-2). Supposing that the two bodies have the same mass $m_1 = m_2 = 81000\ kg$, and $L_{1,0} = 15\ m;\ h = 3\ m;\ \rho_m = 1800\ kg/m^3;\ v_{1,0} = 10\ m/s;\ v_{2,0} = 0\ m/s;\ \beta = 90°;\ \tan\delta_b = 0.29$.

From the variation of impact forces, it emerges that the larger $s_{1,max}$ the lower the peak force value. Since the linear momentum is independent on $s_{1,max}$, with other quantities being equal, the reduction of the flow velocity from $v_{1,0}$ to v_{CM} occurs over a greater distance (as understandable from Equation 5-2). Hence, the impact time T_2 increases with higher values of $s_{1,max}$. This is also reflected in the computation of the kinetic energy over time, where for larger values of $s_{1,max}$ the flow energy reduction is more gradual. For the barrier, lower value of $s_{1,max}$ lead to higher peak of kinetic energy since the same amount of momentum is transferred from the flow to the barrier in a shorter time lapse. The change in τ also leads to different results as for $\tau \longrightarrow 1$ it occurs that $T_1 \longrightarrow T_2$. This also regulates the slope of the rise trend of the impact force diagram, being more inclined for lower values

of T_1. The inclination of the rise period influences the kinetic energy trend being its variation more gradual when τ approaches unity.

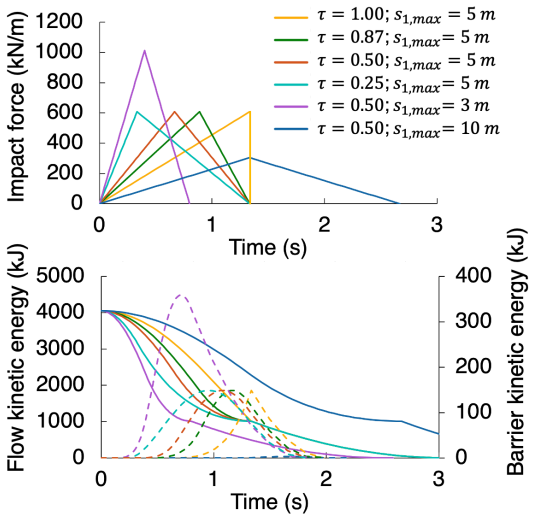

Figure 5-2. Variation of impact forces and kinetic energy of the flow (solid lines) and the barrier (dashed lines), as schematised in the analytical model

5.1.2 Calibration

The analytical model needs the calibration of the quantities $s_{1,max}$ and τ before being adopted for the prediction of landslide-structure interaction. These terms are obtained through Equations 5-7 and 5-22, respectively, using the peak value of the horizontal impact force and peak time T_1 obtained from the MPM simulations.

The input scheme for the numerical simulation is the same used in Sect. 4.5, which considers the flow-like landslide, the rigid barrier that can be unfixed or fixed to the base, and the base material along which a frictional contact ($\tan \delta_b$) is imposed. The chosen initial configuration of the landslide is characterized by a 45°-inclined front and a tail of length equal to three times the flow height. To consider different flow volumes, an i number of squares have been placed between the head and tail portions. Given this shape, the landslide has the same volume of an

equivalent rectangular with the same height h and a length $L_m = (2 + i) \cdot h$, and unitary width. For the barrier it is assumed: non-porous material, frictional contact all around and rigid behaviour. If the barrier is unfixed, the frictional resistance along the base is set equal to the 80% of the strength properties of the base material (Cuomo et al., 2019c). In particular, the contact algorithm in combination with the moving mesh algorithm is used to model the frictional contact between the barrier and the above soil and even between the barrier and the flow.

The flow and barrier are modelled through the single-point MPM formulation, respectively with two-phase and one-phase formulations. The numerical MPM analyses evidently allow the simultaneous simulation of flow propagation and flow-structure interaction. The flow is a saturated mixture with linear distribution of initial pore-water pressure, and non-associative (zero dilatancy) elasto-plastic Drucker-Prager behaviour. The mechanical properties of the saturated flow mass and the friction angle at the contact with the barrier are reported in Table 5-1.

The selected parameters used for assessing the goodness-of-fit for the analytical model under different scenarios are also here the porosity, the impact height, the triggered volume, the initial velocity of the landslide and the inclination of the impacted side of the barrier (Table 5-2).

The results of the calibration for both fixed and unfixed barrier are reported in Figures 5-3 and 5-4. In addition, the trend over time of the kinetic energy is plotted for both the colliding bodies using the calibrated parameters. The ratio $\lambda = s_{1,max}/L_{1,0}$ obtained from calibration is equal to 0.72 and 0.41 for fixed and unfixed barriers, respectively. However, to obtain more precise results for identical flows with different velocities (i.e, Set IIa and Set IIb), the quantities $s_{1,max}$ and τ must be changed so that they are directly and indirectly proportional to the initial velocity $v_{1,0}$, respectively. This means that the ratio $v_{1,0}/s_{1,max}$ and the product $v_{1,0}\tau$ are kept constant. If it happens that $s_{1,max} > L_{1,0}$ then the assumption $s_{1,max} = L_{1,0}$ must be set. Nevertheless, real case landslides have different volumes, density,

impact height, etc. from each other thus estimating $s_{1,max}$ through the calibrated λ is the best solution.

The correspondence of the results is good for the calibration phase (Figure 5-3), since the analytical model can predict quite well the peak of the impact force and its time of occurrence. The trend over time of flow kinetic energy is traced in broad terms for both fixed and unfixed barriers.

The barrier kinetic energy is reproduced quite well during the acceleration phase, but a little worse during the reduction phase since the interaction calculated with MPM lasts longer.

Table 5-1. Mechanical properties

Flow-like landslide										Barrier	
ρ_m (kg/m^3)	n $(-)$	K_0 $(-)$	φ' (°)	c' (kPa)	E' (MPa)	ν $(-)$	k_{sat} (m/s)	μ_L (Pas)	K_L (MPa)	ρ (kg/m^3)	tan (δ_b) $(-)$
1800	0.5	0.66	20	0	2	0.25	10^{-4}	10^{-3}	30	2000	0.29

Table 5-2. Selected parameters for calibration of the analytical model through MPM simulations

	Flow type landslide				Barrier	
	n (-)	*h (m)*	*V_1 (m^3/m)*	*$v_{1,0}$ (m/s)*	*m_2/m_1 (*) (-)*	*β (°)*
Case 1	0.5	3	45 (i=3)	10	1.10	60
Set I	0.3	3	45 (i=3)	10	0.94	60
Set IIa	0.5	3	45 (i=3)	15	1.10	60
Set IIb	0.5	3	45 (i=3)	20	1.10	60
Set III	0.5	3	63 (i=5)	10	0.80	60
Set IV	0.5	3	45 (i=3)	10	1.10	80
Set V	0.5	4	48 (i=1)	10	0.73	60

(*) $m_2/m_1 \rightarrow \infty$ for fixed barriers

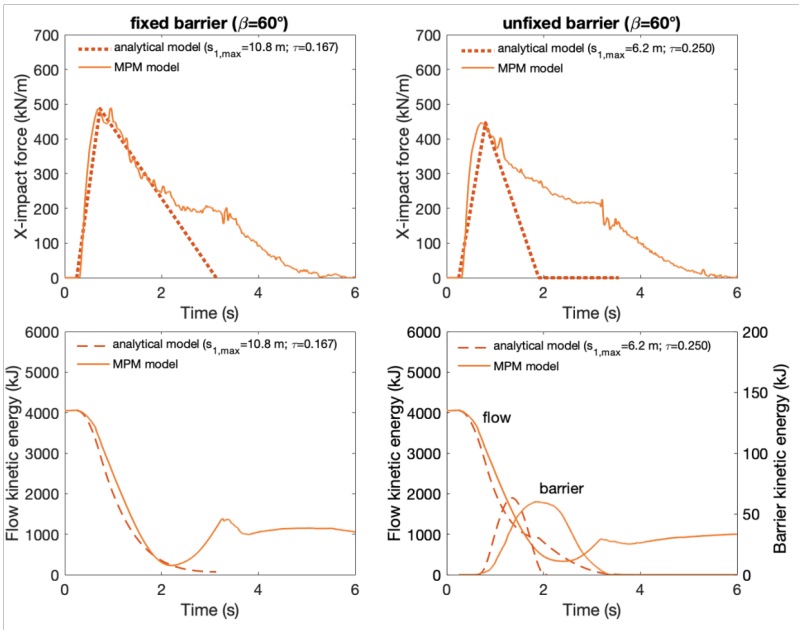

Figure 5-3. Example of calibration of the analytical model through MPM simulations (case 1 in Table 4-8)

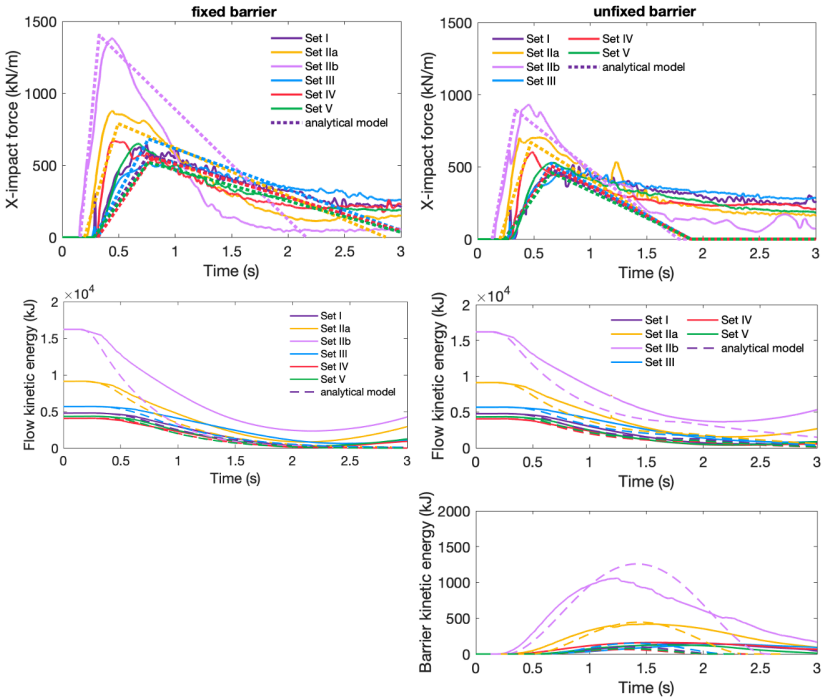

Figure 5-4. Validation results of the analytical model through MPM simulations (cases in Table 5-2)

5.1.3 Validation

To quantify the confidence in the predictive capability of the model, a validation assessment is needed. Considering the impact scenarios used in the above-mentioned analyses, Figures 5-5 and 5-6 show the comparison between MPM and the proposed analytical model in evaluating the most representative quantities in an *LSI* analysis. This can be compared to a validation of the analytical model for the evaluation of T_2 and $E_{k,1}(T_1)$ based on the calibration of F_{peak} and T_1.

It emerges a general agreement among the models, considering both fixed and unfixed barriers. Figure 5-5 shows that the proposed analytical model for fixed artificial barriers predicts quite well the peak impact force with a slight underestimation in some cases. The other quantities (T_1, T_2 and $E_{k,1}(T_1)$) are also characterized by a good match, apart from Set IIa and Set IV that give an overestimation for T_1, T_2 and an underestimation of $E_{k,1}(T_1)$) indicating that the flow velocity and the inclination β are less predicted.

For unfixed barriers (Figure 5-6), there is a high correspondence in terms of F_{peak}, T_1 and $E_{k,1}(T_1)$ for all the scenarios. Even the maximum kinetic energy of the barrier $E_{k,2,max}$ is predicted quite well, apart from Set I and Set IV where the MPM simulations gives higher results. This means that the porosity n and the inclination β are the most influential parameters when evaluating $E_{k,2,max}$ with the analytical model. About the time T_2 and the flow energy $E_{k,1}(T_1)$, the analytical solutions give an underestimation of the MPM results. This is mainly linked to the inability of this analytical model in considering the hydro-mechanical coupling and large deformations within the flow, which play a crucial role during the interaction with the obstacle.

The proposed analytical model is applied to interpret a large dataset of real observations of flow-type landslides measured through a permanent monitoring station. The field dataset from Hong et al. (2015) includes thickness, density, channel width, volume of discharge, velocity and impact forces recorded in real time during debris flow events.

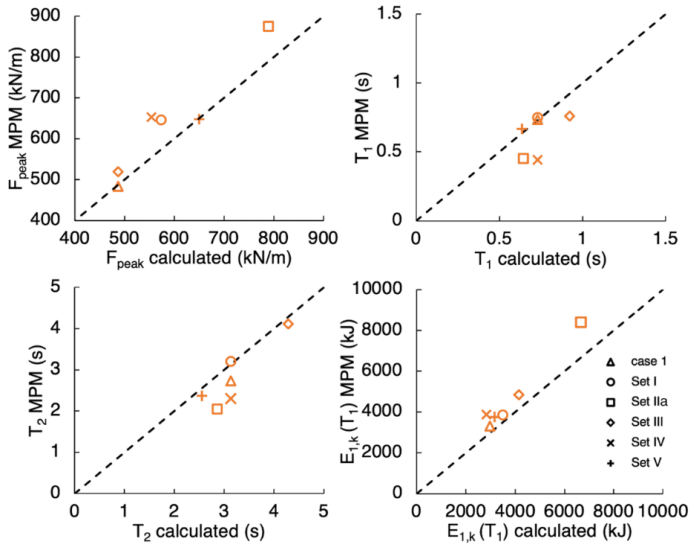

Figure 5-5. Comparison of MPM and analytical model for the cases of fixed barriers

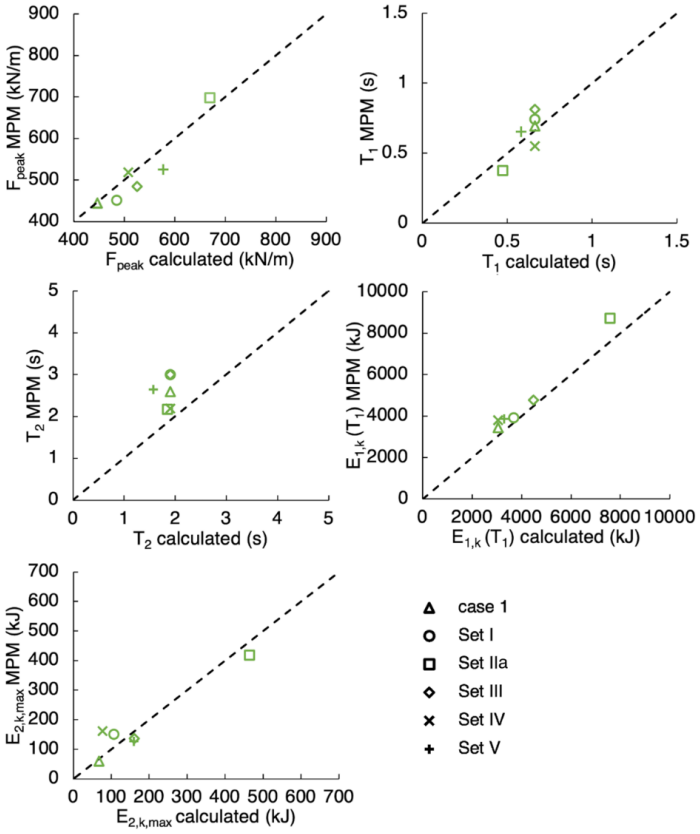

Figure 5-6. Comparison of MPM and analytical model for the cases of unfixed barriers

The data are relative to 139 historical events that took place between 1961 and 2000 in the Jiangjia Ravine basin, located in the Dongchuan area of Yunnan Province in China (Zhang and Xiong, 1997; Kang et al., 2007; Hong et al. 2015). The bulk density ranges from 1600 to 2300 kg/m^3 with fluid concentration ranging from 0.15 to 0.6. The dataset is well suited for the validation purpose as it has a wide range of values: $v_{1,0} = 3 - 14\ m/s$, $h = 0.2 - 2.7\ m$, $V_1 = 269 - 1.75 \cdot 10^6\ m^3$ and $p_{peak} = 14 - 435\ kPa$.

The parameters needed to compute the impact pressure through the analytical model are K_1, q_1 (Eq. 5-13) and $p_{peak} = q_1 \sqrt{s_{1,max}}/h$ (obtained from Equation 5-7). The quantity $s_{1,max}$ is calculated for each flow data as $\lambda L_{1,0}$, using the value $\lambda = 0.72$ calibrated in the case of fixed barriers. The flow length $L_{1,0}$ is obtained dividing the measured volume of discharge by the impact area (which is the product of the channel width and the flow thickness).

The validation results are reported in Figure 5-7 and show a good correspondence with the field data. A slight overestimate is achieved especially for high impact pressures. The application of the numerical MPM model is beyond the scope this study, while it could be a future development of the research.

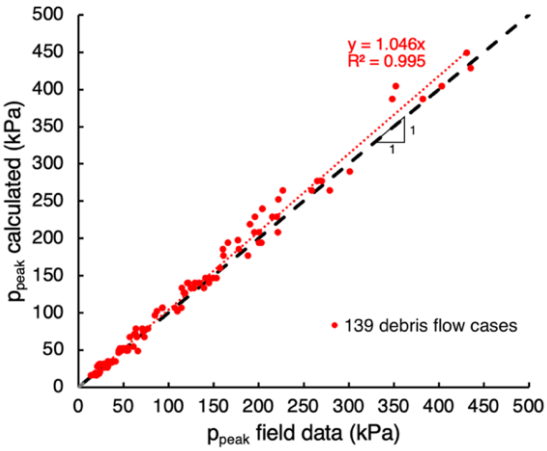

Figure 5-7. Application of the proposed analytical model to the large field dataset (139 cases) collected by Hong et al. (2015).

5.1.4 Discussion

A comparison between the presented models is necessary to assess their strengths and weaknesses in analysing Landslide-Structure-Interaction.

MPM is an advanced numerical method and has proved to be reliable in predicting the impact force trend over time. Moreover, unlike field evidence or laboratory tests, the numerical results provide additional features, through the computation and time-space tracking of different quantities, such as stress, strain, pore pressure, solid and liquid velocities, which cannot be easily monitored or obtained in the field.

Particularly focusing on *LSI*, MPM has many advantages. Primarily, it allows considering all such important aspects of the saturated flows, i.e., hydro-mechanical coupling and large deformations during propagation and impact. It was observed, in fact, that the presence of a liquid phase inside the flow can lead to different impact regimes in respect to dry granular flows, highlighting the importance of considering the solid-fluid interaction in the analyses. The accurate knowledge of the impact mechanism and so the evolution of flow depth and velocity is crucial for the design of mitigation countermeasures. For example, the accurate estimate of the length of the vertical jet must prevent that the retaining structure is overtopped by the flow, thus being ineffective. However, MPM suffers of some limitations, such as the high computational cost and until now the difficulty of being available in engineering practice.

Analytical and empirical models are more immediate and easier to use than MPM, and thus they could be preferable in the assessment of the *LSI* problems for design purposes.

The proposed analytical model is finally compared to some empirical formulations available in the scientific literature (Figure 5-8). The empirical models have been classified into three groups: (i) hydro-static models, which require only flow density and thickness for evaluating the maximum impact pressure; (ii) hydro-dynamic models, based on flow density and the square velocity of the flow; (iii)

mixed models, that include both information about the static and the dynamic component of the flow. The latter group is preferable, thus the chosen empirical formulations are all taken from group (iii): Hübl and Holzinger (2003), Armanini et al. (2011), Cui et al. (2015) and Vagnon (2020).

The large dataset used for the comparison includes 139 debris flow cases (from Hong et al. 2015) already considered in paragraph 4.3. The proposed analytical model reports the highest correspondence among the real data and the computed values, also with a slight safe-side overestimation in the computed values. The empirical models of Armanini et al. (2011) and Vagnon (2020) are also acceptable with a contained dispersion of the calculated values and with a overestimate coefficient of 1.61 and 1.35, respectively. The formulations proposed by Hübl and Holzinger (2003) and Cui et al. (2015) are, in contrast, characterized by a quite relevant variability of the achieved results. In particular, the method proposed by Cui et al. (2015) even leads to underestimate the peak values of impact pressure of about 7%. More in general, while the empirical models require as input data only the flow density, thickness and velocity, they can be used only for the design of fixed barriers, while not for DGRBs that are a promising landslide protection measure. The latter is instead well captured by both the proposed models, the MPM-based model and the energy-based analytical model.

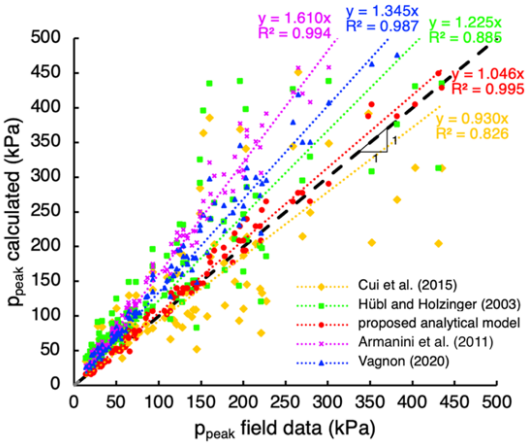

Figure 5-8. The proposed analytical model compared to some empirical models available in the scientific literature

5.1.5 Conclusions

The study has introduced and compared analytical and numerical MPM models to analyse the impact of flow-like landslides against artificial barriers, focusing not only on the evaluation of the peak impact forces but also on the kinematics evolution of both flow and barrier.

A conceptual model for the *LSI* problem was firstly introduced to better focalized the main variables that govern the dynamics of the impact process. This model was then implemented inside a numerical (MPM) model and a new proposed analytical impact model.

For each model, the governing formulation was described, and a parametric analysis was conducted through some demonstrative examples. In this way, the influence of the model parameters on the impact force and kinetic energy trends has been investigated.

Specifically, for the MPM numerical model a parametric analysis was conducted to highlight the wide range of impact scenarios that can be examined, considering all the main aspects in *LSI* issues, such as hydro-mechanical coupling, large deformations and the presence of multi-materials. Different types of barriers and MPM formulations were also used to understand their influence on the temporal trend of impact force, flow kinetic energy and kinematics of unfixed barriers.

Then, a calibration and validation of the analytical model with MPM outcomes was conducted to better monitor the most influential quantities for *LSI* problems, setting their values within the typical ranges for flow-type landslides.

The achieved results reported that for the analytical model all the formulations depend on the calibrated parameter λ, which is found to be equal to 0.72 for fixed barrier and 0.41 for unfixed barriers.

The validated analytical model was applied to a real field dataset collected at Jiangjia Ravine (China), to check their predicting capability. The achieved results are encouraging, showing a high correspondence between analytical results and the measured field data.

A discussion on strengths and limitations of the two proposed models was conducted and can summarized as follows:

1. MPM is an advanced numerical model and referring to *LSI* problems can handle a wide range of variables for both flow and barrier. Apart from this, MPM is a comprehensive method that allows to simulate the entire process of a landslide, from triggering to final deposition. This aspect is particularly important when studying the impact of a landslide against a protection structure since the main weakness of analytical and empirical models is the pre-setting of the flow depth and velocity. The latter parameters are particularly difficult to predict or measure during debris flow event, leading to a high uncertainty of the models. However, the high computational cost and its limited diffusion until now to the research field leaves its use to a small group of engineers.
2. An analytical model can be preferable in practice for designing fixed or unfixed barriers that must resist under the impulsive action of flow landslide. Its strong point is principally the simplicity in computing the main principal quantities in the context of *LSI*. In addition, it furnishes a not exaggerated overestimate of the peak impact pressures compared to those measured in the field.

In conclusion, the models proposed in this study show a good capability to predict the impact dynamics and kinematics of *LSI*. Further measured field data obtained for both fixed and unfixed artificial barrier will be helpful to improve the predictability of the two proposed models. This can be achieved only by monitoring barriers systems against real flow-like landslides, with the final goal of helping to design artificial protection barriers with increasing level of safety and reliability.

5.2 Empirical model

5.2.1 Formulation

In a simplified approach, the landslide mass is here schematized as an equivalent solid-like body, rectangular, with mass m_1, length L_1, depth h, unitary width, density ρ_m, initial velocity $v_{1,0}$ and it is supposed to be completely stopped by the barrier (i.e., $v_1(T_2) = 0$). The latter is assumed as fixed to the base ground and indefinitely high, thus all the landslide volume is supposed to be retained by the barrier.

Based on the previous studies (Hungr et al., 1984; Scotton and Deganutti, 1997; Kwan, 2012), the peak lateral force F_{peak} (Equation 5-27) exerted by the flow on the obstacle is calculated as the sum of a dynamic component $F_{peak,dyn}$ (Figure 5-9a) and a height-dependent static component $F_{peak,stat}$ (Figure 5-9b), as reported in Equations 5-28 and 5-29, respectively.

$$F_{peak} = F_{peak,dyn} + F_{peak,stat} \tag{5-27}$$

$$F_{peak,dyn} = \alpha \rho_m v_{1,0}^2 h \tag{5-28}$$

$$F_{peak,stat} = \frac{1}{2} \kappa \rho_m g h^2 \tag{5-29}$$

The empirical coefficient α has a wide range of values, ranging from 0.4 to 12 in the literature (Vagnon et al., 2020), while the empirical static coefficient κ ranges from 9 to 11 as reported by Armanini (1997) or in the range 3-30 as observed by Scheidl et al. (2013) for $Fr < 3$. This static coefficient is suggested to be assumed equal to 1 (Ng et al., 2021) for saturated flows that are fluidized due to the increasing pore pressure inside the landslide. In the present paper, the coefficient α is calibrated based on the MPM simulation of a selected set of realistic cases.

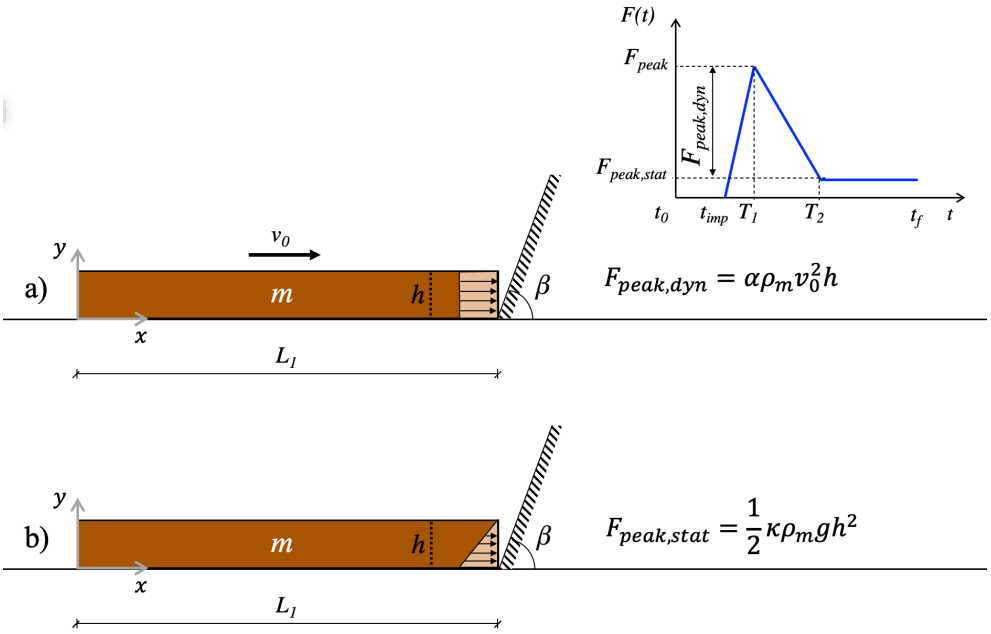

Figure 5-9. Schematic of the impact problem in the proposed empirical model

The landslide kinetic energy during the impact process is derived from its velocity variation over time until the impact process finishes (T_2). From the impulse theorem (Equation 5-30), where the impulse of the impact force is equal to the variation of linear momentum, the link between the impact pressure and velocity variation is obtained. Since the time-trend of the impact force is a piecewise function, the equations system reads as in Equation 5-31.

$$I = \int_0^{T_2} F\,(t)dt = \int_{v_{1,0}}^{0} m_1\,dv \tag{5-30}$$

$$F(t) = \begin{cases} F_{peak}\,t/\,T_1 & 0 < t < T_1 \\ F_{peak}\left[1 - \left(F_{peak,dyn}/F_{peak}\right)\,(t - T_1)/(T_2 - T_1)\right] & T_1 < t < T_2 \end{cases} \tag{5-31}$$

The reduction in landslide velocity is obtained from Equation 5-32, by solving the integrals in Equation 5-31 and replacing the term $F(t)$ with Eq. 5-31. Thus, the flow velocity over time (Equation 5-33) and the corresponding kinetic energy

(Equation 5-34) can be computed.

$$\Delta v(t) = \begin{cases} \frac{F_{peak}}{2m_1 T_1} t^2 & 0 < t < T_1 \\ \left[\frac{F_{peak}}{m_1} + \frac{F_{peak,dyn} T_1}{2m_1 (T_2 - T_1)}\right] t - \frac{F_{peak,dyn}}{2m_1 (T_2 - T_1)} t^2 & T_1 < t < T_2 \end{cases} \quad (5\text{-}32)$$

$$v_1(t) = v_{1,0} - \Delta v_1(t) \quad (5\text{-}33)$$

$$E_{k,1}(t) = \frac{1}{2} m_1 \, {v_1}^2(t) \quad (5\text{-}34)$$

The impact period T_2 is obtained from the application of the impulse theorem, since the integral over time of the impact force (i.e., the impact impulse) is equal to the variation of linear momentum of the landslide (Equation 5-30). The left side of Equation 5-30 can be rewritten as reported in Equation 5-35, where the right side corresponds to the area subtended by the piecewise function reported in Equation 5-31 and plotted in Figure 5-9a. Once known T_2 through Eq. 10, T_1 can be achieved in Eq. 11 by fixing the ratio $\tau = T_1/T_2$ (for example from experimental evidence).

The impulse of the impact force can be rewritten in terms of impact pressure, and its formulation is reported in Equation 5-38. Once known T_2 through Equation 5-36, T_1 can be achieved in Equation 5-37 by fixing the ratio $\tau = T_1/T_2$ (for example from experimental evidence). The description of the impact dynamics is complete. Summing up, the model primary unknown is T_2, while the quantities α, κ and τ, must be calibrated/assessed.

$$\int_0^{T_2} F(t)dt = \frac{1}{2}\left(F_{peak} + F_{peak,stat} - \tau F_{peak,stat}\right) T_2 \quad (5\text{-}35)$$

$$T_2 = 2m_1 v_{1,0} / \left(F_{peak} + F_{peak,stat} - \tau F_{peak,stat}\right) \quad (5\text{-}36)$$

$$T_1 = \tau \, T_2 \quad (5\text{-}37)$$

Some examples are shown in Figure 5-10 to highlight the effect of α, κ and τ on impact force and kinetic energy trend over time. The input quantities of the model are: $L_1 = 15\ m;\ h = 3\ m;\ \rho_m = 1800\ kg/m^3;\ v_{1,0} = 10\ m/s$. For higher values of α the peak force increases, the impact time T_2 decreases and the reduction in flow kinetic energy is more rapid. This means that α can be interpreted as a measure of system deformability, since the decreasing of T_2 with α means that the system is stiffer.

The empirical coefficient κ has similar behaviour compared to α, since high values of κ result in large peak forces and short time T_2. However, the coefficient κ has a minor influence on the system response compared to the coefficient α and its determination is quite complicated. For this reason, the static component of the impact force could be disregarded ($\kappa = 0$), using only the coefficient α for the assessment of the impact scenario. For fluidized flows the assumption of $\kappa = 1$ is preferable (as suggested by Ng et al., 2021) therefore also this value will be employed for the calibration of the model.

Finally, the ratio τ governs the occurrence of the peak time, and thus the shape of the impact force trend. In terms of flow kinetic energy dissipation, the higher the ratio τ, the steeper the dissipation trend up to T_1 and the slower the energy reduction between T_1 and T_2. In a sense, the parameter τ can be interpreted as a measure of the impulsiveness of the impact loading.

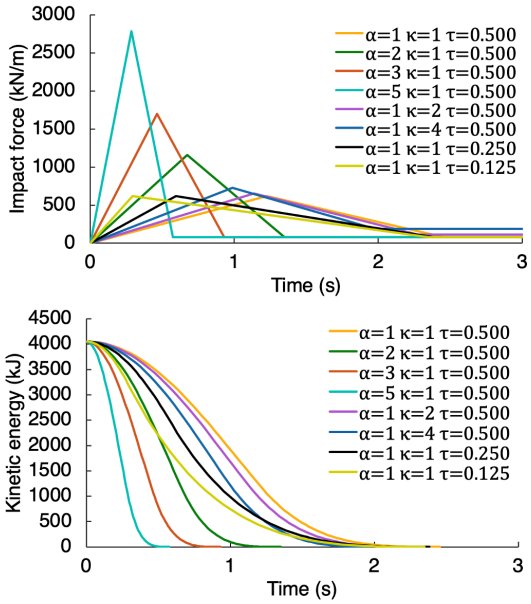

Figure 5-10. Dependence of the impact force and landslide kinetic energy on some model parameters

5.2.2 Calibration

The calibration of the empirical model principally focuses on the evaluation of the empirical coefficients α and τ. On the other hand, the static component of the impact force is not considered in the proposed method, due to its negligible influence and thus κ is assumed equal to zero.

The parameter τ is obtained by imposing the equivalence between T_I calculated from Equation 5-37 and T_I obtained from the MPM simulations.

The coefficient α relates to relevant features of the flow such as the grain size distribution, the barrier type and the flow-structure interaction mechanism such as the formation of vertical jet-like wave at the impact (Canelli et al., 2012). As reported in the literature, this parameter can vary in a wide range (between 0.4 and 12), often leading to an excessive overestimation of the design impact load. However, many authors (Hübl et al., 2009; Proske et al., 2011; Scheidl et al., 2013; Cui et al., 2015;

Vagnon, 2020) found a power law relationship between the coefficient α and the Froude number (Fr), as reported in Equation 5-38. The evaluation of the coefficients a_1 and a_2 requires at least two numerical simulations with different Froude number.

$$\alpha = a_1 Fr^{a_2} \tag{5-38}$$

The input scheme for the numerical simulation is the same used in Sect. 4.5, which considers the flow-like landslide and a rigid barrier fixed to the base. The chosen initial configuration of the landslide is characterized by a 45°-inclined front and a tail of length equal to three times the flow height. To consider different flow volumes, an i number of squares have been placed between the head and tail portions. Given this shape, the landslide has the same volume of an equivalent rectangular with the same height h and a length $L_m = (2 + i) \cdot h$, and unitary width.

The flow and barrier are modelled through the single-point MPM formulation, respectively with two-phase and one-phase formulations. The flow is a saturated mixture with linear distribution of initial pore-water pressure, and non-associative (zero dilatancy) elasto-plastic Drucker-Prager behaviour. The mechanical properties of the saturated flow mass with the barrier are the same reported in Table 5-1.

The data-sets used for the calibration of the model (Table 5-3) span over different values of flow porosity n, thickness h, volume V_1, initial velocity $v_{1,0}$ and the inclination β of the barrier impacted side.

Table 5-3. Selected parameters for calibration of the empirical model through MPM simulations

	Flow type landslide				Barrier
ID	n $(-)$	h (m)	V_1 (m^3/m)	$v_{1,0}$ (m/s)	β (°)
1	0.5	3	45 ($i = 3$)	10	60
1b	0.3	3	45 ($i = 3$)	10	60
2	0.5	3	45 ($i = 3$)	20	60
3	0.5	3	45 ($i = 3$)	10	90
6	0.5	3	45 ($i = 3$)	15	60
7	0.5	3	63 ($i = 5$)	10	60
8	0.5	3	45 ($i = 3$)	10	80
9	0.5	4	48 ($i = 1$)	10	60

Two calibration procedures were followed. The first neglects the static component of the impact force, thus the model can be considered purely hydro-dynamic. The other one assumes an empirical static coefficient κ equal to 1, that is more plausible for saturated flows. In the latter case, the peak impact force resulting from the MPM simulations was depurated of the static component ($0.5\rho_m g h^2$) for obtaining the dynamic one. The best fit values are $a_1 = 1.781$ and $a_2 = -0.515$ for $\kappa = 0$ (Equation 5-39) and $a_1 = 1.432$ and $a_2 = -0.365$ for $\kappa = 1$ (Equation 5-40). The calibrated value for τ is 0.14 for all the cases. The results show a good fitting with the $\alpha - Fr$ curve for all the impact scenarios, and it is relevant that also the trend over time of the impact force is reproduced quite faithfully for both. $\kappa = 0$ (Figure 5-11a) and $\kappa = 1$ (Figure 5-11c).

$$F_{peak} = 1.781 Fr^{-0.515} \rho_m v_{1,0}^2 h \tag{5-39}$$

$$F_{peak} = 1.432 Fr^{-0.365} \rho_m v_{1,0}^2 h + 0.5 \rho_m g h^2 \tag{5-40}$$

Besides achieving a good correspondence with the impact forces, the trend of flow kinetic energy was computed (Equation 5-34) for the impact scenarios (Figures 5-11b and 5-11c), giving for instance better agreement for the case 1 than the case 2. In the latter case, this is explained by the fact that the high energy of the flow produces a more elongated jet, which cannot be reproduced by a simplified empirical method. The flow kinetic energy computed via empirical method is always lower than that computed through MPM (apart from case 7). This is mostly linked to the simplifying hypothesis of neglecting the static component of the impact force. However, it is a safe side approximation, to be considered acceptable in the practice.

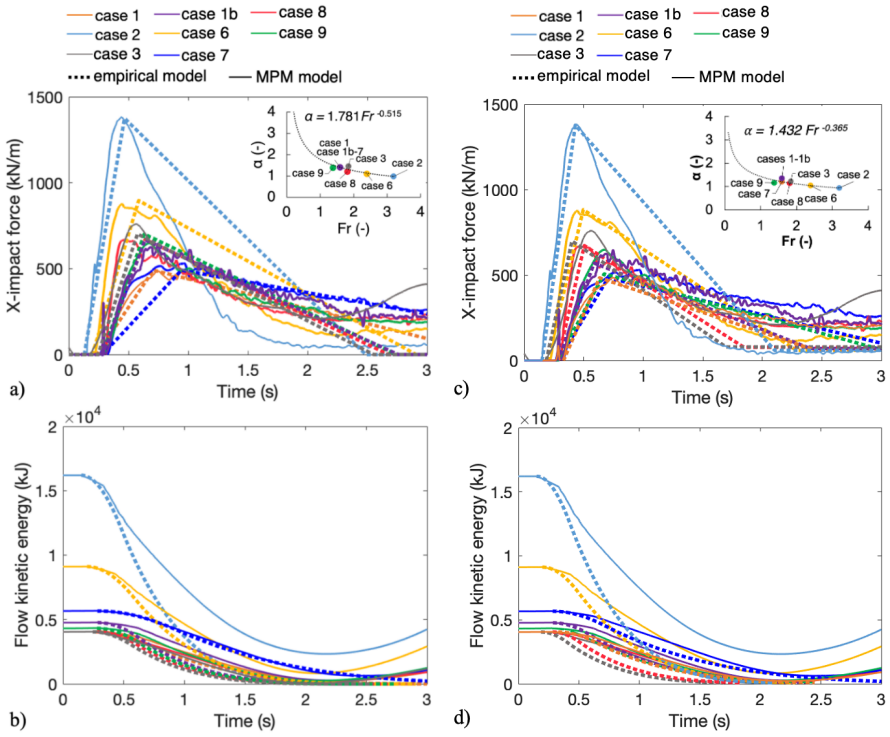

Figure 5-11. Calibration of the empirical model through the MPM simulations (for the cases in Table 2): impact force (a) and kinetic energy (b) time trend for κ=0 and impact force (c) and kinetic energy (d) time trend for κ=1

5.2.3 Validation

The impact scenarios used in the above-mentioned analyses are firstly used to compare the output of the proposed empirical method with the numerical results for the most relevant quantities in *LSI* analysis for the case with $\kappa = 0$ (Figure 5-12). A similar comparison for the case with $\kappa = 1$ was also performed with satisfactory results, and it is omitted here for the sake of the simplicity. Based on the above calibration, the F_{peak} and T_1 computed through the empirical method (Equations 5-28 and 5-37, respectively) fit very well the MPM numerical results for all the scenarios. On the other hand, as a first validation of the method, it is observed that the impact period T_2 (computed from Equation 5-36) is only slightly overestimated by the empirical method especially for those cases with higher velocities. In these

cases, the empirical method is not able to consider the amount of material which overtops the barrier. In fact, as the mass m_1 decreases, this material no longer contributes to the variation of the linear momentum of the landslide (Equation 5-30), therefore a lower value of T_2 is expected from Equation 5-36. The above is also confirmed by the simulation of the indefinite wall (case 3), where the overtopping of the barrier is not allowed, thus the time T_2 perfectly matches the MPM outcome. In this case, even the other calculated quantities correspond to those obtained from MPM since the indefinite wall most resemble the basic assumptions of the empirical model. For the evaluation of the flow kinetic energy at the peak impact force time, i.e., $E_{k,1}(T_1)$, the empirical formulation provides lower values than MPM for the cases with $v_{1,0} > 10\ m/s$,while there is an appreciable matching for the other cases. This is principally linked to the inability of the simplified proposed method to consider the hydro-mechanical coupling and large deformations within the flow, which play a crucial role during the interaction with the obstacle.

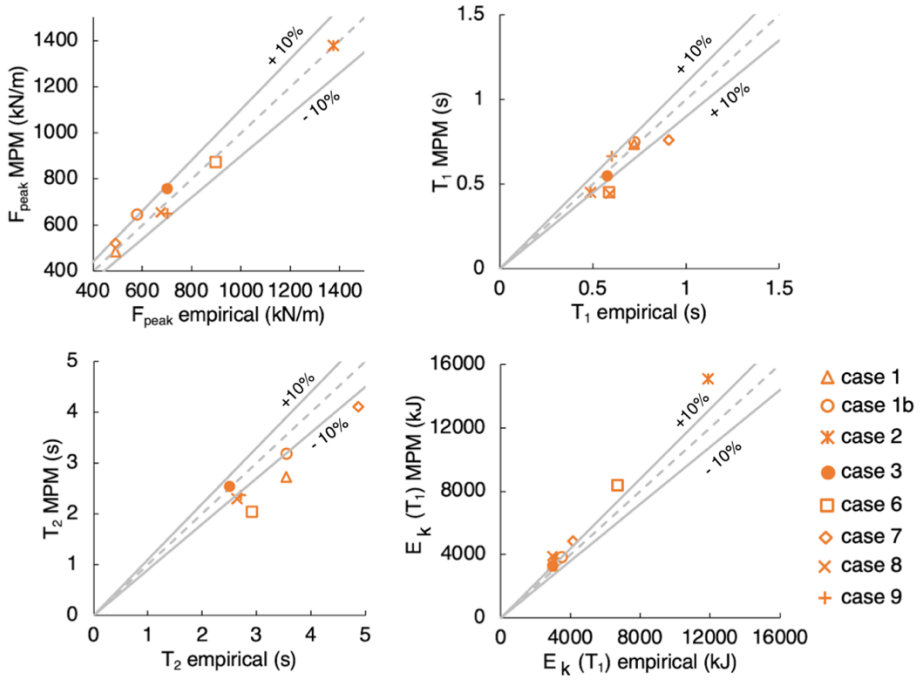

Figure 5-12. Comparison of MPM and proposed empirical model

The proposed empirical method is more thoroughly validated towards the interpretation of a large dataset of real observations of flow-type landslides, achieved through a permanent monitoring station. The field dataset from Hong et al. (2015) includes thickness, density, channel width, volume of discharge, velocity and impact forces recorded in real time during debris flow events.

The data are relative to 139 historical events that took place between 1961 and 2000 in the Jiangjia Ravine basin, located in the Dongchuan area of Yunnan Province in China (Zhang and Xiong, 1997; Kang et al., 2007; Hong et al. 2015). The bulk density ranges from 1600 to 2300 kg/m^3 with fluid concentration ranging from 0.15 to 0.6. The dataset is well suited for the validation purpose as wide ranges of the relevant features are considered such as: $v_{1,0} = 3 - 14\ m/s$, $h = 0.2 - 2.7\ m$, $V_1 = 269 - 1.75 \cdot 10^6\ m^3$ and $p_{peak} = 14 - 435\ kPa$.

The impact peak pressure is calculated through the calibrated power law for the peak force (Equation 5-40) as follows: $p_{\mathrm{peak}} = 1.432 Fr^{-0.365} \rho_m v_{1,0}^2 + \rho_m g h$. The results are reported in Figure 5-13 and show a very good correspondence with the field data, being the difference much less than 10% for most of the cases. . In particular, the empirical model predicts quite well the peak of impact pressure for low values but showing some dispersion for values higher than 150 kPa. The statistical distribution of the error, obtained as the difference between the computed value and the measured value, shows that the median value is 10.7 kPa and the 90th percentile value is 37.65 kPa. The application of the numerical MPM model to such a large field dataset is beyond the scope this paper, while it could be a future development.

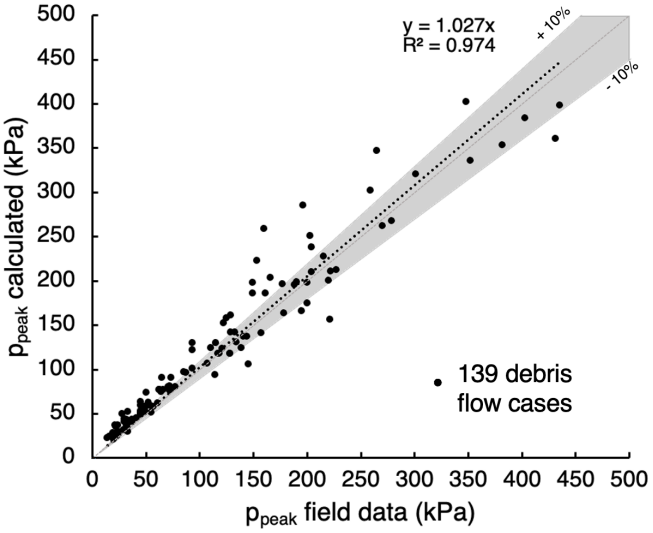

Figure 5-13. Application of the proposed empirical model to the large field dataset (139 cases) collected by Hong et al. (2015).

5.2.4 Discussion

A comparison between the presented methods is necessary to assess their strengths and weaknesses for analyzing Landslide-Structure-Interaction.

MPM is an advanced numerical method and has proved to be reliable in predicting the impact force trend over time. Moreover, unlike field evidence or laboratory tests, the numerical results provide additional features, through the computation and time-space tracking of different quantities, such as stress, strain, pore pressure, solid and liquid velocities, which cannot be easily monitored or obtained in the field.

Particularly focusing on *LSI*, many advantages come from using MPM. Primarily, it allows considering all such important aspects of the saturated flows, i.e. hydro-mechanical coupling and large deformations during propagation and impact. The accurate knowledge of the impact mechanism and so the evolution of flow depth and velocity is crucial for the design of mitigation countermeasures. For example, the accurate estimate of the length of the vertical jet must prevent that the retaining

structure is overtopped by the flow, thus being ineffective. However, MPM suffers of some limitations, such as the high computational cost and until now the difficulty of being available in engineering practice.

Empirical methods are more immediate and easier to use than MPM, since they provide an estimate of the impact quantities considering only the flow density, thickness and velocity as input and thus they could be preferable in the assessment of the *LSI* problems for design purposes.

The proposed empirical method is hence compared to some empirical formulations available in the scientific literature (Figure 5-14). The chosen empirical formulations are those of Hübl and Holzinger (2003), Armanini et al. (2011), Cui et al. (2015) and Vagnon (2020), all classifiable as mixed models. The large dataset used for the comparison includes 139 debris flow cases (from Hong et al. 2015) already considered in paragraph 4.3.

In terms of peak pressure, the results of the empirical models of Armanini et al. (2011) and Vagnon (2020) have a low dispersion in the plot of Figure 5-14, but with an overestimation of 61% and 35%, respectively. The formulations proposed by Hübl and Holzinger (2003) and Cui et al. (2015) are, in contrast, characterized by a quite relevant variability of the achieved results. The empirical model proposed in the present paper has the highest correspondence among the real data and the computed values, with a contained dispersion of the results. Some discrepancy of the results for very high velocities.

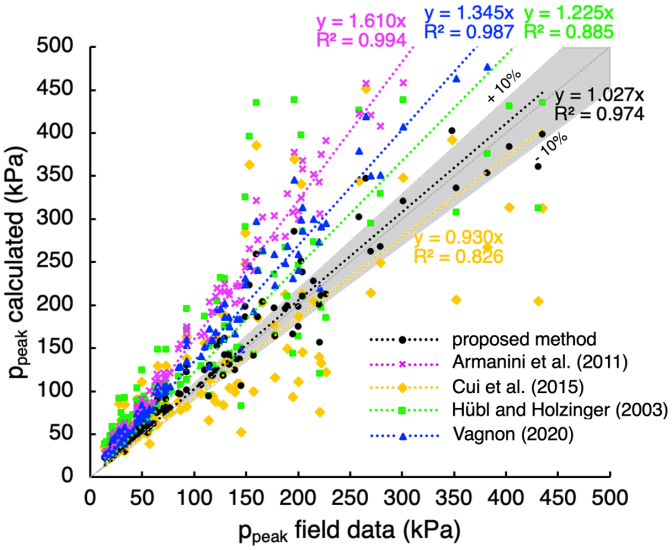

Figure 5-14. The proposed empirical method compared to some literature empirical methods

5.2.5 Conclusions

The present work proposed a conceptual framework and a numerical *MPM* model to analyse the impact of flow-like landslides against artificial barriers, focusing not only on the evaluation of the peak impact forces but also on the kinematics of the landslide during the whole impact process.

The conceptual framework for the Landslide-Structure-Interaction (*LSI*) problem has been then implemented inside the proposed methods: numerical (*MPM*) and empirical. Specifically, parametric MPM analysis has been conducted to highlight the wide range of impact scenarios that can occur considering all the main features of *LSI*, such as the hydro-mechanical coupling, the soil large deformations and the presence of multi-materials.

Then, a calibration of the new proposed empirical method was performed using the *MPM* outcomes was conducted. It was possible to derive a new $\alpha - Fr$ power law relationship to derive the peak impact pressure. This formulation is different

from those in the literature, which are typically calibrated on small-scale laboratory tests, thus giving an excessive overestimation in predicting the impact load that may results in a large increment of costs for structure construction.

Finally, the empirical method was validated referring to a vast dataset of real field evidence collected at Jiangjia Ravine (China). The achieved results are encouraging, showing a high correspondence between the output of the proposed empirical formulation and the measured field data. However, the estimated power law for the empirical model can lead to an underestimation of peak pressures for values above approximately 350 kPa, so it must be used with caution. Nevertheless, also the available literature methods are applied to the same database, and thus the advantages of the new method are outlined.

In conclusion, the models proposed in this study show a good capability to predict the impact dynamics and kinematics. Further research may be directed to an enhancement of the proposed empirical model considering the amount of material that can overtop the barrier, giving more accurate results for the analysis of the *LSI* problem.

6. Introducing two types of protection structures

6.1 Reinforced-Concrete (RC) walls

6.1.1 Introduction

The use of massive protection structures against flow-like landslides, has been pursued with concrete walls or blocks, or combinations of rigid-like vertical elements like baffles.

Reinforced Concrete (RC) walls are commonly used as defence measures in hilly areas to contain falling boulders and landslide debris, and the sliding displacement of these barriers is a key design issue when space is limited.

What is still challenging is: i) the assessment of hydromechanical interaction of the landslide body, which is a mixture of solid skeleton saturated with water; ii) to consider that the protection structure is always somehow deformable. Thus, a multiphase approach is needed and a large deformation formulation is fundamental to properly simulate the kinematic evolution of the flowing materials during the impact with the structure.

RC walls are usually made as slab concrete dams, that can be reinforced with counterfort (Figure 6-1). For such slender constructions, the flow impact dynamics must be carefully evaluated, as the wall must retain the flowing material without tilting or without showing excessive displacements. For these reasons, the foundations of these structures are particularly large. In bedrock, the foundations are usually made by steel tension anchors (ribbed bars), while in loose deposits, the ground must sustain the weight of the concrete construction together with the loads generating from the impact (Barbolini et al., 2009).

The design of these structures requires principally two requirements: i) geographical, geological and site conditions must be firstly considered; ii) the structural resistances must be always greater than the impact loads exerted on the structure. The barrier resistance can be easily evaluated from the resistance of each single component. By contrast, the correct estimation of the dynamic impact of the front of a debris flow against a structure is a key issue of its design procedure. In fact, although the dynamics of fluid-structure interaction is not completely understood yet, its role must be carefully evaluated to determine the possible ultimate limit states of the structure under impact.

Advanced numerical tools, such as Material Point Method, can be used in simulating those complex processes. The numerical model is here used to explore the response of RC protection structures under the impact of typical flow-like landslides. Several impact scenarios are considered, considering different geometries of the barrier and different flow velocities. Numerical simulation has proved to be a promising tool in verification of the structure design.

Figure 6-1. Example of concrete diverting dam at Odda, Norway (Barbolini et al., 2009)

6.1.2 Ultimate Limit States under impact

Failure analysis of protection structures under the impact of flow-like landslides is still an open issue in the structure engineering framework. An effective dynamic analysis method is still needed (Huang and Zhang, 2020), and a comprehensive knowledge is missing about the quantities from which these complex impact mechanisms depend on. Furthermore, the role of interstitial fluid inside the landslide body on the intensity and the time-dependency of the impact actions must be assessed. The different mechanisms of flow-structure interaction play a crucial role in assessing the possible Ultimate Limit States (ULS) of the structure under impact, therefore they must be considered. Advanced numerical analyses can help to fill these gaps.

RC walls are often used to prevent rockfall disasters, but their design methods (Lam et al., 2018; Yong et al. 2019; Yong et al. 2020) cannot be adopted for the design of concrete walls against flow-like landslides, since both load pattern and response of structures are totally different. Specifically, a single boulder exerts a concentrated load on the structure, whereas a flow induces both static and dynamic distributing loads on the barrier according to the predominant impact mechanism. As a consequence, the main path of energy dissipation is linked to the inelastic deformations of the flowing mass (Ng et al., 2021), unlike boulders that dissipate the impact energy through localized deformations of the structure (Huang and Zhang, 2020).

When considering the limit state philosophy, the Eurocode design approach can be adopted by satisfying the condition that the ultimate resistance R_u of the RC structure, computed as a function of the design strength of materials, must be higher than the design load effect E_d (Equation 1).

$$R_u \geq E_d \tag{1}$$

In the context of flow-like landslides impacting a concrete structure, the energy of the flow is transferred to the barrier, which can show different ULS: breakage,

horizontal shifting, tilting, bending of the stem wall, localized shear failure in the cantilever section (Figure 2). Complete breakage of the entire wall is the worst case because it is destroyed by the potential of the flow and therefore has nil protective action.

A free-standing barrier can show sliding movements (Figure 6-2a) or tilting (Figure 6-2b) under impact. In these cases, flow energy is dissipated through the movement of the barrier, therefore extensive structural restraints (e.g., piled foundations) for maintaining the barrier in static conditions are not needed. There are some formulations in the literature based on displacement approach for the prediction of barrier displacements in the case of boulder impacts (Lam et al. 2018; Yong et al. 2019), but the case of impact from flow-like landslides has not been studied in detail yet. To ensure that the structure remains fit for use with appropriate levels of reliability, the ultimate displacement Δ_u and rotation θ_u capacity must be higher than the corresponding displacements and rotations due to the landslide impact.

Another ULS concerns the bending behaviour of the vertical wall (Figure 6-2c), which can be evaluated through a force-based approach according to design practice (Kwan, 2012). When the bending moment generated by the landslide reaches the yielding moment of the stem M_u, the plastic deformations inside the joint between the stem and the foundation increase. The development of this plastic hinge depends on the intensity of the impact force and even on the strength of the wall, which in turns is determined by its cross-sectional area, concrete and steel bar strength, together with the strength of reinforcement and shear stirrups (Zeng et al., 2015).

The force-based approaches usually result in overestimated bending actions because of pre-defined quasi-static forces, which neglect the inertial effects and energy dissipation (Yong et al., 2019). A displacement-based model can be also adopted employing the principles of momentum and energy conservation, as done by Yong et al. 2020, who considered the combined actions of boulder impact and debris flow pressure as concentrated load. However, it would be advisable to take

into account the time trend evolution of the landslide impact pressure in order to obtain more sophisticated results.

Finally, the shear failure of the RC wall is related to the cases in which the damage is concentrated in the cantilever section of the column. The ultimate resistance shear T_u of the column is related to the tension failure of either the concrete or the steel stirrups.

However, the latter ULS cannot be reproduced using the current MPM code simulations due to the limitations of the 3-node element that suffers from shear locking, thus the latter ULS will not take into consideration (for more details see Al-Kafaji, 2013). Moreover, the tilting failure mechanism is not investigated, due to numerical limitation of the current MPM code in simulating large rotations of objects surrounded by contact surface.

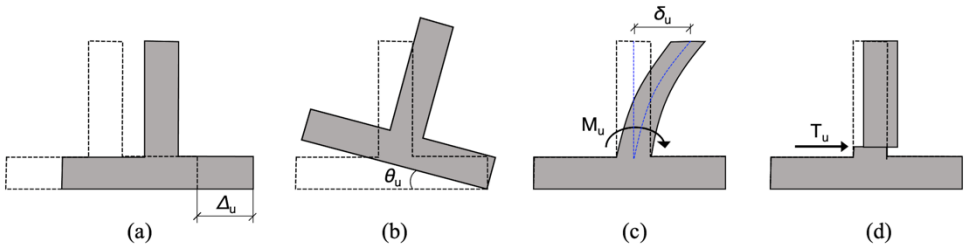

Figure 6-2. Different types of failure for a concrete wall impacted by a flow: (a) horizontal shifting, (b) tilting, (c) bending of the stem wall, (d) localized shear failure in the cantilever section

6.1.3 MPM modelling

Input schemes

To schematize the problem in a realistic way, multiple materials are considered such as: the flow-like landslide, the RC wall and the base soil. The latter is necessary to ensure the frictional contact at the base of the moving barrier (Figure 6-3).

The chosen initial configuration of the landslide is the same proposed in paragraph 4.5, characterized by a 45°-inclined front and a tail of length equal to three times the flow height. The build-up of excess pore pressure in the flow material

during the impact is considered as well as the hydromechanical coupled behaviour and the yield criterion of the flow material. Although simplified, the landslide scheme resembles its main characteristics such as velocity, impact height, non-zero interstitial pressures, with the geometric details shown in Table 6-1.

The flow is a saturated mixture with linear distribution of initial pore-water pressure, and non-associative (zero dilatancy) elasto-plastic Drucker-Prager behaviour.

The RC wall is a dry material, with frictional contact at base and elasto-plastic behaviour. A foundation platform of concrete is also considered as a base for the wall, analysing several barrier geometries (Table 6-3).

The material properties used in the study were determined by Ardiaca (2009) from some design regulations, considering the concrete with a characteristic compressive strength of 25 MPa.

The soil-concrete interface is handled with a frictional contact, imposing a coefficient ($tan\delta_b / tan\varphi'_{base}$) equal to 0.67 (Canacki et al., 2016; Ilori et al., 2017). The mechanical properties of both saturated flow mass and RC wall are reported in Table 6-2.

The numerical MPM analyses allow the simultaneous simulation of flow propagation and flow-structure interaction. The computational unstructured mesh is made of 17249 triangular 3-noded elements with dimensions ranging from 0.30 to 1.00 m. The flow and barrier are modelled through the single-point MPM formulation, respectively with 2-phase and 1-phase. There is no contact interface between the wall and the flow due to the limitation of the current MPM code in simulating large deformations in presence of contact surface. This means that some drainage could occur along the impacted barrier side.

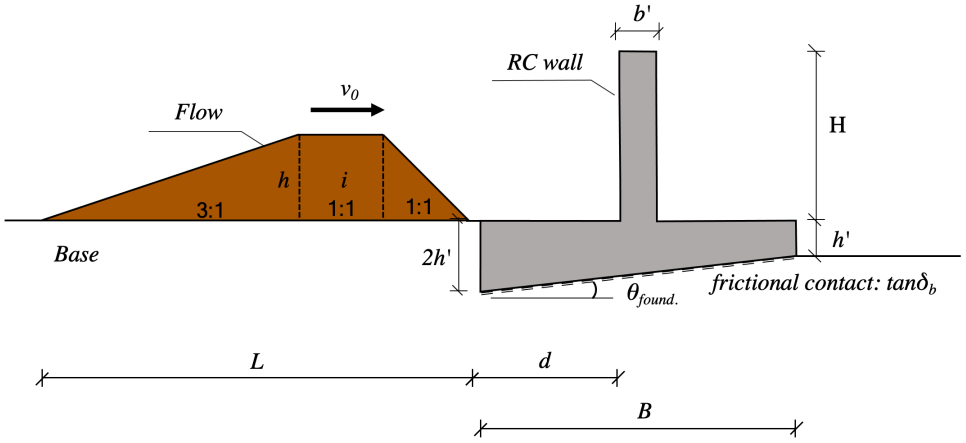

Figure 6-3. Geometric schematization for the LSI numerical simulations with RC walls

Table 6-1. Geometric characteristics of the flow-like landslide

L_l (m)	L_m (m)	i (-)	h (m)	V_l (m^3/m)
21.00	15.00	3	3.00	45.00

Table 6-2. Mechanical properties

Flow-like landslide										
ρ_m (kg/m^3)	n ($-$)	K_0 ($-$)	φ' (°)	c' (kPa)	E' (MPa)	ν ($-$)	k_{sat} (m/s)	μ_L (Pas)	K_L (MPa)	$v_{0,l}$ (m/s)
1800	0.5	0.66	20	0	2	0.25	10^{-4}	10^{-3}	30	5−10

RC wall						
ρ (kg/m^3)	$\tan(\delta_b)$ ($-$)	φ' (°)	c' (kPa)	σ_t (kPa)	E' (MPa)	ν ($-$)
2500	0.24	35	510	750	30000	0.25

Table 6-3. Different RC wall geometries

ID	$\theta_{found.}$ (°)	d (m)	B (m)	b' (m)	H (m)	h' (m)	V (m^3/m)	M (kg)
1	0	3.00	6.00	1.20	6.00	1.20	14.4	36700
2	11.3	3.00	6.00	1.20	6.00	1.20	18.0	45870
3	0	3.00	11.00	1.20	6.00	1.20	20.4	52000
4	6.2	3.00	11.00	1.20	6.00	1.20	27.0	68800
5	0	3.00	6.00	1.80	6.00	1.20	18.0	45870
6	11.3	3.00	6.00	1.80	6.00	1.20	21.6	55040
7	0	3.00	11.00	1.80	6.00	1.20	24.0	61160
8	6.2	3.00	11.00	1.80	6.00	1.20	30.6	78000

Numerical results

Selected results are shown as the spatial distribution of displacements at the final time lapse of the impact process, for all the different schemes of Table 6-3. Firstly, a flow with high kinetic energy is considered (Figure 6-4), thus the influence of the different barrier geometries is pointed out especially focusing on the thickness of the stem wall and on the foundation size. In fact, if the wall is characterized by a low ratio of b'/H (Figure 6-4a) the breakage of the wall is more accentuated than the cases of a thicker wall (Figure 6-4b), as understandable by the internal shear deformations and the maximum displacement of the wall. Particularly, a thin wall always exhibits some rotation (failure mechanism of Figure 6-2c), with the formation of a plastic hinge at the base of the stem column. However, this mechanism is specifically present for large foundation platform since the wall displacements at the end of the impact are smaller and so the only ULS is the failure due to the bending of the vertical wall. A thick wall significantly reduces the presence of a bending ULS, as reported in Figure 6-4b, apart from the case with an inclined foundation, where the total immobility of the barrier favours the bending failure instead of a horizontal shifting mechanism. It is therefore clear that the correct design of the barrier requires a coexistence of the two mechanisms (shifting and bending) in a way that the barrier does not move too far, and the vertical wall does not bend too much (as happened for case 6).

Completely different is the case of a landslide with lower velocity (Figure 6-5), where all the barrier geometries can withstand the potential of the flow. However, the cases 1 and 5 exhibits large displacements, not allowable for a correct design. Moreover, the inclined foundation makes the barrier like fixed to the base, but attention must be paid to the thickness of the stem (case 4).

Another interesting characteristic of these kind of protection structure is that for all the cases without a complete breakage of the wall the amount of flow material that exceed the barrier is very few, therefore the effectiveness of stopping the propagation of all the landslide material is very high.

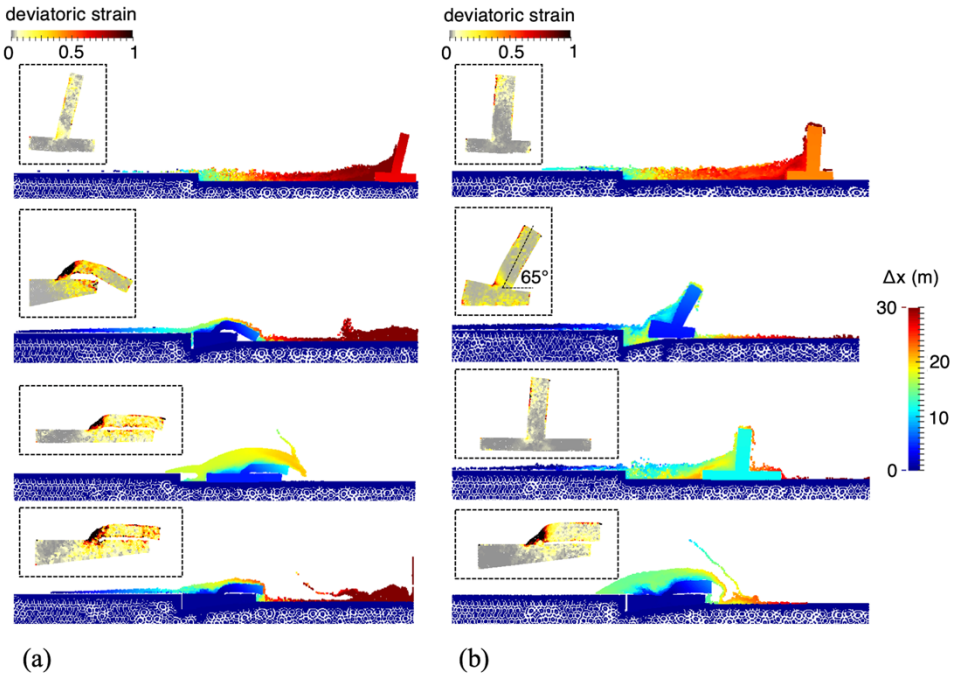

Figure 6-4. Spatial distribution of displacements at final impact time for v_0= 10 m/s: (a) cases 1-2-3-4 (b'/H=0.2); (b) cases 5-6-7-8 (b'/H=0.3).

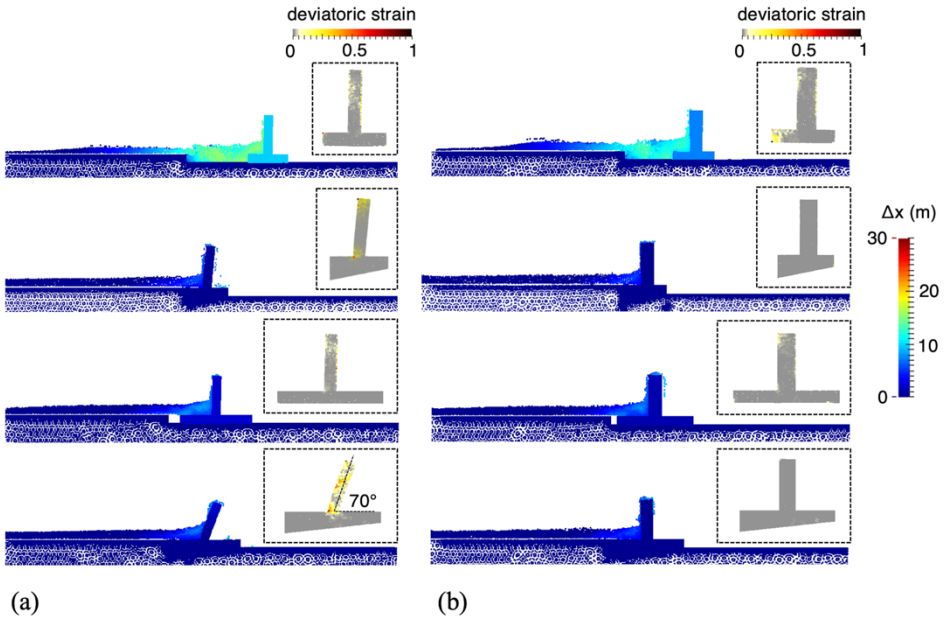

Figure 6-5. Spatial distribution of displacements at final impact time for v_0= 5 m/s: (a) cases 1-2-3-4 (b'/H=0.2); (b) cases 5-6-7-8 (b'/H=0.3).

In more details, the temporal trend of kinetic energy and the amount of work done by the frictional force can be traced for all the scenarios (Figure 6-6).

After the impact with the barrier, the kinetic energy of the flow is totally dissipated in the cases with a perfectly functional wall (cases 2-3-4-6-7-8 with v_0= 5 m/s) or partially transferred to the barrier because of its movement for the cases with significant horizontal shifting.

Interesting is the kinetic energy trend in cases where breakage of the wall occurs. In fact, the kinetic energy diverts its gradual decrease showing a secondary peak. The occurrence of this secondary peak coincides with the moment of failure of the stem and also with the achievement of the maximum work produced by the friction at the base of the barrier.

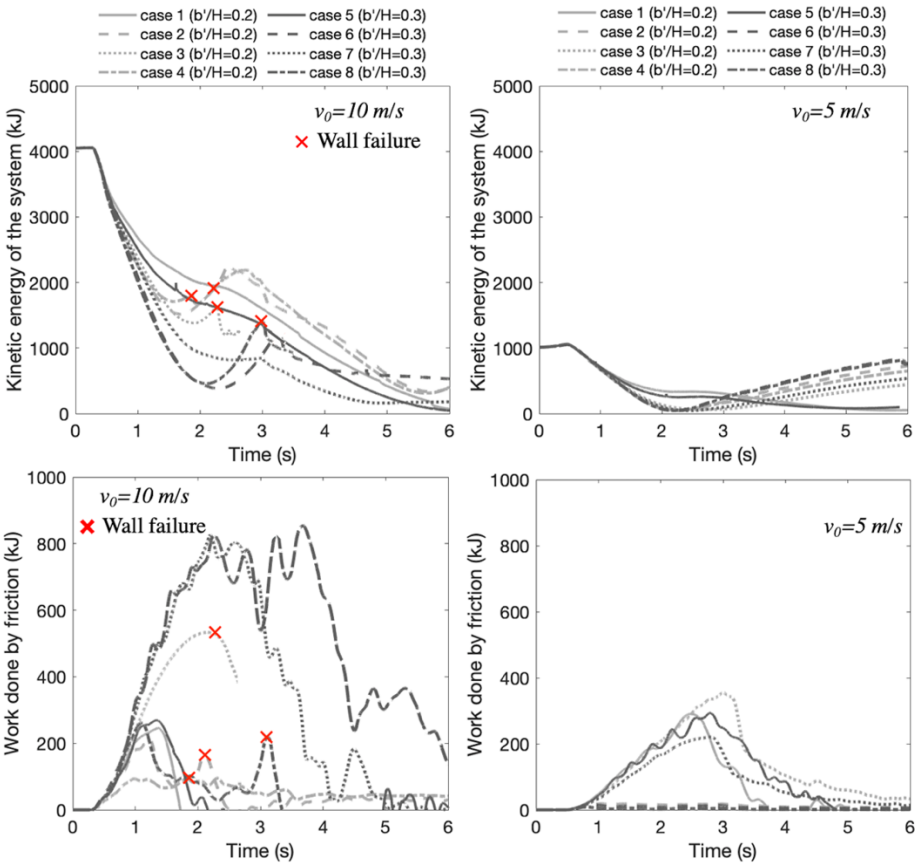

Figure 6-6. Temporal trend of kinetic energy and work done by friction for all the RC wall geometries

To correlate the most relevant quantities obtained from all the simulations, the efficiency diagram of Figure 6-7 is proposed. The ratio between the kinetic energy and its initial value represents the fraction of initial kinetic energy that can be achieved after impact, while the ratio between the barrier displacement Δ and the acceptable value Δ_u (assumed equal to 5 m for convenience) configure a barrier efficiency zone in the diagram. It is immediately comprehensive that all the cases with v_0=10 m/s are unacceptable geometries (expected for case 6), whereas the cases 2-3-4-6-7-8 have an efficient barrier configuration if the flow has v_0=5 m/s.

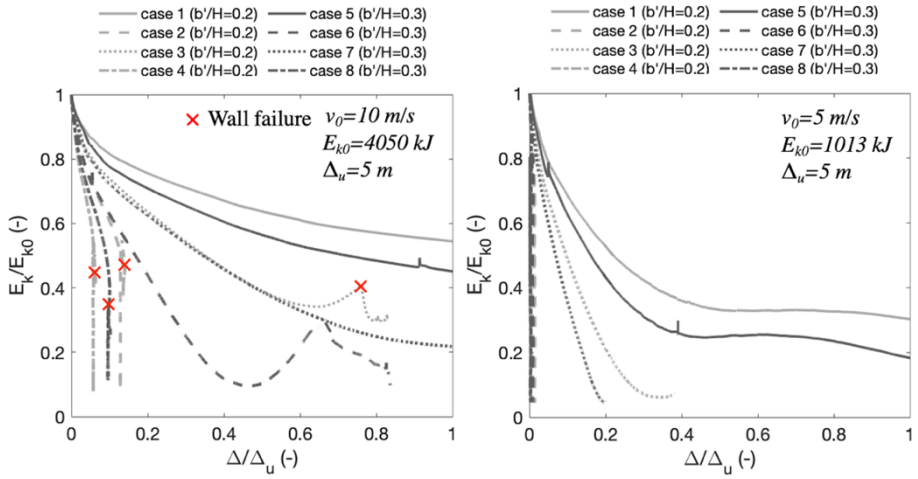

Figure 6-7. Efficiency diagram of the RC barrier for all the considered scenarios

6.1.4 Discussion

The MPM numerical simulations provide new insights in understanding the type of failure mechanisms that a RC protection wall can undergo following the impact of flow-like landslides, related to the many physical properties (e.g., strain, velocity, kinetic energy, among other quantities) that can be accurately computed either in space or time.

Summing up all the achieved results, Figure 6-8 shows the type of failure mechanism related to the variation of v_0, b'/H and B/H. The chosen colour palette

indicates that a combination of shifting and bending mechanisms represents the worst scenario, but the bending failure is somehow worse than the shifting mechanism.

It is immediately noticeable that a flow with relatively low velocity causes less damage to the structure, especially for higher values of *b'/H* and *B/H* (top right corner of the diagram). In contrast, the RC barrier cannot withstand to the potential of a faster flow, especially for lower values of *b'/H*. Moreover, for the lowest value of *B/H* the ULS is always represented by a horizontal failure mechanism. When the ratio *B/H* increases, the bending failure is predominant than the shifting, especially for the cases with inclined foundation. In general, an inclined foundation always avoids the onset of failures due to high horizontal shifting, while a flat foundation platform allows the formation of both ULS of the barrier.

Regarding the amount of volume that is retained by the RC wall, the whole initial flow volume is completely stopped by the structure for all the cases with low kinetic energy of the landslide. For v_0=*10 m/s* the efficiency of the barrier in stopping the propagation of the flow is ensure for flat foundation with *B=H*, but the final displacement of the barrier is excessive.

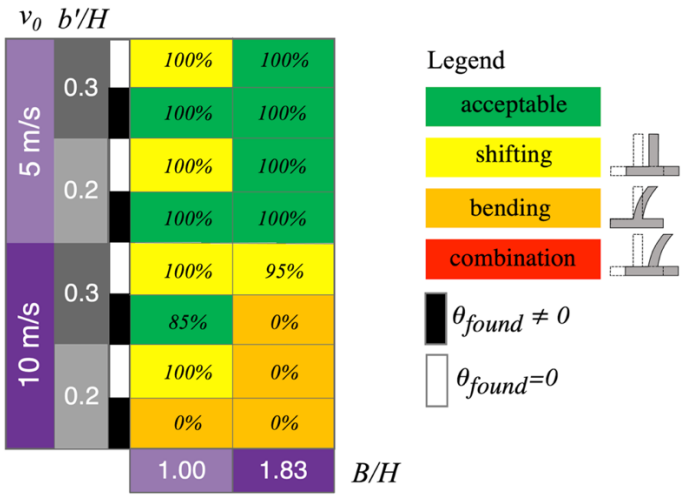

Figure 6-8. Comparison between all the considered scenarios in terms of ULS for RC walls (in the coloured cells the percentage of landslide volume blocked behind the RC wall)

6.1.5 Conclusions

In this paragraph, it was showed the potential of an advanced numerical method such Material Point Method (MPM) in simulating the impact mechanisms of saturated flows against RC barriers, providing novel insights in understanding the ultimate failure mechanisms that the barrier can undergo.

First, the problem has been schematized and the potential flow-obstacle interaction mechanism assessed based on the combination of the flow-obstacle geometry and the kinematic features of the flow. Then, a multiphase approach and a large deformation formulation based on Material Point Method (MPM) numerical technique has been used to properly simulate the complex hydro-mechanical interaction of the flow against the barrier, thus allowing a better understanding of the interaction mechanisms. It has been also noted that some geometric features (such as the ratios b'/H and B/H and the inclination of the foundation base) contribute to reduce the occurrence of catastrophic failures, also preventing the overtopping of the barrier.

In conclusion, the summary scheme of results showed that: i) the RC wall is very efficient for low flow energy, intercepting the whole landslide mass, but the use of an inclined foundation is preferable if large displacement are expected; ii) for elevated flow energy, to lengthen the foundation platform could lead to an undesired breakage of the wall for bending of the stem; iii) increasing the cross-section of the stem could avoid the bending mechanism, principally for a base foundation with the same length of the wall height (*B/H=1)*.

6.2 Mechanically Stabilized Earth (MSE) walls used as Deformable Geosynthetics-Reinforced Barriers (DGRB)

6.2.1 Introduction

Mechanically Stabilized Earth (MSE) walls consist of facing elements, soil mass and reinforcement combined to form a composite solid structure. The stability of the wall system is derived from the interaction between the backfill and soil reinforcements, involving friction and tension. The wall facing is relatively thin, with the primary function of preventing erosion of the structural backfill. The result is a massive structure that is flexible and can withstand various loads combinations.

In the field of protection structures, MSE walls are often used as deformable barriers against snow avalanches (Figure 6-9a) or rockfalls (Figures 6-9b and 6-9c).

The use of MSE walls as Deformable Geosynthetics-Reinforced Barriers (DGRB) which are composed of granular soil and geosynthetics reinforcement elements, such as high tenacity polyester (PET) geogrids, was investigated by many authors (Gioffrè et al., 2017; Cuomo et al, 2019; Moretti 2019; Cuomo et al., 2020b) to reduce the runout and the damage caused by flow-like landslide.

DGRB is an appropriate protection structure when medium to very high kinetic energy events are expected, i.e., from a few hundred kilojoules to tens of megajoules (Descoeudres, 1997). The other advantages are low maintenance costs and reduced visual impact since the lateral slopes can be greened (Brunet et al., 2009). Nevertheless, they are not appropriate on steeper slopes and their construction generally requires extensive space and accessibility for heavy vehicles.

The location of the barrier is usually the first issue to be faced since the protection structure must intercept most of the failed mass in question, and it must have the correct dimensions to protect the exposed objects. To optimise the height and length of the barrier, and therefore the costs, the DGRB must be located far down from the flow path and as close to the protection area as possible. This is also an important

issue concerning the construction itself since the barrier can be shorter and lower as they are located closer to the object to be protected.

Linear-type and piecewise DGRBs allocated at the foothill of the open slopes could be a good option. Such structures may be long some tens or hundreds of meters depending on the site-specific conditions.

When an optimal location has been determined, a decision must be made about its structural design, that requires addressing issues related to the impact forces exerted by the landslide and structure stability. The latter concerns the slope's capability to support the earthwork mass, to withstand the forces of gravity and the impact forces without collapsing.

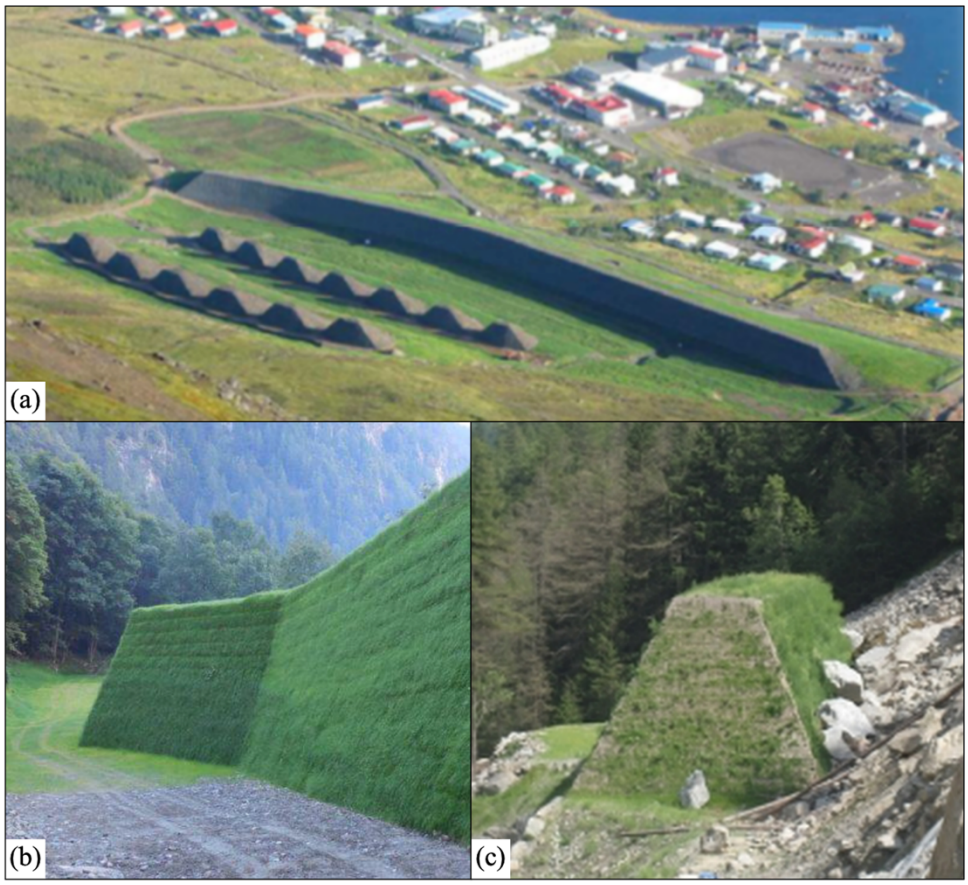

Figure 6-9. Some examples of MSE walls used as protection structures: a) Barbolini et al. (2009); b) Peila et al. (2007); c) Ronco et al. (2009).

6.2.2 Ultimate Limit States under impact

The design of DGRBs exposed to the dynamic load resulting from the impact of a flow-like landslide is complex because of (i) the large and irreversible deformations induced, (ii) the nonlinear soil stress-strain behaviour, and (iii) the interaction between the different components (reinforcement elements and backfill soil). In the following, the possible Ultimate Limit States (ULS) that a DGRB can undergo as a response to the impact of a flowing mass is analysed.

As done for the RC walls in paragraph 6.1, the Eurocode design approach can be adopted by satisfying the condition that the ultimate resistance R_u of the barrier, computed as a function of the design strength of materials, must be higher than the design load effect E_d.

A flow-like landslide impacting a DGRB induces distributing loads on the facing of the barrier according to the impact mechanism exhibited. Differently from rockfalls where the energy of the boulders is dissipated because of the barrier deformation, the main way to dissipate the flow energy is linked to the inelastic deformations that arise in the failed mass (Ng et al., 2021). For this reason, the ULS that is most likely to occur is the horizontal shifting Δ of the barrier that acts as a rigid body (Figure 6-10a). Due to large displacements ($\Delta > \Delta_u$), the failure of the barrier occurs and part of the kinetic energy of the flow is dissipated through friction along the sliding plane.

The barrier can even show a tilting failure mechanism (Figure 6-10b) under impact. To ensure that the structure remains fit for use with appropriate levels of reliability, the ultimate rotation θ_u capacity must be higher than the corresponding rotations θ due to the landslide impact. However, this type of ULS is quite unlikely as it is mainly due to an exaggerated underestimation of barrier dimensions.

If the impacting flow has very high energy, some local deformations (ε) of the infill soil material could occur in the proximity of the impacted area due to compaction (Figure 6-10c). The rest of the structure exhibits almost no significant changes. The flow energy during impact is partially dissipated by compaction, but

this beneficial effect vanishes with time, favouring the shifting failure mechanism over the deformation one.

The geosynthetic reinforcements improve the efficiency of the DGRB to withstand the impact forces since they distribute the load in the longitudinal direction (Peila et al., 2007). Specifically, the deformation of the barrier nearby the impacted zone causes a tension in the layer oriented along the longitudinal axis of the structure. This differs from the static case accounting for gravity loads, where the reinforcement layer is loaded along the transverse axis of the barrier direction (Peila et al., 2007; Brandl and Blovsky, 2004). Moreover, the reinforced layers contain the displacement of the backside facing and thus increases the capability to withstand the impact while the impact force is increased (Lambert and Bourrier, 2012).

The negative aspect is that geosynthetics can reach the ultimate shear resistance (T_u) bringing the barrier to the ULS for excessive relative sliding of the layers along the soil-reinforcement interface (Figure 6-10d).

A combination of all these mechanisms is also possible, as for example it is very easy that the horizontal shifting occurs together with the tilting, and the local deformations can also be accompanied by a relative sliding of the layers.

MPM numerical analyses are carried out to analyse the feasibility of DGRBs to afford the impulsive action of a flow-like landslide, evaluating the total displacements and breakage of the barrier, simulating the complex landslide structure interaction.

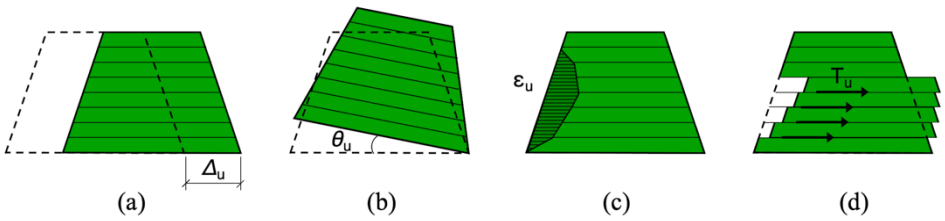

Figure 6-10. Possible failure mechanisms of a DGRB impacted by a flow-like landslide: a) horizontal shifting; b) tilting; c) large local deformations; d) relative sliding of the layers along the soil-geosynthetics interface

6.2.3 MPM modelling

Input schemes and data

The materials employed in the numerical analyses are the flow-like landslide, the protection barrier, and the base soil. The latter is necessary to ensure the frictional contact at the base of the moving barrier (Figure 6-11).

The flow is a saturated mixture with linear distribution of initial pore-water pressure, and non-associative (zero dilatancy) elasto-plastic Drucker-Prager behaviour, with the geometric features reported in Table 6-4. The mechanical properties of the saturated flow mass and the friction angle at the contact with the barrier are reported in Table 6-5.

For the barrier it is assumed: dry material, frictional contact at base and non-associative (zero dilatancy) elasto-plastic Drucker-Prager behaviour. The frictional resistance along the base is set equal to the 80% of the strength properties of the base material (Cuomo et al., 2019c).

The numerical analysis of the geosynthetics-reinforced soil structure becomes quite complex since modelling each component and their interactions is challenging.

For this reason, an equivalent approach is here employed to analyse the DGRB. The composite reinforced soil properties are considered together and hence a smaller number of input parameters are needed to develop the numerical model. However, localized failures cannot be reproduced, as the individual material properties are not considered and the interaction between the soil and the reinforcement cannot be studied independently. This means that the ULS for relative sliding of the layers cannot be modelled.

The assessment of the elasto-plastic parameters to set for the equivalent approach is carried out considering the internal friction angle φ', Young modulus E' and Poisson's ratio ν of the equivalent material equal to those typically employed for the backfill soil for practical applications. In addition, a tensile strength equal to the ultimate shear resistance of the geosynthetics reinforcement is imposed for this equivalent material. What is most difficult to determine is the cohesion value.

In the equivalent approach, the cohesion in the reinforced zone is increased using pseudo cohesion or anisotropic cohesion approach which states that the additional strength of the reinforced soil can be imparted by an apparent anisotropic cohesion (Nquyen et al., 2011; Maji et al., 2016). In this study, the value of cohesion was found by making sure that the Factor of Safety (FS) under gravity load obtained for the composite structure is the same of the equivalent one.

Table 6-5 reports the summary of material properties for the DGRB, considering two combinations. Combination 1 is characterized by an ultimate strength of geosynthetics lower than the combination 2. The achieved cohesion values are: i) 35 kPa with FS=2.71 for combination 1; ii) 57.5 kPa with FS=3.73 for combination 2. The factor of safety is calculated through LEM analysis, with Morgenstern-Price method.

Different DGRB's geometries are considered, as reported in Table 6-6, where the influence of the facing inclination (β) and the major barrier length (B) are considered.

The flow and barrier are modelled through the single-point MPM formulation, respectively with 2-phase and 1-phase. The computational unstructured mesh is made of 20,515 triangular 3-noded elements with dimensions ranging from 0.20 to 1.00 m. The landslide is assumed as approaching the barrier with a fixed geometric configuration and constant velocity, until *LSI* starts.

To investigate the response of the barrier not only focusing on the maximum displacement exhibited (as done in paragraph 4.5), but also in terms of local deformations within the barrier, the moving mesh technique (used in Sect. 4 for rigid barriers) cannot be adopted. Therefore, some numerical instabilities could occur when the material points cross the mesh from one element to another. There is no contact interface between the barrier and the flow due to the limitation of the current MPM code in simulating large deformations in presence of contact surface. This means that some drainage could occur along the impacted barrier side.

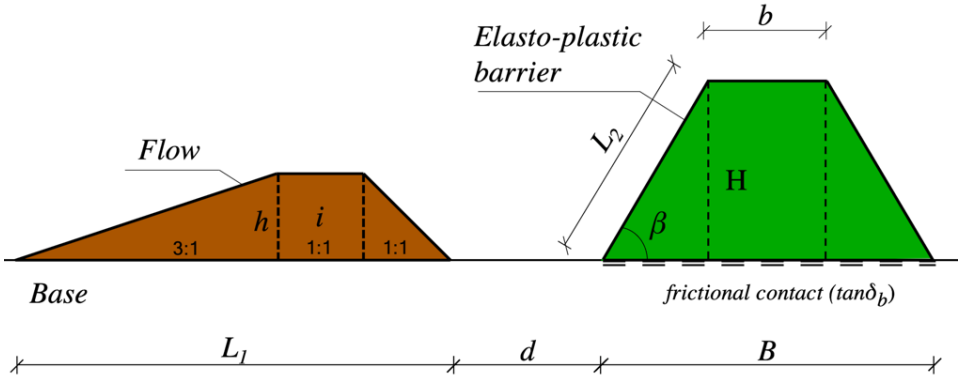

Figure 6-11. Geometric schematization for the LSI numerical simulations with DGRB

Table 6-4. Geometric characteristics of the flow-like landslide

L_l (m)	L_m (m)	i (-)	h (m)	V_l (m^3/m)
21.00	15.00	3	3.00	45.00

Table 6-5. Mechanical properties

Flow-like landslide										
ρ_m (kg/m^3)	n ($-$)	K_0 ($-$)	φ' (°)	c' (kPa)	E' (MPa)	ν ($-$)	k_{sat} (m/s)	μ_L (Pas)	K_L (MPa)	$v_{0,l}$ (m/s)
1800	0.5	0.66	20	0	2	0.25	10^{-4}	10^{-3}	30	5−10

DGRB							
	ρ (kg/m^3	tan (δ_b) ($-$)	φ' (°)	c' (kPa)	σ_t (kPa)	E' (MPa)	ν ($-$)
Comb. 1	2000	0.29	38	35	50	15	0.25
Comb. 2	2000	0.29	38	58	100	15	0.25

Table 6-6. Different DGRB geometries

ID	β (°)	d (m)	L_2 (m)	B (m)	b (m)	H (m)	V (m^3/m)	M (kg)
1	70	3	6.39	6	1.63	6	22.89	45780
2	80	3	6.09	6	3.88	6	29.64	59280
3	70	3	6.39	11	6.63	6	52.89	105780
4	80	3	6.09	11	8.88	6	59.64	119280
5	70	3	6.39	6	1.63	6	22.89	45780
6	80	3	6.09	6	3.88	6	29.64	59280
7	70	3	6.39	11	6.63	6	52.89	105780
8	80	3	6.09	11	8.88	6	59.64	119280

Numerical results

Selected results are shown as the spatial distribution of displacements at the final time lapse of the impact process, for all the different schemes of Table 6-6. Firstly, a flow with high kinetic energy is considered (Figure 6-12), thus the influence of the different types of DGRB is pointed out, especially focusing on the length of the major base (B), the inclination of the impacted side (β) and considering the two material combinations.

If the DGRB is characterized by a low ratio of B/H the breakage of the structure is more accentuated than the cases of a larger barrier (Figure 6-4b), as understandable by the internal yielding points and the maximum displacement of the barrier. Particularly, a larger base of the barrier significantly reduces the final displacement of the structure, since the mass is more than doubled.

The inclination β has also a significant influence. In fact, for $\beta=80°$ the displacements are more contained than the case of $\beta=70°$, as for example the comparison between cases 1 and 2. This is mainly because a more massive barrier can be obtained with a more inclined facing of the barrier, while maintaining the same overall dimensions in plan. Moreover, the more inclined is the impacted barrier side, the more material can be retained by the barrier.

The two different combinations of materials (comb. 1 and comb. 2) do not seem to play a decisive role in the determination of the ULS. In fact, if the barrier is made of low resistance materials (Figure 6-12a) both barrier displacements and yielding zones are quite like those obtained with a more resistant barrier.

Completely different is the case of a landslide with lower velocity (Figure 6-13), where all the barrier geometries can withstand the potential of the flow, showing almost zero displacements. Even the yielding zone are less than in the case with a higher flow velocity. Moreover, the whole landslide volume can be completely stopped by the protection barrier for all the DGRB geometries.

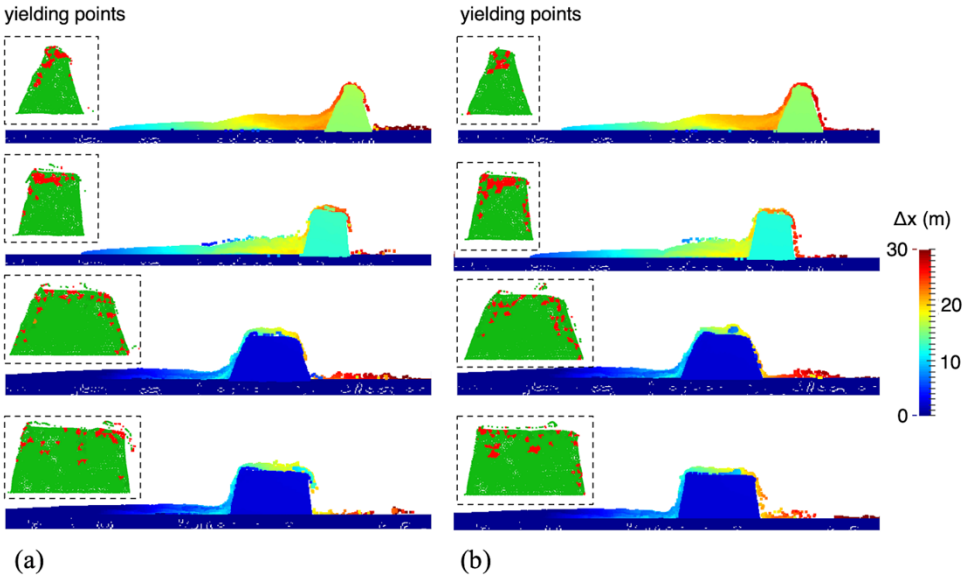

Figure 6-12. Spatial distribution of displacements and yielding points inside the barrier at final impact time for v_0= 10 m/s: (a) cases 1-2-3-4 (comb. 1); (b) cases 5-6-7-8 (comb. 2).

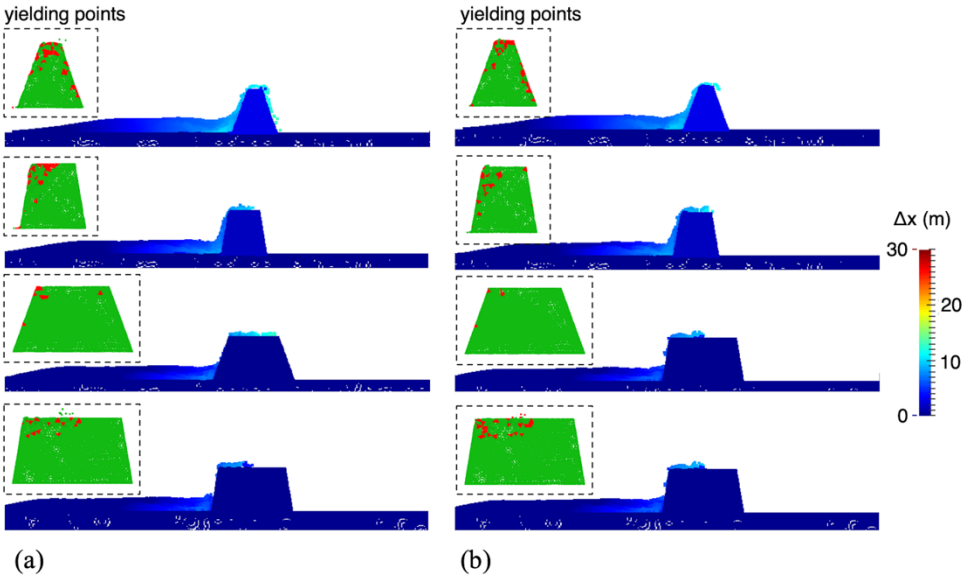

Figure 6-13. Spatial distribution of displacements and yielding points inside the barrier at final impact time for v_0= 5 m/s: (a) cases 1-2-3-4 (comb. 1); (b) cases 5-6-7-8 (comb. 2).

The local deformations (ε_{xx}) of the barriers at the final lapse of the impact are also investigated. The zone influenced by compression is in the proximity of the impacted area and are more visible for high flow velocities (Figure 6-14). The difference between comb. 1 (Figure 6-14a) and comb. 2 (Figure 16b) is practically null. Only for the case 1, that has the weakest geometry, the deformations are more spread over large areas, thus the ULS for large local deformations is reached. For the relatively slow landslide (Figure 6-15) all the structures exhibit almost no significant changes.

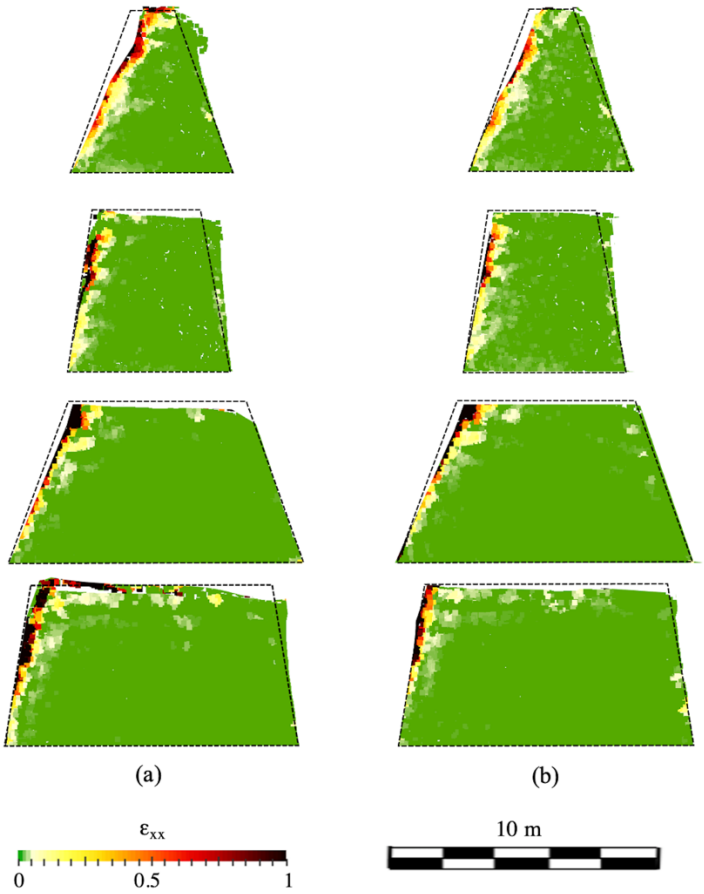

Figure 6-14. Strain distribution due to compression of the DGRB for v_0=10 m/s: (a) comb. 1; (b) comb. 2.

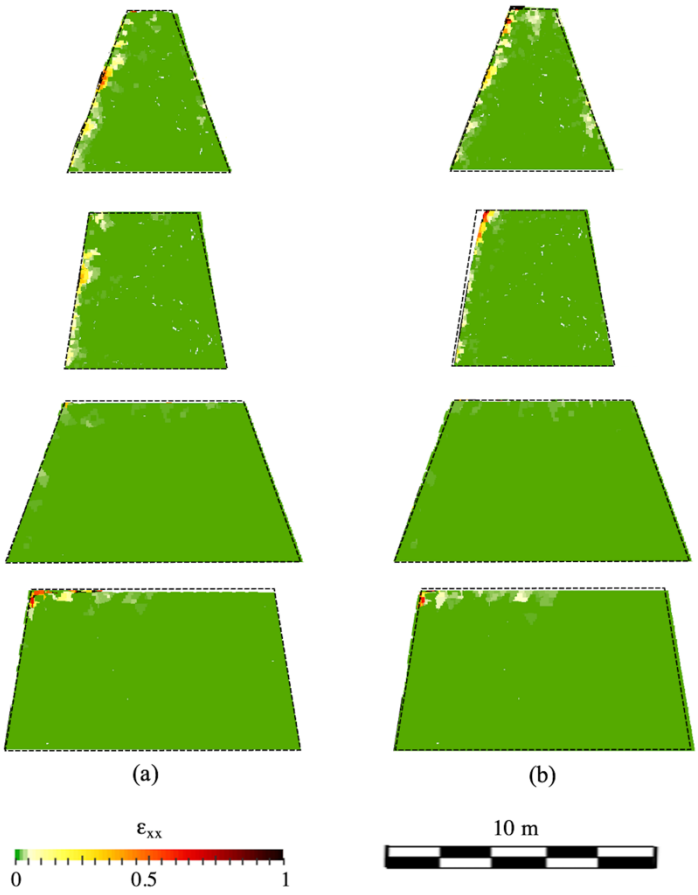

Figure 6-15. Strain distribution due to compression of the DGRB for v_0=5 m/s: (a) comb. 1; (b) comb. 2.

In more details, the temporal trend of kinetic energy and the amount of work done by the frictional force can be traced for all the scenarios (Figure 6-16).

After the impact with the barrier, the kinetic energy of the flow is totally dissipated in the cases where the barrier remains fixed (case 3 and 4) or partially transferred to the barrier because of its movement for the cases with significant horizontal shifting (cases 1 and 2). The chosen material properties for the two combinations give the same results in terms of kinetic energy reduction.

The work done by friction depends on the barrier displacement and on the mobilized shear resistance along the base of the barrier, which in turn depends on the barrier's weight and on the strength properties of the base material.

The higher the work done by friction, the larger the major base for a flow with v_0=*10 m/s*. In the case of low flow velocity, the frictional work made by the barrier is null for a large base since the maximum shear resistance that can be mobilized at the interface between the barrier and the above soil cannot be reached.

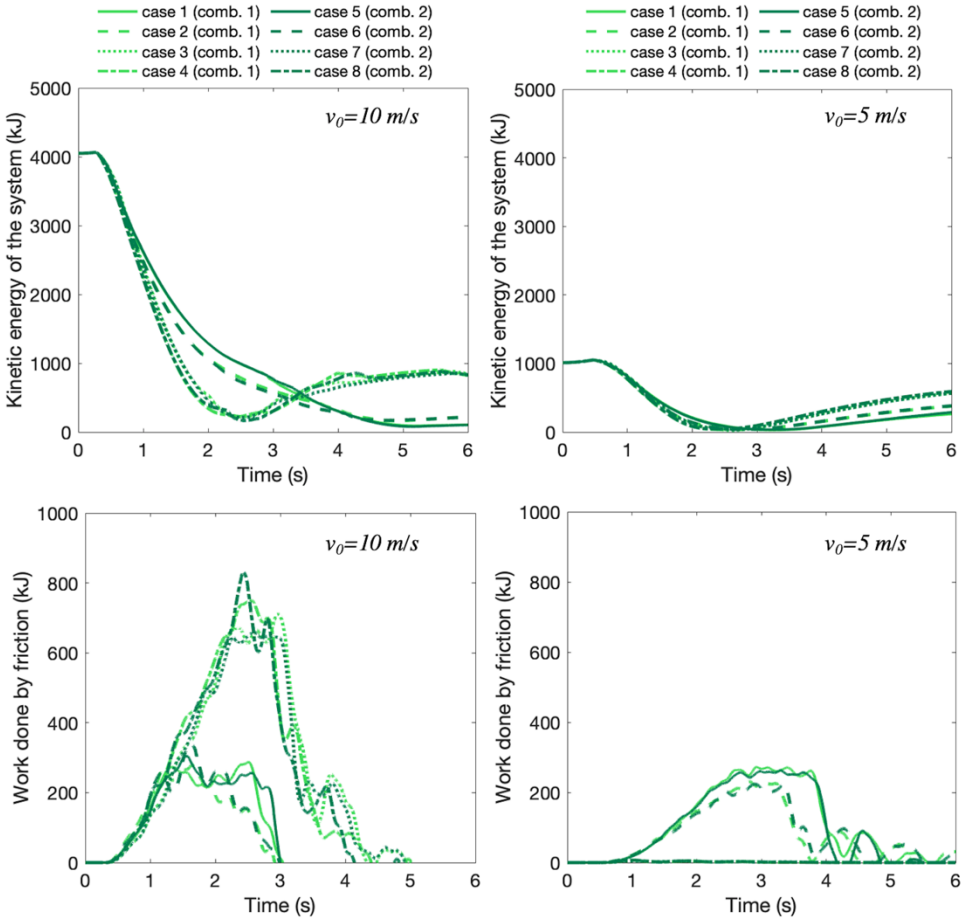

Figure 6-16. Temporal trend of kinetic energy and work done by friction for all the DGRBs geometries

To correlate the most relevant quantities obtained from all the simulations, the efficiency diagram of Figure 6-17 is proposed. The ratio between the kinetic energy and its initial value represents the fraction of initial kinetic energy that can be achieved after impact, while the ratio between the barrier displacement Δ and the acceptable value Δ_u (assumed equal to 5 m for convenience) configure a barrier efficiency zone in the diagram.

For high flow kinetic energy, the cases 1 and 2 that are characterized by a low value of *B/H* are not efficient geometries, while all the geometries result adoptable for a flow with low energy. This means that the extreme geometries of cases 3 and 4 can be avoided because they would require a high construction cost.

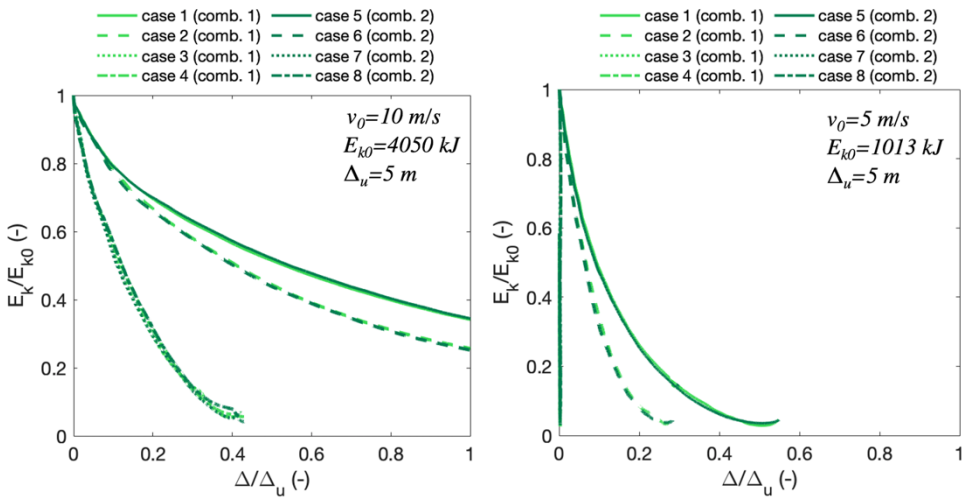

Figure 6-17. Efficiency diagram of the DGRBs for all the considered scenarios

Summing up all the achieved results, Figure 6-18 shows the type of failure mechanism reached by the DGRB related to the variation of v_0, β and *B/H*. The chosen colour palette indicates that a combination of shifting and compaction represents the worst scenario, but the ULS for large deformations inside the structure is somehow worse than the shifting mechanism.

It is immediately noticeable that a flow with relatively low velocity causes less damage to the structure, especially for higher values of β and *B/H*. In contrast, the

DGRB cannot withstand to the potential of a faster flow, especially for lower values of *B/H*. In fact, the worst scenario is reached for the weakest geometry (case 1), where both local deformations and large displacements occurred. Nevertheless, the barrier can block almost all the landslide mass, although becoming inoperative for repeated use.

Only for v_0=*10 m/s,* the lowest value of *B/H* always lead to a horizontal failure mechanism. When the ratio *B/H* increases, the DGRB remains stable, but the percentage of volume retained becomes lower than the cases with *B/H=1*.

For v_0=*5m/s*, all the barrier geometries are capable to withstand the potential of the flow, with high percentages of intercepted material. This means that the DGRBs with *B/H>1* are all oversized, thus not cost-effective.

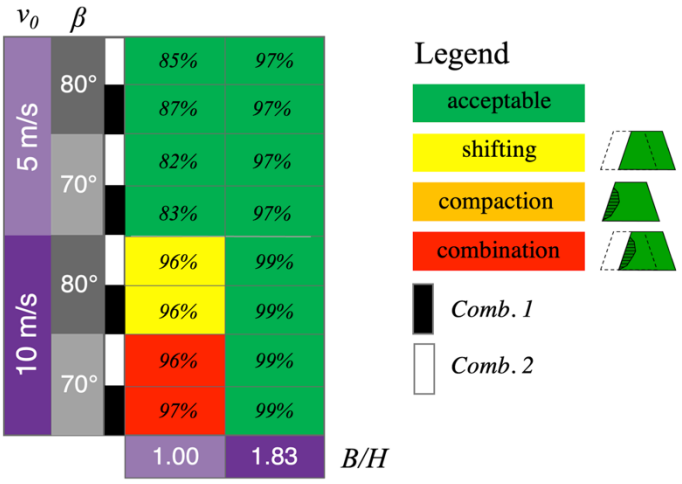

Figure 6-18. Comparison between all the considered scenarios in terms of ULS for DGRBs (in the coloured cells the percentage of landslide volume blocked behind the barrier)

6.2.4 Comparing DGRB with rigid barriers

Deformable Geosynthetics-Reinforced Barriers (DGRBs) are usually designed as rigid barriers since the flowing mass is assumed to be more deformable with respect

to the protective structure. However, if the incoming flow has high kinetic energy some damages to the structure could occur, as seen before.

The hypothesis of rigid barriers can be also related to the construction mode typically used for such kind of DGRBs, which involve the use of 0.6–0.7 m thick layers of coarse materials reinforced through geosynthetics (usually geogrids) with high tensile strength and wrapped around the facing of the barrier. In fact, recent studies have outlined that local deformation of a DGRB or the relative horizontal shifting of its layers may occur under the impact of a flow (Cuomo et al., 2020b), although the horizontal displacement along the base is the prevailing limit state of the barrier. This finding combined to the fact that both the core soil and the geogrids are very resistant materials makes the structure experiencing stress levels much lower than the ultimate values in most parts of the structure.

A comparison between rigid and deformable barriers is therefore needed for understanding the range of solutions that can be achieved depending on the adopted model. Moreover, the influence of a permeable contact along the barrier contour is also highlighted.

The numerical technique of the moving mesh is adopted for a more accurate solution, as the internal deformation of the barriers are not interesting for the purpose.

The MPM results in Figure 6-19 show the pore-water pressure distribution during impact for a rigid barrier with impervious contact (Figure 6-19a), for rigid and deformable barriers with draining contact (Figures 6-19b and 6-19c, respectively). It flows that the shading of the different plotted values inside the landslide is quite similar for all the cases, with the percentage difference of the maximum value reached by the liquid pressure in the order of the 5-7%.

The flow kinetic energy is in general equal for all the cases, but the displacement trend over time results high for the rigid barrier with impervious contact (Figure 6-20). However, the rigid and elastoplastic barriers with permeable interfaces have very close results.

Finally, the trend of the impact forces along the impacted barrier side is obtained in Figure 6-21. Also here, the temporal trend of the forces is quite the same for all the scenarios, even if the rigid impervious barrier exhibits a slightly higher value than the other two cases.

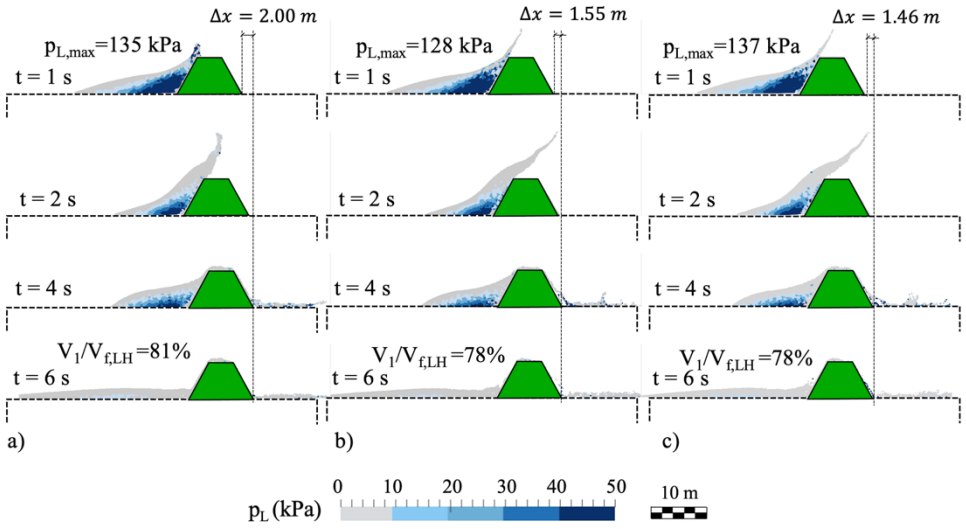

Figure 6-19. Pore-water pressure distribution in the case of rigid impervious barrier (a), rigid permeable barrier (b) and elastoplastic permeable barrier (c).

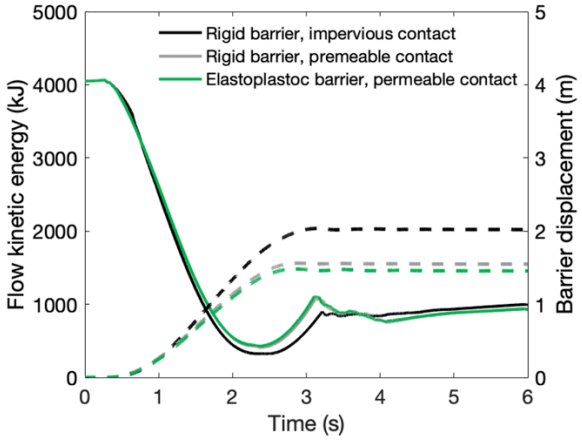

Figure 6-20. Flow kinetic energy (solid line) and barrier displacements (dashed lines) trend over time

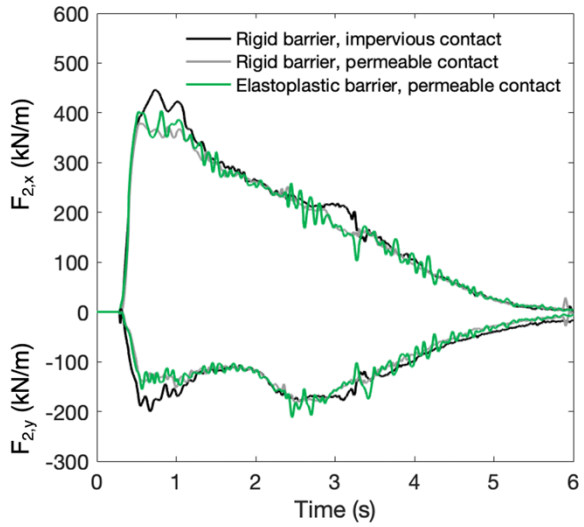

Figure 6-21. Impact forces trend over time for the considered solutions

All these results proved that the assumption of rigid barrier is a practicable solution for analysing the possible ultimate displacements that a barrier can undergo. In particular, some draining systems could be installed over the facing of the barrier, to reduce the impact pressure and the amount of displacements. However, much costs due to the installation are expected and also the feasibility of this kind of structure must be investigated.

6.2.5 Concluding remarks

The MPM simulations outcomes have furnished new insights in understanding the type of failure mechanisms that a deformable protection barrier can undergo following the impact of flow-like landslides, providing interesting options for the design of these structures.

The assessment of many physical properties (e.g., strain, velocity, kinetic energy, among other quantities) can be computed either in space or time thanks to advanced numerical simulations.

The analyses showed the potential of MPM in simulating the impact mechanisms of flow-like landslides against DGRBs, providing novel insights in understanding the ultimate failure mechanisms that the barrier can undergo. However, an equivalent material is adopted for the simulations instead of a compound structure, determining the elasto-plastic parameters through the hypotheses of the equivalent approach.

Then, the problem has been schematized and the landslide interaction mechanism against DGRBs is assessed, taking into account different obstacle geometry and the kinematic features of the flow. It has been also noted that some geometric features (such as the ratio B/H and the inclination of the impacted side of the barrier) contribute to reduce the occurrence of catastrophic failures, also preventing the overtopping of the barrier. The DGRB is very efficient for low flow energy, intercepting the whole landslide mass, hence too massive barriers turn out to be excessive. However, for elevated flow energy, to lengthen the major base remains a good solution for intercepting the flow path without excessive displacements and/or deformations of the barrier.

Finally, the typical assumption of rigid barrier used for the design of these structures has been analysed. The numerical results showed that a rigid barrier with impermeable facing is a more precautionary assumption to be used in the design, even if the impact forces, the displacements and the flow energy reduction trends are practically the same or slightly different than that achieved for a deformable barrier. However, additional stress-strain analyses of the barrier are needed for analysing the extent of deformations over the impacted zones of the DGRBs.

6.3 Comparing RC walls and DGRBs

A comparison between the two solutions (RC walls and DGRBs) proposed as mitigation options is made in this paragraph. From an overall view of the efficiency diagram shown in Figure 6-22, it follows that for a high flow velocity the adequate design geometries are 4 for the DGRB (cases 3, 4, 7, 8), while none of the RC walls can withstand the energy of the flow, even though the two structure typologies have the same ratio of $B/H=1.83$. However, the mass of the barrier is completely different, being higher in the DGRBs cases, especially for the large base. This means that although the two structures have the same base size, the DGRBs provides better performance.

The mass of the barrier obviously plays the major role in the prevention of large displacements. For example, the case 7 of the RC wall and the case 6 of the DGRB have a similar mass, and both can reach quite the same displacement (as reported in Table 6-7), even if the structures are completely different in terms of shape and resistance. Also, the percentage of the flow volume that can be blocked by the structure is approximately the same. However, there are some cases that despite having the same mass are characterized by different displacements. For example, the case 5 for both the protection structures reports a much greater displacement for the RC wall. This is probably because the wall does not show any deformations inside in respect to the DGRB, which is characterized by high level of compaction. This fact highlights another interesting advantage in using DGRBs, that can dissipate flow energy during impact through compaction.

For relatively low energy of the flow, all the DGRBs can stop the flow without excessive displacements, while only the RC walls with slender column and shorter base are inefficient. However, regarding the feasible geometries, an interesting turnaround happens. For example, the RC walls of cases 2 and 6 exhibit quite null shifting than the homonymous DGRBs, which are characterized by an increased volume of 60% and 40%, respectively. This means that higher costs for construction materials are expected.

These excellent results depend on the type of the foundation platform, that in the above-mentioned cases is supposed inclined. In fact, even for the cases without shifting (cases 4 and 8), the RC walls are preferable than DGRBs thanks to their particularly low volumes. In addition, for all the RC walls the flow material is completely retained by the structure.

An overall comparison about the efficiency of RC walls, DGRBs and rigid barriers is reported in Figure 6-23. All the considered simulations are listened in Table 6-8. The comparison shows that many simulation results are in the lower right corner of the diagram, which indicates a high efficiency of the barrier in terms of maximum displacement exhibited and percentage of flow volume retained by the barrier. The outliers refer to the cases where a flow with velocity greater than 10 m/s impacts against rigid barriers and to the cases where both RC walls and DGRBs are characterized by excessively large displacements even if the amount of flow volume retained is acceptable (ULS due to shifting of the structure). The cases in the proximity of the origin are represented by unsuitable geometries of the structure, since all the flowing mass goes beyond the barrier by destroying it.

In conclusions, RC walls and DGRBs are both interesting, affordable and feasible solutions to be used as passive protection structures against flow-like landslides. As demonstrated, DGRBs are the best solution in a context of high-speed flows, while RC walls may be more efficient for flows with low energy.

The proposed study aimed to give an overview about these possible control works against flow-like landslides, always from an engineering point of view. Therefore, further developments and more detailed analyses are necessary to investigate further aspects, as for example a better characterization of the constitutive laws for the materials, but also the quantification of the environmental impacts, that is became a crucial point in the framework of the sustainable development.

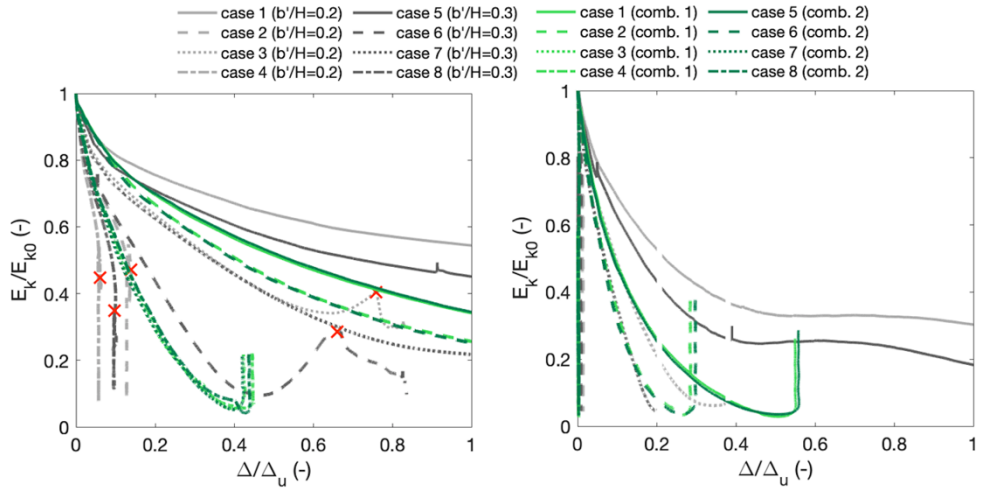

Figure 6-22. Overall comparison of the efficiency diagrams obtained for all the RC walls and DGRBs scenarios

Table 6-7. Summary of the main quantities and results obtained for RC walls and DGRBs

ID	*M (tons)*		*V (m^3/m)*		*$V_{1f,LH}/V_{1,0}$ (%) (v_0=10 m/s)*		*$V_{1f,LH}/V_1$ (%) (v_0=5 m/s)*		*Δ (m) (v_0=10 m/s)*		*Δ (m) (v_0=5 m/s)*	
	RC wall	*DGRB*	*RC wall*	*DGRB*	*RC wall*	*DGRB*	*RC wall*	*DGRB*	*RC wall*	*DGRB*	*RC wall*	*DGRB*
1	36.7	45.8	14.4	22.9	100	97	100	99	26.7	15.3	9.6	2.8
2	45.9	59.3	18.0	29.6	0	96	99	99	0.6	12.3	0.1	1.4
3	52.0	106	20.4	52.9	0	83	100	97	4.2	2.1	1.9	0.0
4	68.8	119	27.0	59.6	0	87	100	97	0.3	2.33	0.0	0.0
5	45.9	45.8	18.0	22.9	100	96	100	99	22.2	15.1	7.1	2.8
6	55.0	59.3	21.6	29.6	85	96	100	99	4.2	11.8	0.0	1.5
7	61.2	106	24.0	52.9	95	82	99	97	11.2	2.1	1.0	0.0
8	78.0	119	30.6	59.6	0	85	100	97	0.5	2.2	0.0	0.0

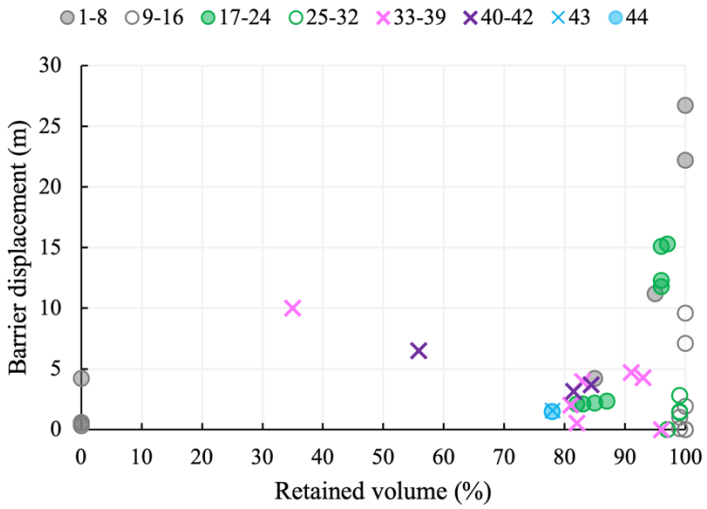

Figure 6-23. Overall comparison between all the MPM simulations in terms of barrier efficiency, including RC walls, DGRBs and rigid barriers (cases in Table 6-8)

Table 6-8. Summary of the MPM simulations referred to RC walls, DGRBs and rigid barriers

ID	*type*	$v_{1,0}$ *(m/s)*	M_1 *(kg)*	M_2 *(kg)*	$V_{1f,LH}/V_{1,0}$ *(%)*	Δ *(m)*	*Notes*
1	RC wall	10	81000	36700	100	26.70	Sect. 6.1; permeable contact
2	RC wall	10	81000	45900	0	0.60	Sect. 6.1; permeable contact
3	RC wall	10	81000	52000	0	4.20	Sect. 6.1; permeable contact
4	RC wall	10	81000	68800	0	0.30	Sect. 6.1; permeable contact
5	RC wall	10	81000	45900	100	22.20	Sect. 6.1; permeable contact
6	RC wall	10	81000	55000	85	4.20	Sect. 6.1; permeable contact
7	RC wall	10	81000	61200	95	11.20	Sect. 6.1; permeable contact
8	RC wall	10	81000	78000	0	0.50	Sect. 6.1; permeable contact
9	RC wall	5	81000	36700	100	9.60	Sect. 6.1; permeable contact
10	RC wall	5	81000	45900	99	0.10	Sect. 6.1; permeable contact
11	RC wall	5	81000	52000	100	1.90	Sect. 6.1; permeable contact
12	RC wall	5	81000	68800	100	0.00	Sect. 6.1; permeable contact
13	RC wall	5	81000	45900	100	7.10	Sect. 6.1; permeable contact
14	RC wall	5	81000	55000	100	0.00	Sect. 6.1; permeable contact
15	RC wall	5	81000	61200	99	1.00	Sect. 6.1; permeable contact
16	RC wall	5	81000	78000	100	0.00	Sect. 6.1; permeable contact
17	DGRB	10	81000	45800	97	15.30	Sect. 6.2; permeable contact
18	DGRB	10	81000	59300	96	12.30	Sect. 6.2; permeable contact
19	DGRB	10	81000	106000	83	2.10	Sect. 6.2; permeable contact

20	DGRB	10	81000	119000	87	2.33	Sect. 6.2; permeable contact
21	DGRB	10	81000	45800	96	15.10	Sect. 6.2; permeable contact
22	DGRB	10	81000	59300	96	11.80	Sect. 6.2; permeable contact
23	DGRB	10	81000	106000	82	2.10	Sect. 6.2; permeable contact
24	DGRB	10	81000	119000	85	2.20	Sect. 6.2; permeable contact
25	DGRB	5	81000	45800	99	2.80	Sect. 6.2; permeable contact
26	DGRB	5	81000	59300	99	1.40	Sect. 6.2; permeable contact
27	DGRB	5	81000	106000	97	0.00	Sect. 6.2; permeable contact
28	DGRB	5	81000	119000	97	0.00	Sect. 6.2; permeable contact
29	DGRB	5	81000	45800	99	2.80	Sect. 6.2; permeable contact
30	DGRB	5	81000	59300	99	1.50	Sect. 6.2; permeable contact
31	DGRB	5	81000	106000	97	0.00	Sect. 6.2; permeable contact
32	DGRB	5	81000	119000	97	0.00	Sect. 6.2; permeable contact
33	Rigid barrier	10	81000	90000	81	2.00	Sect. 4.5; impervious contact; moving mesh
34	Rigid barrier	10	48600	90000	82	0.53	Sect. 4.5; impervious contact; moving mesh
35	Rigid barrier	10	113400	90000	83	3.97	Sect. 4.5; impervious contact; moving mesh
36	Rigid barrier	10	81000	90000	91	4.72	Sect. 4.5; impervious contact; moving mesh
37	Rigid barrier	10	81000	90075	93	4.26	Sect. 4.5; impervious contact; moving mesh
38	Rigid barrier	20	81000	90000	35	10.00	Sect. 4.5; impervious contact; moving mesh
39	Rigid barrier	10	81000	90000	96	0.00	Sect. 4.5; impervious contact; moving mesh
40	Rigid barrier	10	95400	90000	84	3.68	Sect. 5; impervious contact; moving mesh
41	Rigid barrier	15	81000	90000	56	6.50	Sect. 5; impervious contact; moving mesh
42	Rigid barrier	10	86400	90000	81	3.13	Sect. 5; impervious contact; moving mesh
43	Rigid barrier	10	81000	90000	78	1.55	Sect. 6.2.4; permeable contact; moving mesh
44	DGRB	10	81000	90075	78	1.46	Sect. 6.2.4; permeable contact; moving mesh

where $v_{1,0}$*: initial flow velocity;* M_1*: flow mass;* M_2*: barrier mass;* $V_{lf,LH}$*= flow volume upstream of the barrier;* $V_{1,0}$*= initial flow volume;* Δ*= maximum barrier displacement*

7. Conclusions

The thesis has faced a variety of numerical simulations aimed to explore the flow-like landslide dynamics from triggering to propagation and to analyse the complex interaction of the landslide against protection structures, considering both large deformations and hydro-mechanical coupling in the numerical models. This chapter outlines the main conclusions achieved from this study.

An extended literature review was performed reporting the principal features that regulate the pre-failure, failure and post-failure stages of flow-like landslides, also accounting their potential damage to people, structures and infrastructures. From the examination of the scientific literature, it emerges that the study of the impact mechanisms poses several issues since a comprehensive knowledge is still missing about the governing quantities of the process, among which the role of interstitial fluid on the intensity and the time-dependency of the impact actions. The main challenge is choosing a proper numerical method able to reproduce the complex aspects of the dynamics and impact mechanisms of flow-like landslides, under different conditions. Therefore, a review about the existing numerical methods for large deformations was conducted, identifying the Material Point Method (MPM) as the best suitable to satisfy the goals of the thesis since it allows the modelling of large deformations and multiphase materials (Ch. 2).

The capability of MPM was firstly tested in reproducing the inception of debris avalanches (progressive landslide mechanism). The achieved results outline that failure induced by impact loading of an unstable mass can cause further failures in downslope stable deposits, mobilizing additional volumes due to the increase in pore-water pressures, as well simulated through 2D hydro-mechanical coupled analyses. Furthermore, the influence of initial suction and length of the downslope deposit was highlighted, demonstrating that the higher soil suction and shorter slope

length delay the occurrence of failure and even lead to different inception mechanisms. The simulation of rainfall-induced landslides in an unsaturated slope was also analysed, by proposing a multi-tool approach based on three levels, *no-deformation LEM*, *small-deformation FEM*, *large-deformation MPM*. The proposed framework was applied to an international benchmark landslide case (the 1995 Fei Tsui Road landslide in Hong Kong), for its complexity and for the wide dataset available in the scientific literature. Specifically, *large-deformation MPM* modelling simulates the landslide dynamics from failure onset up to soil deposition, also including the modelling of the rainfall infiltration for analysing the pre-failure stage. The effect and evolution of soil suction in relation to soil shear strain during the whole landslide process was particularly investigated. In addition, the *MPM* analyses in axisymmetric conditions assess the effects of lateral spreading during the propagation stage. However, no-deformation *LEM* analyses and small-deformation stress-strain *FEM* analyses provide useful quantitative indications towards the understanding of the failure mechanisms. All these numerical analyses aim to demonstrate the current potentialities of large deformations, hydro-mechanical coupled and multiphase numerical methods for the geomechanical modelling of flow-like landslides (Ch. 3).

The investigation of Landslide-Structures-Interaction (*LSI*) mechanisms is afforded in Ch. 4. The study is focused on the flow features and not on the structure, that is assumed to be rigid. The numerical results provided new insights when analysing the complex impact mechanisms thanks to the possibility of the numerical models to compute and track in space and in time some quantities, such as stress, strain, pore-liquid pressure, solid and liquid velocities, which cannot be easily monitored/obtained from laboratory experiments. The reduced-scale flume tests reported by Moriguchi et al. (2009) and the centrifuge tests of Song et al. (2017) were simulated in a MPM context, in order to analyse the impact of dry and saturated granular flows against a rigid vertical barrier. In both the sets of simulations, the calibration and validation of the numerical model led to a satisfactory correspondence, accurately reproducing the flow depth and velocities and even the

impact force trend over time. This allows to examine the influence of some material properties (such as solid Young modulus, internal friction angle, friction at contact surfaces, soil permeability, soil porosity, Froude number) in order to evaluate their significance on the impact behaviour of dry and saturated flows. It was found that: (*i*) the presence of a liquid phase inside the granular flow can lead to different impact regimes in respect to the dry flows, (*ii*) the soil Young modulus has negligible effects on flow propagation and particularly on the impact force distribution over time, (*iii*) low values of both effective friction angle and base contact friction favour the occurrence of a run-up mechanisms with consequent increase of the peak values of the dynamic force, (*iv*) low values of soil porosity lead to a decrease in Froude number, confirming the effectiveness of solid fraction in energy dissipation and reduction of debris mobility, (*v*) a change in soil permeability affects the liquid pressure inside the flow, which in turn modifies the stress and strain depending on material constitutive response, therefore even soil permeability has a crucial role in the assessment of the impact dynamics. All this stresses how hydro-mechanical coupling is relevant when modelling the flow-structures interaction.

The MPM model was also tested to investigate the failure behaviour of masonry walls under a constant increasing pressure, which can simply be assimilated to the impact pressure of a flow-like landslide. The topic has relevance since field evidence have often shown that the collapse of infill panels can occur independently from the failure of the bearing frame, implicating a risk for the people inside. The MPM computational domain has been set both in 3D and 2D for different purposes. The 3D scheme outcomes well reproduced the mechanical response of the generalized deformation mechanisms and limit states including complex patterns of deformation, failure and post-failure of the wall. However, there is still an issue of long computational time especially when large structures are considered. The 2D model has proved to be a simplified but valuable solution since it was able to properly reproduce the out-of-plane bending, the formation of plastic hinges at the top and bottom of the wall, associated to the accurate evaluation of the load-displacement curve.

Another *LSI* problem addressed in Ch. 4 was the simulation of a huge debris flow (the Wenjia Gully case). The interaction between the propagating flow and the barriers was also examined, providing fundamental information on the loading actions and on the flow kinetic energy reduction over time. The influence of some material properties such as soil porosity, stiffness and basal friction was examined. It emerged that high porosity and low stiffness values lead to higher peak of flow kinetic energy, indicating an elevated mobility of the debris, while the change of frictional contact is quite negligible in terms of flow kinematics.

The final Sect. of Ch. 4 concerned the MPM modelling of different types of flow impact mechanisms introducing a rigid barrier with its own weight and considering several barrier geometries. The different impact mechanisms were obtained by changing the ratio between barrier height and flow depth (H/h), the Froude number (Fr), the amount of flowing mass (by setting different landslide lengths), the slope β of the impacted side of the barrier and the basal constraint for the barrier (which can be fixed or unfixed). To this aim, a conceptual framework has been set, considering the main features of both flow-like landslide and barrier, and then it has been implemented in the numerical model. Through MPM modelling it was possible to accurately derive the spatial and temporal distribution of the stresses generated from the impact on the structure, also separating the contribution of the impact force referred to the liquid phase. It has been shown that the increase in interstitial water pressure can favour the overtopping of the barrier. This issue should be taken into consideration for a correct design of the mitigation structure.

Many works in the literature have evaluated the impact forces assuming the that the energy of the flow is dissipated exclusively within the landslide mass. On the contrary, the proposed study took into consideration other ways for dissipating the flow energy, considering the movement of the barrier.

The numerical results show that a fixed barrier to the base undergoes greater impact forces than an unfixed barrier, since the reaction to the impact of the flow is transferred to the constraints at the base. For this reason, the case of an unfixed barrier was investigated, also considering the role of different landslide volumes.

The installation of unfixed barriers inhibits the overtopping mechanism of the barrier by the flow as the movement of the barrier reduces the increase of liquid pressure within the landslide.

In Ch. 5 the MPM method was employed to find simplified methods for estimating the main *LSI* variables. Analytical and empirical models were derived from the principles of energy and momentum conservation are introduced. However, only the analytical model furnishes the possibility of analysing the impact of flow-types against free-sliding barriers. The methods have been calibrated and validated through the MPM numerical results. The peak value of the impact force and its time of occurrence were considered for the calibration phase, while other quantities (such as the kinetic energy of both the landslide and structure, the time of the whole impact process) were used for the validation of the models. The impact scenarios chosen for calibration considered the most influential quantities for *LSI* problems (such as soil porosity, flow impact height, flow velocity) therefore their values were set within the typical ranges for flow-type landslides. The results reported that for the analytical model all the formulations depend on the calibrated parameter λ, which is found to be equal to 0.72 for fixed barrier and 0.41 for unfixed barriers. The empirical model is based on the calibrated $\alpha - Fr$ power law. The latter is different from those predicted by other studies in the literature, which are typically calibrated on small-scale laboratory tests, thus giving an excessive overestimation in predicting impact load that may results in a large increment of costs for structure construction.

The validation of the analytical/empirical models was also made using a real field dataset collected at Jiangjia Ravine (China) to test their predicting capability. The achieved results are encouraging, showing a high correspondence between analytical/empirical formulations, MPM numerical outcomes and measured field data. The comparison of the achieved results is consistent in several impact scenarios here considered, demonstrating that all the three methods (MPM, analytical and empirical) can be usefully employed in *LSI* problems.

After analysing the types of impact mechanisms that a flow-like landslide can exhibit, even understating the principal governing variables and equations of the

impact process, in Ch. 6 the focus is moved to the failure mechanisms of the protection structure under impact. Two types of protection structures were introduced: Reinforced-Concrete (RC) walls and Deformable Geosynthetics-Reinforced Barriers (DGRB). The first option is commonly used as defence measures in hilly areas to contain landslide debris, while the last one is usually employed for protecting against rockfalls or snow avalanches and has only recently been proposed for intercepting flow-like landslides. Their efficiency was largely analysing through MPM numerical simulations, however considering simplified constitutive models and different geometries for the structure.

The RC wall is very efficient when the flow energy is low, intercepting the whole landslide mass. The use of an inclined foundation proved to be useful if large displacements are expected. Moreover, long foundation platform and large cross-section of the stem could avoid an undesired breakage of the wall for bending of the stem. For DGRBs, it has been noted that some geometric features (such as the ratio B/H and the inclination of the impacted side of the barrier) contribute to reduce the occurrence of catastrophic failures, also preventing the overtopping of the barrier. To lengthen the major base remains a good solution for intercepting the flow path without excessive displacements and/or deformations of the barrier.

The assumption of rigid barrier used for the design of these barriers has been analysed. The numerical results showed that the hypothesis of rigid barrier is acceptable for the sake of safety since it undergoes higher impact forces and displacements than that achieved for a deformable barrier. However, additional stress-strain analyses of the barrier are needed for analysing the extent of deformations over the impacted zones of the structure. Finally, an overall comparison between the two typologies of barriers was conducted, showing that RC walls and DGRBs are both reasonable solutions to be used as passive protection structures against flow-like landslides. DGRBs have proved to be the best solution in a context of high-speed flows, while RC walls might be more efficient for flows with low energy.

8. Future developments

The potential of using a unitary approach for simulating flow-like landslide propagation and the stress-strain response of a structural element could be an interest topic for future research development. The response of a structure under impact remains a crucial issue since a proper constitutive model for the structural material must be found and a 3D modelling is needed to carefully reproduce the deformation mechanisms. However, there is still an issue of long computational time especially when large structures are considered. These limitations must be overcome in the future, expanding the research to new frontiers. For example, more advanced numerical modelling can help in the assessment of vulnerability curves for buildings that are subject to rapid flow landslides. Estimating the level of damage of a specific type of building for a range of landslide intensity parameter values is necessary for a proper landslide risk management.

MPM and other large-deformation modelling tools will play a significant role in the future developments about landslide modelling. For example, more sophisticated constitutive models for the flowing mass could be investigated, even considering the presence of viscous stresses inside the flow. This can help to understand the conditions in which these stresses could change the hydro-mechanical behaviour of the flow. It is also worth remembering that the proposed study is focused on the modelling of flows with a significant volumetric content of solids, this means that the statements made in the thesis could be extended for instance to real debris flows, but hardly to the case of hyperconcentrated flows.

The achieved results also open new frontiers to the study of the mechanisms governing the inception and formation of debris avalanches, thus encouraging the application of the proposed framework to further real cases to enhance the current

capability to forecast the occurrence of these hazardous phenomena. Also here, a 3D modelling of the propagation mechanism can really help in evaluating the amount of lateral spreading which makes the landslide volume increases inside triangular-shaped areas (avalanche formation) due to soil erosion along the landslide propagation path.

The thesis demonstrates that the accurate knowledge of the impact mechanism of the flows is crucial for the design of protection structures. Based on the achieved results, it appears that unfixed barriers may be a reasonable solution to stop the propagation of flow-like landslides. However, further studies are needed to investigate the feasibility of these structures and their practical implications in the framework of the landslide risk mitigation and management.

References

Al-Kafaji, I. (2013). Formulation of a dynamic material point method (MPM) for geomechanical problems. Ph.D. thesis, University of Stuttgart.

Arattano, M., and Franzi, L. J. N. H. (2003). On the evaluation of debris flows dynamics by means of mathematical models. Natural Hazards and Earth System Sciences, 3(6), 539-544.

Arbanas, Ž., Mihalić Arbanas, S., Vivoda, M., Peranić, J., Dugonjić Jovančević, S., & Jagodnik, V. (2014). Identification, monitoring and simulation of landslides in the Rječina River Valley, Croatia. In Proceedings of the SATREPS workshop on landslide risk assessment technology (pp. 29-30).

Armanini A. (1997). On the dynamic impact of debris flows, Recent developments on debris flows. Lecture Notes in Earth Science (Armanini and Michiue, Ed.). Berlin: Springer, 64, 208-224.

Armanini A. and Scotton P. (1993). On the dynamic impact of a debris flow on structures. Proceed. of XXV IAHR Congress, Tokyo Technical Session B, Debris flows and Landslides 3, 203-210.

Armanini, A., Larcher, M., and Odorizzi, M. (2011). Dynamic impact of a debris flow front against a vertical wall. In Proceedings of the 5th international conference on debris-flow hazards mitigation: mechanics, prediction and assessment, Padua, Italy (pp. 1041-1049).

Ashwood, W., and Hungr, O. (2016). Estimating total resisting force in flexible barrier impacted by a granular avalanche using physical and numerical modeling. Canadian Geotechnical Journal, 53(10), 1700-1717.

Bagnold, R. A. (1954). Experiments on a gravity-free dispersion of large solid spheres in a Newtonian fluid under shear. Proceedings of the Royal Society of London. Series A. Mathematical and Physical Sciences, 225(1160), 49-63.

Bandara, S., Ferrari, A., & Laloui, L. (2016). Modelling landslides in unsaturated slopes subjected to rainfall infiltration using material point method. International Journal for Numerical and Analytical Methods in Geomechanics, 40(9), 1358-1380.

Barbolini, M., Domaas, U., Faug, T., Gauer, P., Hákonardóttir, K. M., Harbitz, C. B., Rammer, L. (2009). The design of avalanche protection dams recent practical and theoretical developments.

Bilotta, E., Cascini, L., Foresta, V., & Sorbino, G. (2005). Geotechnical characterisation of pyroclastic soils involved in huge flowslides. Geotechnical & Geological Engineering, 23(4), 365-402.

Biot, M. A. (1941). General theory of three-dimensional consolidation. *Journal of applied physics*, *12*(2), 155-164.

Bishop, A. W. (1954). The use of pore-pressure coefficients in practice. Geotechnique, 4(4), 148-152.

Bowman, E.T., Laue, J., Imre, B., Springman, S.M. (2010). Experimental modelling of debris flow behaviour using a geotechnical centrifuge. Canadian Geotechnical Journal, 47(7), 742-762.

Brandl, H., and Blovsky, S., 2004. Protective barriers against rockfall. Proceedings of the 3rd European Geosynthetics Conference-Eurogéo III, Munich, Germany, pp. 95–100.

Brunet, G., Giacchetti, G., Bertolo, P., Peila, D., 2009. Protection from high energy rockfall impacts using Terramesh embankment: design and experiences. Proceedings of the 60th Highway Geology Symposium, Buffalo, New York, pp. 107–124.

Bugnion, L., McArdell, B. W., Bartelt, P., Wendeler, C. (2012). Measurements of hillslope debris flow impact pressure on obstacles. Landslides, 9(2), 179-187.

Bui, H. H., and Fukagawa, R. (2013). An improved SPH method for saturated soils and its application to investigate the mechanisms of embankment failure: Case of hydrostatic pore-water pressure. International Journal for numerical and analytical methods in geomechanics, 37(1), 31-50.

Calvello, M., Cuomo, S., Ghasemi, P. (2017). The role of observations in the inverse analysis of landslide propagation. *Computers and Geotechnics*, *92*, 11-21.

Calvetti, F., Di Prisco, C. G., Vairaktaris, E. (2017). DEM assessment of impact forces of dry granular masses on rigid barriers. Acta Geotechnica, 12(1), 129-144.

Canelli, L., Ferrero, A. M., Migliazza, M., and Segalini, A. (2012). Debris flow risk mitigation by the means of rigid and flexible barriers–experimental tests and impact analysis. *Natural Hazards and Earth System Sciences*, *12*(5), 1693-1699.

Cascini, L., Cuomo, S., & De Santis, A. (2011b). Numerical modelling of the December 1999 Cervinara flow-like mass movements (Southern Italy). Ital. J. Eng. Geol. Environ, 635644.

Cascini, L., Cuomo, S., & Della Sala, M. (2011a). Spatial and temporal occurrence of rainfall-induced shallow landslides of flow type: A case of Sarno-Quindici, Italy. Geomorphology, 126(1-2), 148-158.

Cascini, L., Cuomo, S., & Guida, D. (2008). Typical source areas of May 1998 flow-like mass movements in the Campania region, Southern Italy. Engineering Geology, 96(3-4), 107-125.

Cascini, L., Cuomo, S., Pastor, M. (2013a). Inception of debris avalanches: remarks on geomechanical modelling. Landslides, 10(6), 701-711.

Cascini, L., Cuomo, S., Pastor, M., & Rendina, I. (2016). SPH-FDM propagation and pore water pressure modelling for debris flows in flume tests. Engineering Geology, 213, 74-83.

Cascini, L., Cuomo, S., Pastor, M., & Sorbino, G. (2010). Modeling of rainfall-induced shallow landslides of the flow-type. Journal of Geotechnical and Geoenvironmental Engineering, 136(1), 85-98.

Cascini, L., Cuomo, S., Pastor, M., Sacco, C. (2013b). Modelling the post-failure stage of rainfall-induced landslides of the flow type. *Canadian Geotechnical Journal*, *50*(9), 924-934.

Ceccato F., Yerro A, Martinelli, M. (2018a). Modelling soil-water interaction with the material point method. Evaluation of single-point and double-point formulation. Numerical Methods in Geotechnical Engineering IX, pp.351-357.

Ceccato, F., Girardi, V., Yerro, A., & Simonini, P. (2019). Evaluation of dynamic explicit MPM formulations for unsaturated soils. VI International Conference on Particle-based Methods – Fundamentals and Applications PARTICLES 2019 E. Oñate, M. Bischoff, D.R.J. Owen P. Wriggers, , & T. Zohdi (Eds), 93-102.

Ceccato, F., Redaelli, I., di Prisco, C., & Simonini, P. (2018b). Impact forces of granular flows on rigid structures: comparison between discontinuous (DEM) and continuous (MPM) numerical approaches. Computers and Geotechnics, 103, 201-217.

Chen, H., and Lee, C. F. (2000). Numerical simulation of debris flows. *Canadian Geotechnical Journal*, *37*(1), 146-160.

Choi, C. E., Au-Yeung, S. C. H., Ng, C. W. W., Song, D. (2015). Flume investigation of landslide granular debris and water runup mechanisms. Géotechnique Letters, 5(1), 28-32.

Choi, C. E., Ng, C. W. W., Goodwin, G. R., Liu, L. H. D., Cheung, W. W. (2016). Flume investigation of the influence of rigid barrier deflector angle on dry granular overflow mechanisms. Canadian Geotechnical Journal, 53(10), 1751-1759.

Conte, E., Pugliese, L., Troncone, A. (2019). Post-failure stage simulation of a landslide using the material point method. Engineering Geology, 253, 149-159.

Corominas, J. (1996). The angle of reach as a mobility index for small and large landslides. Canadian Geotechnical Journal, 33(2), 260-271.

Cui, P., Zeng, C., and Lei, Y. (2015). Experimental analysis on the impact force of viscous debris flow. Earth Surface Processes and Landforms, 40(12), 1644-1655.

Cuomo, S. (2020). Modelling of flowslides and debris avalanches in natural and engineered slopes: a review. *Geoenvironmental Disasters*, 7(1),1-25.

Cuomo, S., and Della Sala, M. (2013). Rainfall-induced infiltration, runoff and failure in steep unsaturated shallow soil deposits. Engineering Geology, 162, 118-127.

Cuomo, S., Calvello, M., Ghasemi, P. (2017b). Propagation modeling and inverse analysis of a landslide in Hong Kong. In *Workshop on World Landslide Forum* (pp. 513-521). Springer, Cham.

Cuomo, S., Cascini, L., Pastor, M., Petrosino, S. (2017a). Modelling the propagation of debris avalanches in presence of obstacles. In Workshop on World Landslide Forum (pp. 469-475). Springer, Cham.

Cuomo, S., Di Perna, A., Ghasemi, P., Martinelli, M., Calvello, M. (2019a). Combined LEM and MPM analyses for the simulation of a fast moving landslide in Hong Kong. In Proc. of II International Conference on the Material Point Method for modelling soil–water–structure interaction. 8–10 January 2019, University of Cambridge, UK.

Cuomo, S., Di Perna, A., Martinelli, M. (2020a). Coupled hydro-mechanical modelling of a 1995 Hong Kong landslide. In E3S Web of Conferences (Vol. 195, p. 01028). EDP Sciences.

Cuomo, S., Moretti, S., Aversa, S. (2019b). Effects of artificial barriers on the propagation of debris avalanches. *Landslides*, *16(6),* 1077-1087.

Cuomo, S., Moretti, S., Frigo, L., & Aversa, S. (2020b). Performances of Geosynthetics-Reinforced Barriers for Protection Against Debris Avalanches. In Workshop on World Landslide Forum (pp. 341-347). Springer, Cham.

Cuomo, S., Moretti, S., Frigo, L., Aversa, S. (2019c). Deformation mechanisms of deformable geosynthetics-reinforced barriers (DGRB) impacted by debris avalanches. Bulletin of Engineering Geology and the Environment, 1-14.

Cuomo, S., Pastor, M., Cascini, L., & Castorino, G. C. (2014). Interplay of rheology and entrainment in debris avalanches: a numerical study. Canadian Geotechnical Journal, 51(11), 1318-1330.

Cuomo, S., Prime, N., Iannone, A., Dufour, F., Cascini, L., & Darve, F. (2013). Large deformation FEMLIP drained analysis of a vertical cut. *Acta Geotechnica*, *8*(2), 125-136.

Dai, Z., Huang, Y., Cheng, H., Xu, Q. (2017). SPH model for fluid–structure interaction and its application to debris flow impact estimation. Landslides, 14(3), 917-928.

De Natale, J. S., Iverson, R. M., Major, J. J., LaHusen, R. G., Fiegel, G. L., and Duffy, J. D. (1999). Experimental testing of flexible barriers for containment of debris flows. Reston: US Department of the Interior, US Geological Survey.

Deng, Q., Gong, L., Zhang, L., Yuan, R., Xue, Y., Geng, X., Hu, S. (2017). Simulating dynamic processes and hypermobility mechanisms of the Wenjiagou rock avalanche triggered by the 2008 Wenchuan earthquake using discrete element modelling. Bulletin of Engineering Geology and The Environment, 76(3), 923-936.

Descoeudres, F., (1997). Aspects géomécaniques des instabilités de falaises rocheuses et des chutes de blocs. Publications De La Société Suisse De Mécanique Des Sols et Des Roches 135, 3–11.

Devoli, G., De Blasio, F. V., Elverhøi, A., and Høeg, K. (2009). Statistical analysis of landslide events in Central America and their run-out distance. Geotechnical and Geological Engineering, 27(1), 23-42.

Ergun, S. (1952). Fluid flow through packed columns. Chemical Engineering Progress, 48, 89-94.

Faella, C., and Nigro, E. (2003). Dynamic Impact of the Debris Flows on the Constructions during the Hydrogeological Disaster in Campania-1998: description and Analysis of the Damages. In Proceedings of Int. Conf. on Fast

Slope Movements-Prediction and Prevention for Risk Mitigation (FSM2003), Napoli (Italy), 11-13.

Faug, T. (2015). Depth-averaged analytic solutions for free-surface granular flows impacting rigid walls down inclines. Physical Review E, 92(6), 062310.

Faug, T., Caccamo, P., & Chanut, B. (2011). Equation for the force experienced by a wall overflowed by a granular avalanche: experimental verification. Physical Review E, 84(5), 051301.

Favier, L., Daudon, D., Donzé, F. V., & Mazars, J. (2009). Predicting the drag coefficient of a granular flow using the discrete element method. Journal of Statistical Mechanics: Theory and Experiment, 2009(06), P06012.

Fern, J., Rohe, A., Soga, K., & Alonso, E. (2019). The material point method for geotechnical engineering: a practical guide. CRC Press.

Genuchten, Van M. (1980). A closed-form equation for predicting the hydraulic conductivity of unsaturated soils. Soil Sci. Soc. Am. J. 44, No. 4, 892-898.

GeoStudio Manual. (2012). Geo-slope international Ltd. Calgary, Alberta, Canada T2P 2Y5.

Ghasemi, P. (2019). Application of inverse analysis to geotechnical problems, from soil behaviour to large deformation modelling. PhD dissertation, University of Salerno, 230 pages.

Ghasemi, P., Cuomo, S., Di Perna, A., Martinelli, M., Calvello, M. (2019). MPM-analysis of landslide propagation observed in flume test. In Proc. of II International Conference on the Material Point Method for modelling soil–water–structure interaction. 8–10 January 2019, University of Cambridge, UK.

Gioffrè D, Mandaglio MC, di Prisco C, Moraci N (2017) Evaluation of rapid landslide impact forces against sheltering structures. Rivista Italiana di Geotecnica 3:79–91

Gras, J. P., Delenne, J. Y., El Youssoufi, M. S. (2013). Study of capillary interaction between two grains: a new experimental device with suction control. Granular Matter, 15(1), 49-56.

Haxaire, A., Galavi, V., & Brinkgreve, R. B. J. (2011). Fully coupled thermo-hydro-mechanical analysis for unsaturated soils in Plaxis. Delft University of Technology.

He, S., Liu, W., Li, X. (2016). Prediction of impact force of debris flows based on distribution and size of particles. Environmental Earth Sciences, 75(4), 298.

Hong, Y., Wang, J. P., Li, D. Q., Cao, Z. J., Ng, C. W. W., Cui, P. (2015). Statistical and probabilistic analyses of impact pressure and discharge of debris flow from 139 events during 1961 and 2000 at Jiangjia Ravine, China. Engineering Geology, 187, 122-134.

Hu, K., Wei, F., Li, Y. (2011). Real-time measurement and preliminary analysis of debris-flow impact force at Jiangjia Ravine, China. Earth Surface Processes and Landforms, 36(9), 1268-1278.

Huang, J., van Asch, T. W. J., Wang, C., Li, Q. (2019). Study on the combined threshold for gully-type debris flow early warning. Natural hazards and earth system sciences, 19(1), 41.

Huang, Y., and Zhang, B. (2020). Challenges and perspectives in designing engineering structures against debris-flow disaster. European Journal of Environmental and Civil Engineering, 1-22.

Hübl, J, and Holzinger, G. (2003). Entwicklung von Grundlagen zur Dimensionierung kronenoffener Bauwerke für die Geschiebebewirtschaftung in Wildbächen: Kleinmassstäbliche Modellversuche zur Wirkung von Murbrechern. WLS Report 50 Band 3, Institute of Mountain Risk Engineering (in German)

Hübl, J., Suda, J., Proske, D., Kaitna, R., Scheidl, C. (2009). Debris flow impact estimation. In Proceedings of the 11th international symposium on water management and hydraulic engineering, Ohrid, Macedonia, 1, 1-5.

Hungr, O., and McDougall, S. (2009). Two numerical models for landslide dynamic analysis. Computers & geosciences, 35(5), 978-992.

Hungr, O., Leroueil, S., Picarelli, L. (2014). The Varnes classification of landslide types, an update. Landslides, 11(2), 167-194.

Hungr, O., Morgan, G. C., Kellerhals, R. (1984). Quantitative analysis of debris torrent hazards for design of remedial measures. *Canadian Geotechnical Journal*, *21*(4), 663-677.

Idelsohn, S. R., Oñate, E., Pin, F. D. (2004). The particle finite element method: a powerful tool to solve incompressible flows with free-surfaces and breaking waves. International journal for numerical methods in engineering, 61(7), 964-989.

Iverson, R. M. (1997). The physics of debris flows. Reviews of geophysics, 35(3), 245-296.

Iverson, R. M., and George, D. L. (2014). A depth-averaged debris-flow model that includes the effects of evolving dilatancy. I. Physical basis. Proceedings of the Royal Society A: Mathematical, Physical and Engineering Sciences, 470(2170), 20130819.

Iverson, R. M., Logan, M., LaHusen, R. G., Berti, M. (2010). The perfect debris flow? Aggregated results from 28 large-scale experiments. Journal of Geophysical Research: Earth Surface, 115(F3).

Jeong, S., and Lee, K. (2019). Analysis of the impact force of debris flows on a check dam by using a coupled Eulerian-Lagrangian (CEL) method. Computers and Geotechnics, 116, 103214.

Kang, Z. C., Cui, P., Wei, F. Q., He, S. F. (2007). Data collection of observation of debris flows in Jiangjia Ravine, Dongchuan Debris Flow Observation and Research Station (1995-2000).

Kirk, P. A., Campbell, S. D. G., Fletcher, C. J. N., Merriman, R. J. (1997). The significance of primary volcanic fabrics and clay distribution in landslides in Hong Kong. *Journal of the Geological Society*, *154*(6), 1009-1019.

Knill, S.J. (1996). GEO REPORT No. 188, Hong Kong.

Koo, R. C. H., Kwan, J. S. H., Lam, C., Goodwin, G. R., Choi, C. E., Ng, C. W. W., Pun, W. K. (2017). Back-analysis of geophysical flows using three-dimensional runout model. *Canadian Geotechnical Journal*, *55*(8), 1081-1094.

Kwan, JSH. (2012). Supplementary technical guidance on design of rigid debris-resisting barriers. GEO Report No. 270, Geotechnical Engineering Office, Civil Engineering and Development Department, Hong Kong SAR Government.

Law, P.H. (2008). Investigations of mobility and impact behavior of granular flows. Ph.D. thesis, Hong Kong University of Science and Technology, Hong Kong.

Lee, W.L., Martinelli, M., Shiehi, C.L. (2019). Modelling rainfall-induced landslides with the material point method: the Fei Tsui Road case. In *Proceedings of the XVII ECSMGE-2019* (pp. 1-8)

Lei, X., He, S., Chen, X., Wong, H., Wu, L., Liu, E. (2020). A generalized interpolation material point method for modelling coupled seepage-erosion-deformation process within unsaturated soils. Advances in Water Resources, 141, 103578.

Leonardi, A., Wittel, F. K., Mendoza, M., Vetter, R., Herrmann, H. J. (2016). Particle–fluid–structure interaction for debris flow impact on flexible barriers. Computer-Aided Civil and Infrastructure Engineering, 31(5), 323-333.

Li, W. C., Deng, G., Cao, W., Xu, C., Chen, J., Lee, M. L. (2019). Discrete element modeling of the Hongshiyan landslide triggered by the 2014 Ms 6.5 Ludian earthquake in Yunnan, China. Environmental Earth Sciences, 78(16), 1-18.

Li, X., Wu, Y., He, S., Su, L. (2016). Application of the material point method to simulate the post-failure runout processes of the Wangjiayan landslide. Engineering Geology, 212, 1-9.

Lin, Y., Liu, G. R., Wang, G. (2019). A particle-based free surface detection method and its application to the surface tension effects simulation in smoothed particle hydrodynamics (SPH). Journal of Computational Physics, 383, 196-206.

Liu, F. Z., Xu, Q., Dong, X. J., Yu, B., Frost, J. D., Li, H. J. (2017). Design and performance of a novel multi-function debris flow mitigation system in Wenjia Gully, Sichuan. Landslides, 14(6), 2089-2104.

Liu, X., Wang, Y., Li, D. Q. (2020). Numerical simulation of the 1995 rainfall-induced Fei Tsui Road landslide in Hong Kong: new insights from hydro-mechanically coupled material point method. Landslides, 17(12), 2755-2775.

Llano-Serna, M.A., Farias, M.M. Pedroso, D.M. An assessment of the material point method for modelling large scale run-out processes in landslides. *Landslides* **13,** 1057–1066 (2016). https://doi.org/10.1007/s10346-015-0664-4

Martinelli, M. and Rohe, A. (2015). Modelling fluidisation and sedimentation using material point method. 1st Pan-American Congress on Computational Mechanics.

Martinelli, M., and Galavi, V. (2021). Investigation of the Material Point Method in the simulation of Cone Penetration Tests in dry sand. Computers and Geotechnics, 130, 103923.

Martinelli, M., Lee, W. L., Shieh, C. L., Cuomo, S. (2020). Rainfall Boundary Condition in a Multiphase Material Point Method. In *Workshop on World Landslide Forum*, Springer, Cham, 303-309.

McMeeking, R. M., and Rice, J. R. (1974). Finite element formulations for problems of large elastic-plastic deformation.

Merodo, J. F., Pastor, M., Mira, P., Tonni, L., Herreros, M. I., Gonzalez, E., & Tamagnini, R. (2004). Modelling of diffuse failure mechanisms of catastrophic landslides. Computer Methods in Applied Mechanics and Engineering, 193(27-29), 2911-2939.

Mieremet, M. M. J., Stolle, D. F., Ceccato, F., Vuik, C. (2016). Numerical stability for modelling of dynamic two-phase interaction. International Journal for Numerical and Analytical Methods in Geomechanics, 40(9), 1284-1294.

Mizuyama, T. (1979). Estimation of impact force on dam due to debris flow and its problems. Journal of the Japan Society of Erosion Control Engineering, 112, 40-43.

Mizuyama, T. (2008). Structural countermeasures for debris flow disasters. International Journal of Erosion Control Engineering, 1(2), 38-43.

Moresi, L., Dufour, F., Mühlhaus, H. B. (2002). Mantle convection modeling with viscoelastic/brittle lithosphere: Numerical methodology and plate tectonic modeling. Pure and applied Geophysics, 159(10), 2335-2356.

Moriguchi, S., Borja, R. I., Yashima, A., Sawada, K. (2009). Estimating the impact force generated by granular flow on a rigid obstruction. Acta Geotechnica, 4(1), 57-71.

Mualem, Y. (1976). A new model for predicting the hydraulic conductivity of unsaturated porous me-dia. Water resources research, 12(3), 513-522.

Ng, C. W. W., Majeed, U., Choi, C. E., and De Silva, W. A. R. K. (2021). New impact equation using barrier Froude number for the design of dual rigid barriers against debris flows. Landslides, 1-13.

Ng, C. W. W., Song, D., Choi, C. E., Liu, L. H. D., Kwan, J. S. H., Koo, R. C. H., and Pun, W. K. (2017). Impact mechanisms of granular and viscous flows on rigid and flexible barriers. Canadian Geotechnical Journal, 54(2), 188-206.

Ng, C. W. W., Wong, H. N., Tse, Y. M., Pappin, J. W., Sun, H. W., Millis, S. W., & Leung, A. K. (2011). A field study of stress-dependent soil-water characteristic curves and permeability of a saprolitic slope in Hong Kong. *Géotechnique*, *61*(6), 511.

Nguyen, T. S., Yang, K. H., Ho, C. C., Huang, F. C. (2021). Postfailure Characterization of Shallow Landslides Using the Material Point Method. Geofluids, 2021.

O'Brien, J. S., Julien, P. Y., and Fullerton, W. T. (1993). Two-dimensional water flood and mudflow simulation. Journal of hydraulic engineering, 119(2), 244-261.

Pastor M, Quecedo M, Gonzalez E, Herreros MI, Merodo JA, Mira P (2004). Modelling of Landslides: (II) Propagation. In: F. Darve and I. Vardoulakis, Eds. Degrad Instab Geomaterials, Springer Vienna, Vienna, 319–367

Pastor M, Quecedo M, Merodo JA, Herrores MI, Gonzalez E, Mira P (2002). Modelling tailings dams and mine waste dumps failures. Géotechnique 52(8):579–591

Pastor, M., Blanc, T., Haddad, B., Petrone, S., Morles, M. S., Drempetic, V., Cuomo, S. (2014). Application of a SPH depth-integrated model to landslide run-out analysis. *Landslides*, *11*(5), 793-812.

Pastor, M., Blanc, T., Pastor, M. J., Sanchez, M., Haddad, B., Mira, P., ... & Drempetic, V. (2007). A SPH depth integrated model with pore pressure coupling for fast landslides and related phenomena. In The 2007 International Forum on Landslide Disaster Management. Ho & Li (Eds.).

Pastor, M., Haddad, B., Sorbino, G., Cuomo, S., Drempetic, V. (2009). A depth-integrated, coupled SPH model for flow-like landslides and related phenomena. *International Journal for numerical and analytical methods in geomechanics*, *33*(2), 143-172.

Pastor, M., Tayyebi, S. M., Stickle, M. M., Yagüe, Á., Molinos, M., Navas, P., Manzanal, D. (2021). A depth integrated, coupled, two-phase model for debris flow propagation. Acta Geotechnica, 1-25.

Peila, D., Oggeri, C., Castiglia, C. (2007). Ground reinforced embankments for rockfall protection: design and evaluation of full scale tests. Landslides, 4(3), 255-265.

Plaxis, B. V. (2018). PLAXIS 2D reference manual. The Netherlands.

Prodan, M. V., Mileusnić, M., Arbanas, S. M., & Arbanas, Ž. (2017). Influence of weathering processes on the shear strength of siltstones from a flysch rock mass along the northern Adriatic coast of Croatia. Bulletin of engineering geology and the environment, 76(2), 695-711.

Proske, D., Suda, J., Hübl, J. (2011). Debris flow impact estimation for breakers. Georisk, 5(2), 143-155.

Qiu, G., Henke, S., Grabe, J. (2011). Application of a Coupled Eulerian–Lagrangian approach on geomechanical problems involving large deformations. Computers and Geotechnics, 38(1), 30-39.

Ronco, C., Oggeri, C., Peila, D. (2009). Design of reinforced ground embankments used for rockfall protection. Natural Hazards and earth system sciences, 9(4), 1189-1199.

Sanchez, M. E., Pastor, M., Romana, M. G. (2013). Modelling of short runout propagation landslides and debris flows. *Georisk: Assessment and Management of Risk for Engineered Systems and Geohazards*, *7*(4), 250-266.

Scheidl, C., Chiari, M., Kaitna, R., Müllegger, M., Krawtschuk, A., Zimmermann, T., Proske, D. (2013). Analysing debris-flow impact models, based on a small scale modelling approach. Surveys in Geophysics, 34(1), 121-140.

Schofield, A. N. (1980). Cambridge geotechnical centrifuge operations. Geotechnique 30(3), 227-268.

Scholtès, L., Hicher, P. Y., Nicot, F., Chareyre, B., Darve, F. (2009). On the capillary stress tensor in wet granular materials. International journal for numerical and analytical methods in geomechanics, 33(10), 1289-1313.

Scotton, P., and Deganutti, A.M. (1997). Phreatic Line and Dynamic Impact in Laboratory Debris Flow Experiments.

Shen, W., Zhao, T., Zhao, J., Dai, F., & Zhou, G. G. (2018). Quantifying the impact of dry debris flow against a rigid barrier by DEM analyses. Engineering Geology, 241, 86-96.

Shieh, C. L., Ting C. H., Pan H. W. (2008). Impulsive force of debris flow on a curved dam. International Journal of Sediment Research 23(2), 149-158.

Soga, K., Alonso, E., Yerro, A., Kumar, K., Bandara, S. (2016). Trends in large-deformation analysis of landslide mass movements with particular emphasis on the material point method. Géotechnique, 66(3), 248-273.

Song, D., Choi, C. E., Ng, C. W. W., Zhou, G. G. D. (2018). Geophysical flows impacting a flexible barrier: effects of solid-fluid interaction. Landslides, 15(1), 99-110.

Song, D., Ng, C. W. W., Choi, C. E., Zhou, G. G., Kwan, J. S., Koo, R. C. H. (2017). Influence of debris flow solid fraction on rigid barrier impact. Canadian geotechnical journal, 54(10), 1421-1434.

Song, D., Zhou, G. G., Chen, X. Q., Li, J., Wang, A., Peng, P., Xue, K. X. (2021). General equations for landslide-debris impact and their application to debris-flow flexible barrier. Engineering Geology, 288, 106154.

Sovilla, B., Faug, T., Köhler, A., Baroudi, D., Fischer, J. T., Thibert, E. (2016). Gravitational wet avalanche pressure on pylon-like structures. Cold Regions Science and Technology, 126, 66-75.

Sulsky, D., Chen, Z., Schreyer, H. L. (1994). A particle method for history-dependent materials. Computer methods in applied mechanics and engineering, 118(1-2), 179-196.

Takahashi T. (2014). Debris flow: mechanics, prediction and countermeasures. CRC Press,

Tang, C., van Asch, T. W., Chang, M., Chen, G. Q., Zhao, X. H., & Huang, X. C. (2012). Catastrophic debris flows on 13 August 2010 in the Qingping area, southwestern China: the combined effects of a strong earthquake and subsequent rainstorms. Geomorphology, 139, 559-576.

Thouret, J. C., Antoine, S., Magill, C., Ollier, C. (2020). Lahars and debris flows: Characteristics and impacts. Earth-Science Reviews, 201, 103003.

Vagnon, F. (2020). Design of active debris flow mitigation measures: A comprehensive analysis of existing impact models. Landslides, 17(2), 313-333.

Vagnon, F., and Segalini, A. (2016). Debris flow impact estimation on a rigid barrier. Natural Hazards and Earth System Sciences, 16(7), 1691-1697.

Wang, B., Vardon, P. J., Hicks, M. A. (2018). Rainfall-induced slope collapse with coupled material point method. Engineering Geology, 239, 1-12.

Wang, F., and Sassa, K. (2010). Landslide simulation by a geotechnical model combined with a model for apparent friction change. *Physics and Chemistry of the Earth, Parts A/B/C*, *35*(3-5), 149-161.

Wang, Y. H., and Yan, W. M. (2006). Laboratory studies of two common saprolitic soils in Hong Kong. *Journal of Geotechnical and Geoenvironmental Engineering*, *132*(7), 923-930.

Wendeler C, Volkwein A, Denk M, Roth A, Wartmann S. (2007). Field measurements used for numerical modelling of flexible debris flow barriers. Proceedings of fourth international conference on debris flow hazards mitigation: mechanics, prediction, and assessment, 10–13 September 2007. Chengdu, China, pp 681–687

Wendeler C. (2016). Debris flow protection systems for mountain torrents - basic principles for planning and calculation of flexible barriers. WSL Bericht 44. ISSN 2296-3456

Xu, Q., Zhang, S., Li, W. L., Van Asch, T. W. (2012). The 13 August 2010 catastrophic debris flows after the 2008 Wenchuan earthquake, China. Natural Hazards and Earth System Sciences, 12, 201-216.

Yerro Colom, A. (2015). MPM modelling of landslides in brittle and unsaturated soils. PhD Dissertation, UPC, Spain.

Yerro, A., Alonso, E., Pinyol, N. (2016). Modelling large deformation problems in unsaturated soils. In E3S Web of Conferences (Vol. 9, p. 08019). EDP Sciences.

Yerro, A., Soga, K., Bray, J. (2019). Runout evaluation of Oso landslide with the material point method. Canadian Geotechnical Journal, 56(9), 1304-1317.

Yifru, A. L., Laache, E., Norem, H., Nordal, S., Thakur, V. (2018). Laboratory investigation of performance of a screen type debris-flow countermeasure. HKIE Transactions, 25(2), 129-144.

Yu, B., Zhu, Y., Wang, T., Chen, Y., Zhu, Y., Tie, Y., Lu, K. (2014). A prediction model for debris flows triggered by a runoff-induced mechanism. Natural hazards, 74(2), 1141-1161.

Yuan, C., Moscariello, M., Cuomo, S., Chareyre, B. (2019). Numerical simulation of wetting-induced collapse in partially saturated granular soils. *Granular Matter*, *21*(3), 64.

Yuan, W. H., Liu, K., Zhang, W., Dai, B., Wang, Y. (2020). Dynamic modeling of large deformation slope failure using smoothed particle finite element method. *Landslides*, 1-13.

Zeng, C., Cui, P., Su, Z., Lei, Y., and Chen, R. (2015). Failure modes of reinforced concrete columns of buildings under debris flow impact. Landslides, 12(3), 561-571.

Zhang S. C. (1993). A comprehensive approach to the observation and prevention of debris flows in China. Natl Hazards 7(1),1-23

Zhang, J., and Xiong, G. (1997). Data collection of kinematic observation of debris flows in Jiangjia Ravine, Dongchuan, Yunnan (1987-1994).

Zhao, C. F., Kruyt, N. P., Millet, O. (2019). Capillary bridges between unequal-sized spherical particles: Rupture distances and capillary forces. Powder technology, 346, 462-476.

Zhao, L., Liu, X., Mao, J. (2020). Three-dimensional distance potential discrete element method for the numerical simulation of landslides. *Landslides* **17,** 361–377.

Zhou, G. G. D., Song, D., Choi, C. E., Pasuto, A., Sun, Q. C., and Dai, D. F. (2018). Surge impact behavior of granular flows: effects of water content. Landslides, 15(4), 695-709.

Zienkiewicz, O. C., Chan, A. H. C., Pastor, M., Schrefler, B. A., & Shiomi, T. (1999). Computational geomechanics (Vol. 613). Chichester: Wiley.

Appendix 1. Material Point Method: main features

A 1. 1. Fundamental aspects

The Material Point Method (MPM) can be considered a modification of the well-known FEM, and it is particularly suited for large deformations (Sulsky et al. 1994). The continuum body is schematized by a set of Lagrangian points, called Material Points (MPs). Large deformations are modelled by a set of MPs moving through a background mesh, which covers also the domain where the material is expected to move. The MPs carry all the physical properties of the continuum such as stress, strain, density, momentum, material parameters and other state parameters, whereas the background mesh is used to solve the governing equations without storing any permanent information. The information is transferred from MPs to the computational mesh. The governing equations are solved at the grid nodes, whereas strains and stresses are calculated at the MPs. The position of the MPs is then updated using nodal displacements. Lastly, the computational mesh is reset back to its initial configuration.

The interaction between phases (solid and liquid in a saturated soil) can be tacked through the *two-phase single-point* formulation (Jassim et al, 2013; Ceccato et al. 2018), where the liquid and the solid acceleration fields ($\mathbf{a}_S - \mathbf{a}_L$ formulation) are the primary unknowns (Fern et al. 2019). Instead, the so-called *one-phase single-point* formulation can be opportunely adopted for dry soils.

A 1. 2. One-phase formulation

The conservation of mass is reported in Eq. A1 and is automatically satisfied as the solid mass remains constant in each MP during deformation.

$$\frac{d\rho}{dt} + \rho\nabla \cdot \mathbf{v} = \mathbf{0} \tag{A1}$$

The conservation of momentum includes the conservation of both linear and angular momentum. The former is represented by the equation of motion, even known as Newton's second law (Eq. A2), while the conservation of angular momentum refers to the symmetry condition of the stress matrix ($\boldsymbol{\sigma} = \boldsymbol{\sigma}^T$).

$$\rho \frac{d\mathbf{v}}{dt} = \nabla\boldsymbol{\sigma}^T + \rho\boldsymbol{g} \tag{A2}$$

Finally, the constitutive equation needs to be expressed to include the stress-strain dependency (Eq. A3). To simulate large deformations and rotations, the Jaumann stress rate can be considered, unlike the Cauchy one which is limited to small strain rate.

$$\mathrm{d}\dot{\boldsymbol{\sigma}} = \mathbf{D} \cdot \mathrm{d}\dot{\boldsymbol{\varepsilon}} \tag{A3}$$

In undrained conditions, the stress state can be described in terms of effective stresses. The excess pore pressures can be computed by means of the so-called Effective Stress Analysis (Eq. A4), which assumes strain compatibility between the solid skeleton and the interstitial liquid (Vermeer, 1993).

$$\Delta p_L = \mathrm{K}_L \Delta\varepsilon_{vol} \tag{A4}$$

The time integration scheme considered in MPM is explicit, since most of the dynamic problems, including wave or shock propagation, cannot be treated properly by an implicit integration which tends to smooth the solution (Fern et al., 2019).

Let's consider the critical time step Δt_{cr} as the time increment during which a wave with speed c crosses the smallest element length *d* (Eq. A5).

$$\Delta t_{cr} = \frac{d}{c} = \frac{d}{\sqrt{E/\rho}} \quad \text{(A5)}$$

The critical time step defines the biggest time increment which can be used for a stable calculation, but often it can't be estimated in case of non-linear problems. For this reason, the critical time step is multiplied by an additional factor C_{NB} (namely Courant number) in order to reach stability. The Courant number has values between 0 and 1. Generally, the smaller the Courant number and the smaller the time step, improving the accuracy of the numerical results.

A 1. 3. Two-phase formulation

A saturated porous medium is schematized as a solid phase which represents the solid skeleton, whereas the liquid phase fills the voids among the grains. Each MP represents a volume of the mixture V, given by the sum of the solid V_S and liquid V_L phases volumes. The behaviour of a saturated porous medium is here described using only one set of MPs, in which the information about both the solid and liquid constituents is stored.

The velocity field of solid and liquid phases are both used, but the material points move throughout the mesh with the kinematics of the solid skeleton. The equations to be solved concern the balance of dynamic momentum of solid and liquid phases, the mass balances, and the constitutive relationships of solid and liquid phases. The accelerations of the two phases are the primary unknowns: the solid acceleration $\mathbf{a}_S$, which is calculated from the dynamic momentum balance of the solid phase (Eq. A6), and the liquid acceleration $\mathbf{a}_L$, which is obtained by solving the dynamic momentum balance of the liquid phase (Eq. A7). The interaction force between solid and liquid phases is governed by Darcy's law (Eq. A8). Numerically, these equations are solved at grid nodes considering the Galerkin method (Luo et al., 2008) with standard nodal shape functions and their solutions are used to update the

MPs velocities and momentum of each phase. The strain rate $\dot{\boldsymbol{\varepsilon}}$ of MPs is computed from the nodal velocities obtained from the nodal momentum.

$$n_S \rho_S \mathbf{a}_S = \nabla \cdot (\sigma - n p_L \mathbf{I}) + (\rho_m - n\rho_L)\mathbf{b} + \mathbf{f}_d \tag{A6}$$

$$\rho_L \mathbf{a}_L = \nabla p_L - \mathbf{f}_d \tag{A7}$$

$$\mathbf{f}_d = \frac{n\mu_L}{k}(\mathbf{v}_L - \mathbf{v}_S) \tag{A8}$$

The resolution of solid and liquid constitutive laws (Eqs. A9-A10) allows calculating the increment of effective stress $d\boldsymbol{\sigma}'$ and excess pore pressure dp_L, respectively. The mass balance equation of the solid skeleton is then used to update the porosity of each MP (Eq. A11), while the total mass balance serves to compute the volumetric strain rate of the liquid phase (Eq. A12) since fluxes due to spatial variations of liquid mass are neglected ($\nabla n\rho_L = 0$).

$$\mathrm{d}\boldsymbol{\sigma}' = \mathbf{D} \cdot \mathrm{d}\boldsymbol{\varepsilon} \tag{A9}$$

$$\mathrm{d}p_L = \mathbf{K}_L \cdot \mathrm{d}\varepsilon_{\boldsymbol{vol}} \tag{A10}$$

$$\frac{Dn}{Dt} = n_S \nabla \cdot \mathbf{v_S} = \mathbf{0} \tag{A11}$$

$$\frac{D\varepsilon_{vol}}{Dt} = \frac{n_S}{n}\nabla \cdot \mathbf{v_S} + \nabla \cdot \mathbf{v_L} \tag{A12}$$

In the two-phase single-point formulation the liquid mass, and consequently the mass of the mixture, is not constant in each material point but can vary depending on porosity changes. Fluxes due to spatial variations of liquid mass are neglected and Darcy's law is used to model solid-liquid interaction forces. For this reason, this formulation is generally used in problems with small gradients of porosity, and laminar and stationary flow in slow velocity regime. However, this formulation proves to be suitable for studying flow-structured-interaction (Cuomo et al., 2021). The water is assumed linearly compressible via the bulk modulus of the fluid $\mathbf{K}_L$ and shear stresses in the liquid phase are neglected.

The current MPM code uses 3-node elements which suffer kinematic locking, which consists in the build-up of fictitious stiffness due to the inability to reproduce the correct deformation field (Mast et al., 2012). A technique used to mitigate volumetric locking is the strain smoothening technique, which consists of smoothing the volumetric strains over neighbouring cells. The reader can refer to Al-Kafaji (2013) for a detailed description.

Regarding the critical time step, the influence of permeability and liquid bulk modulus must be considered as well (Mieremet et al., 2016). In particular, the time step required for numerical stability is smaller in soil with lower permeability (Eq. A13).

$$\Delta t_{cr} = min\left(\frac{d}{\sqrt{(E+\mathbf{K}_L/n)/\rho_m}}; \frac{2(\rho_m+(1/n-2)\rho_L)k_{sat}}{\rho_L \boldsymbol{g}}\right) \quad \text{(A13)}$$

The sliding modelling of the flowing mass on the rigid material is handled by a frictional Mohr-Coulomb strength criterion. The contact formulation was used to ensure that no interpenetration occurs, and the tangential forces are compatible with the shear strength along the contact. The reaction force acting on the structure at node *j* was calculated as in Eq. A14.

$$F_j(t) = m_{j,S}\Delta a_{S,contact} + m_{j,L}\Delta a_{L,contact} \quad \text{(A14)}$$

The terms $\Delta a_{S,contact}$ and $\Delta a_{L,contact}$ are the change in acceleration induced by the contact formulation, for both solid and liquid phase, and $m_{i,S}$ and $m_{i,L}$ are the corresponding nodal masses. The total reaction force is the integral of the nodal reaction forces along the barrier.